Investigating pro-metastatic functions of the MNK1/2-eIF4E signaling axis in breast cancer

Samuel Preston
Division of Experimental Medicine, Faculty of Medicine
McGill University, Montréal, Canada
April 2023

A thesis submitted to McGill University in partial fulfilment of the requirements of the degree of Doctor of Philosophy (Ph.D.)

Table of Contents

Abstract

Breast cancer is the most commonly diagnosed cancer in females, and the leading cause of cancer-related death. For patients with metastatic disease, there are currently no curative treatment options and survival rates remain low. Thus, the ability to successfully target breast cancer metastasis remains an unmet clinical need. Dysregulation of mRNA translation is known to promote mechanisms of breast cancer onset and progression, as exemplified by the MNK1/2-eIF4E signaling axis. This thesis investigates hitherto unknown pro-metastatic functions of MNK1/2-eIF4E signaling in multiple components of the tumor microenvironment.

We first explored the role of eIF4E phosphorylation in regulating the composition of the mammary gland extracellular matrix (ECM). By performing proteomics on isolated murine ECM samples, we demonstrated that phospho-eIF4E-deficient mice have reduced deposition of collagen type I in naïve and tumor-bearing mammary glands, compared to wild-type mice. Consequently, this collagen type I-poor matrix inhibited ECM-induced tumor cell invasion *in vitro* and metastasis *in vivo*. Moreover, using second harmonic generation microscopy, we showed that phospho-eIF4E impacts collagen fiber topology at the tumor-stroma boundary. Tumors formed in phospho-eIF4E-deficient mammary glands are surrounded by fibers that run parallel to the tumor edge, while more radially-aligned fibers were observed surrounding tumors grown in wild-type mice. We additionally observed that targeting eIF4E phosphorylation genetically and pharmacologically helps to resist anti-PD-1 therapy-induced intratumoral collagen deposition, which correlated with an increased anti-tumor response to immunotherapy.

Finally, we developed immunostaining protocols to identify a positive correlation between collagen-I and phospho-eIF4E protein levels in patient-derived tumor samples and improved our understanding of the spatial heterogeneity of stromal phospho-eIF4E expression.

Next, we investigated the role of tumor-intrinsic MNK1 kinase activity in influencing breast cancer stem cell properties. We used CRISPR/Cas9 gene editing to generate MNK1 knock-out (KO) breast cancer cell lines and observed a reduction of stemness properties *in vitro*, resulting in slowed tumor growth *in vivo*. Analysis of proteomic and RNA-sequencing data suggested that MNK1 KO cells had rewired their metabolism by downregulating expression of glycolysis-related enzymes. We validated this finding using stable isotope tracer analysis and bioenergetic assessment, and further demonstrated a subsequent energetic dependence on oxidative phosphorylation. Overall, these changes led to a restriction of metabolic flexibility in MNK1 KO tumor cells that could be therapeutically exploited. This translated to suppressed metastasis of MNK1 KO tumor cells to the liver *in vivo*, but not the lung. Finally, we analyzed publicly available protein expression data from patient-derived tumor samples and found a strong positive correlation between MNK1 and several glycolytic enzymes.

Together, these studies define previously unknown consequences of targeting the MNK1/2-eIF4E axis in breast cancer, including regulation of mammary gland collagen architecture and tumor cell metabolism. This thesis further helps to position inhibitors of mRNA translation, particularly MNK1/2 inhibitors, as promising therapeutic options to augment the efficacy of existing anti-cancer therapies.

Résumé

Le cancer du sein est le cancer le plus fréquemment diagnostiqué chez les femmes ainsi que la première cause de mortalité liée au cancer. Pour les patientes atteintes d'un cancer métastatique, il n'existe actuellement aucune option de traitement curatif et le taux de survie reste faible. Pouvoir cibler avec succès les métastases du cancer du sein demeure donc un besoin clinique non satisfait. Le déséquilibre de la traduction de l'ARNm est connu pour favoriser les mécanismes de cancérisation du cancer du sein, comme l'illustre l'axe de signalisation MNK1/2-eIF4E. Cette thèse étudie les fonctions pro-métastatiques jusqu'à présent inconnues de la signalisation MNK1/2-eIF4E dans de multiples composants du microenvironnement tumoral.

Nous avons d'abord regardé le rôle de la phosphorylation d'eIF4E dans la régulation de la composition de la matrice extracellulaire (ECM) de la glande mammaire. En réalisant des analyses protéomiques sur des échantillons de la matrice extracellulaire murine, nous avons démontré que chez les souris déficientes en phospho-eIF4E, les glandes mammaires naïves et porteuses de tumeurs ont une déposition réduite de collagène de type I, par rapport aux souris de type sauvage. Par conséquent, cette matrice appauvrie en collagène de type I permet de bloquer l'invasion des cellules tumorales facilitées par l'ECM *in vitro* et les métastases *in vivo*. De plus, en utilisant la microscopie à génération de seconde harmonique, nous avons montré que phospho-eIF4E a un impact sur la topologie des fibres de collagène à la ligne de démarcation entre la tumeur et le stroma. Les tumeurs formées dans des glandes mammaires déficientes en phospho-eIF4E sont entourées de fibres parallèles au bord de la tumeur, alors que

l’opposé a été observé autour des tumeurs cultivées chez des souris de type sauvage. Nous avons également remarqué que le cibler de façon génétique et pharmacologique phosphorylation de l'eIF4E permettait de résister au dépôt de collagène au sein de tumeur traitées aux anti-PD-1, conduisant à une réponse anti-tumorale accrue aux immunothérapies. Enfin, nous avons développé des protocoles d'immunomarquage démontrant une corrélation positive entre les niveaux de collagène de type I et de la protéine phospho-eIF4E dans des échantillons de patients et nous avons amélioré notre compréhension de l’organisation spatiale de l'expression phospho-eIF4E et son hétérogénéité dans le stroma.

Nous avons ensuite étudié la manière dont la kinase MNK1 propre à la tumeur influence les propriétés de cellules souches du cancer du sein. Nous avons utilisé la technique d'édition de gènes CRISPR/Cas9 pour générer des lignées cellulaires de cancer du sein dépourvues de MNK1 (MNK1 KO) et avons observé une réduction des propriétés de pluripotence *in vitro*, résultant en un ralentissement de la croissance tumorale *in vivo*. L'analyse des données protéomiques et de séquençage de l'ARN suggère que les cellules MNK1 KO ont modifié leur métabolisme en réduisant l'expression d’enzymes liées à la glycolyse. Nous avons validé cette découverte en utilisant des traceurs isotopiques stables pour l’évaluation bioénergétique des cellules. Nous avons également démontré une dépendance énergétique conséquente à la phosphorylation oxydative. Dans l'ensemble, ces changements ont conduit à une restriction dans la flexibilité métabolique des cellules tumorales MNK1 KO qui peut être exploitée sur le plan thérapeutique. Cela s'est traduit par la suppression des métastases

des cellules tumorales MNK1 KO dans le foie *in vivo*, mais pas dans le poumon. Enfin, nous avons analysé les données d'expression des protéines disponibles publiquement à partir d'échantillons de tumeurs dérivées de patients et avons trouvé une forte corrélation positive entre MNK1 et plusieurs enzymes glycolytiques.

Ces études présentent des répercussions jusqu'alors inconnues du ciblage de l'axe MNK1/2-eIF4E dans le cancer du sein, y compris la régulation de l'architecture du collagène de la glande mammaire et du métabolisme des cellules tumorales. Cette thèse contribue également à installer les inhibiteurs de la traduction de l'ARNm, en particulier les inhibiteurs de MNK1/2, comme des options thérapeutiques prometteuses pour augmenter l'efficacité des thérapies anticancéreuses existantes.

Acknowledgements

First and foremost, I would like to first thank my supervisors, Dr. Sonia del Rincón and Dr. Wilson Miller, for funding my projects, accepting me in their lab, and creating an uplifting environment in which to pursue research. I have enormous gratitude for Dr. del Rincón, who saw potential in me when I did not. She has been instrumental to my growth as a scientist and a person, and will remain a source of inspiration during the many adventures to come. My successes are deeply rooted in her insightful guidance, the importance of which cannot be overstated – thank you Sonia. I deeply appreciate the guidance, critique, and banter of Dr. Miller. His scientific input has been invaluable, and his passion to translate findings from bench to bedside has framed my work.

Special thanks must be given to the members of my supervisory committee: Dr. Stephanie Lehoux, Dr. Josie Ursini-Siegel, and Dr. Alexandre Orthwein. Their encouragement and feedback have been immensely helpful. To Dr. Koren Mann, thank you for being a fabulous mentor and an even better friend. In addition, I want to thank Kathy Ann Forner and Véronique Michaud for their assistance in animal modelling and Christian Young for his help in learning flow cytometry. Their expertise and patient training provided much needed support in the face of daunting technical challenges. I further extend my gratitude to Dr. René Zahedi, Dr. Vincent Richard, Dr. François Légaré, and Arash Aghigh, for their outstanding collaboration.

It has been a joy to work with the incredible people of the del Rincón, Miller and Mann teams, and I express my deep appreciation to them all. The support of Christophe Gonçalves is immeasurable. I owe much of my scientific training to his teaching and wisdom. Without his dedication, and that of Cynthia Guilbert, the lab simply would not function. Thank you to Dr. Fan Huang, Madelyn Abraham and Julian Smith-Voudouris for their comradery in the lab and, more importantly, their friendship outside of it. Thank you to Dr. Michael Dahabieh and Cassandra Bellver for grounding me and providing much-needed perspective. Thank you to Dr. Margarita Bartish, Dr. Qianyu Guo and Natascha Gagnon for their generous support with countless experiments. I am grateful for every team member that I have had the pleasure of working alongside.

Finally, a special thanks must go to my friends and family. It is difficult to summarize how important their unwavering love and support has been in helping me through the highs and lows of the last five years. Mum and Dad, you have always been a

phone call away, and have never failed to tell me how pursuing my passion has made you proud. I am eternally grateful for all that you have sacrificed. To my friends back home, thank you for always being there, even when a pandemic kept us apart. Finally, to the wonderful people I met when I first moved to Montréal, you made a new city feel like home. This journey has been more transformative than I could have ever predicted, and without you all I would have had nowhere near as much fun.

Contribution to original knowledge

Metastatic breast cancer remains an unmet clinical need with limited therapeutic options available for patients. This thesis investigates the contribution of the MNK1/2-eIF4E signaling axis in promoting mechanisms of breast cancer progression and metastasis. The elements of the included work that are original scholarship, and distinct contributions to knowledge, are outlined below.

- In Chapter 2, we performed novel characterization of how the MNK1/2-eIF4E axis regulates the composition of the mammary gland ECM. This study was the first to assess how targeting eIF4E phosphorylation in fibroblasts specifically impacts the matrisomal proteins they produce.
- We identified collagen-I as a previously unknown target of translational regulation by phospho-eIF4E, but emphasize that control of collagen-I deposition by the MNK1/2-eIF4E axis likely occurs through multiple mechanisms.
- In addition to collagen-I deposition, Chapter 2 is the first study to identify that eIF4E phosphorylation can alter the alignment of collagen fibers both *in vitro* and *in vivo*.

- We showed that targeting eIF4E phosphorylation genetically or therapeutically inhibits anti-PD-1-mediated intratumoral collagen deposition to maintain sensitivity to treatment. This builds on previously-reported evidence from our team to suggest that MNK1/2 inhibition can augment the efficacy of immunotherapies.
- Using dual-target immunostaining protocols, we revealed that phospho-eIF4E and collagen-I protein levels are positively correlated in breast cancer patient samples. We further improved our knowledge of eIF4E phosphorylation heterogeneity in the breast TME, showing that stromal phospho-eIF4E is influenced by spatial proximity to the tumor.
- In Chapter 3, we generated novel MNK1-null murine breast cancer cell lines to perform multi-omics analysis and assess the differential expression of genes and proteins in a tumor-intrinsic MNK1-deficient context.
- We uncovered a link between MNK1 kinase expression and regulation of cellular metabolism. In particular, we showed that MNK1-null tumor cells downregulate glycolytic activity and subsequently increase their dependence on oxidative phosphorylation. We are the first to demonstrate that targeting MNK1 kinase can restrict tumor cell metabolic flexibility, and propose a novel therapeutic combination of MNK1/2 inhibitors and inhibitors of mitochondrial metabolism.
- Chapter 3 was the first study to assess how tumor-intrinsic MNK1 kinase can influence site-specific metastatic potential. Using murine models of experimental metastasis, we demonstrated that MNK1-null tumor cells have an impaired ability to colonize the liver, but not the lung.

- Finally, we analyzed publicly-available protein data from breast cancer patient samples to uncover a strong correlation between MNK1 expression level and the expression of glycolytic enzymes.

Contribution of Authors

The candidate, Samuel Preston, performed the majority of the research described in this thesis under the supervision of Dr. Sonia del Rincón and Dr. Wilson Miller. The detailed contributions of authors to this work are outlined below.

Chapters 1 and 4:

The candidate wrote and revised both chapters, and created Figures 1.1, 1.2 and 1.3. Sonia del Rincón reviewed and edited both chapters.

Chapter 2:

The candidate, Sonia del Rincón, Christophe Gonçalves, Vincent Richard, René Zahedi, Christoph Borchers, Arash Aghigh, and François Légaré helped design and conceptualize research studies. The candidate performed the majority of data acquisition and analysis. Margarita Bartish, Vincent Richard, Arash Aghigh, Christophe Gonçalves, Julian Smith-Voudouris, and Fan Huang contributed to data acquisition and provided technical support. Vincent Richard, Arash Aghigh, and René Zahedi aided data analysis and interpretation. Lynne-Marie Postovit, Réjean Lapointe, Paméla Thébault, and Aurélie Cleret-Buhot facilitated access to patient-derived samples and clinical data. The candidate wrote the manuscript and created all figures (Graphical abstract, Figures 2.1-2.7, and Supplementary Figures 2.1-2.5). Margarita Bartish, Vincent Richard, Arash

Aghigh, Réjean Lapointe, François Légaré, Lynne-Marie Postovit, René Zahedi, Christoph Borchers, Wilson Miller, and Sonia del Rincón reviewed the manuscript. The candidate revised the manuscript. Sonia del Rincon and Wilson Miller. supervised the study. Sonia del Rincón, Wilson Miller, René Zahedi, and Christoph Borchers secured study funding.

Chapter 3:

The candidate, Sonia del Rincón, Michael Dahabieh, Vincent Richard, René Zahedi, Christoph Borchers, and Russell Jones helped design and conceptualize research studies. The candidate performed the majority of data acquisition and analysis. Michael Dahabieh, Vincent Richard, Natascha Gagnon, and Eleanor Dakin contributed to data acquisition and provided technical support. Michael Dahabieh, Vincent Richard, and Christophe Gonçalves aided data analysis and interpretation. The candidate wrote the manuscript and created all figures (Figures 3.1-3.6 and Supplementary Figures 3.1-3.4). Sonia del Rincón and Wilson Miller reviewed the manuscript. The candidate edited the manuscript. Sonia del Rincón and Wilson Miller supervised the study and secured study funding.

Publications arising from this work

Chapter 2 was published as an original research article:

Preston SEJ, Bartish M, Richard VR, Aghigh A, Gonçalves C, Smith-Voudouris J, Huang F, Thébault P, Cleret-Buhot A, Lapointe R, Légaré F, Postovit L-M, Zahedi RP, Borchers CH, Miller Jr. WH, del Rincón SV. Phosphorylation of eIF4E in the stroma

drives the production and spatial organisation of collagen type I in the mammary gland. *Matrix Biology* (2022). 111:264-288.

Chapter 3 contains material to be included in a manuscript in preparation as an original research article:

Preston SEJ, Dahabieh MS, Richard VR, Gagnon N, Dakin E, Zahedi RP, Jones RG, Miller Jr. WH, del Rincón SV. Targeting tumor-intrinsic MNK1 kinase restricts metabolic flexibility to diminish breast cancer liver metastasis. *In preparation* (2023)

Publications that include work performed by the candidate, but not included in the presentation of this thesis:

- Aghigh A, Preston SEJ, Jargot G, Ibrahim H, del Rincón SV, Légaré F. Non-linear microscopy and deep learning classification for mammary gland microenvironment studies. *Biomedical Optics Express* (2023).
- Preston SEJ, Richard VR, del Rincón SV, Borchers CH, Zahedi RP. Proteomic Assessment of the Murine Mammary Gland Extracellular Matrix. *Methods in Molecular Biology* (2022). 2614:261-271.
- Mitsa G, Guo Q, Gonçalves C, Preston SEJ, Lacasse V, Aguilar-Mahecha A, Benlimame N, Basik M, Spatz A, Batist G, Miller Jr. WH, del Rincón SV, Zahedi RP, Borchers CH. A Non-Hazardous Deparaffinization Protocol Enables Quantitative Proteomics of Core Needle Biopsy-Sized Formalin-Fixed Paraffin-Embedded (FFPE) Tissue Specimens. *International Journal of Molecular Sciences* (2022). 23(8):4443.

- Preston SEJ, Emond A, Pettersson F, Dupéré-Richer D, Abraham MJ, Riva A, Kinal M, Rys RN, Johnson NA, Mann KK, del Rincón SV, Licht JD, Miller Jr. WH. Acquired Resistance to EZH2 Inhibitor GSK343 Promotes the Differentiation of Human DLBCL Cell Lines toward an ABC-Like Phenotype. *Molecular Cancer Therapeutics* (2022). 21(4):511-521.
- Srour N, Villarreal OD, Hardikar S, Yu Z, Preston SEJ, Miller Jr. WH, Szewczyk MM, Barsyte-Lovejoy D, Xu H, Chen T, del Rincón SV, Richard S. PRMT7 ablation stimulates anti-tumor immunity and sensitizes melanoma to immune checkpoint blockade. *Cell Reports* (2022). 38(13):110582.
- Guo Q, Bartish M, Gonçalves C, Huang F, Smith-Voudouris J, Krisna SS, Preston SEJ, Emond A, Li VZ, Duerr CU, Gui Y, Cleret-Buhot A, Thébault P, Lefrère H, Lenaerts L, Plourde D, Su J, Mindt BC, Hewgill SA, Cotechini T, Hindmarch CCT, Yang W, Khoury E, Zhan Y, Narykina V, Wei Y, Floris G, Basik M, Amant F, Quail DF, Lapointe R, Fritz JH, del Rincón SV, Miller Jr. WH. The MNK1/2-eIF4E Axis Supports Immune Suppression and Metastasis in Postpartum Breast Cancer. *Cancer Research* (2021). 81(14):3876-3889.
- Bartish M, Tong D, Wallerius M, Pan Y, Liu H, Ristau J, Ferreira SdS, Wallmann T, van Hoef V, Masvidal L, Kerzel T, Joly A, Gonçalves C, Preston SEJ, Ebrahimian T, Seitz C, Bergh J, Pietras K, Lehoux S, Naldini L, Andersson J, Leonardo Squadrito M, del Rincón SV, Larsson O, Rolny C. MNK2 governs the macrophage anti-inflammatory phenotype. *Proceedings of the National Academy of Sciences of the United States of America* (2020). 117(4):27556-27565.

- Guo Q, Li VZ, Nichol JN, Huang F, Yang W, Preston SEJ, Talat Z, Lefrère H, Yu H, Zhang G, Basik M, Gonçalves C, Zhan Y, Plourde D, Su J, Torres J, Marques M, Habyan SA, Bijian K, Amant F, Witcher M, Behbod F, McCaffrey L, Alaoui-Jamali M, Giannakopoulos NV, Brackstone M, Postovit L-M, del Rincón SV, Miller Jr. WH. MNK1/NODAL signaling promotes invasive progression of breast ductal carcinoma in situ. *Cancer Research* (2019). 79(7):1646-1657.

List of figures and tables

- Figure 2.5: Phospho-eIF4E deficiency governs the fiber alignment and deposition of collagen-I at the tumor-stroma boundary.
- Figure 2.6: Characterization of phospho-eIF4E and collagen-I in tumor and stroma regions of human breast cancer patients.
- Figure 2.7: Genetic and pharmacological reduction of eIF4E phosphorylation protects against anti-PD-1-induced intratumoral collagen deposition.
- Supplementary Figure 2.1: Additional data assessing the impact of mammary gland-derived ECM on tumor cell invasion and proliferation.
- Supplementary Figure 2.2: Additional details of proteomics data acquired from mammary gland-derived ECM samples.
- Supplementary Figure 2.3: Polysome profiling of *COL1A1* mRNA in wild-type and phospho-eIF4E-deficient mammary gland-derived fibroblasts.
- Supplementary Figure 2.4: Confirmation of siRNA-mediated DDR2 knockdown.
- Supplementary Figure 2.5: Schematic summary of immuno-stainings performed on breast cancer patient tissue samples.
- Figure 3.1: MNK1 ablation in 4T1 cells alters stemness phenotypes *in vitro* and *in vivo*.
- Figure 3.2: Multi-omics analysis highlights alterations in glycolysis and oxidative phosphorylation pathways in MNK1 KO 4T1 cells.
- Figure 3.3: Experimental metastasis models demonstrate that MNK1 ablation significantly dampens metastatic tumor outgrowth in the liver, but not the lung.

Abbreviations

4E-BP: eIF4E-binding protein; ABC: ATP-binding cassette; ADAM: Disintegrin and metalloproteinase; ADAMT: Disintegrin and metalloproteinase with thrombospondin motif; ALDH: Aldehyde dehydrogenases; ATP: Adenosine triphosphate; BC: Breast cancer; BCA: Bicinchoninic acid; BCLM: Breast cancer liver metastasis; BCSC: Breast cancer stem cell; BM: Basement membrane; BRCA: Breast Cancer; BSA: Bovine Serum Albumin; CAF: Cancer-associated fibroblast; cPLA2: cytosolic phospholipase A2; CRC: Colorectal cancer; CSC: Cancer stem cell; CTLA-4: Cytotoxic T-lymphocyte-associated antigen 4; DCIS:; MCF10DCIS.com cells; DDA: Data dependent acquisition; DDR1/2: Discoidin domain receptor 1/2; DNA: Deoxyribonucleic acid; cDNA: complementary DNA; DTT: Dithiothreitol; ECAR: Extracellular acidification rate; ECM: Extracellular matrix; eIF: Eukaryotic initiation factor; EMT: Epithelial-to-mesenchymal transition; ER: Estrogen receptor; ETC: Electron transport chain; FADH: Flavin adenine dinucleotide; FAO: Fatty acid oxidation; FAP: Fibroblast activation protein; FCCP: Carbonyl cyanide-4 (trifluoromethoxy) phenylhydrazone; FDA: The United States Food and Drug Administration; FDR: False discovery rate; FFPE: Formalin-fixed paraffin embedded; GSEA: Gene set enrichment analysis; GSH: Glutathione; HA: Hyaluronan; H&E: Hematoxylin and eosin; HER2: Human epidermal growth factor receptor 2; hnRNPA1: heterogeneous nuclear riboprotein A1; ICI: Immune checkpoint inhibitor; IDC: Invasive ductal carcinoma; iECM: Urea-insoluble extracellular matrix; IF: Immunofluorescence; IHC: Immunohistochemistry; IM: Interstitial matrix; KO: Knock-out; LC-MS/MS: Liquid chromatography with tandem mass spectrometry; LFQ: Label-free quantitation; LOX:

Lysyl oxidase; MAPK: Mitogen-activated protein kinase; MG: mammary gland; MHC: Major histocompatibility complex; MID: Mass isotopomer distribution; MMP: Matrix metalloproteinase; MNK1/2: Mitogen-activated Protein Kinase Interacting Kinases 1/2; mRNA: Messenger ribonucleic acid; mTOR: Mammalian target of rapamycin; mTORC1: Mammalian target of rapamycin complex 1; NADH: Nicotinamide adenine dinucleotide; NES: Normalized enrichment score; NF: Normal fibroblast; NSABP: National surgical adjuvant breast and bowel project; NSAF: Normalized spectral abundance factors; OCR: Oxygen consumption rate; OxPhos: Oxidative phosphorylation; PARP: Poly (ADP-ribose) polymerase; PBS: Phosphate buffered saline; PDAC: Pancreatic ductal adenocarcinoma; PD-1: Programmed cell death protein 1; PD-L1/2: Programmed death-ligand 1/2; PFA: Paraformaldehyde; PPBC: Post-partum breast cancer; PR: Progesterone receptor; PRM: Parallel reaction monitoring; PSF: polypyrimidine tract-binding protein-associated splicing factor; R/AA: Rotenone/Antimycin A; RNA: Ribonucleic acid; ROI: Region of interest; ROS: Reactive oxygen species; S209: serine 209; S209A: eIF4E with serine 209 mutated to alanine; SDS: Sodium dodecyl sulfate; sECM: Urea-soluble extracellular matrix; SHG: Second harmonic generation; SITA: Stable isotope tracer analysis; ssGSEA: single sample GSEA projection; SPRY2: Sprouty2; STRAP: Suspension trapping; TACS: Tumor-associated collagen signatures; TBST: Tris-buffered saline with Tween; TCA: Tricarboxylic acid; TCGA: The Cancer Genome Atlas; TCR: T cell receptor; TIC: Tumor-initiating cell; TMA: Tissue microarray; TME: Tumor microenvironment; TNBC: Triple-negative breast cancer; VEGF: Vascular endothelial growth factor; WT: wild-type.

Chapter 1 – Introduction and literature review

1.1 Breast cancer

1.1.1 Epidemiology and risk factors

Breast cancer is a global clinical problem. It is the most frequently diagnosed cancer in women, with 2.26 million new cases in 2020[1], and accounting for 626,679 deaths in 2018[2]. This is a leading cause of cancer-related death in women worldwide with an age-adjusted death rate of 13.6 per 100,000[1]. Moreover, global incidence of breast cancer is increasing annually by 3.1% on average[3], a trend that is predicted to continue. Between 1990 and 2016, breast cancer incidence rates have more than doubled in 60 countries, while death rates have doubled in 43 countries[4]. In part, this is thought to be due to increasing population growth and ageing.

It is important to acknowledge that breast cancer incidence and mortality rates can be stratified by country development status. High-income countries have higher disease incidence (92 per 100,000 in North America) than low-income countries (27 per 100,000 in middle Africa and eastern Asia)[5,6]. Opposingly, women diagnosed with breast cancer in high-income countries are more likely to survive than women in low- and middle-income countries. With access to developed health care, 5-year survival rates are 90% for localized cancer, compared to 76% in less-developed countries[7]. This can be explained by differences in risk factors (discussed below) and earlier diagnosis due to the availability of mammography, as prognosis improves the earlier breast cancer is diagnosed[8]. A variety of modifiable and non-modifiable risk factors have been identified for the development of breast cancer. These are outlined in Table 1.1 below.

Table 1.1. Breast cancer risk factors (adapted from Lukasiewicz *et al.*, 2021)

Risk factor	Description
NON-MODIFIABLE FACTORS	
Sex	• Female sex is a major factor due to enhanced hormonal stimulation; circulating estrogens and androgens are associated with an increased risk of breast cancer[9]. • Hormonal risk is increased in pre- and post-menopausal females[10–12]. • Less than 1% of all breast cancers occur in males[13].
Age	• 80% of breast cancer patients are over 50 years old, 40% are over 65 years old. Risk of onset increases with age[14,15].
Family History	• Between 13% and 19% of breast cancer patients have a first-degree relative with the same condition[16]. • This is independent of age, and thought to be driven by epigenetic changes and environmental triggers in common[17].
Genetic mutations	• Mutations in *BRCA1* and *BRCA2* are linked to increased risk of breast carcinogenesis (up to 85% risk) and have high penetrance[18]. • Other highly penetrant genes include: *TP53*[19], *CDH1*[20], *PTEN*[21], *STK11*[22]. Other frequently mutated/amplified genes include: *PIK3CA*, *MYC*, *CCND1*, *ERBB2*, *FGFR2*, *GATA3*[23]. • Several DNA repair genes that interact with BRCA (including *ATM*[24], *PALB2*[25], *BRIP1*[26], *CHEK2*[27]) are also known to impact tumorigenesis, but at a much lower penetrance than BRCA mutations[18].
Ethnicity	• Breast cancer incidence rates remain highest among white non-Hispanic women[28,29]. • African and African-American women experience significantly higher mortality and lower survival rates[30]. • Asian women present with breast cancer earlier (40-50 years old) than their western counterparts (60-70 years old)[31–33].
Reproductive History	• The hormone imbalances associated with pregnancy, breastfeeding, involution, menstruation, and menopause are crucial points of induction of tumorigenesis[34]. • Full-term pregnancy is associated with reduced breast cancer risk; protection increases with the number of pregnancies[34,35]. • Early menopause lowers breast cancer risk[36].
Breast Tissue Density	• In both pre- and post-menopausal women, greater breast tissue density is associated with greater breast cancer risk[37].

MODIFIABLE FACTORS (Table 1.1 continued)	
Physical Activity	• Regular physical activity is considered to be a protective factor against breast cancer, although the precise mechanisms behind this remain unknown[38,39].
Obesity/BMI	• Obese women with breast cancer have poorer clinical outcomes[40]. • Increased BMI is associated with more aggressive tumors and higher rates of metastasis[41]. • Proposed mechanisms of action include upregulated systemic inflammation and altered circulating hormone levels[42].
Diet & Alcohol	• Excessive alcohol consumption is associated with increased risk due to disrupted hormonal balance and increased fat gain[43,44]. • Consumption of highly-processed food increases breast cancer risk, partly due to a subsequent obesity predisposition[45].
Smoking	• Active and passive smoking increases breast cancer risk as carcinogens found in tobacco can travel to the breast tissue, thereby increasing the likelihood of genetic mutation[46].

1.1.2 Classification of breast cancer

Breast cancer is a heterogeneous group of diseases, characterized by a spectrum of molecular, cellular, and histological features. The latest edition of the World Health Organisation classification determines there to be 19 major subtypes[47]. The most frequent of these are invasive carcinomas of no special type, previously referred to as invasive ductal carcinomas (IDC), which represent 70-75% of patients[47]. In these cases, invasive disease is preceded by the development of ductal carcinoma *in situ*, which is considered pre-invasive or non-invasive disease, characterized by the aberrant proliferation of mammary ductal epithelial cells that remain confined to the duct by myoepithelial cells and the basement membrane. Once these malignant cells break through the basement membrane, thereby enabling migration and invasion into the surrounding stroma, they become an IDC[48]. Additionally, 10% of cases are lobular carcinomas, and the remainder

are carcinomas of special types including tubular, cribriform, mucinous, and micropapillary[47].

Other than histological classifications, the American Joint Committee on Cancer created an internationally-accepted TNM staging system based on anatomical assessment: tumor size (T), lymph node metastasis (N), distant metastasis (M)[49]. Beyond this, breast cancers can be grouped by their molecular subtype. Largely based on seminal microarray expression work from Perou *et al.* (2000), the field has identified four intrinsic molecular subtypes: Luminal A, Luminal B, HER2-enriched and Triple-negative[50,51]. It is worth noting that clinical practice typically uses a surrogate classification of subtypes, based on histological and molecular characteristics, to allow for easier assessment of therapeutic benefit for specific patients. These include triple-negative, HER2-enriched (non-luminal), Luminal B-like HER2+, Luminal B-like HER2-, and Luminal A-like[52].

1.1.2.1 Luminal breast cancer

Luminal breast cancers cover 70% of cases and are estrogen receptor (ER) positive[53]. Gene clusters associated with cell proliferation and normal luminal epithelial cells distinguish two subtypes further: Luminal A and Luminal B tumors. Luminal A tumors are positive for ER and/or progesterone receptor (PR), while negative for HER2. Mechanistically, ER-related transcription factors activate genes that are typical of luminal epithelium cells[54], and genes relating to proliferation are lowly expressed[55]. Resulting tumors are low-grade and slow-growing, often leading to good prognosis. In contrast, Luminal B tumors are ER positive and may be PR negative and/or HER2 positive. Clinically, these cases are higher grade and have worse prognosis, with heightened

expression of proliferation-related genes including recurrent copy number alterations in the oncogene *ZNF703* which stimulates the Wnt and Notch signaling pathways[56].

1.1.2.2 HER2-enriched breast cancer

HER2-enriched tumors are the second intrinsic subtype, representing 10-15% of cases[53]. As the name suggests, this group is characterized by a high expression of HER2 and absent expression of ER and PR. These cancers grow quicker than luminal cancers due to their expression of clusters of genes and proteins associated with proliferation[57], alongside increased mutagenesis mediated by APOBEC3B, a DNA cytosine deaminase[58]. Prognosis has increased from poor to intermediate since the introduction of HER2-targeted therapies (see below).

1.1.2.3 Basal-like (triple-negative) breast cancer

The terms basal-like and triple-negative breast cancer (TNBC) are often used interchangeably. However, TNBC represents a much larger array of breast cancer types, with basal-like tumors accounting for one of six subgroups. The other subgroups include mesenchymal, mesenchymal stem-like, immunomodulatory, luminal androgen receptor, and unknown[59,60]. Collectively, this group of tumor types are negative for ER, PR and HER2 and constitute approximately 20% of cases[53]. Interestingly, TNBC are strongly associated with *BRCA1* germline mutations and high levels of genomic instability[61]. With limited therapeutic options for this group of patients, prognosis remains poor due to tumor aggressiveness and subsequently high risk of metastasis[62].

1.1.3 Metastatic breast cancer

If breast cancer is diagnosed in the early-stages prognosis is highly favorable, with 5-year survival rates above 90%[63]. It is difficult to accurately assess the true number of metastatic breast cancers, as this depends on several factors including mass screening availability, treatment quality and access, and protocols used for collecting and recording patient tumor data[64,65]. Nevertheless, it is estimated that one-third of breast cancer patients will develop metastatic (stage IV) disease, after which 5-year survival rates drop to 27%[63]. Roughly one-quarter of these patients are diagnosed with metastatic breast cancer at first presentation[64,65]. The intrinsic subtype of the tumor can influence its metastatic potential, time to relapse and/or recurrence, and tropism for specific distant tissues. Biologically, metastasis is a multi-step process that involves the interaction of several cell types. Following initial tumorigenesis, malignant cells proliferate, develop invasive features, and promote neo-angiogenesis through a variety of mechanisms. Subsequently, local invasion of the primary tumor takes place, leading to tumor cells escaping from the mammary gland, via the vasculature or the lymphatic system, and colonizing a distant secondary site[66,67] (see *Fig. 1.1* below).

Concerningly, metastatic breast cancer is virtually incurable using currently available therapies. Instead, clinical responses aim to relieve symptoms and to improve quality-adjusted life expectancy. Metastases remain the cause of death in almost all patients, and median overall survival is 2-3 years[68]. Common secondary sites of metastasis include the bone (67%), the lungs (36.9%), the liver (40.8%) and the brain (12.6%)[68,69]. For patients diagnosed with breast cancer liver metastasis (BCLM),

prognosis is particularly poor. Median survival for BCLM cases is only 4-8 months without treatment[70]. Even with systemic chemotherapy, hormonal and targeted therapies (discussed below), median overall survival among BCLM patients is 20 months[71]. It is clear that improved therapeutic options are needed for these patients. The work presented in this thesis contributes to an ever-growing pool of research trying to improve our understanding of the mechanisms and pathways that govern breast cancer metastasis.

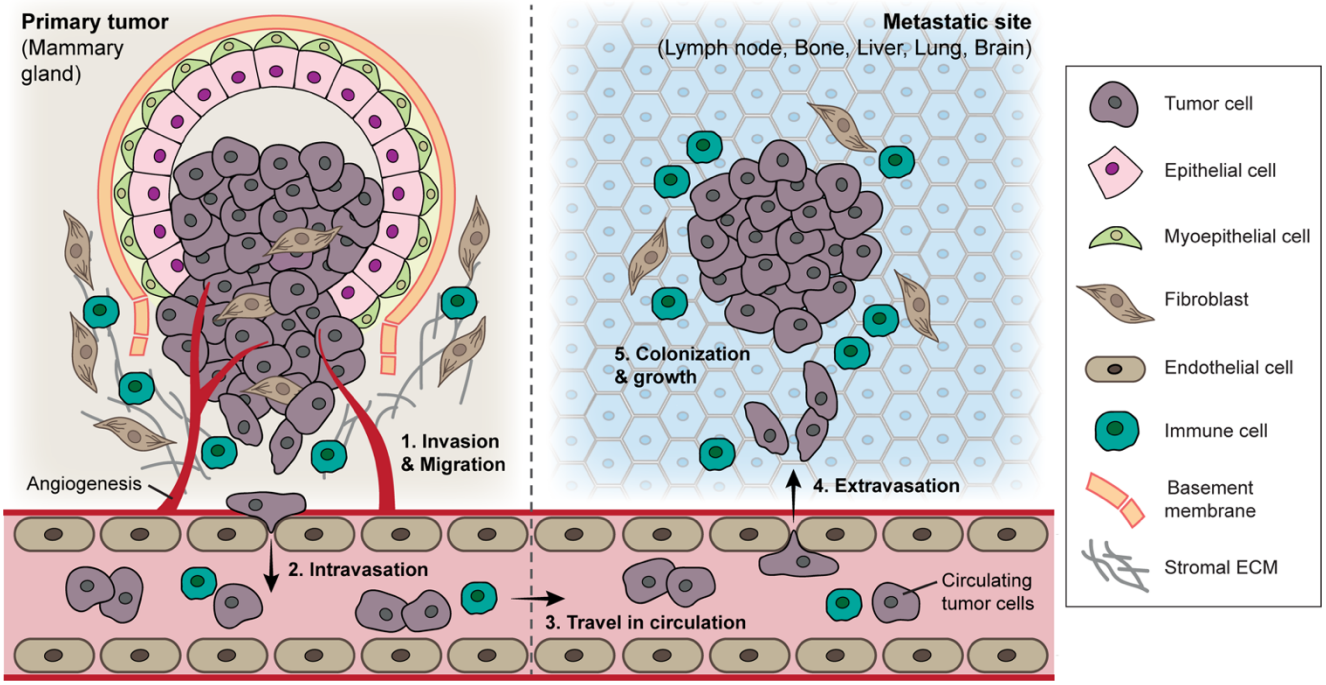

Figure 1.1. Schematic summary of the essential steps of breast cancer metastatic cascade. This process begins with tumorigenesis in the mammary gland, most often in the epithelial cells lining ductal structures, leading to formation of the primary lesion. Tumor cells continue to proliferate and develop invasive cellular features which, in collaboration with non-tumor cell types in the TME, promote degradation of the basement membrane. Tumor cells then invade into the surrounding stroma (local invasion) and intravasate through the endothelial barrier and into the circulation (vasculature or lymphatic system). Circulating tumor cells must then survive shear stresses and evade clearance by the immune system before reaching the metastatic site. After attaching to blood vessels at secondary sites, tumor cells extravasate into the surrounding tissue. If successful, these metastatic tumor cells colonize and outgrow in the metastatic tissue.

1.1.4 Current treatment strategies for breast cancer

Patients diagnosed with breast cancer have a variety of treatment modalities available that target disease at the local and systemic levels (reviewed in-depth in Harbeck *et al.,* 2019[52]). Surgery remains the cornerstone of curative breast cancer treatment. Either a partial or complete mastectomy can be used to remove cancerous tissue while preserving intact breast tissue. Partial mastectomies, also referred to as breast-conserving surgeries, are becoming more common due to the widespread use of neoadjuvant systemic therapies to de-bulk tumors and the advancement of oncoplastic techniques[72]. Typically following surgery comes another locoregional treatment – radiation therapy – used to target any remaining tumor cells left behind from the surgery. Definite choice of radiation type and application technique are dependent on the oncological situation of individual patients. Despite some minor side-effects such as skin irritation and fatigue, radiotherapy has been significantly associated with improved overall survival and lowered risk of disease recurrence[73].

To tackle treatment at the systemic level, chemotherapy is commonly prescribed in either the neoadjuvant or adjuvant setting, which differ based on whether they are delivered before or after the primary therapy, respectively. In 1988, The National Surgical Adjuvant Breast and Bowel Project (NSABP) initiated the NSABP-B18 randomized trial, which was the first to demonstrate that there is no difference in survival outcomes between dosing of chemotherapy in the pre- versus post-operative period[74]. Currently available therapies are often simultaneously applied and can include the following drugs: carboplatin, cyclophosphamide, 5-fluorouracil, taxanes (paclitaxel, docetaxel), and

anthracyclines (doxorubicin, epirubicin). Drug choices are made according to tumor characteristics as different intrinsic subtypes respond differently to specific chemotherapeutics[75]. Even then, although chemotherapy is considered to be effective, there are often severe side effects that can impact patient quality of life and mental well-being.

For patients with ER positive Luminal-subtype tumors, endocrinal (hormonal) therapy may also be applied in the neoadjuvant or adjuvant settings. For early-stage luminal cancers, 5 years of endocrinal therapy following surgery is standard practice. These therapies aim to block activity of the ER by (1) lowering estrogen levels through use of aromatase inhibitors (letrozole, anastrozole, exemestane), and (2) blocking the estrogen-ER interaction using selective ER modulators (tamoxifen, toremifene) and/or selective ER degraders (fulvestrant)[76,77]. Both adjuvant hormone therapy and chemotherapy have been shown to reduce breast cancer mortality by one-third, independent of each other[78,79]. Unfortunately, development of acquired resistance to hormonal therapy is seen in approximately 50% of patients, necessitating its frequent combination with chemotherapy[77].

Targeted therapies present promising treatment options for specific subsets of breast cancer patients, and can be utilized at any stage of disease. For HER2-enriched tumors, it has become standard of care to combine chemotherapy either pre- or post-surgery with HER2-targeting therapies, including monoclonal antibodies (trastuzumab, pertuzumab)[80,81] and pharmacological inhibitors (lapatinib, neratinib)[82,83]. For HER2-negative Luminal cancers, patients may receive the mammalian target of rapamycin

(mTORC1)-targeting inhibitor everolimus in combination with exemestane[84]. CDK4/6 inhibitors, which interrupt cell cycle, have also shown clinical promise in several randomized Phase III trials, and are now frequently combined with endocrinal therapy as standard of care to treat hormone receptor positive tumors[85,86]. Encouragingly, a breadth of clinical and preclinical studies, largely focussed on patients with metastatic disease, continue to improve existing therapies and identify potential new targets. These include inhibitors targeting the PI3K-Akt-mTOR pathway[87,88], histone deacetylase inhibitors (epigenetic regulators)[89], targeting angiogenesis with anti-VEGF antibodies[90], and PARP inhibitors[91,92].

Immunotherapies, the fourth pillar of cancer treatment, have revolutionized oncology by providing durable responses and survival improvement across multiple cancer types[93]. Broadly, these therapies are designed to boost anti-tumor immunity and enhance T cell function, often by interrupting the activation of signaling pathways (such as the CTLA-4 and PD-1/PD-L1 axes, see *Figure 1.2*) that lead to T cell exhaustion and inactivity. In breast cancer, however, early trials of immune checkpoint inhibitors (ICIs) as monotherapies resulted in limited objective responses[94]. It is thought that these underwhelming results reflect the fact that breast cancer is considered to be poorly immunogenic, and subsequently the use of ICIs in breast cancer treatment was not prioritized[95,96]. Since then, the field has gained an improved understanding of differential immunogenic activity between breast cancer subtypes[97]. TNBC cancers in particular have the strongest immunogenicity[98], characterized by increased immune cell infiltration and high tumor mutational burden[99,100]. As such, ICIs have now been identified as a promising

therapeutic option for this sub-group of patients. Results from the IMpassion130 trial in 2019 led to FDA approval of atezolizumab (an anti-PD-L1 antibody) in metastatic TNBC patients[101], but this was later withdrawn due to a subsequent trial that failed to show an improvement in progression-free survival[102]. Pembrolizumab (an anti-PD-1 antibody) remains the only FDA-approved immunotherapy regimen for TNBC patients, having shown clinically-relevant survival advantages in trials such as KEYNOTE-355. It has shown efficacy in combination with chemotherapy in both metastatic and high-risk early-stage TNBC patients[103,104].

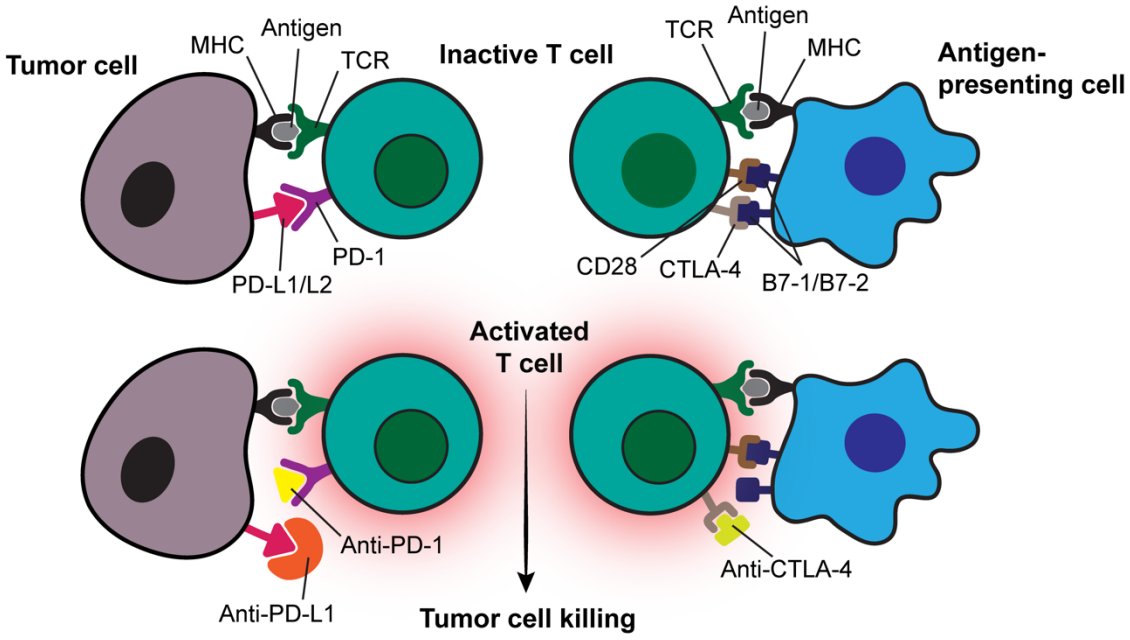

Figure 1.2. Schematics of the PD-1:PD-L1 and CTLA-4:B7-1/2 immune checkpoints and therapeutic targeting using immune checkpoint inhibitors. Programmed cell death protein 1 (PD-1, a.k.a. CD279) is a member of the B7/CD28 family expressed on T cells, B cells, NK cells, dendritic cells, and monocytes. It binds to programmed death ligand 1 and 2 (PD-L1/2) and negatively regulates adaptive immune responses. Cytotoxic T-lymphocyte-associated antigen 4 (CTLA-4 a.k.a. CD152) is a homolog of CD28, and acts as another essential brake on T cell immune responses. In order to be primed, T cells require activation of the T cell receptor (TCR) by binding of major histocompatibility complex (MHC) peptides, and a co-stimulatory signal through CD28:B7-1/2 binding. Binding of CTLA-4 to B7-1/2, however, acts as a co-inhibitory signal to impede T cell activation. Antibody-based blocking of these checkpoints (PD-1, PD-L1 and CTLA-4) helps to boost anti-tumor immune responses.

1.2 The breast tumor microenvironment: extracellular matrix

Beyond just the tumor cell, breast cancers develop and evolve in a complex tumor microenvironment (TME) comprised of several cell types[105,106]. The immune microenvironment, including lymphocytes, macrophages, and myeloid-derived immune cells, facilitates malignant progression according to the principles of immune surveillance and immune editing[107]. In early-stage disease, the immune system exerts predominantly anti-tumor effects, by activating effector lymphocytes to infiltrate the TME and eliminate tumor cells. As disease becomes more invasive, however, the tumor co-opts its neighbouring cells, including immune cells and fibroblasts, to alter the cytokine content of the local environment and promote immune suppression[107,108]. Furthermore, interaction between tumor cells, endothelial cells, and pro-angiogenic signals from tumor-supportive immune cells (such as macrophages) induce vascularization of the TME, a key determinant of subsequent proliferation and metastasis[109].

Cross-talk between these parties of cells does not happen in free space, but instead is underpinned by the extracellular matrix (ECM). This highly dynamic protein network provides structural support to tissues, facilitates wound-healing, maintains tissue homeostasis, and provides biophysical and biochemical stimuli to control cellular functions[110]. The core matrisome is composed of unique matrix macromolecules, in addition to bound soluble factors such as growth-factors, and ECM-associated proteins (discussed in more detail below)[110]. A variety of cell-surface receptors interact with these factors and ECM molecules directly to regulate cell signaling pathways across biological functions, including proliferation, differentiation, migration, and apoptosis. The biophysical

and topographical properties of ECM components further impact cells and their function[111]. While the ECM can be produced by multiple cell types, including tumor cells themselves, the major producers of matrisomal proteins are fibroblasts, either tissue-resident or cancer-associated (CAFs), which are a highly abundant stromal cell type in the TME[112,113].

The ECM has two forms: the basement membrane (BM) and the interstitial matrix (IM)[111]. In the mammary gland, the BM sits between the epithelium and the stroma, surrounding ductal, alveolar and vasculature structures, and providing an essential signal for establishing cell polarity[114]. The IM is a porous network that interconnects cells of varying types in the stroma, regulates processes such as differentiation and migration, and guarantees structural integrity of the tissue. The BM is a stable, dense, sheet-like structure, whereas the IM is remodelled continuously in response to force stress or trauma such as wound repair or physiologic tissue regeneration. Dysregulation of this process is characteristic of breast cancers, resulting in alterations to ECM composition and structure that induce a range of changes in tissue stiffness, cellular signaling and motility, tumor progression and metastasis[111]. In fact, it has been suggested that the ECM contributes to the acquisition of each of the hallmarks of cancer, and is therefore critical for malignancy[115].

1.2.1 Key components of the mammary gland extracellular matrix

Advanced tissue manipulation protocols combined with proteomics-based approaches have been fundamental in investigating ECM composition[116,117]. Pioneered

largely by the Hynes and Naba research groups, studies over the last decade have integrated and annotated mass spectrometry data across species and tissue types to define the mammalian matrisome. This consists of 274 core matrisomal proteins and 1110 matrisome-associated proteins that are classified into collagens, proteoglycans, glycoproteins, ECM regulators, and secreted factors[118]. These components are subject to a variety of post-translational modifications that are critical for their function, including hydroxylation, glycosylation, phosphorylation, and cross-linking.

Individual components of the mammary gland ECM can be divided into three groups: structural proteins, colloid-forming proteins, and adhesive proteins[119]. Structural proteins include collagens (see below) and elastin, which gives the ECM strength and flexibility to withstand tissue stretching. Both glycosaminoglycans and proteoglycans can form water-based colloid structures; gel-like substances that provide a substrate to contain other matrix components. Hyaluronan, also called hyaluronic acid (HA), is one important example of an aminoglycan in the ECM. Consisting of repeated units of glucuronic acid and disaccharides, HA exists in a curled state within solution due to the hydrophilic groups on its surface binding numerous water molecules. Moreover, it plays many biological roles in normal and pathological processes by interacting with other extracellular proteins and cellular receptors[120]. Finally, adhesive proteins, such as laminin and fibronectin, are used to bind to the stroma. Laminin is a large, complex glycoprotein that can connect to multiple cell types through an array of binding sites and is an integral component of the BM[121]. Fibronectin, another large glycoprotein, is manipulated into fibrils

in the IM through formation of di-sulfide bonds and subsequent cross-linking to specific subsets of cells (including fibroblasts)[122].

Collagens are a particularly important group of ECM proteins. They are the most abundant protein in animals, accounting for approximately one-third of the human whole-body total protein content. There are 28 known subtypes of collagen, each encoded by a different gene and with different chemical structures and biological properties[123]. Some of these are fibrillar subtypes that interact laterally to form bundles of parallel molecules with high tensile strength. This includes collagen type I, III and V, all of which are core components of the mammary gland IM. Other types, such as type IV, are network-forming collagens that are vital in the formation of the BM. All collagens are formed in long triple-helix structures, characterized by an abundance of glycine, proline and hydroxyproline repeating units[124]. They are initially synthesized as pro-collagen precursors that are transported alongside chaperone proteins to the endoplasmic reticulum where they undergo a variety of processing reactions, including glycosylation of hydroxylysine groups, hydroxylation to promote helix stability, and interaction of intrachain di-sulfide bonds to promote triple-helix formation. These precursor molecules are then secreted, undergo cleavage of pro-peptides in their terminal regions, and polymerize into fibrils in the extracellular space[124]. These post-translational modifications are critical to ensure that this multi-step biosynthesis yields correctly matured collagen.

1.2.2 Extracellular matrix remodelling throughout breast cancer progression

Breast tumorigenesis disrupts ECM homeostasis to reinforce disease progression. Tumor-mediated ECM remodelling occurs gradually, often involving the "re-education" of non-tumor cell types in the TME to aid in remodelling mechanisms. These mechanisms can include changes in ECM production and degradation, and force-mediated alterations in matrix conformation[111]. As desmoplasia is a key feature of breast cancers[125], changes in ECM deposition and post-translational modifications are particularly relevant. The most common alteration in a tumorigenic ECM is the increased generation of fibrillar collagen[126], alongside other matrix components such as fibronectin and HA. This desmoplastic reaction has been linked directly to increased tumor aggressiveness and metastasis using breast cancer mouse models[127]. Mechanistically, this occurs in part via collagen-mediated signaling through its binding to many surface receptors, including unique receptor tyrosine kinases Discoidin Domain Receptors (DDR1 and DDR2), Notch, and multiple integrins. For example, it has been shown that interaction of collagen with DDR1 in the breast TME is critical for metastatic outgrowth via activation of STAT3 signaling[128], and that DDR2 further facilitates metastasis by stimulating ERK2 activity and stabilizing the Snail1 protein[129].

Post-translational modifications of collagen can be further altered in a tumor-controlled microenvironment to cause changes in ECM architecture and impact disease. For example, lysyl hydroxylases (encoded by PLOD genes) and lysyl oxidases (encoded by LOX and LOX-like genes) are frequently over-expressed in breast cancers, leading to increased collagen cross-linking and tumor progression[130,131]. In tandem with increased

collagen production, this results in a stiffer, denser tissue which has been observed as a strong independent risk factor for the development of breast cancer[132–134]. Breast density refers to the amount fibrous and glandular tissue (more dense) relative to fatty adipose tissue (less dense) in a given breast. However, organisation and composition of the ECM, rather than density alone, is crucial for influencing tumor cell motility[135]. Culturing non-invasive breast cancer cells in a fibrillar collagen-I matrix is known to potentiate their invasion compared to culturing in Matrigel, which largely contains non-fibrillar collagen-IV[136]. In normal breast tissue, collagen fibers in the IM are curly and oriented in parallel with the epithelium, often protecting against the early-stages of tumorigenesis by activating cellular signaling pathways that promote cell-cell junction formation and downregulate mesenchymal-specific genes[137]. As tumors grow, however, fibers at the tumor-stroma boundary become highly linearized and oriented perpendicular to the tumor edge, providing migration tracks to facilitate local invasion and eventual metastasis[130,138]. This feature of breast cancer is known as tumor-associated collagen signatures (TACS), and increased abundance of bundled perpendicular fibers (TACS-3) is associated with poor patient survival[139]. These “collagen highways” are similarly important for non-tumor cells. T cells and dendritic cells migrate towards TME-derived chemoattractants along collagen-I fibers[140], but can be precluded from local regions with highly dense collagen and fibronectin deposition as they lack intrinsic proteolytic activity to modulate the matrix[141]. Beyond collagen, many ECM proteins are glycosylated, including HA and its receptor CD44. These glycoproteins and glycolipids can form into complex structures on the cell surface, termed the glycocalyx, which mediates cell-matrix interactions and

mechanoresponses[142]. Tumor cells have been shown to upregulate certain glycoproteins on their surface to form bulky glycocalyx, which applies increased tension to ECM-bound integrins to promote their clustering and increase pro-tumorigenic signaling[142].

The ECM can be degraded or cleaved by target-specific proteases that are counterbalanced by complementary protease inhibitors. Examples of these proteases include matrix metalloproteinases (MMPs), disintegrin and metalloproteinases (ADAMs), and disintegrin and metalloproteinases with thrombospondin motifs (ADAMTs)[111]. While our understanding of specific protease-substrate pairings remains incomplete, their secretion throughout tumor progression by stromal and tumor cells fulfills three main roles[143]. Firstly, degradation of physiologically normal ECM allows for its replacement by tumor-supportive ECM. Secondly, deformation of the matrix is an important component of tumor cell motility. Finally, ECM protein cleavage can release bound signaling molecules and soluble factors, or produce bioactive protein fragments termed matrikines, either of which can have a range of functions that are pro- or anti-tumorigenic[143]. The activity of MMPs have been particularly well-studied in breast cancer, with a range of substrate specificities and functional consequences for different MMP subtypes. Remodelling of the basement membrane, thereby promoting breast tumor cell invasion, is largely impacted by the degradation activity of membrane-bound MT1-MMP (also called MMP-14)[144,145]. Further movement of tumor cells through the IM is also largely controlled by MT1-MMP-mediated degradation of collagen migration barriers[146,147]. Moreover, tumor-associated macrophages and neutrophils are both key sources of the collagenase and gelatinase MMP-9, as well as other matrix components. The MMP-9 secreted by

these cells is not complexed with its inhibitor TIMP-1, unlike other cellular sources[148], and plays vital roles in IM collagen clearance[149] and pro-angiogenic regulation[150,151]. CAFs can similarly produce and secrete MMPs to promote proteolytic ECM degradation[152]. However, CAFs can also utilize their profound contractile ECM-remodelling capacities as an MMP-independent mechanism of remodelling, often through the activity of α3 and α5 integrins and Rho-mediated regulation of myosin light chain activity[153]. CAFs use these mechanisms to apply physical forces on both the BM and IM to widen pre-existing holes in the matrix, create stable migratory tracks, and act as leader cells to facilitate tumor cell migration and invasion[154,155].

1.2.3. Anti-cancer therapeutics and the extracellular matrix

In addition to the pro-tumorigenic processes discussed above, cumulating evidence has indicated a role for the ECM in mediating therapeutic resistance in breast cancer[156,157]. A recent study identified LOX as a key inducer of chemotherapy resistance, as increased collagen cross-linking was shown to reduce drug penetration into the TME and promote resistance through activation of the Src/FAK pathway[158]. In 2008, Helleman *et al.* showed that increased expression of FN1, LOX, and SPARC were associated with poor prognosis in patients with metastatic breast cancer, and that tenascin C was associated with resistance to first-line tamoxifen treatment[159]. Furthermore, fibronectin and laminin have been documented to mediate resistance to ionizing radiation in human breast cancer cells *in vitro*[160]. In syngeneic mouse lung cancer models, it was even demonstrated that tumors upregulate intratumoral collagen deposition as a mechanism

of acquired resistance to anti-PD-1 or anti-PD-L1 immunotherapy, due to the binding of collagen to LAIR1 receptor on T cells to promote their exhaustion[161].

It is clear that combination therapies which include targeting pro-tumorigenic ECM remodelling may be a clinically relevant option for patients with breast cancer. Many strategies have thus been investigated in pre-clinical studies including inhibition of ECM components and remodelling enzymes, blocking cell surface receptors that bind to the matrix, or targeting ECM-producing CAFs directly[119]. Promisingly, several therapies targeting the ECM have undergone clinical trials in multiple cancer types (trials including breast cancer patients are summarized in Table 1.2 below) but so far have proven to be largely ineffective. Fibroblast activation protein (FAP) was an attractive candidate as it is expressed in CAFs exclusively, but early trials using the FAP-targeting antibody Sibrotuzumab showed poor outcome and reduced survival[162]. Subsequent trials are using a novel engineered variant of interleukin-2 that binds to FAP and is retained within tumors, in combination with other therapeutics such as trastuzumab or cetuximab (NCT02627274). Targeting of the TGFβ pathway at the ligand (using trabedersen), receptor-ligand (using fresolimumab), and intracellular levels (using galunisertib) have shown limited effects[163]. Similarly, targeting of multiple MMPs to control ECM degradation using drugs such as marimastat or incyclinide led to no survival advantage and severe side-effects due to a lack or target specificity[164]. Increased research is therefore needed to improve our understanding of ECM composition and regulation, and improve therapeutic performance as existing options remain complex and ineffective.

Table 1.2. Clinical trials of ECM-targeting therapies in breast cancer.

Target	Therapeutic Agent	Effect on ECM	Trial ID
MT1-MMP	BT17 (drug conjugate) as mono-therapy	Induces cell death of MT1-MMP expressing cells	NCT03486730
LOX and LOXLs	Tetrathiomolybdate (non-specific copper chelate) as mono-therapy	Copper chelation lowers serum LOXL2 concentrations[165]. mAb targeting of LOXL2 inhibits its activity, resulting in decreased collagen cross-linking.	NCT00195091
TGFβ	Fresolimumab (CG1008, anti-TGFβ mAb) in combination with radiotherapy	Diminishes fibrosis associated with radiation therapy in breast cancer	NCT01401062
FAP	RO6874281 (interleukin-2 variant) as mono-therapy and in combination with trastuzumab (anti-HER2 mAb).	Reduces the activity of cancer-associated fibroblasts specifically through targeting of the FAP (fibroblast activation protein) protease	NCT02627274
RTKs	Sitravatinib (MGCD516) as monotherapy	Inhibits several cell-surface receptor tyrosine kinases including VEGFR, PDGFR and DDR2.	NCT02219711

1.3 Oncometabolism and breast cancer stem cells

1.3.1 General introduction to cellular metabolism and oncometabolism

In non-transformed or slowly proliferating cells, mitochondrial metabolism is the main source of energy production. Various carbon sources (glucose, glutamine, pyruvate etc.) feed into the tricarboxylic (TCA) cycle to produce reducing equivalents, such as nicotinamide adenine dinucleotide (NADH) and flavin adenine dinucleotide (FADH), that are subsequently used as electron donors in the electron transport chain (ETC). Electrons

are transported across ETC complexes in the mitochondrial inner membrane to generate proton gradients that provide a motive force for adenosine triphosphate (ATP) production by ATP synthase – a process known as oxidative phosphorylation (OxPhos)[166]. Glycolysis sits upstream of the TCA cycle as a second important mechanism of ATP production, by converting glucose into pyruvate via a multi-step reaction, which can then feed into the TCA cycle or be converted into lactate. While the glycolytic rate of ATP production is faster than OxPhos, the energetic yield is much lower at only 2 ATP per molecule of glucose compared to the 32 ATP produced by OxPhos[167].

In contrast, tumor cells are characterised by heightened energetic demand due to high rates of proliferation, and thus need to adapt their metabolism through rapid ATP generation to maintain energy balance, nutrient incorporation to form biomass macromolecules, and regulation of cellular redox status[168]. The Warburg Effect has served as the bedrock of the oncometabolism field since its seminal discovery in the 1920s by Otto Warburg[169]. It describes a state in which tumor cells preferentially generate ATP from glycolysis even in the presence of sufficient oxygen concentrations in the TME (so-called aerobic glycolysis), resulting in high rates of glucose uptake. This glucose can also be metabolized by other mechanisms, including the pentose phosphate pathway, to produce large quantities of the macromolecules necessary to generate the materials needed for proliferation[168].

It was originally proposed by Warburg that this counter-intuitive behaviour could be explained by dysfunctional mitochondria in tumor cells[170]. While this is true of some cancers[171,172], increasing evidence suggests that the majority of tumors have fully-

functioning mitochondria[173–176]. Moreover, we now have an improved understanding of tumor metabolism inter- and intra-heterogeneity, with some cells that maintain a glycolytic-dominant metabolism while others predominantly use OxPhos for ATP generation[173,174,177–179]. Rather, the metabolic alterations of a given tumor cell depend on a plethora of factors including gene expression and mutations, environmental hypoxia, and proliferation rate[180]. Beyond aerobic glycolysis, upregulated glutamine catabolism is another key feature of transformed cells[181]. Glutamine acts as both a nitrogen and carbon donor and contributes to all core metabolic tasks, including complementing glucose metabolism to facilitate TCA cycle activity and the production of macromolecules, maintain nucleotide synthesis, and support cellular antioxidant responses[182]. It is worth emphasizing that our understanding of cancer metabolism continues to evolve and that many pathways beyond glucose and glutamine metabolism have been identified as relevant to tumor cell function and disease progression[177]. Clearly, the Warburg Effect does not fully explain oncometabolic mechanisms.

1.3.2 Metabolic flexibility and cooperation in the TME

In addition to meeting their own high-demand proliferation rate, tumor cells must do so in metabolically challenging conditions. The TME is characterized by spatially and temporally heterogeneous concentrations of oxygen, glucose, and glutamine, which are often in short supply. If tumor cells are to successfully colonize a tissue, they must therefore be metabolically flexible. This flexibility is partly tumor-intrinsic, through rewiring of metabolic states according to environmental nutrient availability or biological function

(for example, cellular proliferation versus invasion). Additionally, when carbon sources such as glucose or glutamine are in short-supply, tumor cells form metabolic networks to create symbiotic relationships with their neighbouring cells (reviewed in Danhier *et al.,* 2017[177]). Glycolytic and oxidative tumor cells have been shown to swap lactate for glucose, taking advantage of lactate gradients between high-glycolytic and well-perfused OxPhos-dominant regions[178]. In 2009, Pavlides *et al.* (2009) proposed a new theory, termed the Reverse Warburg Effect, in which CAFs undergo aerobic glycolysis in order to supply tumor cells with energy-rich metabolites that can enter the TCA cycle and be used for OxPhos[183]. As another example of this important metabolic relationship, Ko *et al.* (2011) observed that co-culturing of CAFs with MCF7 breast cancer cells increased autophagy in the fibroblasts, leading to upregulated CAF-derived glutamine secretion which fueled mitochondrial metabolism in the tumor cells[184].

1.3.2.1 Metabolic dependencies of breast cancer metastasis

Metabolic adaptability is especially crucial throughout the metastatic cascade, where conditions are constantly in flux, necessitating a series of sequential rewiring events to maintain plasticity. In fact, it has been suggested that only metabolically flexible cells have the intrinsic capacity to survive in secondary sites[185]. Focal control points include changes in intra- and extracellular pH levels, glycolytic enzymes performing as autocrine cytokines, shifts in mitochondrial activity, and altered lipid metabolism (reviewed in-depth in Payen *et al.,* 2016[186] and Porporato *et al.,* 2016[187]). Tumor cells attempting to colonize a secondary site must adapt to the local nutrient environment, and energy (ATP) generation has emerged as a critical output for successful tumor cell seeding, although

the reasons for this are still unclear[188,189]. Interestingly, a recent theory by Schild *et al.*[190], alongside the "Seed and Soil" dogma, proposes that specific tumor cells evolve to have distinct metabolic features that pre-determine their ability to colonize specific sites. As such, we are beginning to improve our understanding of tissue-specific metabolic requirements in breast cancer. Breast cancer cells that metastasize to the lung have been shown to upregulate PGC1α expression (a key regulator of metabolism) and enhance global bioenergetic capacity[191], uptake environmental pyruvate to remodel the extracellular matrix[192], and are reliant on OxPhos[193]. In contrast, breast cancer cells in the liver depend on glycolytic energy production[194], and those in the brain require fatty acid synthesis to fuel their growth[195]. Ongoing and future studies should aim to assess metabolic flexibility (one tumor cell using multiple fuel sources) versus rigidity (pre-determined capabilities for specific cell subsets) in breast cancer metastasis. Moreover, if organ-specific metastases possess metabolic vulnerabilities, these may represent a newly-emerging therapeutic target.

1.3.3 Breast cancer stem cell metabolism

The metabolic phenotypes of cancer stem cells (CSCs), also referred to as tumor-initiating cells (TICs), have been the subject of intense research in recent years. Although the CSC concept remains incompletely understood, it is clear that not all malignant cells are functionally equal, and a newly emerging field is focussed on investigating their metabolic properties. In particular, CSCs have metabolic signatures that are distinct from their non-CSC counterparts, allowing them to maintain a marked ability to reprogram their

metabolism to adapt to environmental changes[196]. This makes them a highly relevant therapeutic target.

1.3.3.1 Brief introduction to breast cancer stem cells

Similar to stem cells in non-malignant tissues, CSCs are populations of undifferentiated cells that sit at the apex of the tumor cell hierarchy. They are characterized by the ability to self-renew, long-term tumorigenicity *in vivo*, and the generation of more differentiated progeny that constitute the bulk of a tumor[197]. Increasing evidence suggests that breast cancer stem cells (BCSCs) are the powerhouse behind tumor progression, therapeutic resistance, and metastasis[198–204]. Indeed, it is reported that the phenotypic and molecular heterogeneity of breast cancers are a result of their CSC content[204]. There are several biomarkers used to identify and isolate BCSCs, multiple theories behind their cellular origin, and various known regulatory signaling mechanisms (reviewed in Zhang *et al.,* 2020[205]). Al-Hajj *et al.* (2003) were the first to identify BCSCs using the cell surface markers CD44 and CD24[206]. The other most commonly used marker of BCSCs is aldehyde dehydrogenase 1 (ALDH1), which is a predictor of poor patient outcome[207]. Generally, one of four main methods is used to isolate and study BCSCs: cell sorting using cell surface markers, the side population assay (based on high expression of ATP-binding cassette ABC transporter proteins), fluorescent ALDEFLUOR assay to isolate cells with high ALDH enzymatic activity, and spheroid formation assays (culture in non-adherent conditions)[205]. Signaling such as Notch, Wnt, Hippo and Hedgehog pathways are crucial for regulating stemness

properties[205], alongside the expression and activity of pluripotent transcription factors, including Oct4, Sox2, and Nanog[208].

1.3.3.2 Metabolic phenotypes of breast cancer stem cells

Given the importance of BCSCs in disease progression, metastasis and recurrence, the ability to target BCSC-specific metabolic traits could prove useful. Unfortunately, reported studies so far have provided contradictory results. The majority of these findings have suggested that BCSCs maintain a glycolytic-dominant metabolism[209,210]. Functionally, it has been shown that forcing a metabolic switch from OxPhos to glycolysis, through silencing of the *FBP1* promoter, regulates BCSC behaviour and enhances tumorigenicity *in vitro* and *in vivo*[211]. Furthermore, it has been shown that inhibiting glycolysis in human breast cancer cells inactivates ABC transporters on CSCs, which resulted in enhanced intracellular drug accumulation and retention[212]. This highlights how glycolysis-dependent metabolic programming in BCSCs may contribute to treatment resistance. Opposingly, Lee *et al.* (2017) demonstrate that BCSCs exhibit enhanced mitochondrial respiration due to c-Myc-mediated induction of mitochondrial biogenesis, thereby promoting therapeutic resistance and tumor formation[213]. In addition, fatty acid oxidation (FAO) has been implicated as an important metabolic pathway in BCSCs. Mechanistically, JAK/STAT3 signaling promotes stemness features through expression of carnitine palmitoyltransferase genes, which encode critical FAO enzymes. Inhibition of FAO inhibits BCSC function *in vivo*, sensitizes tumors to chemotherapy, and impairs radiotherapy resistance[214,215]. Simultaneous targeting of multiple CSC-specific metabolism-related pathways is an attractive target, as it is likely that the “metabolic

freedom" of BCSCs contributes to their persistence under standard therapies. Future studies are needed, however, to further identify these vulnerabilities and assess the feasibility of targeting such a complex network of enzymes and metabolites.

1.4 Regulation of mRNA translation initiation

1.4.1 Eukaryotic mRNA translation and the MNK1/2-eIF4E axis

The initiation step of mRNA translation is rate-limiting in eukaryotic cells. This involves recruitment of ribosomal subunits to mRNA strands to form elongation-competent ribosomes[216]; a process that is mediated by the eukaryotic initiation factor 4F (eIF4F) complex[217,218]. eIF4F is a heterotrimeric complex composed of the scaffolding protein eIF4G, the RNA helicase eIF4A, and eIF4E[219]. Originally discovered by Sonenberg *et al*.[220,221], eIF4E binds to the 7-methylguanosine cap that sits at the 5' end of eukaryotic mRNAs. This structure promotes RNA stability by preventing degradation, regulates mRNA processing, and facilitates translation initiation[218]. Binding of eIF4E to the cap allows eIF4F and the 43S pre-initiation complex, formed from multiple other initiation factors, to unwind the mRNA which is subsequently loaded into the 40S ribosomal subunit. The ribosome then scans the target mRNA for a start codon, at which point the initiation factors are released and the 60S ribosomal subunit is added to the 40S subunit to form an elongation-competent 80S ribosome. Thus, translation is initiated and continues, codon by codon, in the 5' to 3' direction. See *Figure 1.3* below for a summary of this process.

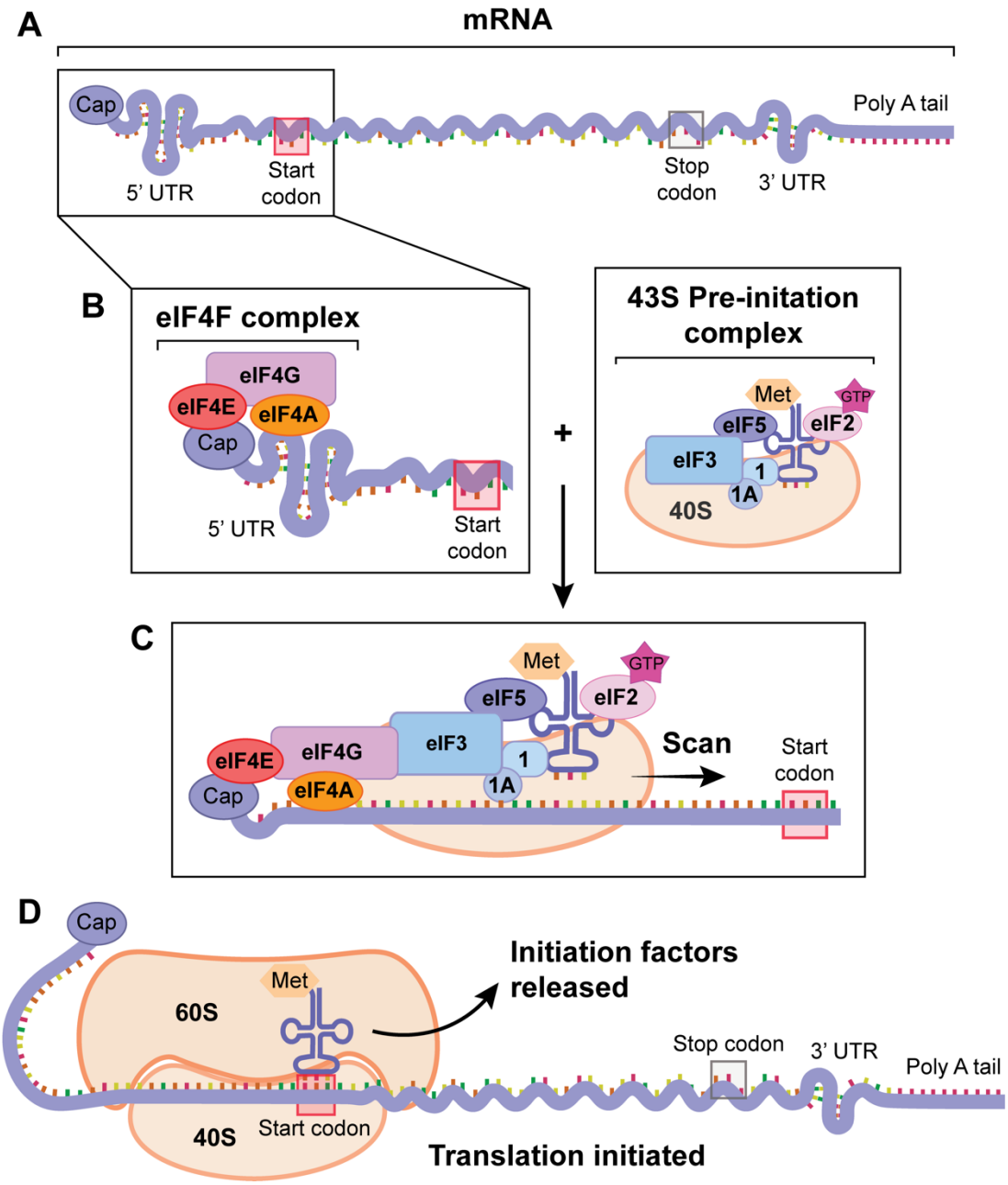

Figure 1.3. Overview of cap-dependent eukaryotic mRNA translation initiation. (**A**) Overview of eukaryotic mRNA structure. (**B**) eIF4E complex binds to the 5' mRNA cap through eIF4E and recruits the 43S pre-initiation complex to form the 48S initiation complex. (**C**) This complex scans along the mRNA to locate a start codon. (**D**) Initiation factors are released and the 60S ribosomal subunit is recruited to form an elongation-competent ribosome. Translation is initiated.

The function of eIF4E is tightly regulated through two main mechanisms. The first of these controls eIF4E availability through competitive binding between eIF4G and eIF4E-binding proteins (4E-BPs). To facilitate translation initiation, binding of eIF4G to eIF4E increases its affinity for the 5' mRNA cap[222]. In contrast, 4E-BPs inhibit translation by competing with eIF4G for the same binding site on eIF4E and sequestering it away from the eIF4F complex[223]. This interaction is precluded, however, when 4E-BPs are phosphorylated by mTOR; a dual-specificity kinase that sits downstream of PI3K/Akt signaling. Secondly, eIF4E activity is regulated through its phosphorylation uniquely at serine 209 (S209)[224] by Mitogen-activated Protein Kinase Interacting Kinases 1/2 (MNK1/2), for which eIF4E is the only *in vivo* validated substrate[225]. The precise mechanistic consequences of this phosphorylation event remain a point of contention in the field (see Chapter 4 for a more detailed discussion). In the context of cancer, however, it is clear that phosphorylation of S209 enhances eIF4E-mediated cellular transformation[226]. Functionally, eIF4E phosphorylation bolsters the translation of a specific subset of mRNAs involved in cell proliferation, survival, invasion, and metastasis[227–229]. Notably, it has been shown that mice with a single allele knock-out for *Eif4e* and phospho-eIF4E-deficient mice (eIF4E$^{S209A/S209A}$ double-allele knock-in mutation) maintain normal development. Both models are also characterized by reduced tumorigenesis, which can be attributed to the impaired translation of specific pro-oncogenic genes, without impairment of global protein synthesis[227,230]. This is beneficial for the clinical development of therapeutic inhibitors directed at MNK1/2 (discussed below).

MNK1 and MNK2 are serine-threonine kinases encoded by the genes *MKNK1* and *MKNK2*, respectively. Both kinases were identified independently by phosphorylation screening for ERK substrates[231,232]. In humans, each *MKNK* exists as a full length "a" isoform or a truncated "b" isoform, which lacks a MAPK-binding motif but maintains a catalytic domain, while in mice only the full-length form has been identified[233,234]. MNK1 and MNK2 are directly activated by the ERK and p38 Mitogen-activated Protein Kinases (MAPKs), which phosphorylate two threonine residues in response to mitogenic- and stress-stimuli[225,231,232,235]. Interestingly, MNK2 activity is higher than MNK1 under basal conditions, while MNK1 activity is greatly increased upon cellular stimulation[235,236]. It has been suggested that this basal phosphorylation of eIF4E is responsible for maintaining the synthesis of proteins essential for cell survival[233].

1.4.2 Rationale for targeting MNK1/2-eIF4E signaling in breast cancer

Upstream cancer-associated mutations frequently increase signaling through MNK1/2-eIF4E, resulting in aberrant mRNA translation and protein synthesis that contributes to disease progression. For example, our group has shown that the receptor tyrosine kinase C-KIT, which drives tumorigenesis in acral/mucosal melanoma, stimulates MNK1/2 to upregulate the translation of mRNAs associated with tumor cell migration and invasion[237]. Furthermore, we showed that $BRAF^{V600E}$, the most common activating mutation in cutaneous melanoma, activates MNK1/2-eIF4E signaling to promote phenotype switching and immune suppression via translational control of *NGFR* and *CCL5*, respectively[238]. As a result, both elevated expression of eIF4E and increased

eIF4E phosphorylation are associated with poor patient prognosis across cancer types[227,239,240]. Focussing on breast cancer, we have demonstrated that phospho-eIF4E-deficient mice have delayed tumorigenesis and develop fewer lung metastases in spontaneous and orthotopic murine breast cancer models[228,229,241]. Tumor-intrinsic MNK1 has also been shown to control the transition from ductal carcinoma *in situ* to IDC, which subsequently supports local tumor invasion[242]. Beyond the tumor cell, there is a growing field of literature that explores the role of the MNK1/2-eIF4E axis in non-tumoral components of the breast TME. This includes regulation of the immune system, where phospho-eIF4E is known to dictate the survival of pro-metastatic neutrophils in the lung[228], and MNK2 has been shown to control macrophage anti-inflammatory functions[243]. Moreover, in patient tumors derived from an aggressive form of breast cancer (post-partum breast cancer, PPBC), $CD8^+$ T cells were observed to have higher phospho-eIF4E levels when compared to $CD8^+$ T cells present in breast cancers diagnosed outside the postpartum period, which correlated with increased expression of the exhaustion marker PD-1[241]. In the stromal cell compartment, phospho-eIF4E-deficient fibroblasts displayed reduced expression of the pro-invasive cytokine IL-33 when co-cultured with tumor cells[241]. Our study, presented in Chapter 2, further identified phospho-eIF4E as a regulator of collagen type I deposition and spatial orientation in the mammary gland, impacting metastatic progression and resistance to anti-PD-1 therapy. It is clear that this important signaling node plays a pleiotropic role across compartments of the TME.

1.4.3 Inhibitors of mRNA translation as a new class of therapeutic agent

There is accumulating evidence linking activity of the MNK1/2-eIF4E axis with disease initiation and progression in breast, and other, cancers. Translational machinery has become a promising therapeutic strategy as a result, with several classes of inhibitors currently in stages of pre-clinical and clinical testing. These include eIF4A inhibitors, inhibitors of eIF4E-eIF4G binding, and MNK1/2 inhibitors. Promisingly, all three of these approaches have shown promise in pre-clinical studies targeting breast cancer. Use of the eIF4A inhibitor Zotafirin resulted in significant tumor regression when combined with Alpelisib (PI3K inhibitor) or Ipatasertib (Akt inhibitor)[244]. The 4EGI-1 inhibitor of 4E-4G interaction induces endoplasmic reticulum stress and apoptosis in tumor cells[245,246], resulting in reduced tumor outgrowth when used as a single agent in two independent studies[247][248]. Similarly, the MNK1/2 inhibitor Cercosporamide decreased tumor outgrowth when used in combination with doxorubicin[249], and SEL201 diminished lung metastasis in a PPBC model[241]. Excitingly, Zotafirin and the MNK1/2 inhibitor Tomivosertib (EFT508) are currently in Phase I/II clinical trials (NCT04092673, NCT04261218) in patients with breast cancer. As a whole, these studies underscore the importance of pursuing translational machinery, particularly the MNK1/2-eIF4E axis, as a clinically relevant target in breast cancer.

1.5 Rationale and objectives

Breast cancer metastasis represents a major clinical challenge. From the literature discussed above, it has become clear over the last decade that the MNK1/2-eIF4E axis

functions across cell types of the breast TME to promote mechanisms of disease progression. Appropriate use of MNK1/2 inhibitors, in combination with standard of care or experimental drugs, is therefore a promising therapeutic option that requires continued research. However, our understanding of the full contribution of this signaling pathway to breast cancer metastasis, and the subsequent impact of targeting it, remains incomplete.

The primary goal of this thesis is to continue expanding our current knowledge in this field, focussing specifically on two elements of breast cancer disease in which the function of MNK1/2-eIF4E signaling is unstudied. My overall hypothesis for this body of work, which serves as the foundation for the two studies outlined below, is that contextualizing a tumor within its microenvironment is critical to understand the role that MNK1/2-eIF4E signaling plays in primary tumor progression and metastatic colonization. Murine breast cancer models have identified critical roles for phospho-eIF4E-expressing tumor-supportive cells in the breast TME, but how this translational control impacts stromal cell-derived ECM is entirely unknown. Thus, in the study presented in Chapter 2, we examined the impact of eIF4E phosphorylation on the composition and pro-tumorigenic potential of the mammary gland ECM. Additionally in Chapter 3, given the recently identified link between MNK1 and BCSC behaviours[242], I chose to further characterize the tumor-intrinsic function of this kinase, particularly with respect to its control of pro-metastatic features. More detailed objectives for these studies are listed below:

1. To determine whether the MNK1/2-eIF4E axis plays a role in regulating the composition of the mammary gland ECM.

2. To investigate if ECM derived from a phospho-eIF4E-deficient context contributes to a less metastatic TME compared to wild-type.
3. To improve our understanding of the functional role that tumor-intrinsic MNK1 kinase plays in regulating BCSC populations and/or features.
4. To identify previously unknown consequences of pharmacologically inhibiting MNK1/2, and test the efficacy of these inhibitors in reducing breast cancer metastasis *in vivo*.
5. To explore the potential clinical relevance of targeting the MNK1/2-eIF4E axis through the translation of our findings into breast cancer patient samples.

Chapter 2 – Phosphorylation of eIF4E in the stroma drives the production and spatial organisation of collagen type I in the mammary gland

This chapter was published as an original research article (open access):

Preston SEJ, Bartish M, Richard VR, Aghigh A, Gonçalves C, Smith-Voudouris J, Huang F, Thébault P, Cleret-Buhot A, Lapointe R, Légaré F, Postovit L-M, Zahedi RP, Borchers CH, Miller Jr. WH, del Rincón SV. Phosphorylation of eIF4E in the stroma drives the production and spatial organisation of collagen type I in the mammary gland. *Matrix Biology* (2022). 111:264-288.

The online version of this article, and all supplementary material associated with it, can be found at: https://doi.org/10.1016/j.matbio.2022.07.003

2.1 Abstract

The extracellular matrix (ECM) plays critical roles in breast cancer development. Whether ECM composition is regulated by the phosphorylation of eIF4E on serine 209, an event required for tumorigenesis, has not been explored. Herein, we used proteomics and mouse modelling to investigate the impact of mutating serine 209 to alanine on eIF4E (i.e., S209A) on mammary gland (MG) ECM. The proteomic data have been deposited to the ProteomeXchange Consortium via the PRIDE partner repository with the dataset identifier PXD028953. We discovered that S209A knock-in mice, expressing a non-phosphorylatable form of eIF4E, have less collagen-I deposition in native and tumor-bearing MGs, leading to altered tumor cell invasion. Additionally, phospho-eIF4E-deficiency impacts collagen topology; fibers at the tumor-stroma boundary in phospho-eIF4E-deficient mice run parallel to the tumor edge but radiate outwards in wild-type mice.

Finally, a phospho-eIF4E-deficient tumor microenvironment resists anti-PD-1 therapy-induced collagen deposition, correlating with an increased anti-tumor response to immunotherapy. Clinically, we showed that collagen-I and phospho-eIF4E are positively correlated in human breast cancer samples, and that stromal phospho-eIF4E expression is influenced by tumor proximity. Together, our work defines the importance of phosphorylation of eIF4E on S209 as a regulator of MG collagen architecture in the tumor microenvironment, thereby positioning phospho-eIF4E as a therapeutic target to augment response to therapy.

Graphical abstract:

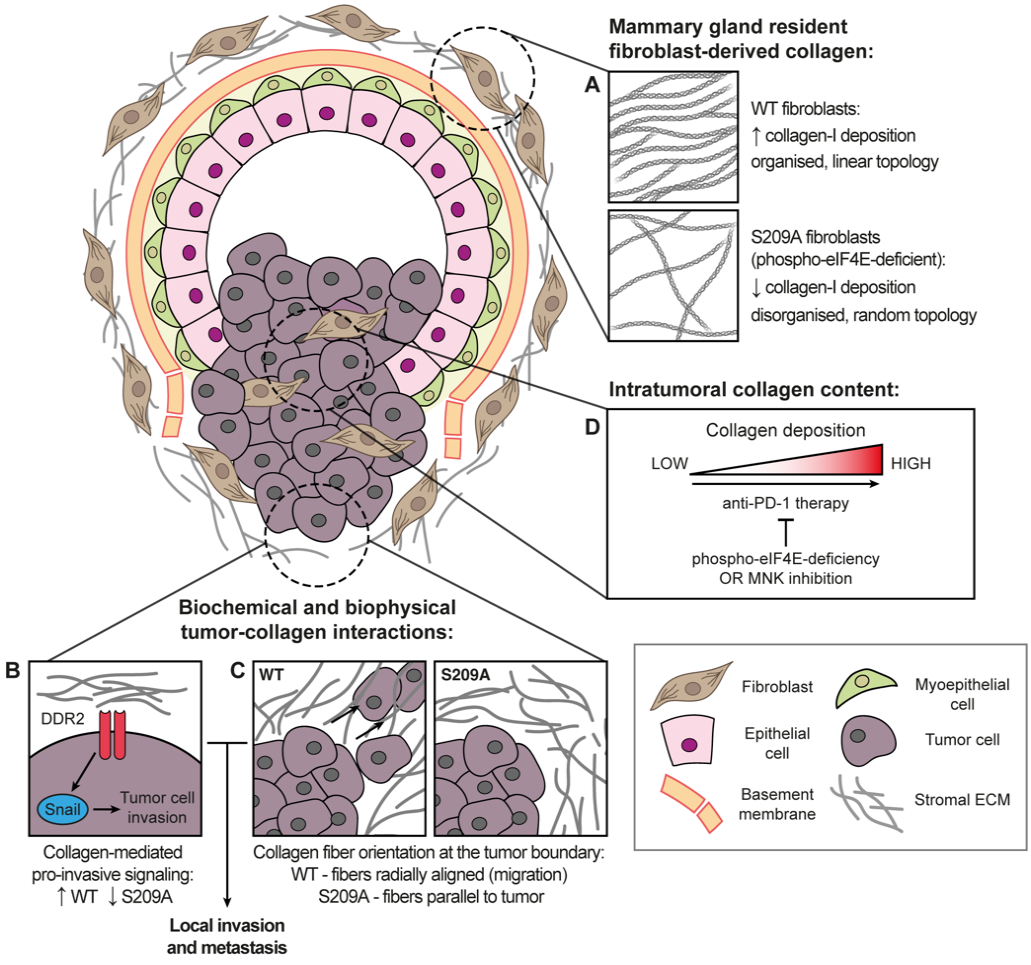

2.2 Introduction

The extracellular matrix (ECM) is a three-dimensional protein network that undergoes continuous remodelling to maintain tissue homeostasis[1]. More than simply a structural support, the ECM exists as a solid-phase reservoir of ligands and growth factors that can define cellular responses at biophysical and biochemical levels. Cell-ECM interactions modulate diverse cellular functions, including proliferation, migration and differentiation[1]. Moreover, dysregulation of ECM composition and structure contributes to multiple pathophysiological processes. In the context of cancer, the ECM represents one part of an evolving tumor microenvironment (TME) that adapts to each stage of neoplastic progression[2]. Deregulation of the ECM contributes to the acquisition of the hallmarks of cancer, and homeostatic control over its production and remodelling is lost in the presence of a tumor[3]. In particular, collagens, biglycan, fibronectin, matrix proteases and other extracellular proteins have been shown to be crucial components of tumorigenic ECM remodelling processes that facilitate tumor cell invasion, immune evasion and metastasis[2].

The use of proteomics-based approaches has been fundamental in probing the protein composition of the mammalian ECM, termed the matrisome, across multiple species and tissue types[4,5]. *In silico* analysis pipelines have concurrently been created to annotate the output from these proteomics studies, allowing the definition of 274 core matrisomal proteins and 1110 matrisome-associated proteins[6]. These include 44 collagen subunits, 36 proteoglycans, numerous glycoproteins, ECM regulators and secreted factors[1]. We know that the composition of the ECM fundamentally underpins its function.

However, the technical limitations of working with acellular samples have meant that many aspects of matrix biology remain under-studied.

It is well supported that perturbations in mRNA translation promote cellular transformation and tumor progression[7]. A critical role of translational control in non-tumoral components of the TME is emerging[8–12], but whether it impacts stromal cell-derived ECM remains underexplored. The MNK1/2-eIF4E signaling axis exemplifies how gene regulation at the level of translation initiation can act abnormally to promote cancer progression[13]. Eukaryotic initiation factor 4E (eIF4E) binds to the 5' 7-methylguanosine cap of mRNAs to mediate cap-dependent translation. eIF4E is phosphorylated on serine 209 by Mitogen-activated Protein Kinase Interacting Kinases 1/2 (MNK1/2)[14,15]. The function of this phosphorylation event remains a point of contention in the literature. Some studies suggest a role for phosphorylated eIF4E in promoting cap-binding, eIF4F complex formation and translation initiation[16–23], while other studies conclude that the function of this phosphorylation event is unclear[24–26]. Despite this lack of clarity, it is clear that phosphorylation of S209 greatly enhances eIF4E-mediated cellular transformation[27]. In addition, the phosphorylation of eIF4E results in increased translation of a subset of mRNAs involved in cell survival, invasion, and metastasis, including MMP3 and MMP9[28], *BCL2*[11], *SNAI1*[12]. Clinically, the expression of phospho-eIF4E is associated with increased tumor aggressiveness and poor patient prognosis across cancers[28,29], and thus MNK1/2 inhibitors are in clinical trials.

Breast cancer (BC) is the most common cancer in women and the second leading cause of death from cancer[30]. Unlike early-stage disease, metastatic breast cancer is

considered incurable using currently available therapies, and the ability to reduce metastasis remains an urgent clinical need. We have previously shown that mice deficient in phospho-eIF4E (harboring a double allelic serine-to-alanine mutation at S209, herein referred to as S209A mice) develop fewer lung metastases in the PyMT murine breast cancer model[12]. Additionally, we have shown that S209A mice resist lung metastasis following orthotopic injection of phospho-eIF4E-expressing breast cancer cells into the mammary gland (MG), as compared to wild-type (WT) mice. In contrast, implanting these cells into WT versus S209A mice has no impact on primary tumor initiation or outgrowth[10,11]. If the same breast cancer cells are injected via the tail vein, therefore bypassing the growth of a primary tumor in the MG, the protection against development of lung metastases in phospho-eIF4E-deficient mice is lost[11]. These data indicate that phospho-eIF4E-expressing tumor-associated cells within the MG TME play a crucial role in metastasis. We hypothesized that the phosphorylation of eIF4E in stromal cells regulates ECM deposition and that WT versus S209A MG ECM are compositionally distinct. We further postulated that the ECM of a phospho-eIF4E-deficient MG will contribute to a less metastatic TME compared to their WT counterparts.

Here, we show that the ECM extracted from S209A MGs influences tumor cells to be less invasive, compared to the same cells grown in the presence of WT MG-derived ECM. Our proteomic analysis revealed that MG-derived ECM from WT and S209A mice differ in their composition. Notably, a phospho-eIF4E-deficient MG harbours less collagen-I in the presence or absence of a tumor. Reorganisation of collagen fibers at the tumor periphery is known to promote local invasion in the mammary gland[31,32]. Second

Harmonic Generation (SHG) microscopy is a powerful label-free imaging technique for tissues rich in collagen type I[33,34]. We used SHG to show that a non-phosphorylatable form of eIF4E shapes collagen topology, in addition to deposition. Tumors implanted into S209A MGs are surrounded by a collagen landscape in which fibers run more parallel with the tumor interface compared to the same tumors grown in WT MGs. Our analysis of human BC biopsies revealed that phospho-eIF4E and collagen-I protein levels are positively correlated in patients, and that stromal phospho-eIF4E expression is increased at sites most proximal to the tumor cells. Finally, we demonstrated that genetic and pharmacologic disruption of eIF4E phosphorylation reduces anti-PD-1-induced intratumoral collagen deposition. Overall, this study defines a previously unknown role for the phosphorylation of eIF4E on S209 as a regulator of collagen in the MG and highlights how modulating the ECM using MNK1/2 inhibitors may increase the efficacy of breast cancer treatments.

2.3 Results

2.3.1 ECM enrichment from murine mammary glands.

To reliably isolate ECM from WT and S209A murine MGs, we chose a frequently used[35,36] protocol specifically designed to enrich for matrisomal proteins from this organ[37] (*Fig. 2.1A*). Most extracellular proteins are inherently insoluble. We can therefore homogenize MG tissue in a high-salt lysis buffer and significantly enrich for matrisomal proteins by centrifugation, while reducing cellular protein content, thereby isolating our total ECM protein fraction (*Fig. 2.1A*). Some of these isolated ECM proteins can be either

fully or partially re-solubilized in the presence of urea, which acts as a chaotropic buffer reagent, allowing them to be used in downstream assays. Centrifugation of ECM samples homogenized in urea will therefore yield urea-insoluble (iECM) and urea-soluble (sECM) protein fractions. The latter is dialyzed to remove remaining urea and salt residues for use in *in vitro* assays (*Fig. 2.1A*). The isolated ECM fractions of WT and S209A mammary glands were analyzed by Western blotting, confirming the presence of fibronectin, an abundant ECM protein, as well as the absence of the intracellular protein GAPDH (*Supp. Fig. 2.1A*). It is known that cell-matrix interactions are vital in controlling MG development, branching ductal morphogenesis, polarization and differentiation[38,39]. Carmine red staining of whole-mount MG preparations showed no overt defects in the branching ductal networks in S209A mice compared to WT mice (*Fig. 2.1B*). Furthermore, using H&E staining we observed no changes in overall tissue architecture or duct structure in the context of phospho-eIF4E-deficiency (*Fig. 2.1C*). Curiously, quantifying the total protein concentration of soluble ECM fractions from weight-matched tissue revealed that the ECM isolated from S209A MGs is less concentrated than ECM from WT MGs (*Fig. 2.1D*). Together, these data suggest that WT and S209A MG ECMs may differ in their composition in a manner that still permits normal mammary gland development.

2.3.2 The ECM isolated from phospho-eIF4E-deficient mammary glands directs breast cancer cells to be less metastatic and invasive, compared to wild-type ECM.

Breast tumor initiation occurs in native mammary gland ECM. Thus, we chose to investigate whether MG ECM derived from WT and S209A mice would impact breast

cancer cell phenotypes. For this purpose, we used murine D2.OR and human MCF10DCIS.com (herein referred to as DCIS) tumor cells. Both cell lines model the early stages of breast cancer development and their proliferative, invasive, and metastatic potentials are known to change as a result of their surrounding matrix[40,41]. To model the impact of our MG-derived ECM on these tumor cells, GFP-tagged D2.OR cells were pre-cultured in either WT- or S209A-derived sECM for 4 days prior to tail vein injection into S209A host mice (*Fig. 2.1E*). From this, we observed that fewer tumor cells had successfully infiltrated the lung if they were pre-cultured in S209A-derived ECM, compared to WT-derived ECM (*Fig. 2.1F*). When the same cells pre-cultured in WT or S209A MG ECM were injected into WT host mice, we saw no difference in the number of tumor cells in the lung between conditions (Supp. *Fig. 2.1B*). To support these data, we performed *in vitro* migration-invasion assays using transwell Boyden chambers and found that culturing either D2.OR or DCIS cells in media supplemented with WT MG-derived sECM was sufficient to significantly increase their invasive capacity when compared to cells in normal culturing media alone (*Fig. 2.1G, 2.1H*). This increase in invasion was not observed when culturing the same tumor cells in the presence of S209A MG-derived ECM (*Fig. 2.1G, 2.1H*). Importantly, these differences in tumor cell invasion were not due to altered cell growth, as we observed no difference in the proliferation rates of either cell line grown for up to 4 days in either WT or S209A MG-derived ECM versus media alone (*Supp. Fig. 2.1C*). These data emphasize the importance of ECM composition in impacting tumor cell behaviour and add ECM regulation to the pro-tumor activities regulated by phosphorylated eIF4E, specifically in tumor-associated cells.

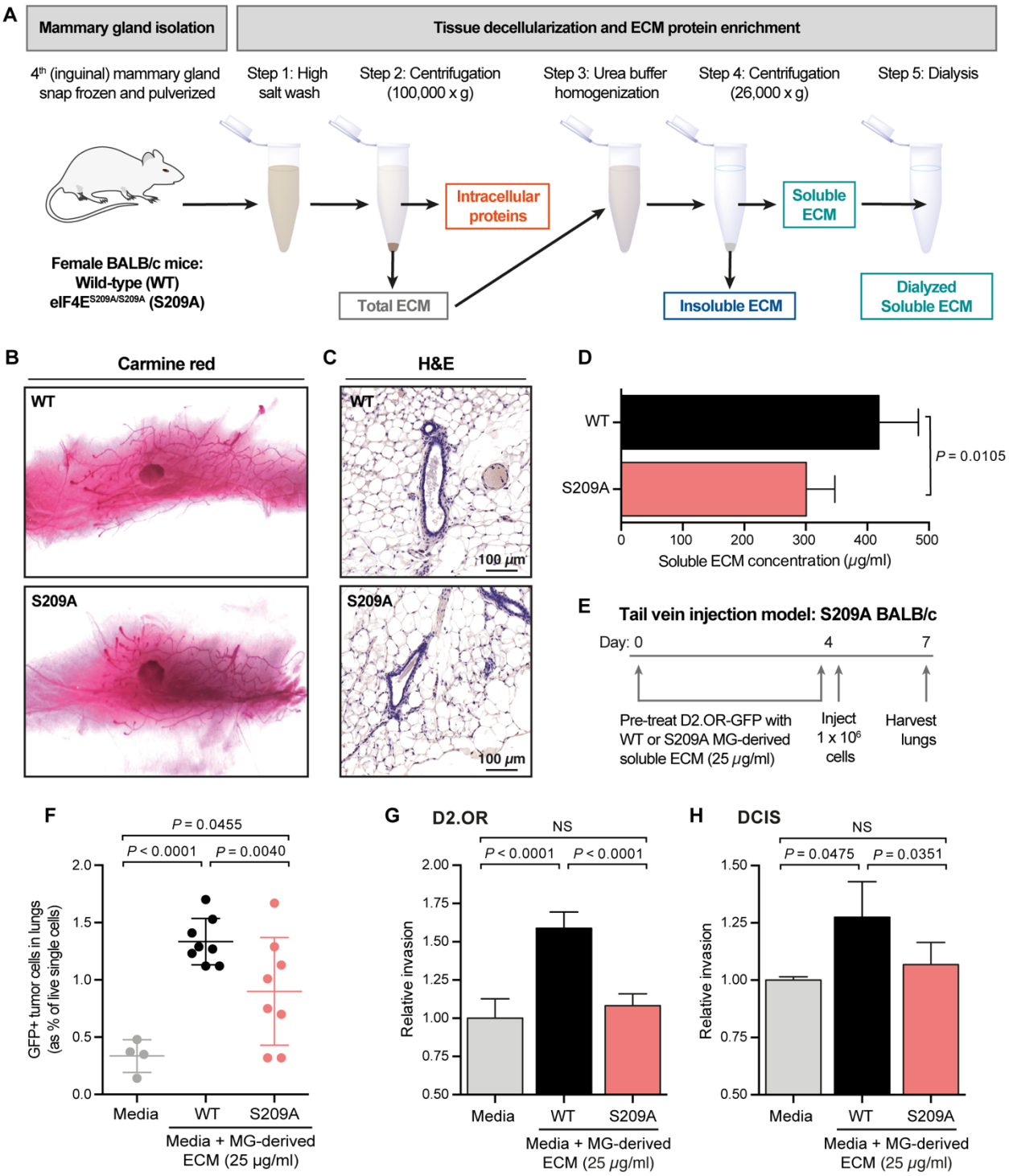

Figure 2.1. Phospho-eIF4E-deficiency reduces the pro-invasive impact of culturing breast cancer cells in mammary gland-derived ECM. (**A**) Schematic of ECM enrichment from murine mammary glands. (**B**) Representative images of whole-mount WT and S209A mammary gland preparations stained with carmine red. (**C**) Representative images of H&E-stained WT and S209A mammary glands. (**D**) Quantification of soluble ECM protein fractions enriched from

1 gram of WT or S209A mammary gland tissue. Error bars represent SD. Paired *t* test, $n = 6$ per group. (**E**) Schematic of experimental design for tail vein experimental metastasis assay. (**F**) Number of GFP^+ tumor cells in the lungs of S209A mice injected with D2.OR-GFP cells cultured in the indicated conditions. Data are expressed as a percentage of live, single cells. Error bars represent SD. One-way ANOVA with Tukey's multiple comparison test, $n = 4$ (media only), $n = 8$ (WT and S209A ECM). (**G** and **H**) Relative invasion of D2.OR (**G**) and MCF10DCIS.com (**H**) cells in indicated conditions. All data are normalized against the media only control (grey bars). Error bars represent SD. One-way ANOVA with Tukey's multiple comparison test, $n = 3$. For all statistics: NS, $p > 0.05$.

2.3.3 The mammary gland matrisomes of $eIF4E^{WT}$ and $eIF4E^{S209A/S209A}$ mice differ.

We next chose to investigate the possible mechanism underpinning the reduced invasion and experimental metastasis of tumor cells when they are cultured in S209A MG ECM (*Fig. 2.1E-H*). To determine whether the MG ECM composition of WT and S209A mice differed, we employed mass spectrometry to quantify the protein constituents of both soluble and insoluble ECM fractions using label-free quantitation (LFQ). Each of our biological replicates represents the ECM enriched from a weight-matched pool of mammary gland tissue, isolated from 4 to 5 mice per group, with each batch of starting material processed on different days. The LFQ intensities of unique peptides were then used to calculate protein normalized abundance for each protein and sample, similar to the methodology of previous publications[42]. The normalized abundances of biological replicates were then used to determine for each protein a fold-change between S209A ECM and WT ECM. LFQ datasets were then combined to calculate an average fold change across repeats. We have taken advantage of recent pipelines designed specifically to use proteomics as a tool to probe matrix composition[43–45], and chosen to focus on those proteins that were common to all replicates. We quantified 327 and 158 proteins on average in our soluble and insoluble ECM fractions respectively, with 16%

(sECM) and 45% (iECM) of them having a greater than 2-fold difference in expression between WT and S209A samples (*Fig. 2.2A*). Using the Matrisome Annotator (https://matrisome.org) to curate our dataset enabled us to focus only on targets that correspond to known ECM proteins (*Fig. 2.2B*). As anticipated, the number of identified peptide spectral matches, peptides and proteins belonging to the core matrisome, matrisome-associated or non-matrisomal compartments is in line with previously published work[43] (Supp. *Fig. 2.2A*). Moreover, we observed considerable overlap in the matrisomal proteins identified between our biological triplicates by LC-MS/MS (Supp. *Fig. 2.2B*), indicating that we are enriching similar ECM components from batch to batch. Utilizing the Matrisome Annotator further allowed us to match each identified protein with its matrisome category (e.g., collagen, glycoprotein, proteoglycan) (*Fig. 2.2C*). Next, normalized spectral abundance factors (NSAF[46]) based on the number of peptide spectrum matches and the molecular weights of each identified protein were calculated to estimate the relative contribution of a given protein to the entirety of the detected proteome. When using these values to compare the overall composition of the MG ECM, we observed a remarkably similar distribution of proteins between matrisomal categories for WT and S209A mammary glands, reflecting their identical tissue architecture (*Fig. 2.1B, 2.1C*). For example, approximately 17% of the sECM and 42% of the iECM was comprised of collagens, in both WT and S209A mice (*Fig. 2.2D*). At the level of individual targets, several proteins known to be important in cancer progression and metastasis were found to be comparatively downregulated in S209A-derived ECM, including Prolargin[47], Annexin A5[48], Biglycan[49] and Perlecan[50] (*Fig. 2.2E*). Notably, SerpinH1 was

robustly decreased in both ECM fractions derived from S209A MGs (*Fig. 2.2E*). SerpinH1 is a collagen-specific molecular chaperone, known to be indispensable for the proper formation and maturation of collagen[51]. Given this knowledge, and the high abundance of collagens in the MG ECM (*Fig. 2.2D*), we utilized parallel reaction monitoring (PRM) based targeted mass spectrometry as a more sensitive and precise method of quantifying the abundance of specific collagen subtypes in the MG ECM[52]. The data acquired from this approach showed that most collagen-I subunits were downregulated in S209A-derived ECM compared to WT (*Fig. 2.2F*).

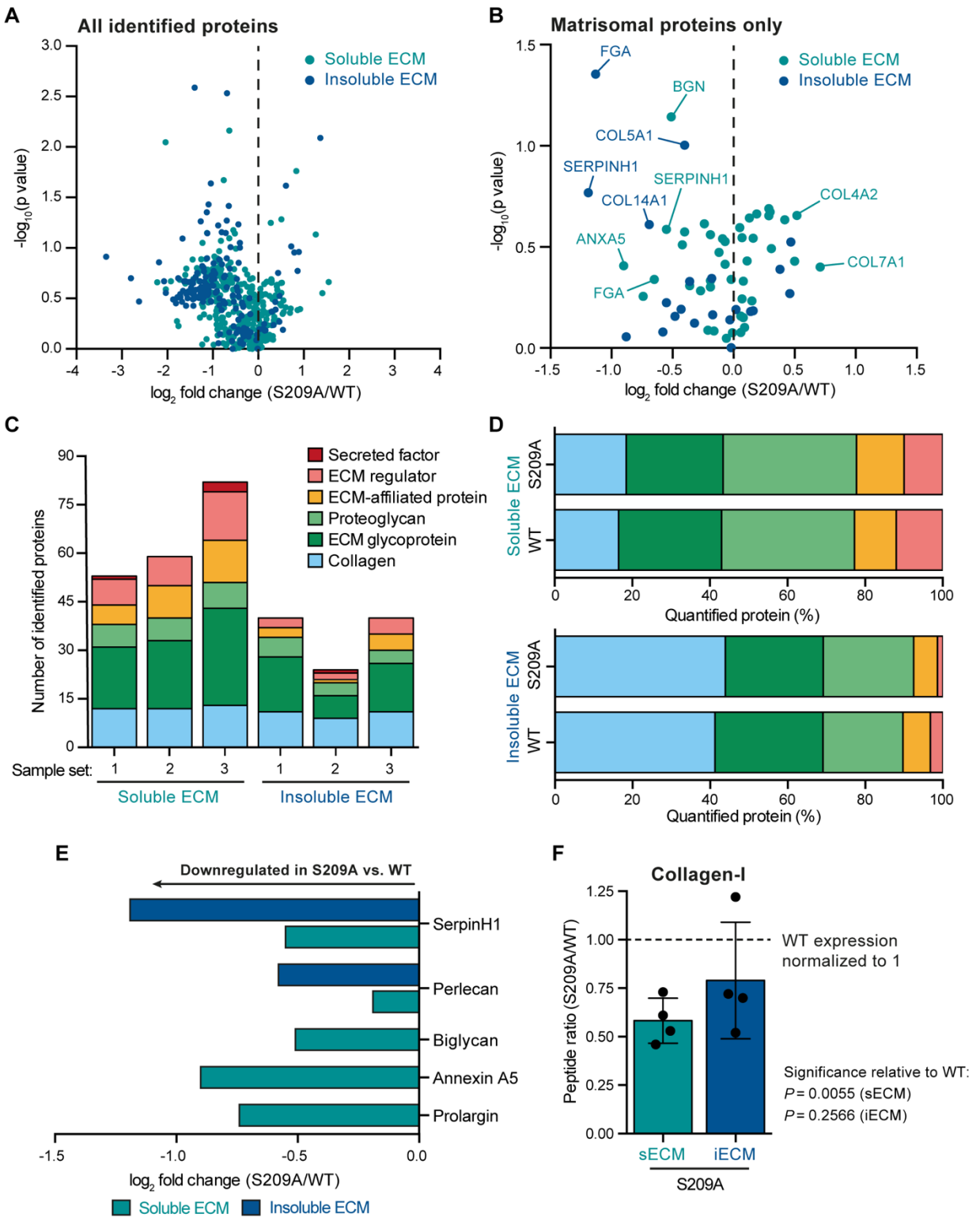

Figure 2.2. Proteomics reveals that WT and S209A mammary gland ECM are compositionally different. (**A** and **B**) Protein volcano plots comparing the expression of all hits identified in the MS dataset (**A**) or only hits known to be matrisomal proteins (**B**). All data are

averages of three independent biological replicates. Only hits identified in all three replicates are shown. Two-tailed paired *t* test. (**C**) Number of matrisomal proteins identified in each MS dataset. Bar colour represents ECM protein category (see legend). (**D**) Overall composition of soluble and insoluble ECM fractions enriched from WT and S209A mammary glands. Bar colour represents ECM protein category (see legend in panel C). Each bar displays the abundance (based on NSAF values) of the indicated category as a percentage of the total amount of matrisomal proteins identified. Data are averages of three independent biological replicates. (**E**) Fold change expression values of indicated proteins in soluble and insoluble ECM fractions. Values are calculated from normalized peptide counts in the discovery MS dataset. (**F**) Relative peptide ratios of four collagen-I subunits in soluble and insoluble S209A MG ECM fractions. Values are calculated from normalized peptide abundances in the PRM MS dataset and shown as relative to the WT condition. Statistical significance is listed, unpaired two-tailed *t* test with Welch's correction. Error bars represent SD. Peptide sequences corresponding to the 4 collagen-I subunits: GETGPAGPAGPIGPAGAR, GFSGLDGAK, GPSGPQGIR, GVVGPQGAR.

2.3.4 Collagen-I production is reduced in the mammary glands of S209A knock-in mice.

Pro-tumor signaling can be induced through binding of collagen-I in the MG to multiple receptors on tumor cells, thus influencing breast cancer onset and progression[2]. We therefore wanted to verify whether collagen-I expression differed between WT and S209A MGs. To this end, we first used picrosirius red staining to image the abundance of fibrillar collagens (*Fig. 2.3A*), observing a significant decrease in collagen content in phospho-eIF4E-deficient MGs (*Fig. 2.3B*). Western blotting of whole tissue lysates from WT and S209A MGs supported the lower collagen-I protein abundance in phospho-eIF4E deficient MGs and confirmed the decreased SerpinH1 expression originally detected via mass spectrometry (*Fig. 2.3C*). Fibroblasts synthesize ECM, including stromal collagens, and are a major cell type in the MG. We postulated that S209A MG-resident fibroblasts produce less collagen-I than their WT counterparts. To test this, we isolated primary fibroblasts from age-matched WT or S209A MGs. Western blotting confirmed a reduced expression of collagen-I in the phospho-eIF4E-deficient fibroblasts compared to WT (*Fig.*

2.3D). No significant difference in the number of fibroblasts isolated per gland between genotypes was observed, suggesting that differential collagen-I expression in the MG is not a result of decreased fibroblast number in S209A mice (*Fig. 2.3E*). Notably, as shown by qPCR, decreased protein expression of collagen-I and SerpinH1 was not paralleled by a decrease in *COL1A1* or *SERPINH1* mRNA (*Fig. 2.3F, 2.3G*). We next chose to model collagen synthesis in our primary MG fibroblasts using an *ex vivo* matrix production assay (*Fig. 2.3H*). L-ascorbic acid is known to induce pro-collagen synthesis by preferentially enhancing the transcription of type I and III collagen genes[53]. Culturing fibroblasts in media supplemented with L-ascorbic acid is well-established to enable the production of a cell-derived matrix *in vitro*[54,55]. Using this methodology, we could visualize by immunofluorescence the production of collagen-I in our cultures of primary MG fibroblasts (*Fig. 2.3I*). Under these conditions, we further verified by Western blot that the matrices produced by S209A MG fibroblasts have less collagen-I compared to WT-derived matrices (*Fig. 2.3J*). These data illustrate that, despite the addition of a potent stimulator of collagen transcription, phospho-eIF4E-deficient fibroblasts remain unable to boost collagen-I protein expression to the same extent as WT MG fibroblasts. Together these data support that collagen-I production is repressed in primary S209A MG fibroblasts.

Given the robust decrease in collagen-I protein in S209A samples, but not mRNA, we next sought to assess whether this could be explained by translational control of collagen-I by phospho-eIF4E. To address this question, we performed polysome profiling on primary MG fibroblasts isolated from WT and S209A mice (Supp. *Fig. 2.3A*). Profiling was performed in biological triplicate, with each replicate combining primary fibroblasts

from 4 inguinal MGs pooled from 2 mice. We first chose to enrich for polysome-associated mRNA through the use of a non-linear two-step sucrose gradient, optimized to isolate efficiently translated mRNAs from primary cells[56]. qPCR of RNA isolated from these fractions showed a significant reduction of *COL1A1* polysome-associated mRNA in primary MG fibroblasts derived from S209A mice, compared to WT MG fibroblasts (Supp. *Fig. 2.3B*). In contrast, we saw no difference in the abundance of *COL1A1* mRNA in whole cell lysate-derived RNA from the same cell preparations (Supp. F*ig. 2.3C*). Encouraged by these findings, we repeated the polysome profiling using a linear sucrose gradient approach, which we have used in the past[9,57]. Representative polysome gradient profiles from WT and S209A fibroblasts were largely overlapping (*Supp. Fig. 2.3D*), consistent with the function of phospho-eIF4E in regulating selective mRNA translation[28]. qPCR was subsequently performed on RNA isolated from individual light and heavy polysome-bound fractions in WT and S209A fibroblasts, revealing a modest redistribution of *COL1A1* mRNAs from heavy (efficiently translated, fractions 12 to 15) to light (poorly translated, fraction 11) polysome fractions (*Supp. Fig. 2.3E*). These data are consistent with the paradigm of the phosphorylation of eIF4E engendering the translation of *COL1A1* mRNA, but we cannot exclude the possibility of other mechanisms simultaneously acting to regulate *COL1A1* translation in primary MG fibroblasts (see Discussion).

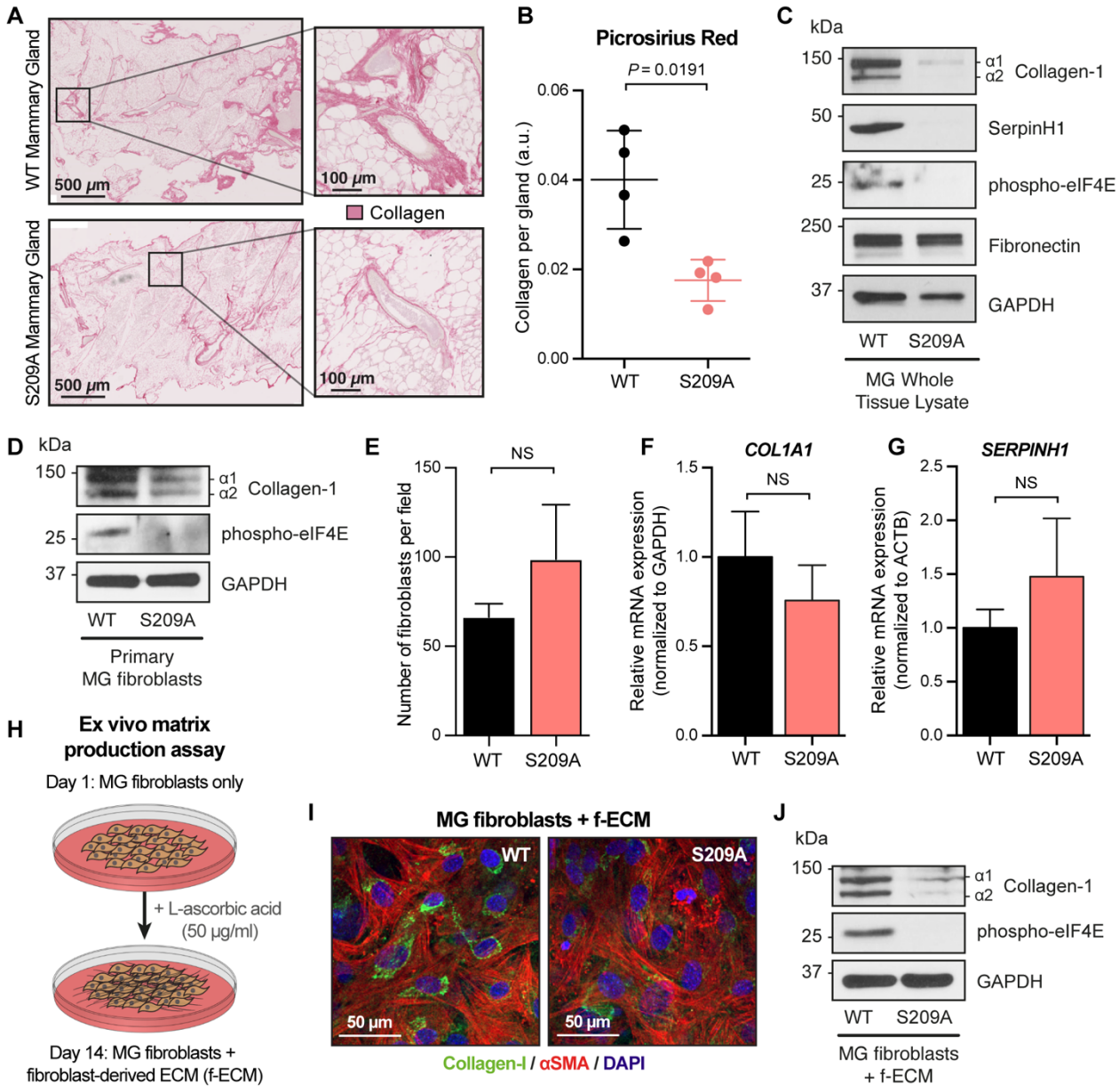

Figure 2.3. Phospho-eIF4E controls the production of collagen-I in the naïve mammary gland. (**A** and **B**) Representative images (**A**) and positive staining quantification (**B**) of WT and S209A mammary glands stained with picrosirius red. Error bars represent SD. Unpaired two-tailed *t* test with Welch's correction, $n = 4$ per group. (**C** and **D**) Western blot analysis of the indicated proteins in WT and S209A mammary gland whole tissue lysates (**C**) and primary mammary gland-derived fibroblasts (**D**). (**E**) Number of primary fibroblasts isolated from WT and S209A mammary glands. Data are represented as the number of cells counted per field of view. Error bars represent SD. Mann-Whitney test, $n = 4$ (WT), $n = 5$ (S209A). ROUT outlier test was used to remove one datapoint (Q = 1%). (**F** and **G**) Fold change in expression of the indicated mRNAs in S209A samples relative to WT. Unpaired two-tailed *t* test with Welch's correction, $n = 4$ for *COL1A1*, $n = 3$ for *SERPINH1*. (**H**) Schematic of *ex vivo* fibroblast-derived matrix production assay. (**I**) Representative immunofluorescence images of the indicated markers in

WT and S209A fibroblast-derived matrices. (**J**) Western blot analysis of the indicated proteins in WT and S209A mammary gland fibroblast-derived matrices. For all statistics: NS, $p > 0.05$.

2.3.5 Fibroblast-derived collagen-I matrix topology is altered by phospho-eIF4E-deficiency.

Aside from its function as a biochemical ligand, the biophysical orientation of collagen can promote tumor cell migration and invasion[2]. When culturing fibroblast-derived matrices *ex vivo (Fig. 2.3H)*, we noted that the topology of the cells differed depending on whether they were WT or S209A (*Fig. 2.4A*). WT fibroblasts displayed a strong degree of linearity against one another, with an average of 42.0% of cells aligning within 40 degrees of the modal angle of orientation for a given sample. This percentage was reduced to 30.3% for S209A fibroblasts, reflecting a more disorganised spatial assembly that lacks inherent linearity (*Fig. 2.4B*). Differences in cellular alignment may be due to underlying matrix topology, so we next assessed whether phospho-eIF4E-deficiency was impacting the orientation of collagen-I. Using immunofluorescence staining specifically for collagen-I, in sample preparations where fibroblasts were ablated after matrix production, we were able to visualize and quantify the orientation of individual collagen-I fibers (*Fig. 2.4C*). Encouragingly, we observed the same pattern in the distribution of orientation of collagen-I fibers in WT- versus S209A-derived matrices; 38.5% of WT-derived fibers lay within 40 degrees of the modal orientation angle compared to 29.8% of S209A-derived fibers (*Fig. 2.4D*). Our lab has previously shown that the MNK1/2 inhibitor SEL201 robustly decreases the phosphorylation of eIF4E[10,57,58]. We showed that producing WT fibroblast-derived matrices in the presence of SEL201 recapitulated the S209A fibroblast and matrix phenotypes (*Fig. 2.4A-D*). We can therefore

conclude that the topology of collagen-I produced by MG fibroblasts *in vitro* is impacted by the (1) genetic mutation on S209 that precludes eIF4E from being phosphorylated, and (2) pharmacologic repression of eIF4E phosphorylation.

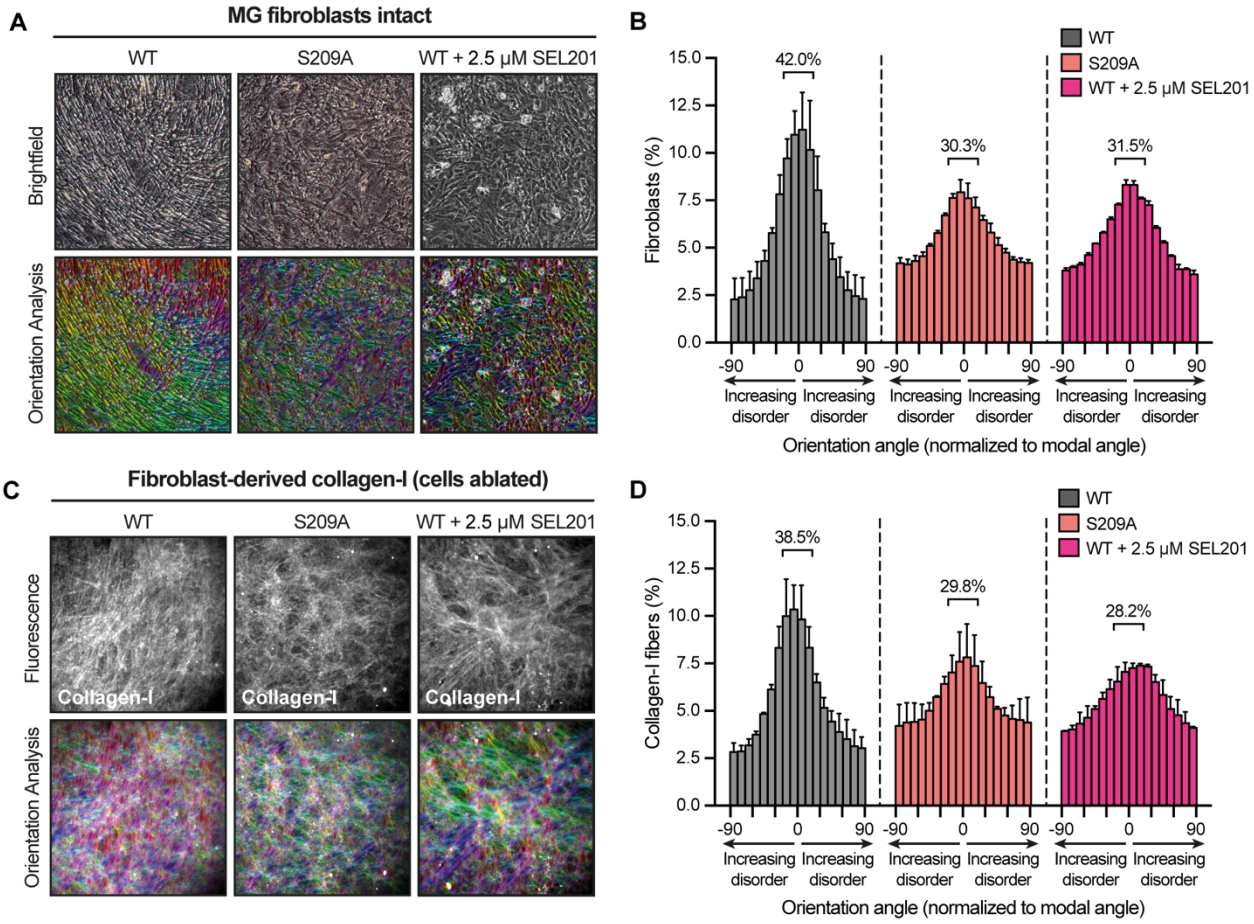

Figure 2.4. The spatial organisation of *ex vivo* fibroblast-derived collagen-I is altered in a phospho-eIF4E-deficient context. (**A**) Representative images of mammary gland fibroblasts cultured for 14 days under matrix-producing conditions. Upper panels: brightfield images, lower panels: visual representation of analysis completed using ImageJ's OrientationJ plugin. (**B**) Quantification of fibroblast orientation relative to the modal angle of orientation. Histogram colour denotes sample condition. Indicated percentages represent the number of fibroblasts that are ± 20 degrees away from the modal orientation angle. Data are averaged across repeats, error bars represent SD. (**C**) Representative images of collagen-I matrices deposited by mammary gland fibroblasts after 14 days being cultured under matrix-producing conditions. Upper panels: immunofluorescence images specific for collagen-I, lower panels: visual representation of analysis completed using ImageJ's OrientationJ plugin. (**D**) Quantification of collagen-I fiber orientation relative to the modal angle of orientation. Histogram colour denotes sample condition. Indicated percentages represent the number of fibers that are ± 20 degrees

away from the modal orientation angle. Data are averaged across repeats, error bars represent SD. For all experiments: $n = 3$.

2.3.6 Tumor-associated collagen deposition and fiber alignment in the mammary gland is shaped by eIF4E phosphorylation

Our group, and others, have shown that tumors implanted into phospho-eIF4E-deficient MGs have a reduced ability to metastasize compared to the same tumors growing in WT MGs[10,11]. We therefore wanted to investigate whether the altered collagen landscape in S209A MGs contributes to this diminished metastatic ability. We have shown that phospho-eIF4E-deficiency impacts upon the spatial topology of fibroblast-derived collagen-I *in vitro* (*Fig. 2.4*), but next wanted to expand our findings into BC mouse models. 4T1 cells were orthotopically injected into WT and S209A BALB/c mice, and the primary tumor with surrounding stroma was harvested at two weeks post-injection (*Fig. 2.5A*). This timepoint was chosen due to our previously published data showing that tumor-bearing S209A mice have significantly fewer tumor cells circulating in the peripheral blood at 14 days post-injection compared to tumor-bearing WT mice[10]. To visualize individual collagen fibers within the tumor-associated landscape, we performed SHG microscopy on selected regions of interest (ROIs) at the tumor edge (*Fig. 2.5B*). It is known that reorganisation of collagen fibers at the tumor-stroma boundary helps to facilitate local invasion and metastasis; a characteristic of breast cancer known as tumor-associated collagen signatures (TACS)[31]. Classification of TACS is based on assessing the angle of collagen fibers relative to a border. Bulk assessment of the tumor-associated collagen in our samples revealed that tumors in S209A MGs have fewer fibers oriented between 60° and 90° against the tumor boundary and more fibers oriented between 0°

and 30° (*Fig. 2.5C*). The net result is that tumors residing in S209A MGs are surrounded by fibers that run predominantly in parallel with the tumor boundary, an observation associated with reduced local invasion and disease spread[31], compared to tumors in WT MGs that have more radially aligned fibers. Furthermore, quantification of individual fiber metrics (*Fig. 2.5D*) revealed that tumor-associated collagen fibers in S209A glands are marginally longer than those present in WT glands (*Fig. 2.5E*), a phenotype that has been associated with an increased incidence of non-invasive disease in triple-negative breast cancer (TNBC) patients[59]. In contrast, no differences in fiber width (*Fig. 2.5F*) or straightness (*Fig. 2.5G*) between groups were detected. Picrosirius red staining was additionally performed to assess collagen abundance at the tumor-stroma boundary. We observed that tumors growing in the MGs of S209A mice were surrounded by less collagen, compared to tumors present in WT glands (*Fig. 2.5H*). Thus, phospho-eIF4E-deficient glands maintain reduced collagen content even in the presence of a growing tumor. Larger amounts of deposited collagen can lead to increased induction of pro-tumor signaling, and we have shown that culturing tumor cells in WT, but not S209A, MG ECM is capable of augmenting invasive cellular behaviour (*Fig 2.1G, 2.1H*). We next questioned whether our MG-derived ECM was impacting invasion through collagen-mediated signaling. The collagen-specific receptor tyrosine kinase DDR2 mediates 4T1 cell invasion *in vitro* and metastasis *in vivo*[60]. As with D2.OR cells (*Fig. 2.1G*), the invasiveness of 4T1 cells was significantly increased in the presence of WT MG ECM, but this augmented invasive capacity was lost upon siRNA-mediated depletion of DDR2 in 4T1 cells (*Fig. 2.5I*). Mechanistically, DDR2 promotes invasion and metastasis by

stabilizing the Snail1 protein (*Fig. 2.5J*) [60]. We observed that 4T1 cells cultured in the presence of WT MG ECM for 48 hours had increased Snail1 protein levels, compared to cells cultured in S209A MG ECM or cells cultured in complete media alone (*Fig. 2.5K*). Efficient knockdown of DDR2 at the RNA level was confirmed by qPCR (Supp. *Fig. 2.4A*), resulting in a reduction in DDR2 protein abundance of approximately 60% relative to control siRNA transfected 4T1 cells (Supp. *Fig. 2.4B, 2.4C*). These data suggest that increased 4T1 cell invasion in the presence of WT MG ECM is at least partially driven by extracellular collagen signaling through DDR2. Overall, our *in vivo* modelling highlights the impact of phospho-eIF4E-deficiency on the orientation and abundance of collagen in a tumor-bearing MG, thereby reducing the pro-metastatic impact of collagen both biophysically and biochemically.

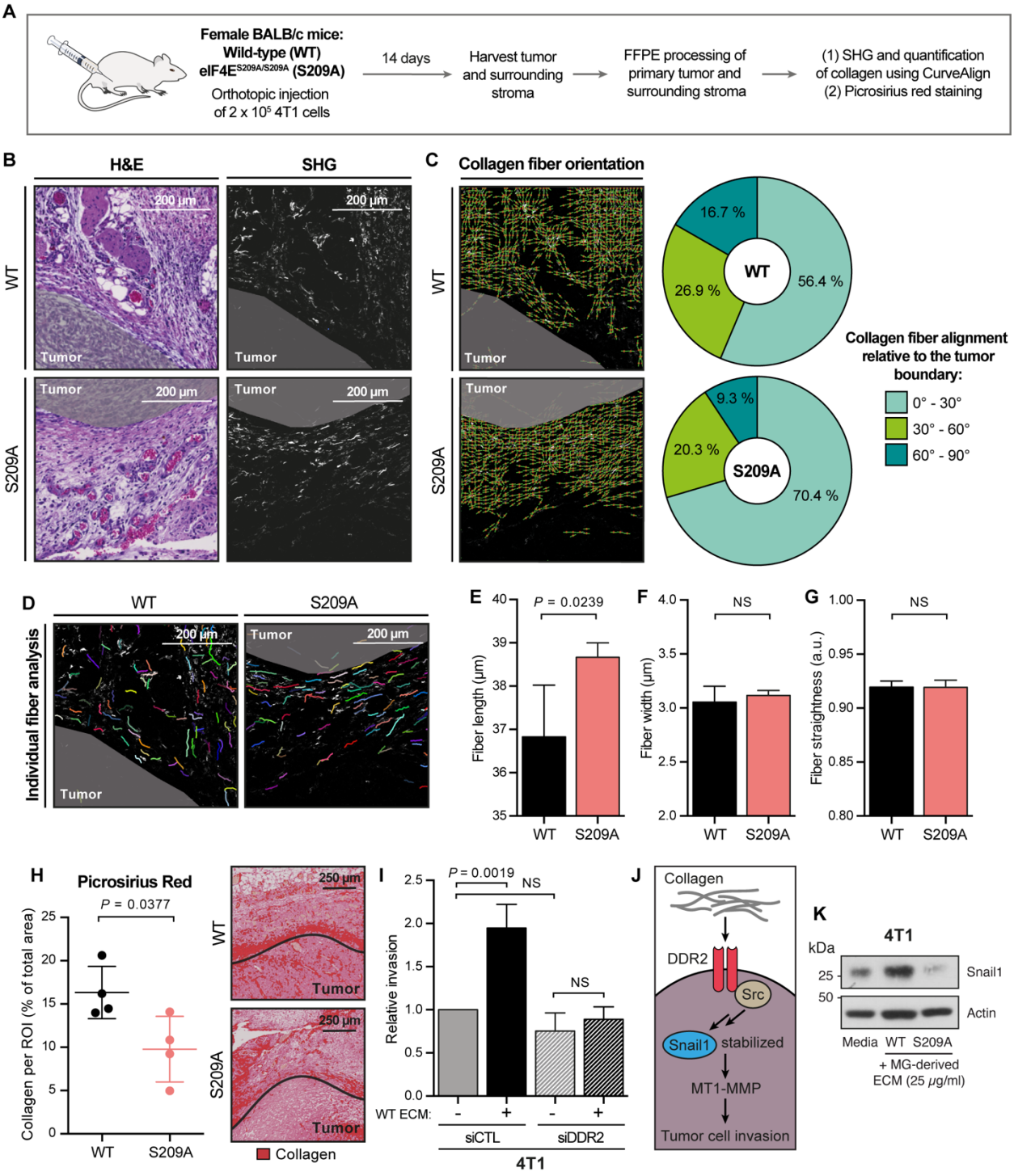

Figure 2.5. Phospho-eIF4E deficiency governs the fiber alignment and deposition of collagen-I at the tumor-stroma boundary. (**A**) Schematic detailing the experimental design for orthotopic 4T1 cell injection and tissue processing at endpoint. (**B**) Representative images of H&E staining and SHG in WT and S209A tumor-bearing mammary glands. Tumor area is indicated in grey. Images show one ROI per group. (**C**) Left: representative images of

CurveAlign orientation analysis from WT and S209A tumor-bearing mammary gland ROIs. Right: Pie chart depicting grouped orientation of collagen fibers at the tumor-stroma boundary in WT and S209A tumor-bearing mammary glands, analyzed using CurveAlign software. Fiber orientation is expressed as relative to the tumor boundary. Data are averages of all samples within a group, n = 5 per group (three ROIs selected and analysed per mouse, 15 ROIs total per group). (**D**) Representative images of individual collagen fiber analysis performed using CT-FIRE software in WT and S209A tumor-bearing mammary glands. (**E-G**) Collagen-I fiber length (**E**), width (**F**) and straightness (**G**) as measured using CT-FIRE software in WT and S209A tumor-bearing mammary glands. Data are expressed as mean values, error bars represent SD. Unpaired two-tailed *t* test with Welch's correction, $n = 5$ per group (three ROIs selected and analysed per mouse, 15 ROIs total per group). (**H**) Quantification of positive staining (left) and representative images (right) of WT and S209A tumor-bearing mammary glands stained with picrosirius red. Data shown are averaged across all ROIs analysed per mouse, error bars represent SD. Unpaired two-tailed *t* test with Welch's correction, $n = 4$ per group (three ROIs selected and analysed per mouse, 12 ROIs total per group). (**I**) Relative invasion of 4T1 cells in the indicated conditions. All data are normalized to the media only control (grey bar). One-way ANOVA with Tukey's multiple comparison test, $n = 3$. NS, $p > 0.05$. (**J**) Schematic depicting how collagen signaling via DDR2 promotes tumor cell invasion. (**K**) Western blot analysis of the listed proteins in 4T1 cells across the indicated conditions. All MG ECM treatments were for 48 hours.

2.3.7 Characterization of phospho-eIF4E and collagen-I in tumor and stroma regions of human breast cancer patients.

Stromal desmoplasia, due in large part to increased collagen-I expression[61], is characteristic of breast cancer progression and is associated with tumor-promoting properties (reviewed in [2]). Our data support that the phosphorylation status of eIF4E influences collagen abundance in a pre-clinical tumor-bearing mouse model (*Fig. 2.5*). We next wanted to assess whether this regulatory axis has clinical relevance. The workflow detailing the staining carried out on multi-center patient tumors is shown for clarity in *Supp. Fig. 2.5*. We developed a dual-stain immunohistochemistry (IHC) protocol to visualize the relative abundance of phospho-eIF4E and collagen-I within one tissue section (*Fig. 2.6A*), from which we performed expression correlation analysis. We detected a positive correlation between phospho-eIF4E and collagen-I across all samples

(*Fig. 2.6B*), despite a wide range in expression of each protein between patients. Interestingly, when stratifying patients by disease stage, we observed that the correlation was stronger in early-stage (stage 0 or I) samples, with a r value of 0.41, compared to 0.25 in late-stage (stage II or III) samples (*Fig. 2.6C*). We speculate that the regulation of collagen-I by phopsho-eIF4E may be relevant in human breast cancer, particularly earlier in disease progression. Next, we chose to correlate collagen-I expression with the patients' TNM classification, a system used for cancer staging[62]. When ranking patients by collagen-I expression and comparing the highest and lowest 20%, the high expression group had an increased incidence of T4 scoring, describing a primary tumor that has invaded into nearby tissues and local structures – 22% compared to 0% in the low expression group (*Fig. 2.6D*). Additionally, we observed that the high expression group had a marginally greater frequency of regional lymph node (LN) metastases, denoted by an N score greater than 0, with 22% of patients having detectable metastases compared to 17% in the low expression group. Of note, most patients in the high expression group had 4 or more tumor-bearing LNs (N2), while in the low expression group no patient had metastasis in more than 3 LNs (N1) (*Fig. 2.6E*). These correlations support the importance of collagen-I in facilitating breast cancer local invasion and subsequent metastasis.

To further characterize the cellular heterogeneity of phospho-eIF4E expression in human BC samples we next completed dual-colour immunofluorescence (IF) to detect phospho-eIF4E and vimentin, which is a marker routinely used to identify the stroma[63,64] (*Fig. 2.6F*). Using this strategy, we could delineate tumoral versus stromal areas of the

TME and assess phospho-eIF4E expression in each compartment independently (*Fig. 2.6G*). In addition to using a subset of the patient samples stained by IHC in *Fig. 2.6A-C*, we generated a patient tissue microarray (TMA) designed to include stroma from tumor-adjacent and peripheral regions from the same patient. Similar to our IHC data, phospho-eIF4E-positive staining was most intense in tumor regions. However, upon closer inspection of vimentin-positive stromal regions, we identified cells staining double positive for vimentin and phospho-eIF4E (*Fig. 2.6H*). We noted that stromal cells, with fibroblast-like morphology, which were spatially closer to tumor regions had phospho-eIF4E expression comparable to neighbouring tumor cells (*Fig. 2.6H*). To quantify these observations, we performed cell segmentation analysis and subsequently classified cells by their expression of vimentin and phospho-eIF4E. From this we confirmed that tumor cells have significantly stronger expression of phospho-eIF4E compared to stromal cells (*Fig. 2.6I*). Additionally, approximately 57% and 43% of phospho-eIF4E-expressing cells were found in the tumor and stroma respectively, independent of expression level (*Fig. 2.6J*). Regardless, we observed a strong positive correlation between the levels of tumor- and stroma-derived phospho-eIF4E within a given sample (F*ig. 2.6K*). Next, to investigate the impact of tumor proximity on stromal phospho-eIF4E expression, we focussed on patients from which we had samples from tumor-adjacent and peripheral stroma (*Fig. 2.6L*). We quantified that stromal (vimentin-positive) cells closer to the tumor have a significantly higher expression of phospho-eIF4E compared to those in the periphery (*Fig. 2.6M*). In addition, the percentage of stromal cells that are phospho-eIF4E-positive decreased as the distance away from the tumor increased (*Fig. 2.6N*). Taken together,

these data suggest the potential clinical relevance of blocking the phosphorylation of eIF4E in tumor cells and in stromal cells of the TME.

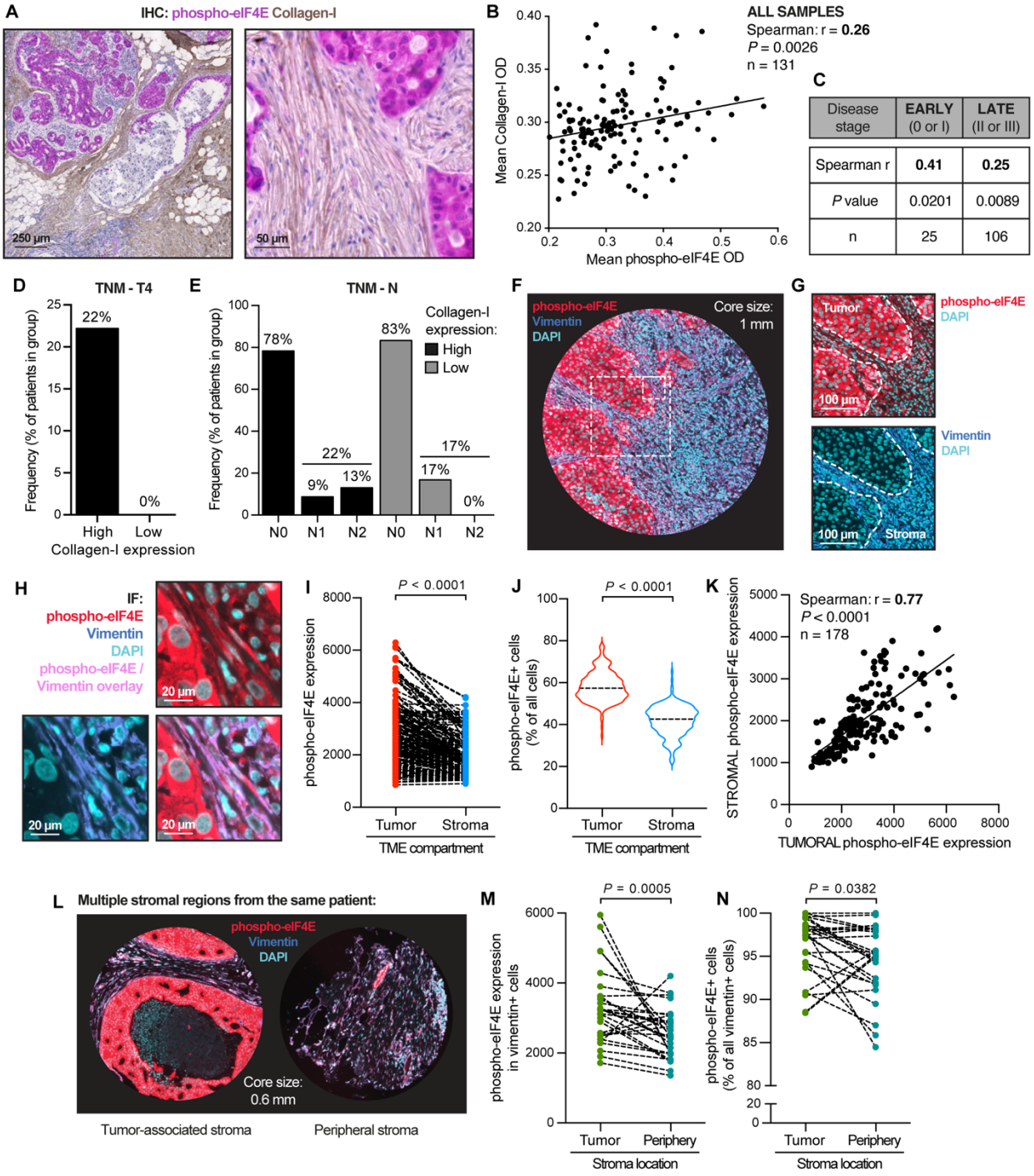

Figure 2.6 (legend on following page)

Figure 2.6: Characterization of phospho-eIF4E and collagen-I in tumor and stroma regions of human breast cancer patients. (**A**) Representative low-resolution (left) and high-resolution (right) images of IHC staining against collagen-I (DAB) and phospho-eIF4E (Magenta) in patient samples. (**B and C**) Correlation analysis of phospho-eIF4E and collagen-I staining intensities across all stained samples (**B**) or stratified by early versus late disease stage (**C**). Spearman rank-order. Black trendline shows linear regression. *P*, r, and *n* values are indicated. ROUT outlier test was used to remove 2 datapoints (Q = 1%). (**D**) Incidence of a locally invasive primary tumor in late-stage samples stratified by high versus low collagen-I expression. Data are presented as the percentage of samples in each group with a T4 annotation (TNM grading). (**E**) Incidence of regional lymph node metastasis in late-stage samples stratified by high versus low collagen expression. Data are presented as the percentage of patients in each group with N0, N1 or N2 scores (TNM grading). (**D** and **E**) High versus low collagen-I expression was determined by selecting the highest and lowest quintile of patients when ranked according to collagen-I staining intensity. *N* = 23 (high), *n* = 24 (low). (**F-H**) Representative images of IF staining against vimentin and phospho-eIF4E (plus DAPI) in patient samples. Dashed boxes in the low-resolution image (**F**) correspond to areas used for mid-resolution (**G**) and high-resolution (**H**) zoom-ins. Dashed lines in **G** denote boundaries between tumor and stroma regions (as indicated). (**I**) Staining intensity of phospho-eIF4E comparing tumor and stroma regions of the same sample. Dashed lines connect datapoints from the same sample. Wilcoxon matched-pairs rank test. (**J**) Distribution of phospho-eIF4E-positive cells between tumor and stroma compartments. Data are averaged across all samples and shown as violin plots, dashed lines show median values. Wilcoxon matched-pairs rank test, *n* = 191. (**K**) Correlation of phospho-eIF4E expression between tumor and stroma regions of the same sample. Spearman-rank order. Black trendline shows linear regression. *P*, r, and *n* values are indicated. **For I and K**: *n* = 178. ROUT outlier test was used to remove 13 datapoints. (**L**) Representative images of tumor-associated and peripheral stroma regions from the same patient. (**M-N**) Phospho-eIF4E staining intensity (**M**) and percentage of phospho-eIF4E-positive stromal cells (**N**) comparing tumor-associated and peripheral stroma regions from the same patient. Dashed lines connect datapoints from the same sample. Wilcoxon matched-pairs rank test, *n* = 29 (**M**), *n* = 27 (**N**). ROUT outlier test was used to remove 1 datapoint in **M** and 3 datapoints in **N** (Q = 1%). **For I, K, M**: Data represent mean cellular intensity values.

2.3.8 Genetic and pharmacological inhibition of eIF4E phosphorylation reduces anti-PD-1-mediated intratumoral collagen deposition.

Programmed cell death protein 1 (PD-1), expressed on multiple immune cell types, is bound by its ligands programmed death-ligand 1 and 2 (PD-L1 and PD-L2), expressed on tumor cells, to diminish anti-tumor immune responses[65]. In recent years, therapies aimed at blocking the PD-1/PD-L1 interaction, and more broadly known as immune checkpoint inhibitors (ICIs), have revolutionized cancer treatment[65]. Interestingly,

increased intratumoral collagen deposition is a recently identified mechanism of resistance to anti-PD-1/PD-L1 therapy, resulting in reduced T cell infiltration and increased T cell exhaustion[66]. Our prior work has shown that inhibition of the MNK1/2-eIF4E axis sensitizes tumor bearing mice to anti-PD-1 immunotherapy[9,10]. We therefore investigated whether a phospho-eIF4E-deficient TME resists anti-PD-1 therapy-induced collagen deposition and correlates with an increased anti-tumor response. WT and S209A mice were orthotopically injected with 4T1 cells, known to be resistant to anti-PD-1 therapy[67], and subsequently administered anti-PD-1 (*Fig. 2.7A*). Treatment with anti-PD-1 was sufficient to increase intratumoral collagen in 4T1 tumors grown in WT mice, as measured by picrosirius red analysis (*Fig. 2.7B, 2.7C*). However, in 4T1 tumors grown in S209A mice this effect was reduced (*Fig. 2.7B, 2.7C*), suggesting that a phospho-eIF4E-deficient host would maintain sensitivity to anti-PD-1 treatment. Accordingly, we observed that administration of anti-PD-1 therapy resulted in a modest, albeit significant, decrease in the size of 4T1 tumors grown in S209A mice (*Fig. 2.7D*), but not in WT mice (*Fig. 2.7E*). Our data thereby support that collagen is a potential marker of resistance to anti-PD-1 therapy. Moreover, using previously banked 66cl4 tumors (a cell line derived as a subclone of the 4T1 model) from mice treated with SEL201 and anti-PD-1 therapy[10], we showed that pharmacological inhibition of MNK1/2 also protected against anti-PD-1-mediated collagen deposition. As anticipated, anti-PD-1 therapy augmented tumoral collagen content, but the addition of SEL201 abolished this increase (*Fig. 2.7F, 2.7G*). These data are clinically relevant as they illustrate the potential for MNK1/2 inhibitors to be used to thwart the acquisition of resistance to ICIs.

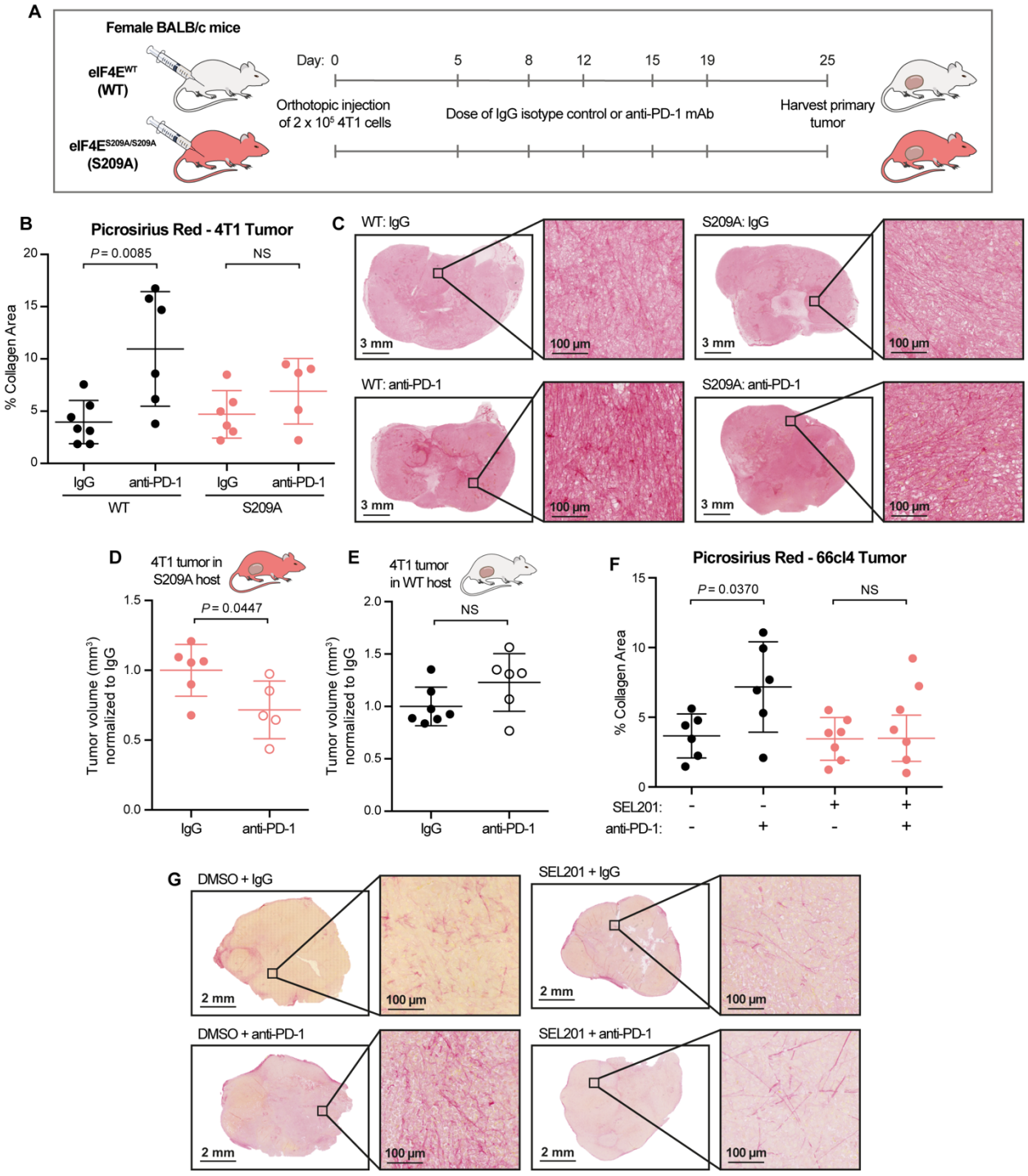

Figure 2.7. Genetic and pharmacological reduction of eIF4E phosphorylation protects against anti-PD-1-induced intratumoral collagen deposition (**A**) Schematic detailing the experimental design for orthotopic 4T1 injection and anti-PD-1 treatment, depicting drug dose timings and tissue collection at endpoint. (**B-C**) Positive staining quantification (**B**) and representative images (**C**) of 4T1 tumors grown in either WT or S209A mammary glands, treated with IgG isotype control or anti-PD-1 (as indicated), stained with picrosirius red. Data are

presented as the positive staining area as a percentage of the total tumor area, error bars represent SD. Two-way ANOVA with Tukey's multiple comparison test. (**D-E**) Volume of 4T1 tumors grown in S209A (**D**) or WT (**E**) mammary glands, 25 days post-injection. Data are normalized to the average of the IgG group within each panel, error bars represent SD. Unpaired two-tailed *t* test with Welch's correction. For **B-E**: $n = 7$ (WT: IgG), $n = 6$ (WT: anti-PD-1, S209A: IgG), $n = 5$ (S209A: anti-PD-1). (**F-G**) Positive staining quantification (**F**) and representative images (**G**) of 66cl4 tumors grown in either WT or S209A mammary glands, stained with picrosirius red. Mice were treated with either SEL201 or DMSO control in combination with anti-PD-1 or IgG isotype control (as indicated). Data are presented as the positive staining area as a percentage of the total tumor area, error bars represent SD. Two-way ANOVA with Tukey's multiple comparison test, $n = 6$ (DMSO + IgG, DMSO + anti-PD-1), $n = 7$ (SEL201 + IgG, SEL201 + anti-PD-1). For all statistics: NS, $p > 0.05$.

2.4 Discussion

The ECM influences each of the hallmarks of cancer to impact tumorigenesis and therapeutic resistance. Cell-ECM interactions, both biochemical and biophysical, elicit a plethora of cellular responses that promote metastasis. The role of tumor-intrinsic MNK1/2-eIF4E activity is well documented as leading to pro-invasive and pro-metastatic phenotypes[9,12,58], but comparatively little is known about how this signaling axis functions in stromal cells of the TME to impact breast cancer progression. Here we used proteomics, *in vitro* investigation, SHG microscopy, and *in vivo* modelling to better understand how modulating the MNK1/2-eIF4E axis affects the composition and oncogenic properties of the ECM produced by stromal cells.

We first showed that ECM produced in mice engineered to express a mutation of a phosphorylatable residue on eIF4E, rendering the mice phospho-eIF4E-deficient, differentially affects the invasiveness of tumor cells compared to WT-derived ECM. Tumor-intrinsic phospho-eIF4E has been well-documented to promote tumor cell invasion[58,68]. This study has shown that phospho-eIF4E in the stroma may also contribute to tumor cell invasive potential via cell-matrix interactions. Our data showed that culturing

tumor cells in WT-derived MG ECM bolstered their invasive capacity, but not if the ECM was S209A-derived (*Fig. 2.1G, 2.1H*). When we injected these cells (pre-treated with WT- or S209A-derived MG ECM) into phospho-eIF4E-deficient mice, we observed the same trend (*Fig. 2.1F*). However, when injected into WT mice, the phenotype was lost (*Supp. Fig. 2.1B*). This would suggest that any effects of culturing tumor cells in MG-derived ECM prior to injection may be negated by a host environment that is phospho-eIF4E-competent. Alternatively, it may be true that this *in vivo* system is not accurately modelling changes in tumor cell invasion, but instead highlighting differences in cell survival or adhesive properties. Regardless, our findings confirm a role for the MNK1/2-eIF4E axis in controlling MG ECM composition.

Importantly, this study sheds light on how collagen-I may be post-transcriptionally regulated within MG fibroblasts. To our knowledge, it is unknown how the translation of collagen is controlled in breast cancer, although prior work has implicated the mTOR signaling axis in other biological settings, including tendon cells[69] and models of fibrosis[70,71]. We can rule out direct transcriptional regulation, as the levels of *COL1A1* mRNA in WT versus S209A MG fibroblasts were not significantly different (*Fig. 2.3F*). The data acquired from our polysome profiling suggest that *COL1A1* mRNA may be regulated translationally by phospho-eIF4E, as we observed a reduction in the abundance of heavy polysome-bound (efficiently translated) *COL1A1* mRNA in S209A MG fibroblasts compared to WT (*Supp Fig. 2.3*). We present these polysome profiling data with caution, fully acknowledging the limitations that exist when working with and culturing primary MG fibroblasts. Removing fibroblasts from their surrounding MG matrix *in vivo* and

continuously culturing them on plastic *in vitro* has been shown to alter their gene expression profiles and phenotypic responses[72–75]. Additionally, the number of fibroblasts we isolate per MG is low, making it unfeasible to acquire sufficient starting material for polysome profiling without necessitating *in vitro* expansion. We also cannot ignore the possibility that phospho-eIF4E-dependent control of collagen-I may occur indirectly through SerpinH1, which is critical for the proper formation of collagen[51]. Having validated the decreased expression of SerpinH1 in S209A-derived MG ECM compared to WT, we predict that this may contribute to altered collagen-I deposition, perhaps by influencing protein stability rather than production. Recent evidence in pancreatic ductal adenocarcinoma also suggests there may be a bi-directional relationship between phospho-eIF4E and collagen-I in cancer, as extracellular collagen can increase MNK1/2 activation[76]. In addition, *COL1A1* expression in cancer-associated fibroblasts is regulated by the transcription factor ATF4[77], of which one direct target is 4E-BP1, which functions to sequester eIF4E and suppress its activity[78]. Furthermore, it has been shown in a model of cutaneous squamous cell carcinoma that collagen deposition is regulated by Act1-mediated translational control of HIF1α and downstream P4H/LOX[79]. Overall, it is likely that multiple pathways regulate the collagen-I life-cycle simultaneously, and a comprehensive understanding of the direct or indirect role of phospho-eIF4E in these processes requires additional studies focussed exclusively on this aspect.

Insight into the control of collagen-I production is of strong relevance in the mammary gland. Breast density is influenced by the deposition and cross-linking of collagen type I and has been established as an important risk factor in the development

of BC[80–82]. Interestingly, our group has previously used the PyMT murine BC model to illustrate that phospho-eIF4E-deficient mice exhibit a delay in spontaneous tumor onset compared to WT controls[12]. It remains unknown whether this observation is related to collagen deposition. In this study, we demonstrated that phospho-eIF4E-deficiency alters the abundance of collagen-I in the MG, which is at least partially responsible for promoting tumor cell invasion via signaling through the DDR2 receptor (*Fig. 2.5I, 2.5K*). This is evidence of how interrupting eIF4E phosphorylation could be a useful strategy to modulate tumor-matrix crosstalk. Collagen-I can further influence cellular motility in a biophysical sense. Increased deposition of collagen leads to increased alignment of these fibers, which then act as migration tracks for tumor cells to leave the primary site[83–85]. Alternatively, collagen production can suppress tumor growth by mechanically restraining the tumor, overriding its own mechanosignaling[86]. The impact of collagen as pro-tumor versus anti-tumor is largely dependent on its spatial orientation at the tumor periphery, and here we showed that phospho-eIF4E deficiency dictates collagen fiber alignment. We used SHG microscopy to show that tumors formed in phospho-eIF4E-deficient MGs are surrounded by a stroma that contains less collagen (*Fig. 2.5H*), with fibers that are aligned more in parallel with the tumor boundary, compared to tumors in WT glands (*Fig. 2.5C*). These findings may help to understand the mechanisms that control TACS-3 formation; a state in which bundles of aligned collagen are oriented perpendicular to the tumor interface, which is a prognostic signature associated with poor survival in patients[32].

Of potential clinical relevance to the use of MNK1/2 inhibitors as anti-cancer agents, we found that the expression of phospho-eIF4E and collagen-I are positively

correlated in human BC samples (*Fig. 2.6B*). Interestingly, the reduction of this correlation across disease progression suggests that this regulation may become uncoupled as homeostatic control of the tumor-associated stroma is diminished. In addition, we provided novel insight into the expression of phospho-eIF4E in the stroma. Our data highlight that tumor regions express more phospho-eIF4E than their surrounding stroma (*Fig. 2.6I, 2.6J*) and that phospho-eIF4E is not uniformly expressed within the stroma, with more strongly-expressing stromal cells residing spatially closer to a tumor (*Fig. 2.6M*). Nevertheless, the expansion of our findings into human models emphasizes the potential use of MNK1/2 inhibitors in targeting the ECM in cancer. Several promising therapies designed to target collagen production and processing have proven ineffective in the clinic[2]. The appropriate use of a MNK1/2 inhibitor, however, could potentially serve as a brake on the self-propagating desmoplastic reaction that is characteristic of many cancers[2], including breast cancer[87], and other fibrotic diseases[74]. In addition, recent publications have emphasized how collagen content in the TME can functionally impact the immune landscape, by instigating immune exclusion[88] and mediating resistance to anti-PD-1/PD-L1 immunotherapy[66]. In this regard our data, including our previous publications, continue to provide strong rationale for the use of MNK1/2 inhibitors in combination with anti-PD-1 immunotherapy. This is particularly relevant for TNBC patients, many of whom have shown promising clinical response to ICI therapy[89].

In conclusion, this study demonstrates a role for the MNK1/2-eIF4E axis in controlling the protein landscape of the ECM. These results support a model in which eIF4E phosphorylation, likely via multiple pathways, controls the production and spatial

organisation of collagen-I in the mammary gland. While our data validate the importance of this signaling node in human disease, further exploration will prove useful in better understanding the complex cell-matrix interactions that exist within the TME and their potential to be therapeutically exploited.

2.5 Experimental Procedures

Mouse model and mammary gland isolation

Wild-type (WT) female BALB/c mice were purchased from Charles River Laboratories. eIF4E$^{S209A/S209A}$ (S209A) mice were generated on a BALB/c background and kindly donated by Dr. Nahum Sonenberg (Goodman Cancer Institute-McGill University). At approximately 8 weeks of age, WT and S209A mice were euthanized, and the 4th (inguinal) mammary fat pad was removed and snap-frozen in liquid nitrogen. Lymph nodes were removed prior to excision. When required, tissue was pooled from 4 to 5 mice per group to allow for sufficient starting material weight. All animal experiments were conducted according to the regulations established by the Canadian Council of Animal Care, under protocols approved by the McGill University Animal Care and Use Committee.

Breast cancer mouse models

For tail-vein injection models: 1 x 10^6 D2.OR-GFP cells were injected into the tail vein of WT and S209A BALB/c mice. Cells were pre-cultured for 4 days prior to injection in either WT or S209A MG-derived sECM at a concentration of 25 μg/mL. At endpoint (3

days post-injection), mice were euthanized, lungs were excised and dissociated into single cells. Cell suspensions were then analyzed on an LSR Fortessa (BD) for the presence of GFP+ cells. For orthotopic mouse models: 2 x 10^5 4T1 cells were injected into the mammary fat pad of BALB/c WT and S209A mice. Primary tumors and surrounding stroma (where applicable) were removed and FFPE-processed at either 14 days (*Fig. 2.5*) or 25 days (*Fig. 2.7*) post-injection. Tumors were measured in length (L) and width (W) with tumor volume calculated using the formula: $V = 3.1416/6*L*W^2$. For the anti-PD-1 treatment cohort, all mice were randomly grouped prior to treatment. The anti-mouse PD-1 monoclonal antibody (RMP1-14) and IgG isotype control (Bio X Cell) were diluted in PBS and administered by intraperitoneal injection at 10mg/kg bodyweight per mouse, twice per week.

Enrichment of extracellular proteins (ECM) from murine mammary glands

Matrisomal proteins were enriched from murine mammary gland tissue following a previously described protocol[37]. In summary, 1 gram of frozen mammary gland per condition was pulverized under liquid nitrogen to a fine powder using a pestle and mortar. Samples were resuspended in 2 mL of a high salt buffer (3.4 M NaCl, 50 mM Tris-HCl pH 7.4, 4 mM EDTA-Na_2) and homogenized using a tissue homogenizer (Polytron), then centrifuged at 100,000 x g for 30 min at 4°C. The resultant lipid layer was discarded, and the supernatant (cellular protein fraction) was stored at -80°C. Homogenization and centrifugation steps were repeated once to yield an ECM-enriched pellet. This pellet was re-homogenized in 1.8 mL of urea extraction buffer (0.2 M NaCl, 50 mM Tris-HCl pH 7.4,

4 mM EDTA-Na_2, 2 M urea) and left shaking at 4°C overnight. The following day, samples were centrifuged at 26,000 x g for 1 hour at 4°C. The pellet (insoluble ECM) was frozen at -80°C. The supernatant (soluble ECM) was placed in cellulose dialysis tubing (MWCO 12-14 kDa, Spectrum Labs) and dialyzed against dialysis buffer (0.15 M NaCl, 50 mM Tris-HCl pH 74, 4 mM EDTA-Na_2) supplemented with 2 mM N-ethylmaleimide, 100 μg/mL phenylmethylsulfonyl fluoride and 30 μg/mL gentamicin for a total of 48 hours at 4°C. Following this, dialysis buffer was replaced with serum-free DMEM/Ham's F-12 media (Wisent Bio Products) for a subsequent 24 hours of dialysis. The protein concentration of the final matrix preparation was measured by NanoDrop before storing at -80°C.

Cell culture and treatment

MCF10DCIS.com (DCIS) cells were purchased from Wake Forest University and cultured in DMEM/Ham's F-12 (Wisent Bio Products) supplemented with 5% horse serum, 10 mmol/L HEPES, 1.05 mmol/L $CaCl_2$ and antibiotics. D2.OR-GFP cells were kindly donated by Dr. Pepper Schedin (Oregon Healthy & Science University) and cultured in DMEM high glucose (Wisent Bio Products) supplemented with 10% FBS and antibiotics. Primary mammary gland fibroblasts were isolated from the 4^{th} fat pad of WT and S209A non-tumor-bearing BALB/c mice. The fat pad was minced, digested in DMEM/Ham's F-12 with 1 mg/ml Collagenase IV for 1 hour at 37°C, passed through a 70 μm cell strainer and centrifuged at 400 x g for 10 minutes. Pelleted cells were cultured in DMEM high glucose (Wisent Bio Products) with 10% FBS and antibiotics, changing culture media 1 hour after plating to enrich for fibroblasts. For all cell treatments, soluble

ECM or drug were supplemented into normal growth media at stated concentrations. Cells were maintained at low passage number prior to use.

Sample preparation of proteolytic digestion of ECM proteins

iECM and sECM samples were suspended in 5% sodium dodecyl sulfate (SDS), 100 mM TRIS pH 7.8. Samples were subsequently heated to 99°C for 10 minutes and subjected to probe-based sonication using a Thermo Sonic Dismembrator at 25 % amplitude for 3 cycles x 5 seconds. Remaining debris was pelleted by centrifugation at 20,000 x g for 5 minutes. An aliquot of the supernatant was diluted to <1% SDS and used for estimation of protein concentration by bicinchoninic acid assay (BCA) (Pierce/Thermo). The remainder of the supernatant was transferred into a new reaction tube, and disulfide bonds were reduced by the addition of tris(2-carboxyethyl)phosphine to a final concentration of 20 mM and incubated at 60°C for 30 minutes. Free cysteines were alkylated using iodoacetamide at a final concentration of 25 mM and subsequent incubation at 37°C for 30 minutes in the dark. An equivalent of 10 μg of total protein was used for proteolytic digestion using suspension trapping (STRAP)[90]. In brief, proteins were acidified through the addition of phosphoric acid to a final concentration of 1.3% v/v. The sample was subsequently diluted 6-fold in STRAP loading buffer (9:1 methanol:water in 100 mM TRIS, pH 7.8) and loaded onto a STRAP Micro cartridge (Protifi LLC, Huntington NY) and spun at 4000 x g for 2 minutes. Samples were washed three times using 200 μL of STRAP loading buffer. Proteins were then proteolytically digested using sequencing grade trypsin (Promega) at a 1:10 enzyme to substrate ratio for 2 hours at

47°C. Peptides were sequentially eluted with 50 mM ammonium bicarbonate, 0.1% formic acid in water, and 50% acetonitrile. Peptide containing samples were then vacuum concentrated, and desalted using homemade R3-STAGE-tip desalting cartridges[91]. Desalted peptides were vacuum concentrated and reconstituted in 0.1% formic acid prior to analysis by nanoLC-MS/MS.

LC-MS/MS acquisition and data analysis

Samples were analyzed by data dependent acquisition (DDA), using an Easy-nLC 1200 online coupled to a Q Exactive Plus (both Thermo Fisher Scientific). Samples were loaded onto the precolumn (Acclaim PepMap 100 C18, 3 μm particle size, 75 μm inner diameter x 2 cm length) in 0.1% formic acid (buffer A). Peptides were separated using a 100-min binary gradient ranging from 3-40% of buffer B (84% acetonitrile, 0.1% formic acid) on the main column (Acclaim PepMap 100 C18, 2 μm particle size, 75 μm inner diameter x 25 cm length) at a flow rate of 300 nL/min. Full MS scans were acquired from m/z 350-1,500 at a resolution of 70,000, with an automatic gain control target of 1×10^6 ions and a maximum injection time of 50 ms. The 15 most intense ions (charge states +2 to +4) were isolated with a window of m/z 1.2, an AGC target of 2×10^4 and a maximum injection time of 64 ms and fragmented using a normalized higher-energy collisional dissociation energy of 28. MS/MS were acquired at a resolution of 17,500, and the dynamic exclusion was set to 40 s. For PRM experiments, the same instrumentation and similar settings were used as described above, but this method included a target list of peptides to select for MS/MS fragmentation. DDA MS raw data was processed with

Proteome Discoverer 2.4 (Thermo Scientific) and searched using Sequest HT against a human UniProt FASTA database (release 23. January 2019; 20,414 target entries). The enzyme specificity was set to trypsin with a maximum of 2 missed cleavages. Carbamidomethylation of cysteine was set as fixed modification and oxidation of methionine as variable modification. The precursor ion mass tolerance was set to 10 ppm, and the product ion mass tolerance was set to 0.02 Da. Percolator was used to assess posterior error probabilities and the data was filtered using a false discovery rate (FDR) <1% on peptide and protein level. The Minora feature detector node of Proteome Discoverer was used for label free quantitation based on precursor areas. Normalized spectral abundance factors (NSAF) were calculated[46] and S209A to WT protein abundance ratios (fold change values) were determined for proteins quantified with at least one protein-unique peptide. Volcano plots were generated by combining LFQ datasets to calculate average peptide ratios and *P* values. The quantitation of the PRM data was performed using Skyline version 20.2[92].

Fibroblast-derived matrix production and visualization (immunofluorescence)

Fibroblast-derived matrices were cultured as previously reported[93]. Briefly, cells were cultured at 100% confluency for 14 days in complete media supplemented with 50 *μ*g/mL L-ascorbic acid (media change every 24 hours). At endpoint, if required, cells were ablated by incubating in extraction buffer (0.5% Triton X-100, 20 mM NH_4OH), before fixing in 4% paraformaldehyde (PFA). IF staining was then used to visualize deposited matrices. Briefly, samples were blocked in 10% BSA for 1 hour at room temperature,

before incubating in collagen-I antibody (see *Supp. Table 2.1*) diluted in 2% BSA overnight at 4°C. The next day, samples were washed in PBS, stained for 1 hour in secondary antibody diluted in 2% BSA, washed again and mounted using Prolong Gold. Images were acquired the following day using a Leica spinning-disk confocal microscope. Orientation analysis was conducted using the OrientationJ plugin for ImageJ, as previously published[93].

Polysome profiling

Polysome profiling was performed as previously described[57]. Briefly, WT and S209A mammary gland-derived fibroblasts were isolated and expanded *in vitro* for 7 days. Each biological replicate was a pool of fibroblasts from 4 mammary glands (2 per mouse, 2 mice in total per replicate). A media change (serum-stimulation) was performed 24 hours and 2 hours prior to harvest. Cells were then treated with cycloheximide (100 μg/mL) 5 minutes, washed in cold PBS containing 100 μg/mL cycloheximide and centrifuged for 5 minutes at 390 x g at 4°C. Resulting pellets were lysed in hypotonic buffer (5 mM Tris-HCl [pH 7.5], 2.5 mM $MgCl_2$, 1.5 mM KCl) and 1X protease inhibitor cocktail containing 1 mM DTT and RNase inhibitor (100 U). Samples were left to lyse on ice for 15 minutes, then centrifuged at 13,523 x g for 15 minutes at 4°C. Supernatants were loaded onto either: (1) a 5%-34%-55% two-step sucrose density gradient, or (2) a 5%-50% linear sucrose density gradient, and centrifuged at 260,110 x g for 2 hours at 4°C. The polysomal fractions were then monitored and collected using a Teledyne ISCO one-rack Foxy R1 fraction collector.

Second Harmonic Generation (SHG) microscopy

SHG microscopy was performed using a custom-built laser scanning inverted microscope as previously described[94]. The excitation source was a mode-locked Titanium-Sapphire laser (Tsunami, Spectra Physics) capable of delivering 150fs pulses at 80MHz repetition rate at 810nm excitation wavelength. The Tsunami was pumped by a 12 W Millenia Pro laser (Spectra Physics). Using a half-wave plate and a Glan-Thompson polarizer, the average power was adjusted to 100mW. Samples were placed on a high speed motorized XY scanning stage (MLS203, Thorlabs, Newton, NJ) and mechanical and piezoelectric motors (PI Nano Z, USA) were used for the coarse and fine vertical movement of the objective, permitting focus adjustment. For illumination, an air immersion objective (UplanSApo 20X, NA 0.75, Olympus, Japan) was used and the SHG light from the sample was collected by using a condenser (NA 0.55) and detected on a photomultiplier tube (R6357, Hamamatsu Photonics) set at 800V for tissue imaging. Appropriate spectral filters were used to isolate the SHG signal (two FF01-720/SP-25 and a FF01-405/10-25). Scanning and signal acquisition were synchronized using a custom-written Python software and a multichannel I/O board (National Instruments). 1000X1000 μm^2 to 1200X1200 μm^2 images were recorded in the forward direction with a pixel dwell time of 50μs and a pixel size of 800nm. Raw data visualization was performed using Fiji-ImageJ (NIH, USA). Collagen fiber alignment relative to the tumor boundary was analyzed in SHG images using the curvelet-based alignment analysis software CurveAlign (Laboratory for Optical and Computational Instrumentation, University of Wisconsin-Madison), as had previously been reported[95]. Tumor area was outlined by assessment of

H&E staining performed on the same ROIs, and CurveAlign software was used to measure the angle of collagen fibers within a pre-set pixel distance. Angles of interaction were reported as between 0 and 90 and binned into three categories: 0-30°, 30-60° and 60-90°. Individual collagen fiber metrics (length, width, straightness) were analyzed using CT-FIRE tool[96].

Immunostaining (IHC and IF) of human breast cancer patient samples

See supplementary information (*Supp. Fig. 2.5*) for a schematic overview of patient sample stainings. Early-stage ductal carcinoma in situ human breast cancer samples were obtained in collaboration with Dr. Lynne Postovit (Queen's University, Canada) and approved by the Research Ethics Board at the University of Western Ontario (REB 102254). Written informed consent was obtained from all patients in accordance with the Declaration of Helsinki. A commercially available invasive (late-stage) human breast cancer TMA (BR1505e) was purchased from USBioMax. A TMA including tumor-associated and peripheral stromal regions was constructed in collaboration with Dr. Réjean Lapointe (Université de Montréal, Canada). 0.6 mm cores of primary diagnostic breast invasive ductal carcinoma formalin-fixed paraffin-embedded tissue were used from 34 patients. Cores were chosen from tumor-containing and peripheral regions, as determined by clinical pathologists at the Centre hospitalier de l'Université de Montréal (CHUM: Montréal, Canada). Collection of these samples was approved by the CHUM Research Ethics Board (2005-1893, BD 04.002 – BSP). Written informed consent was obtained from all patients in accordance with Declaration of Helsinki. Available clinical

annotations for all patient samples are detailed in supplementary *Supp. Table 2.4*. For IHC studies, tissues were stained with antibodies specific to collagen-I (1:100 dilution) and phopsho-eIF4E (1:50 dilution) using a stepwise dual-stain protocol. Collagen-I staining and phospho-eIF4E were visualized using ImmPACT DAB (Vector Laboratories) and Magenta Red (Dako) chromagen reagents respectively, and counter-stained with 20% Harris-modified hematoxylin (Thermo Fisher Scientific). Stained samples were analyzed for positive staining intensity using QuPath v0.1.2. For IF studies, tissues were stained with antibodies specific to vimentin (1:500 dilution) and phospho-eIF4E (1:50 dilution), followed by appropriate highly cross-adsorbed fluorescent secondary antibodies. DAPI was used to stain DNA. Stained samples were analyzed using QuPath v0.2.3 by performing cellular segmentation followed by classification of cells based on binary expression of vimentin and phospho-eIF4E. All stained slides were imaged using a ZEISS Axio Sca.Z1. See *Supp. Table 2.1* for all antibody details. The specificity of phospho-eIF4E staining was validated using the lungs of S209A mice infiltrated by WT metastases.

Histology stainings (H&E and picrosirius red)

Mammary fat pads from 8-week-old WT and S209A, non-tumor-bearing, BALB/c mice were excised and fixed for 48 hours at 4°C. Following fixation, samples were embedded in paraffin and serially sectioned. For picrosirius red staining, slides were stained according to kit instructions (Polysciences Inc. #24901), dehydrated in 100% ethanol, and mounted with Permount. Slides were scanned and positive staining

quantified using QuPath (v 0.1.2). Murine tissue sections were stained using hematoxylin and eosin as previously described[68].

Migration and invasion assay

Cells were seeded at a density of 1 x 10^6 per 10 cm dish in complete media. The following day, media was switched to serum-free media and cells were serum-starved. Approximately 16 hours later, Boyden chambers (Corning) were coated with 20 μg/mL collagen as previously reported[68]. 200,000 (DCIS or 4T1) or 50,000 (D2.OR-GFP) cells were seeded into the Boyden chamber in serum-free media, with companion plate (Corning) wells filled with complete media supplemented with ECM as detailed above. Cells were allowed to migrate and invade for 24 hours. Migrated cells were fixed with 5% glutaraldehyde, stained with 0.5 % Crystal Violet and quantified.

Proliferation assay

DCIS or D2.OR-GFP cells were seeded into 96-well plates at a density of 1000 cells per well. Cells were harvested every 24 hours, up to 96-hours post-seeding, by fixing in 4% PFA for 15 min at room temperature and stored in 0.4% PFA in 4°C. Upon assay completion, fixed cells were stained with 0.5% Crystal Violet for 30 min at room temperature and allowed to dry overnight. The following day, crystal violet was dissolved in 10% acetic acid and absorbance was measured at 590 nm using a plate reader. Cell proliferation over time was calculated by comparison against a standard curve of known cell numbers.

Immunoblotting

Protein lysates were isolated from cell pellets using RIPA buffer (150 mmol/L Tris-HCl pH 7, 150 mmol/L NaCl, 1% NP-40, 1% sodium deoxycholate, 0.1% SDS) supplemented with protease and phosphatase inhibitors (Roche). Mammary fat pad whole tissue lysates were prepared by homogenizing pulverized frozen tissue in RIPA buffer. Samples were lysed on ice for 30 minutes, vortexed briefly and sonicated once for 4 seconds at 50% amplitude. Following centrifugation at 15,000 x g for 5 mins (repeated 3 times for whole tissue preparations to remove lipids), protein concentration was measured by Bradford reagent assay (Bio-Rad). Proteins were separated on a 10% SDS-PAGE gel and transferred to nitrocellulose membrane. Membranes were blocked in 5% non-fat milk for 1 hour at room temperature and incubated in primary antibody dilutions overnight at 4°C. The following day, membranes were washed in Tris Buffered Saline with Tween (TBST) and incubated with secondary antibody at room temperature for 1 hour. Membranes were revealed using ECL Prime Western Blotting Detection Reagent (Amersham) and Ultra-High Contrast Western Blotting film. Antibody information is listed in *Supp. Table 2.1*.

Quantitative PCR

RNA was isolated using E.Z.N.A. total RNA isolation kit (OMEGA Bio-Tek). cDNA preparations were made from 1 μg total RNA, using the iScript cDNA Synthesis kit (Bio-Rad). Target genes were quantified using the Applied BioSystems 7500 Real-Time PCR System with SYBR Green. Primer lists can be found in *Supp. Table 2.2*.

Statistical analysis

Prism 9 software (GraphPad) was used to perform statistical analyses. Details of the statistical testing performed for all relevant figure panels can be found in the supplementary information (*Supp. Table 2.3*), or in figure legends. All data are presented as mean ± SD. Prior to determining the statistical significance of differences between groups, all data were subject to outlier testing (ROUT outlier test), followed by a test of normality (Shapiro-Wilk test). *P* values for the differences of mean between groups were then calculated using paired two-tailed *t* test, unpaired two-tailed *t* test, Mann-Whitney test, Wilcoxon matched-pairs rank test, one-way ANOVA, two-way ANOVA, or Spearman rank order correlation calculation, with multiple comparison tests as appropriate. *P* values < 0.05 were considered statistically significant.

2.6 Data availability

The mass spectrometry proteomics data have been deposited to the ProteomeXchange Consortium via the PRIDE partner repository with the dataset identifier PXD028953. All other data that support the findings of this study are in the paper and/or supplementary files, or available from the corresponding author at reasonable request.

2.7 Funding information

This research was funded by the Canadian Institutes of Health Research (CIHR) (grant PJT-162260 to SVDR and grant PJT-156269 to WHM and SVDR) and by the Canadian Cancer Society (grant #707140). SEJP was supported by a fellowship from

Fonds de recherche du Québec (Santé) and the Epstein Fellowship in Women's Health (Faculty of Medicine, McGill University). MB was supported by the International Postdoc Fellowship from the Swedish Research Council. JSV was supported by a Canada Graduate Scholarship from the Canadian Institutes of Health Research (CIHR). CHB, RPZ and VRR were supported through the Genomics Technology Platform (GTP: 264PRO), and by financial support from the Terry Fox Research Institute.

2.8 Declaration of competing interests

CHB is the CSO of MRM Proteomics, Inc. RPZ is the CEO of MRM Proteomics, Inc. All other authors declare no conflicts of interest.

2.9 Acknowledgements

The authors wish to thank the Molecular Pathology Platform (CHUM), the CHUM breast cancer tissue repository of the Québec Cancer Network (supported by FRSQ and QBCF), the IRIC Histology Core Facility (Université de Montréal), Dr. Naciba Benlimame and Lilian Canetti for their technical support. We also thank Dr. Ivan Topisirovic for use of their Teledyne ISCO fraction collector.

2.10 References

1. Bonnans, C., Chou, J. & Werb, Z. Remodelling the extracellular matrix in development and disease. *Nat. Rev. Mol. Cell Biol.* **15**, 786–801 (2014).
2. Winkler, J., Abisoye-Ogunniyan, A., Metcalf, K. J. & Werb, Z. Concepts of extracellular matrix remodelling in tumour progression and metastasis. *Nat. Commun.* **11**, 5120

(2020).
3. Pickup, M. W., Mouw, J. K. & Weaver, V. M. The extracellular matrix modulates the hallmarks of cancer. *EMBO Rep.* **15**, 1243–1253 (2014).
4. Naba, A. *et al.* The matrisome: in silico definition and in vivo characterization by proteomics of normal and tumor extracellular matrices. *Mol. Cell. Proteomics* **11**, M111.014647-M111.014647 (2012).
5. Krasny, L. *et al.* Comparative proteomic assessment of matrisome enrichment methodologies. *Biochem. J.* **473**, 3979–3995 (2016).
6. Naba, A. *et al.* The extracellular matrix: Tools and insights for the “omics” era. *Matrix Biol.* **49**, 10–24 (2016).
7. Chu, J., Cargnello, M., Topisirovic, I. & Pelletier, J. Translation Initiation Factors: Reprogramming Protein Synthesis in Cancer. *Trends Cell Biol.* **26**, 918–933 (2016).
8. Bartish, M. *et al.* MNK2 governs the macrophage antiinflammatory phenotype. *Proc. Natl. Acad. Sci. U. S. A.* **117**, 27556–27565 (2020).
9. Huang, F. *et al.* Inhibiting the MNK1/2-eIF4E axis impairs melanoma phenotype switching and potentiates antitumor immune responses. *J. Clin. Invest.* **131**, (2021).
10. Guo, Q. *et al.* The MNK1/2-eIF4E Axis Supports Immune Suppression and Metastasis in Postpartum Breast Cancer. *Cancer Res.* **81**, 3876–3889 (2021).
11. Robichaud, N. *et al.* Translational control in the tumor microenvironment promotes lung metastasis: Phosphorylation of eIF4E in neutrophils. *Proc. Natl. Acad. Sci. U. S. A.* **115**, E2202–E2209 (2018).
12. Robichaud, N. *et al.* Phosphorylation of eIF4E promotes EMT and metastasis via translational control of SNAIL and MMP-3. *Oncogene* **34**, 2032–2042 (2015).
13. Lazaris-Karatzas, A., Montine, K. S. & Sonenberg, N. Malignant transformation by a eukaryotic initiation factor subunit that binds to mRNA 5’ cap. *Nature* **345**, 544–547 (1990).
14. Waskiewicz, A. J., Flynn, A., Proud, C. G. & Cooper, J. A. Mitogen-activated protein kinases activate the serine/threonine kinases Mnk1 and Mnk2. *EMBO J.* **16**, 1909–1920 (1997).
15. Waskiewicz, A. J. *et al.* Phosphorylation of the cap-binding protein eukaryotic translation initiation factor 4E by protein kinase Mnk1 in vivo. *Mol. Cell. Biol.* **19**, 1871–1880 (1999).
16. Bonneau, A. M. & Sonenberg, N. Involvement of the 24-kDa cap-binding protein in regulation of protein synthesis in mitosis. *J. Biol. Chem.* **262**, 11134–11139 (1987).
17. Huang, J. T. & Schneider, R. J. Adenovirus inhibition of cellular protein synthesis involves inactivation of cap-binding protein. *Cell* **65**, 271–280 (1991).
18. Morley, S. J., Rau, M., Kay, J. E. & Pain, V. M. Increased phosphorylation of eukaryotic initiation factor 4 alpha during activation of T lymphocytes correlates with increased eIF-4F complex formation. *Biochem. Soc. Trans.* **21**, 397S (1993).
19. Boal, T. R. *et al.* Regulation of eukaryotic translation initiation factor expression during T-cell activation. *Biochim. Biophys. Acta* **1176**, 257–264 (1993).
20. Beretta, L. *et al.* Differential regulation of translation and eIF4E phosphorylation during human thymocyte maturation. *J. Immunol.* **160**, 3269–3273 (1998).
21. Pyronnet, S., Dostie, J. & Sonenberg, N. Suppression of cap-dependent translation in mitosis. *Genes Dev.* **15**, 2083–2093 (2001).
22. Takei, N., Kawamura, M., Hara, K., Yonezawa, K. & Nawa, H. Brain-derived neurotrophic factor enhances neuronal translation by activating multiple initiation processes: comparison with the effects of insulin. *J. Biol. Chem.* **276**, 42818–42825 (2001).
23. Dyer, J. R. *et al.* An activity-dependent switch to cap-independent translation triggered by eIF4E dephosphorylation. *Nat. Neurosci.* **6**, 219–220 (2003).

24. Knauf, U., Tschopp, C. & Gram, H. Negative regulation of protein translation by mitogen-activated protein kinase-interacting kinases 1 and 2. *Mol. Cell. Biol.* **21**, 5500–5511 (2001).
25. McKendrick, L., Morley, S. J., Pain, V. M., Jagus, R. & Joshi, B. Phosphorylation of eukaryotic initiation factor 4E (eIF4E) at Ser209 is not required for protein synthesis in vitro and in vivo. *Eur. J. Biochem.* **268**, 5375–5385 (2001).
26. Morley, S. J. & Naegele, S. Phosphorylation of eukaryotic initiation factor (eIF) 4E is not required for de novo protein synthesis following recovery from hypertonic stress in human kidney cells. *J. Biol. Chem.* **277**, 32855–32859 (2002).
27. Topisirovic, I., Ruiz-Gutierrez, M. & Borden, K. L. B. Phosphorylation of the eukaryotic translation initiation factor eIF4E contributes to its transformation and mRNA transport activities. *Cancer Res.* **64**, 8639–8642 (2004).
28. Furic, L. *et al.* eIF4E phosphorylation promotes tumorigenesis and is associated with prostate cancer progression. *Proc. Natl. Acad. Sci. U. S. A.* **107**, 14134–14139 (2010).
29. Carter, J. H. *et al.* Phosphorylation of eIF4E serine 209 is associated with tumour progression and reduced survival in malignant melanoma. *Br. J. Cancer* **114**, 444–453 (2016).
30. Bray, F. *et al.* Global cancer statistics 2018: GLOBOCAN estimates of incidence and mortality worldwide for 36 cancers in 185 countries. *CA. Cancer J. Clin.* **68**, 394–424 (2018).
31. Provenzano, P. P. *et al.* Collagen reorganization at the tumor-stromal interface facilitates local invasion. *BMC Med.* **4**, 38 (2006).
32. Conklin, M. W. *et al.* Aligned collagen is a prognostic signature for survival in human breast carcinoma. *Am. J. Pathol.* **178**, 1221–1232 (2011).
33. Campagnola, P. J. & Loew, L. M. Second-harmonic imaging microscopy for visualizing biomolecular arrays in cells, tissues and organisms. *Nat. Biotechnol.* **21**, 1356–1360 (2003).
34. Campagnola, P. Second harmonic generation imaging microscopy: applications to diseases diagnostics. *Anal. Chem.* **83**, 3224–3231 (2011).
35. Bruno, R. D. *et al.* Mammary extracellular matrix directs differentiation of testicular and embryonic stem cells to form functional mammary glands in vivo. *Sci. Rep.* **7**, 40196 (2017).
36. Chamberlin, T., Thompson, V., Hillers-Ziemer, L. E., Walton, B. N. & Arendt, L. M. Obesity reduces mammary epithelial cell TGFβ1 activity through macrophage-mediated extracellular matrix remodeling. *FASEB J.* **34**, 8611–8624 (2020).
37. O'Brien, J., Fornetti, J. & Schedin, P. Isolation of mammary-specific extracellular matrix to assess acute cell-ECM interactions in 3D culture. *J. Mammary Gland Biol. Neoplasia* **15**, 353–364 (2010).
38. Muschler, J. & Streuli, C. H. Cell-matrix interactions in mammary gland development and breast cancer. *Cold Spring Harb. Perspect. Biol.* **2**, a003202–a003202 (2010).
39. Schedin, P. & Keely, P. J. Mammary gland ECM remodeling, stiffness, and mechanosignaling in normal development and tumor progression. *Cold Spring Harb. Perspect. Biol.* **3**, a003228–a003228 (2011).
40. Barkan, D. *et al.* Metastatic growth from dormant cells induced by a col-I-enriched fibrotic environment. *Cancer Res.* **70**, 5706–5716 (2010).
41. Lyons, T. R. *et al.* Postpartum mammary gland involution drives progression of ductal carcinoma in situ through collagen and COX-2. *Nat. Med.* **17**, 1109–1115 (2011).
42. Solari, F. A. *et al.* Combined Quantification of the Global Proteome, Phosphoproteome, and Proteolytic Cleavage to Characterize Altered Platelet Functions in the Human Scott

Syndrome * . *Mol. Cell. Proteomics* **15**, 3154–3169 (2016).
43. Naba, A. *et al.* Characterization of the Extracellular Matrix of Normal and Diseased Tissues Using Proteomics. *J. Proteome Res.* **16**, 3083–3091 (2017).
44. Goddard, E. T. *et al.* Quantitative extracellular matrix proteomics to study mammary and liver tissue microenvironments. *Int. J. Biochem. Cell Biol.* **81**, 223–232 (2016).
45. Naba, A., Clauser, K. R., Lamar, J. M., Carr, S. A. & Hynes, R. O. Extracellular matrix signatures of human mammary carcinoma identify novel metastasis promoters. *Elife* **3**, e01308–e01308 (2014).
46. Paoletti, A. C. *et al.* Quantitative proteomic analysis of distinct mammalian Mediator complexes using normalized spectral abundance factors. *Proc. Natl. Acad. Sci.* **103**, 18928 LP – 18933 (2006).
47. Chen, R. *et al.* Proteins associated with pancreatic cancer survival in patients with resectable pancreatic ductal adenocarcinoma. *Lab. Invest.* **95**, 43–55 (2015).
48. Sun, X. *et al.* Annexin A5 regulates hepatocarcinoma malignancy via CRKI/II-DOCK180-RAC1 integrin and MEK-ERK pathways. *Cell Death Dis.* **9**, 637 (2018).
49. Jacobsen, F. *et al.* Up-regulation of Biglycan is Associated with Poor Prognosis and PTEN Deletion in Patients with Prostate Cancer. *Neoplasia* **19**, 707–715 (2017).
50. Elgundi, Z. *et al.* Cancer Metastasis: The Role of the Extracellular Matrix and the Heparan Sulfate Proteoglycan Perlecan. *Front. Oncol.* **9**, 1482 (2020).
51. Ito, S. & Nagata, K. Biology of Hsp47 (Serpin H1), a collagen-specific molecular chaperone. *Semin. Cell Dev. Biol.* **62**, 142–151 (2017).
52. Blank-Landeshammer, B. *et al.* Proteogenomics of Colorectal Cancer Liver Metastases: Complementing Precision Oncology with Phenotypic Data. *Cancers (Basel).* **11**, (2019).
53. Tajima, S. & Pinnell, S. R. Ascorbic acid preferentially enhances type I and III collagen gene transcription in human skin fibroblasts. *J. Dermatol. Sci.* **11**, 250–253 (1996).
54. Stanisavljevic, J. *et al.* Snail1-expressing fibroblasts in the tumor microenvironment display mechanical properties that support metastasis. *Cancer Res.* **75**, 284–295 (2015).
55. Grossman, M. *et al.* Tumor Cell Invasion Can Be Blocked by Modulators of Collagen Fibril Alignment That Control Assembly of the Extracellular Matrix. *Cancer Res.* **76**, 4249 LP – 4258 (2016).
56. Liang, S. *et al.* Polysome-profiling in small tissue samples. *Nucleic Acids Res.* **46**, e3 (2018).
57. Zhan, Y. *et al.* MNK1/2 inhibition limits oncogenicity and metastasis of KIT-mutant melanoma. *J. Clin. Invest.* **127**, 4179–4192 (2017).
58. Yang, W. *et al.* MNK1 signaling induces an ANGPTL4-mediated gene signature to drive melanoma progression. *Oncogene* **39**, 3650–3665 (2020).
59. Gole, L. *et al.* Quantitative stain-free imaging and digital profiling of collagen structure reveal diverse survival of triple negative breast cancer patients. *Breast Cancer Res.* **22**, 42 (2020).
60. Zhang, K. *et al.* The collagen receptor discoidin domain receptor 2 stabilizes SNAIL1 to facilitate breast cancer metastasis. *Nat. Cell Biol.* **15**, 677–687 (2013).
61. Iacobuzio-Donahue, C. A., Argani, P., Hempen, P. M., Jones, J. & Kern, S. E. The desmoplastic response to infiltrating breast carcinoma: gene expression at the site of primary invasion and implications for comparisons between tumor types. *Cancer Res.* **62**, 5351–5357 (2002).
62. Brierley, J. D., Gospodarowicz, M. K. & Wittekind, C. *TNM classification of malignant tumours*. (John Wiley & Sons, 2017).
63. Pavlides, S. *et al.* The reverse Warburg effect: aerobic glycolysis in cancer associated fibroblasts and the tumor stroma. *Cell Cycle* **8**, 3984–4001 (2009).

64. Heatley, M., Whiteside, C., Maxwell, P. & Toner, P. Vimentin expression in benign and malignant breast epithelium. *J. Clin. Pathol.* **46**, 441–445 (1993).
65. Morad, G., Helmink, B. A., Sharma, P. & Wargo, J. A. Hallmarks of response, resistance, and toxicity to immune checkpoint blockade. *Cell* **184**, 5309–5337 (2021).
66. Peng, D. H. *et al.* Collagen promotes anti-PD-1/PD-L1 resistance in cancer through LAIR1-dependent CD8(+) T cell exhaustion. *Nat. Commun.* **11**, 4520 (2020).
67. Bagati, A. *et al.* Integrin αvβ6-TGFβ-SOX4 Pathway Drives Immune Evasion in Triple-Negative Breast Cancer. *Cancer Cell* **39**, 54-67.e9 (2021).
68. Guo, Q. *et al.* MNK1/NODAL Signaling Promotes Invasive Progression of Breast Ductal Carcinoma In Situ. *Cancer Res.* **79**, 1646–1657 (2019).
69. Mousavizadeh, R. *et al.* β1 integrin, ILK and mTOR regulate collagen synthesis in mechanically loaded tendon cells. *Sci. Rep.* **10**, 12644 (2020).
70. Walker, N. M. *et al.* Mechanistic Target of Rapamycin Complex 1 (mTORC1) and mTORC2 as Key Signaling Intermediates in Mesenchymal Cell Activation. *J. Biol. Chem.* **291**, 6262–6271 (2016).
71. Woodcock, H. V *et al.* The mTORC1/4E-BP1 axis represents a critical signaling node during fibrogenesis. *Nat. Commun.* **10**, 6 (2019).
72. Agorku, D. J. *et al.* CD49b, CD87, and CD95 Are Markers for Activated Cancer-Associated Fibroblasts Whereas CD39 Marks Quiescent Normal Fibroblasts in Murine Tumor Models. *Frontiers in Oncology* vol. 9 (2019).
73. Balestrini, J. L., Chaudhry, S., Sarrazy, V., Koehler, A. & Hinz, B. The mechanical memory of lung myofibroblasts. *Integr. Biol. (Camb).* **4**, 410–421 (2012).
74. Parker, M. W. *et al.* Fibrotic extracellular matrix activates a profibrotic positive feedback loop. *J. Clin. Invest.* **124**, 1622–1635 (2014).
75. Sahai, E. *et al.* A framework for advancing our understanding of cancer-associated fibroblasts. *Nat. Rev. Cancer* **20**, 174–186 (2020).
76. Kumar, K. *et al.* Differential Regulation of ZEB1 and EMT by MAPK-Interacting Protein Kinases (MNK) and eIF4E in Pancreatic Cancer. *Mol. Cancer Res.* **14**, 216–227 (2016).
77. Verginadis, I. I. *et al.* A stromal Integrated Stress Response activates perivascular cancer-associated fibroblasts to drive angiogenesis and tumour progression. *Nat. Cell Biol.* (2022) doi:10.1038/s41556-022-00918-8.
78. Yamaguchi, S. *et al.* ATF4-mediated induction of 4E-BP1 contributes to pancreatic beta cell survival under endoplasmic reticulum stress. *Cell Metab.* **7**, 269–276 (2008).
79. Chen, X. *et al.* IL-17-induced HIF1α drives resistance to anti-PD-L1 via fibroblast-mediated immune exclusion. *J. Exp. Med.* **219**, (2022).
80. Guo, Y. P. *et al.* Growth factors and stromal matrix proteins associated with mammographic densities. *Cancer Epidemiol. biomarkers Prev. a Publ. Am. Assoc. Cancer Res. cosponsored by Am. Soc. Prev. Oncol.* **10**, 243–248 (2001).
81. McCormack, V. A. & dos Santos Silva, I. Breast density and parenchymal patterns as markers of breast cancer risk: a meta-analysis. *Cancer Epidemiol. biomarkers Prev. a Publ. Am. Assoc. Cancer Res. cosponsored by Am. Soc. Prev. Oncol.* **15**, 1159–1169 (2006).
82. Kerlikowske, K. *et al.* Automated and Clinical Breast Imaging Reporting and Data System Density Measures Predict Risk for Screen-Detected and Interval Cancers: A Case-Control Study. *Ann. Intern. Med.* **168**, 757–765 (2018).
83. Ray, A., Slama, Z. M., Morford, R. K., Madden, S. A. & Provenzano, P. P. Enhanced Directional Migration of Cancer Stem Cells in 3D Aligned Collagen Matrices. *Biophys. J.* **112**, 1023–1036 (2017).
84. Riching, K. M. *et al.* 3D collagen alignment limits protrusions to enhance breast cancer

cell persistence. *Biophys. J.* **107**, 2546–2558 (2014).
85. Fraley, S. I. *et al.* Three-dimensional matrix fiber alignment modulates cell migration and MT1-MMP utility by spatially and temporally directing protrusions. *Sci. Rep.* **5**, 14580 (2015).
86. Bhattacharjee, S. *et al.* Tumor restriction by type I collagen opposes tumor-promoting effects of cancer-associated fibroblasts. *J. Clin. Invest.* **131**, (2021).
87. Walker, R. A. The complexities of breast cancer desmoplasia. *Breast Cancer Res.* **3**, 143 (2001).
88. Sun, X. *et al.* Tumour DDR1 promotes collagen fibre alignment to instigate immune exclusion. *Nature* (2021) doi:10.1038/s41586-021-04057-2.
89. Yi, H. *et al.* Immune Checkpoint Inhibition for Triple-Negative Breast Cancer: Current Landscape and Future Perspectives. *Frontiers in Oncology* vol. 11 1501 (2021).
90. Zougman, A., Selby, P. J. & Banks, R. E. Suspension trapping (STrap) sample preparation method for bottom-up proteomics analysis. *Proteomics* **14**, 1000–1006 (2014).
91. Dickhut, C., Radau, S. & Zahedi, R. P. Fast, efficient, and quality-controlled phosphopeptide enrichment from minute sample amounts using titanium dioxide. *Methods Mol. Biol.* **1156**, 417–430 (2014).
92. MacLean, B. *et al.* Skyline: an open source document editor for creating and analyzing targeted proteomics experiments. *Bioinformatics* **26**, 966–968 (2010).
93. Franco-Barraza, J., Beacham, D. A., Amatangelo, M. D. & Cukierman, E. Preparation of Extracellular Matrices Produced by Cultured and Primary Fibroblasts. *Curr. Protoc. cell Biol.* **71**, 10.9.1-10.9.34 (2016).
94. Pinsard, M. *et al.* Single-scan interferometric second harmonic generation microscopy using a kHz phase-scanner. *Opt. Express* **27**, 38435–38450 (2019).
95. Kenny, T. C. *et al.* Patient-derived Interstitial Fluids and Predisposition to Aggressive Sporadic Breast Cancer through Collagen Remodeling and Inactivation of p53. *Clin. Cancer Res.* **23**, 5446 LP – 5459 (2017).
96. Bredfeldt, J. S. *et al.* Computational segmentation of collagen fibers from second-harmonic generation images of breast cancer. *J. Biomed. Opt.* **19**, 16007 (2014).

2.11 Supplementary material

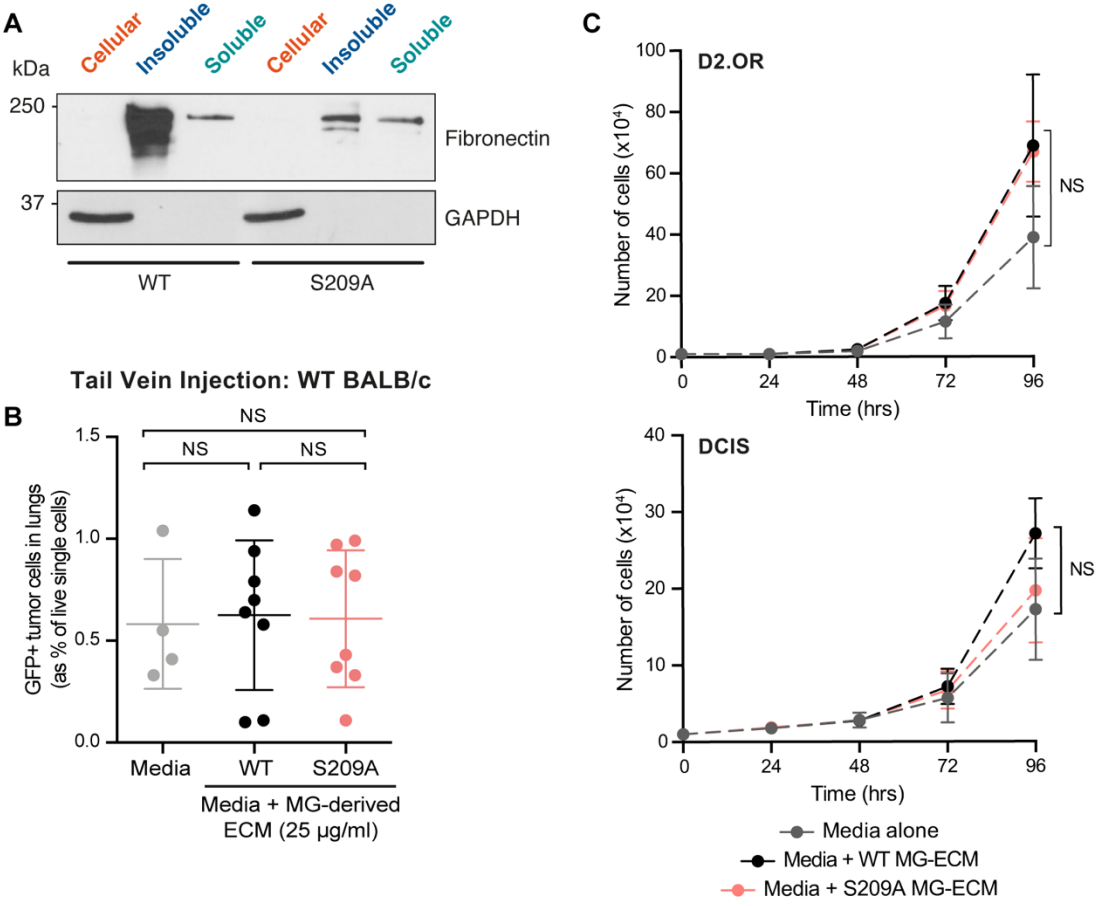

Supplementary Figure 2.1. (**A**) Western blot analysis of the indicated proteins in cellular, urea-insoluble ECM and urea-soluble ECM protein fractions from WT and S209A mammary glands. (**B**) Number of GFP+ tumor cells in the lungs of WT mice injected with D2.OR-GFP cells cultured in the indicated conditions. Data are expressed as a percentage of live, single cells. Error bars represent SD. One-way ANOVA with Tukey's multiple comparison test, $n = 4$ (media only), $n = 8$ (WT and S209A ECM). (**C**) Proliferation of either D2.OR (upper) or DCIS (lower) cells grown in the indicated conditions. Data presented as average values, error bars represent SD. Two-way ANOVA with Tukey's multiple comparison test, $n = 3$. NS, $p > 0.05$.

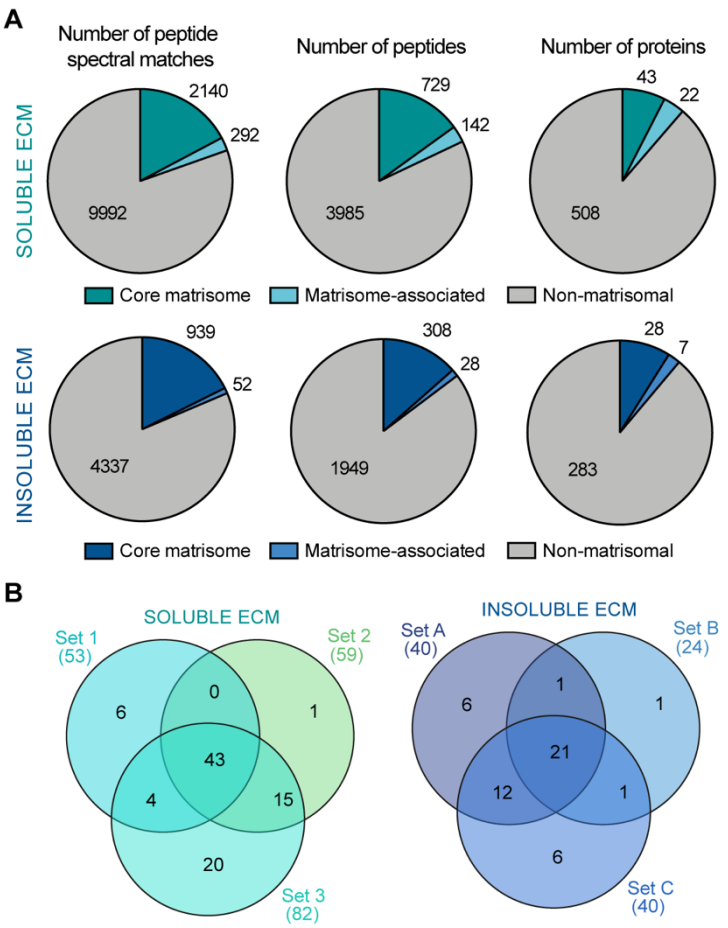

Supplementary Figure 2.2. (**A**) The number of peptide spectral matches, peptides and proteins identified in soluble and insoluble ECM samples analyzed by LC-MS/MS. Wedge color denotes whether a given peptide/protein is part of the core matrisome, matrisome-associated or non-matrisomal. All data are averaged across three biological repeats. (**B**) Overlap of known matrisomal proteins, identified by LC-MS/MS in soluble and insoluble ECM samples, between biological repeats.

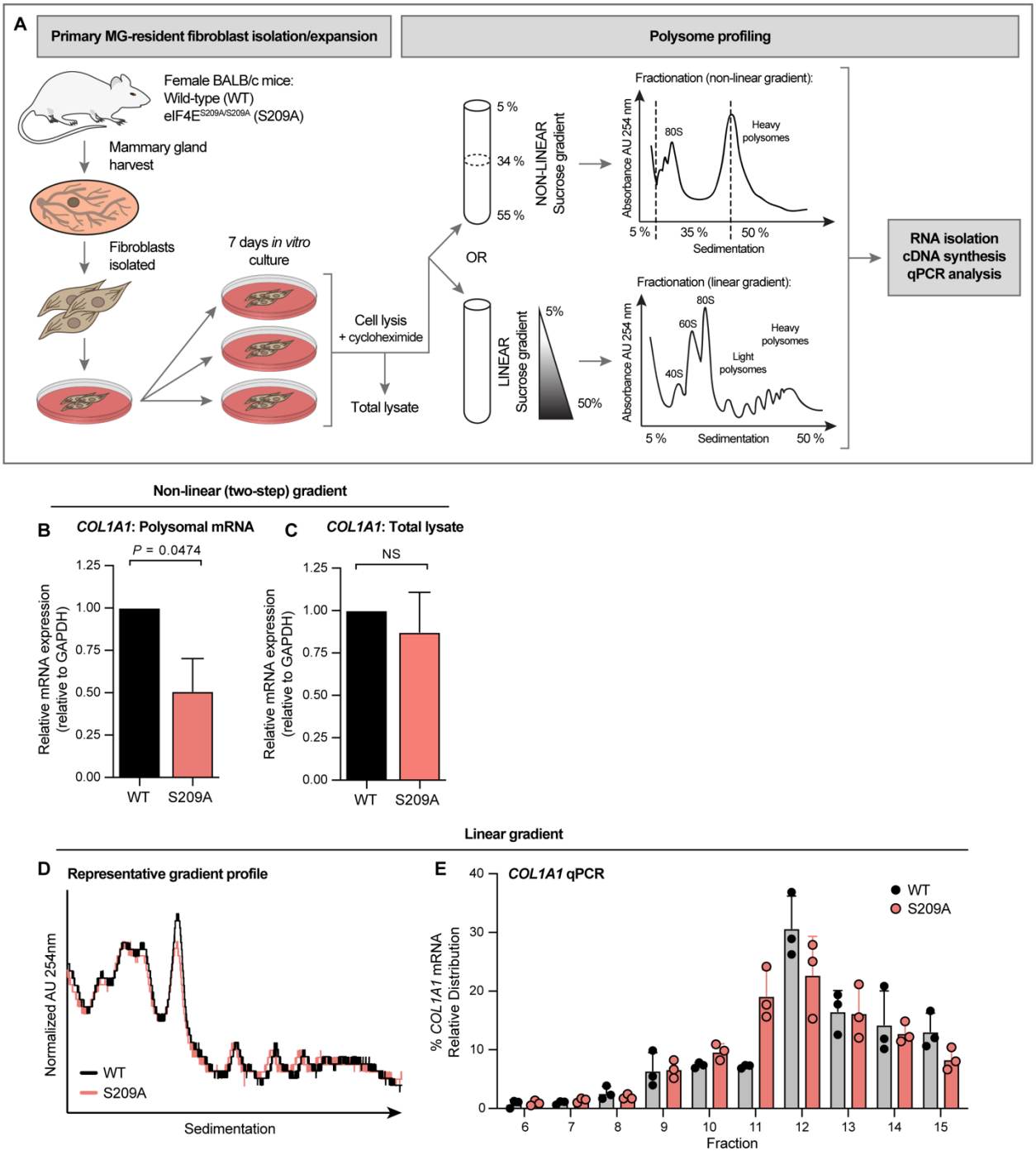

Supplementary Figure 2.3. (**A**) Schematic depicting the workflow undertaken to perform polysome profiling on WT and S209A primary mammary gland-derived fibroblasts, using either a linear or non-linear sucrose gradient to enrich for polysome-associated fractions. (**B and C**) Fold change in expression of *COL1A1* mRNA from heavy polysome-associated fractions (**B**) and whole cell lysates (**C**) in S209A fibroblasts relative to WT. Data generated from samples enriched across a non-linear sucrose gradient and quantified by qPCR. Error bars represent SD. Unpaired two-tailed t test with Welch's correction, $n = 3$. (**D**) Representative gradient

profiles from WT and S209A cell lysates enriched across a linear sucrose gradient. (**E**) Relative distribution of *COL1A1* mRNA transcripts in each fraction enriched across a linear sucrose gradient, as measured by qPCR. Each sample is normalized to *GAPDH*, with distribution expressed as a percentage of the total *COL1A1* abundance across all fractions. Error bars represent SD, $n = 3$.

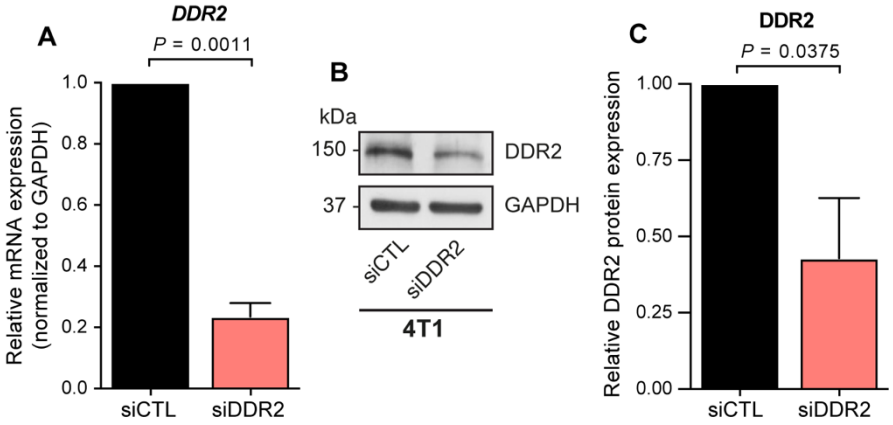

Supplementary Figure 2.4. (**A**) Expression of DDR2 mRNA in 4T1 cells following DDR2 knockdown, relative to the expression in 4T1 cells transfected with control siRNA. (**B**) Western blot analysis of the indicated proteins in 4T1 cells transfected with the listed siRNAs. (**C**) Relative expression of DDR2 protein level in 4T1 cells transfected with control siRNA or siDDR2, as measured by western blot densitometry. For **A and C**: Unpaired two-tailed t test with Welch's correction, $n = 3$.

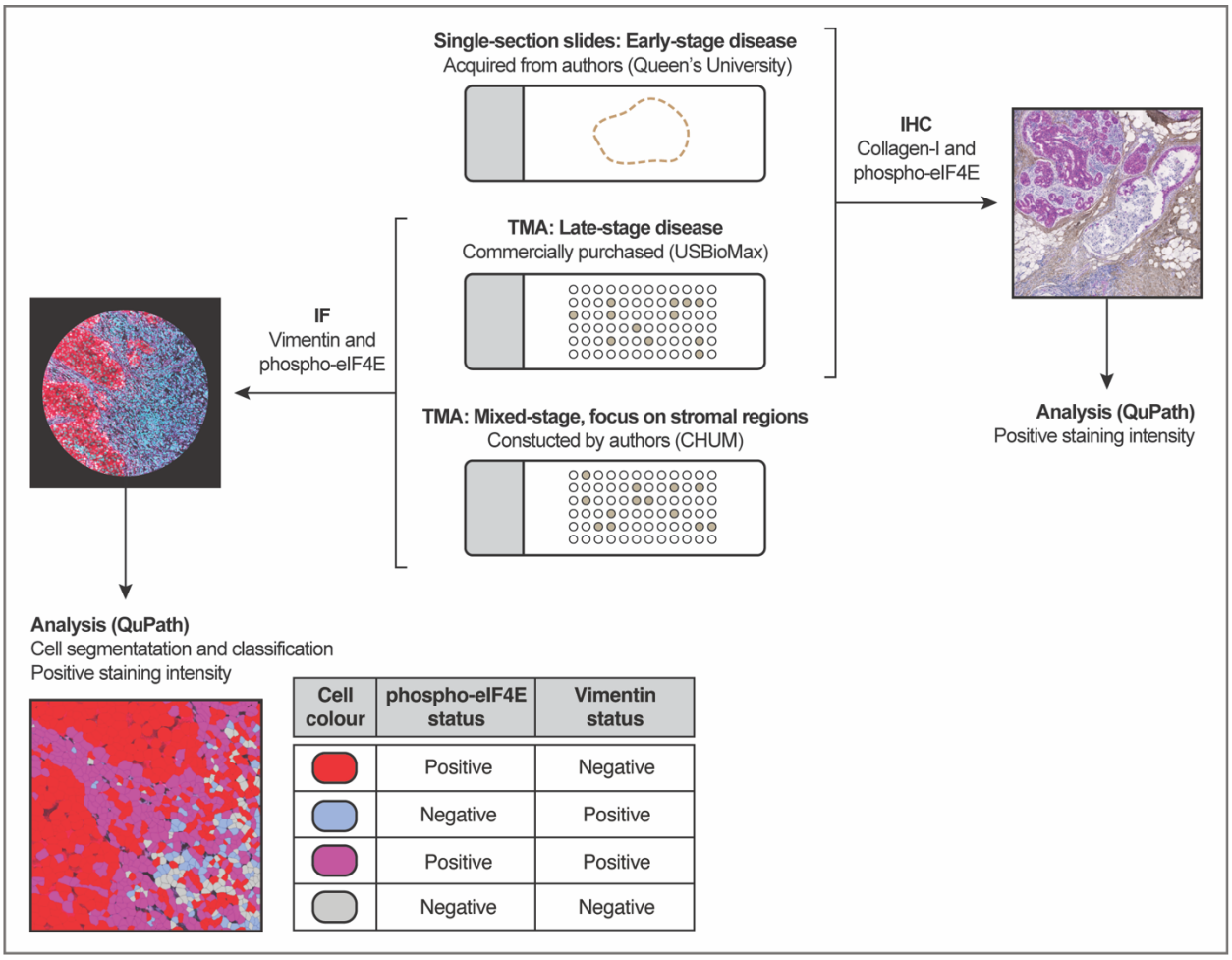

Supplementary Figure 2.5. Schematic detailing the immuno-stainings (IHC and IF) performed on breast cancer patient-derived samples.

Supplementary Table 2.1: Antibody information - all antibodies used for western blotting (WB), immunohistochemistry (IHC) and immunofluorescence (IF)

Target	Reactivity	Application	Supplier	Catalog	Clone
Collagen-I	Mouse	WB and IF	Abcam	ab21286	
Collagen-I	Mouse, Human	IHC	Abcam	ab88147	3G3
SerpinH1	Mouse, Human	WB	Invitrogen	PA5-27832	
Phospho-eIF4E (S209)	Human, Mouse, Rat, Monkey	WB	Cell Signaling	9741L	
Phospho-eIF4E (S209)	Mouse, Rat, Human, Pig	IHC and IF	Abcam	ab76256	EP2151Y
Vimentin	Rat, Human	IF	Abcam	ab8069	V9
Fibronectin	Multi-species (incl. Human, Mouse, Rat)	WB	BD	610077	10
DDR2	Human, Mouse, Rat	WB	Invitrogen	PA5-87602	
Snail	Human, Mouse, Rabbit	WB	Cell Signaling	3895S	L70G2
GAPDH	Human, Mouse, Rat, Monkey	WB	Cell Signaling	5174S	D16H11
Actin	Multi-species (incl. Human, Mouse, Rat)	WB	Sigma-Aldrich	A5441	AC-15

Supplementary Table 2.2: Primer and siRNA sequences

qPCR PRIMER SEQUENCES (5'-3')	
COL1A1	Fwd: CGTATCACCAAACTCAGAAG Rev: GAAGCAAAGTTTCCTCCAAG
SERPINH1	Fwd: GCAGCAGCAAGCAACACTACAACT Rev: AGAACATGGCGTTCACAAGCAGT
DDR2	Fwd: CAGAAGCCGACATAGTGAATCT Rev: CTCTTCCACAGCCACATCTT
GAPDH	Fwd: CACCACCAACTGCTTAGCC Rev: GTCTTCTGGGTGGCAGTGAT
ACTB	Fwd: GGCTGTATTCCCCTCCATCG Rev: CCAGTTGGTAACAATGCCATGT
siRNA DUPLEX SEQUENCES (5'-3')	
siDDR2	rArArArGrArArArUrGrUrUrArCrUrUrGrArUrArUrArCrCAA rUrUrGrGrUrArUrArUrCrArArGrUrArArCrArUrUrUrCrUrUrUrUrA
siCTL	N/A (Proprietary, All Star Neg. Control siRNA, Qiagen, #1027218)

Supplementary Table 2.3: Detailed statistical testing information. Statistical testing was performed in Prism 9. Outliers were detected using the ROUT outlier test (Q = 1%). In figures: all error bars represent standard deviation, *P* values are indicted, NS: $P < 0.05$.

Panel	Outliers	Shapiro-Wilk test Pass/Fail (*P* value)	Statistical test used	n value
1D	None	Pass (WT: 0.39, S209A: 0.30)	Paired two-tailed t-test	6 per group
1F	None	Pass (Media: 0.80, WT: 0.47, S209A: 0.56)	One-way ANOVA with Tukey's multiple comparison test	Media: 4 WT: 8 S209A: 8
1G	None	Pass (Media: 0.74, WT: 0.97, S209A: 0.81)	One-way ANOVA with Tukey's multiple comparison test	3
1H	None	Pass (Media: 1, WT: 0.258, S209A: 0.56)	One-way ANOVA with Tukey's multiple comparison test	3
S1B	None	Pass (Media: 0.36, WT: 0.51, S209A: 0.26)	One-way ANOVA with Tukey's multiple comparison test	Media: 4 WT: 8 S209A: 8
S1C	None	Pass (D2.OR – 24 hrs: 0.19, 48 hrs: 0.24, 72 hrs: 0.91, 96 hrs: 0.99. DCIS – 24 hrs: 0.18, 48 hrs: 0.34, 72 hrs: 0.15, 96 hrs: 0.34)	Two-way ANOVA with Tukey's multiple comparison test	3
2F	None	Pass (sECM: 0.99, iECM: 0.39)	Unpaired two-tailed t-test with Welch's correction	4
3B	None	Pass (WT: 0.99, S209A: 0.62)	Unpaired two-tailed t-test with Welch's correction	4 per group
3E	1	Fail (WT: 0.043, S209A: 0.40)	Mann-Whitney test (two-tailed)	WT: 4 S209A: 5
3F	None	Pass (WT: 1, S209A; 0.8023)	Unpaired two-tailed t-test with Welch's correction	4
3G	None	Pass (WT: 0.90, S209A: 0.57)	Unpaired two-tailed t-test with Welch's correction	3
S3B	None	Pass (WT: N/A, S209A: 1)	Unpaired two-tailed t-test with Welch's correction	3
S3C	None	Pass (WT: N/A, S209A: 0.73)	Unpaired two-tailed t-test with Welch's correction	3
5E	None	Pass (WT: 0.09, S209A: 0.51)	Unpaired two-tailed t-test with Welch's correction	5 per group
5F	None	Pass (WT: 0.99, S209A: 0.33)	Unpaired two-tailed t-test with Welch's correction	5 per group
5G	None	Pass (WT: 1, S209A: 0.51)	Unpaired two-tailed t-test with Welch's correction	5 per group
5H	None	Pass (WT: 0.36, S209A: 1)	Unpaired two-tailed t-test with Welch's correction	4 per group
5I	None	Pass (siCTL no ECM: N/A, siCTL WT ECM: 0.41, siDDR2 no ECM: 0.92, siDDR2 WT ECM: 0.91)	One-way ANOVA with Tukey's multiple comparison test	3
S4A	None	Pass (siCTL: N/A, siDDR2: 0.36)	Unpaired two-tailed t-test with Welch's correction	3
S4B	None	Pass (siCTL: N/A, siDDR2: 0.97)	Unpaired two-tailed t-test with Welch's correction	3

6B	2	Fail (phospho-eIF4E: 0.000021, collagen-I: 0.00125)	Spearman correlation	131
6C	2	Fail (EARLY phospho-eIF4E: 0.084, EARLY collagen-I: 0.0093, LATE phospho-eIF4E: 0.0012, LATE collagen-I: 0.0080)	Spearman correlation	Early: 25 Late: 106
6I	13	Fail (Tumor: 0.0000011, Stroma: 7.25e-8)	Wilcoxon matched-pairs rank test	178
6J	None	Fail (Tumor: 0.012, Stroma:	Wilcoxon matched-pairs rank test	191
6K	13	Fail (Tumor: 0.0000011, Stroma: 7.25e-8)	Spearman correlation	178
6M	1	Fail (Tumor: 0.029, Periphery: 0.68)	Wilcoxon matched-pairs rank test	29
6N	3	Fail (Tumor: 0.0012, Periphery: 0.0043)	Wilcoxon matched-pairs rank test	27
7B	None	Pass (WT IgG: 0.53, WT anti-PD-1: 0.35, S209A IgG: 0.83, S209A anti-PD-1: 0.23)	Two-way ANOVA with Tukey's multiple comparison test	WT IgG: 7 WT PD-1: 6 S209A IgG: 6 S209A PD-1: 5
7D	None	Pass (IgG: 0.48, anti-PD-1: 0.99)	Unpaired two-tailed t-test with Welch's correction	IgG: 6 Anti-PD-1: 5
7E	None	Pass (IgG: 0.10, anti-PD-1: 0.63)	Unpaired two-tailed t-test with Welch's correction	IgG: 7 Anti-PD-1: 6
7F	None	Pass (WT IgG: 0.93, WT anti-PD-1: 0.98, S209A IgG: 0.96, S209A anti-PD-1: 0.86)	Two-way ANOVA with Tukey's multiple comparison test	DMSO IgG: 6 DMSO PD-1: 6 SEL201 IgG: 7 SEL201 PD-1: 7

Supplementary Table 2.4: Patient sample clinical data (Sheet 1: TMA constructed by authors)

								CLINICAL ANNOTATIONS													
ID	Diagnostic age		Diagnosis	Laterality	Clinical TNM	TNMPT	TNMPN	TNMPM	Pathology TNM	TNM G	Lymph Node Status	HER2NEU	ER	PR	Metastasis (at diagnosis)	Survival (months)	Cause of death	Censure
90078	36	Breast	Invasive ductal carcinoma	Right	I	pT1b	pN0		I	3	Negative	0/3 +	Positive	Negative	no	121		0
90361	33	Breast	Invasive ductal carcinoma	Right	I	pT1c	pN1a		IIA	2	Positive	3/13 +	Positive	Positive	no	86		0
101456	36	Breast	Invasive ductal carcinoma	Right	IIB	pT2	pN1a		IIB	3	Positive	3/12 +	Doubtful	Positive	no	93		0
101561	33	Breast	Invasive ductal carcinoma	Right	IIA	pT1c	pN3a		IIIC	3	Positive	16/24 +	Positive	Positive	no	34	Breast cancer	1
101648	37	Breast	Invasive ductal carcinoma	Left	IIA	pT1c	pN2a		IIIA	3	Positive	8/14 +	Negative	Positive	no	72		0
101715	42	Breast	Invasive ductal carcinoma	Right	IIB	pT1c	pN1a		IIA	2	Positive	1/14 +	Negative	Positive	no	79		0
101695	36	Breast	Invasive ductal carcinoma	Left	IA	pT2	pN0		IIA	3	Negative	0/3 +	Negative	Positive	no	79		0
101849	31	Breast	Invasive ductal carcinoma	Left	IIA	pT1b	pN1a		IIA	3	Positive	1/5 +	Negative	Negative	no	62		0
102507	39	Breast	Invasive ductal carcinoma	Right	IIA	pT1c	pN1mi		IB		Positive	1/2 +	Negative	Positive	no	9		0
102554	30	Breast	Invasive ductal carcinoma	Left	IA	pT2	pN1a	cM0	IB		Positive	1/1 +	Negative	Positive	no	21		0
102561	42	Breast	Invasive ductal carcinoma	Right	IIA	pT1c	pN1a	cM0	IB		Positive	1/4 +	Negative	Positive	(CYTO)Positive	18		0
102565	40	Breast	Invasive ductal carcinoma	Right	IIA	pT1c	pN0	cM0	IA		Negative	0/2 +	Negative	Positive	no	20		0
102568	29	Breast	Invasive ductal carcinoma	Right	IB	pT1c	pN0	cM0	IB		Negative	0/2 +	Negative	Negative	no	16		0
102599	39	Breast	Invasive ductal carcinoma	Left	IB	pT2	pN1a	cM0	IIA		Positive	2/5 +	Negative	Positive	no	7		0
102677	42	Breast	Invasive ductal carcinoma	Left	IA	pT2	pN1a	cM0	IB		Positive	1/3 +	Negative	Positive	no	17		0
102574	36	Breast	Invasive ductal carcinoma	Left	IA	pT1c	pN1mi		IB	3	Positive	2/5 +	Negative	Positive	no	30		0
102041	37	Breast	Invasive ductal carcinoma	Right	IIB	pT2	pN2a		IIIA		Positive	4/24 +	Negative	Positive	no	53		0
102430	45	Breast	Invasive ductal carcinoma	Left	IA	pT1b	pN0(i-)		IA	1	Negative	0/4 +	Negative	Positive	no	11		0
102473	42	Breast	Apocrine adenocarcinoma	Right	IA	pT1c	pN0(i-)		IA		Negative	0/6 +	Positive	Positive	no	12		0
102474	45	Breast	Lobular carcinoma	Right	IA	pT1b	pN0(i-)		IA	3	Negative	0/9 +	Negative	Positive	no	12		0
100209	38	Breast	Invasive ductal carcinoma	Left	I	pT1c	pN0	pMX	I	2	Negative	0/8 +	Negative	Positive	no	125		0
100451	36	Breast	Invasive ductal carcinoma	Left	I	pT1c	pN0		I	2	Negative	0/2 +	Negative	Positive	no	127		0
91034	35	Breast	Invasive ductal carcinoma	Right	IIB	pT1c	pN2a		IIIA	3	Positive	6/12 +	Negative	Positive	no	114		0
101069	42	Breast	Invasive ductal carcinoma	Right	IIA	pT1c	pN0(i-)		IA	3	Negative	0/4 +	Positive	Positive	no	115		0
90809	43	Breast	Invasive ductal carcinoma	Right	IA	pT1c	pN0		IA	2	Negative	0/6 +	Negative	Positive	no	117		0
90311	40	Breast	Invasive ductal carcinoma	Right	IIA	pT1c	pN2a		IIIA	3	Positive	5/19 +	Negative	Positive	no	50	Breast cancer	1
101350	34	Breast	Invasive ductal carcinoma	Right	IA	pT2	pN1mi		IIB	3	Positive	1/8 +	Positive	Positive	no	106		0
101376	43	Breast	Invasive ductal carcinoma	Right	IA	pT1b	pN0		IA	2	Negative	0/5 +	Negative	Positive	no	90		0
90053	44	Breast	Invasive ductal carcinoma	Right	IIA	pT3	pN2a		IIIA		Positive	5/16 +	Negative	Positive	no	106		0
101494	30	Breast	Invasive ductal carcinoma	Left	IA	pT1c	pN0(i-)		IA	3	Negative	0/1 +	Negative	Positive	no	95		0
101750	37	Breast	Invasive ductal carcinoma	Left	IIA	pT2	pN0		IIA		Negative	0/1 +	Positive	Positive	no	37		0
101900	45	Breast	Invasive ductal carcinoma	Right	IA	pT1b	pN0(i-)		IA		Negative	0/9 +	Negative	Positive	no	61		0
101893	30	Breast	Invasive ductal carcinoma	Right	IIB	pT2	pN2a		IIIA		Positive	5/12 +	Negative	Negative	no	32	Breast cancer	1
101926	40	Breast	Invasive ductal carcinoma	Left	IIB	pT2	pN2a		IIIA	2	Positive	3/4 +	Negative	Positive	no	57		0

Supplementary Table 2.4: Patient sample clinical data (Sheet 2: purchased from USBioMax)

CLINICAL ANNOTATIONS												
ID	Age	Sex	Organ	Pathology diagnosis	TNM	Grade	Stage	Type	ER	PR	HER2	Ki67
1	45	F	Breast	Invasive carcinoma of no special type	T2N0M0	1	IIA	Malignant	+	+++	0	+, 3%
2	51	F	Breast	Invasive carcinoma of no special type	T2N0M0	1	IIA	Malignant	+++	+++	0	+, 15%
3	47	F	Breast	Invasive carcinoma of no special type	T2N0M0	1	IIA	Malignant	+++	+++	0	+, 20%
4	46	F	Breast	Invasive carcinoma of no special type	T4N0M0	2	IIIB	Malignant	+++	+++	0	+, 15%
6	48	F	Breast	Invasive carcinoma of no special type	T2N0M0	1	IIA	Malignant	+++	+++	2+	+, 40%
7	51	F	Breast	Invasive carcinoma of no special type	T4N1M0	2	IIIB	Malignant	-	+	3+	-
9	45	F	Breast	Invasive carcinoma of no special type	T2N2M0	2	IIB	Malignant	+++	+++	0	+, 20%
10	67	F	Breast	Invasive carcinoma of no special type	T2N0M0	2	IIA	Malignant	-	-	3+	+, 3%
11	52	F	Breast	Invasive carcinoma of no special type	T1N1M0	2	IIA	Malignant	+++	-	0	+, 10%
12	38	F	Breast	Invasive carcinoma of no special type	T3N0M0	3	IIB	Malignant	+++	+++	0	+, 10%
13	59	F	Breast	Invasive carcinoma of no special type	T2N0M0	2	IIA	Malignant	-	-	0	+, 80%
15	66	F	Breast	Invasive carcinoma of no special type	T3N0M0	2	IIB	Malignant	-	+	3+	+, 20%
16	45	F	Breast	Invasive carcinoma of no special type	T2N0M0	1	IIA	Malignant	+	+++	0	+, 3%
17	51	F	Breast	Invasive carcinoma of no special type	T2N0M0	1	IIA	Malignant	+++	+++	0	+, 5%
18	47	F	Breast	Invasive carcinoma of no special type	T2N0M0	2	IIA	Malignant	+++	+++	0	+, 20%
19	46	F	Breast	Invasive carcinoma of no special type	T4N0M0	2	IIIB	Malignant	+++	+++	0	+, 30%
20	54	F	Breast	Invasive carcinoma of no special type	T2N0M0	2	IIA	Malignant	++	-	3+	+, 20%
21	48	F	Breast	Invasive carcinoma of no special type	T2N0M0	2	IIA	Malignant	+++	+++	2+	+, 40%
22	51	F	Breast	Invasive carcinoma of no special type	T4N1M0	2	IIIB	Malignant	-	+	3+	-
24	45	F	Breast	Invasive carcinoma of no special type	T2N2M0	2	IIB	Malignant	+++	+++	0	+, 20%
26	52	F	Breast	Invasive carcinoma of no special type	T1N1M0	2	IIA	Malignant	+++	-	0	+, 10%
27	38	F	Breast	Invasive carcinoma of no special type	T3N0M0	3	IIB	Malignant	+++	+++	0	+, 3%
28	59	F	Breast	Invasive carcinoma of no special type	T2N0M0	2	IIA	Malignant	-	-	0	+, 80%
30	66	F	Breast	Invasive carcinoma of no special type	T3N0M0	2	IIB	Malignant	-	+	3+	+, 20%
31	45	F	Breast	Invasive carcinoma of no special type	T1N1M0	2	IIA	Malignant	-	-	0	+, 3%
32	53	F	Breast	Invasive carcinoma of no special type	T2N0M0	2	IIA	Malignant	+++	+++	0	+, 10%
33	67	F	Breast	Invasive carcinoma of no special type	T2N0M0	2	IIA	Malignant	+++	+++	0	+, 5%
34	63	F	Breast	Invasive carcinoma of no special type	T2N0M0	2	IIA	Malignant	+++	++	1+	+, 10%
35	49	F	Breast	Invasive carcinoma of no special type	T2N0M0	2	IIA	Malignant	+++	+++	0	+, 50%
36	63	F	Breast	Invasive carcinoma of no special type	T2N0M0	2	IIA	Malignant	+	-	3+	+, 3%
37	62	F	Breast	Invasive carcinoma of no special type	T3N0M0	2	IIB	Malignant	+++	++	0	+, 10%
38	61	F	Breast	Invasive carcinoma of no special type	T3N1M0	2	IIIA	Malignant	-	-	3+	+, 20%
39	48	F	Breast	Invasive carcinoma of no special type	T2N0M0	2	IIA	Malignant	+++	+++	1+	+, 30%
40	45	F	Breast	Invasive carcinoma of no special type	T3N1M0	2	IIIA	Malignant	-	-	0	+, 10%
41	50	F	Breast	Invasive carcinoma of no special type	T2N0M0	2	IIA	Malignant	+++	-	3+	+, 30%
43	59	F	Breast	Invasive carcinoma of no special type	T2N0M0	2	IIA	Malignant	+	-	3+	+, 20%
44	48	F	Breast	Invasive carcinoma of no special type	T3N0M0	2	IIB	Malignant	+++	++	0	+, 20%
45	46	F	Breast	Invasive carcinoma of no special type	T2N0M0	2	IIA	Malignant	-	-	3+	+, 60%
46	45	F	Breast	Invasive carcinoma of no special type	T1N1M0	2	IIA	Malignant	-	-	0	+, 3%
47	53	F	Breast	Invasive carcinoma of no special type	T2N0M0	2	IIA	Malignant	+++	+++	0	+, 5%
48	67	F	Breast	Invasive carcinoma of no special type	T2N0M0	2	IIA	Malignant	+++	+++	0	+, 10%
49	63	F	Breast	Invasive carcinoma of no special type	T2N0M0	2	IIA	Malignant	+++	++	1+	+, 20%
50	49	F	Breast	Invasive carcinoma of no special type	T2N0M0	2	IIA	Malignant	+++	+++	0	+, 10%
51	63	F	Breast	Invasive carcinoma of no special type	T2N0M0	2	IIA	Malignant	+	-	3+	+, 5%
52	62	F	Breast	Invasive carcinoma of no special type	T3N0M0	2	IIB	Malignant	+++	++	0	+, 10%
53	61	F	Breast	Invasive carcinoma of no special type	T3N1M0	2	IIIA	Malignant	-	-	3+	+, 20%
54	48	F	Breast	Invasive carcinoma of no special type	T2N0M0	2	IIA	Malignant	+++	+++	1+	+, 30%
55	45	F	Breast	Invasive carcinoma of no special type	T3N1M0	2	IIIA	Malignant	-	-	0	+, 10%
56	50	F	Breast	Invasive carcinoma of no special type	T2N0M0	2	IIA	Malignant	+++	-	3+	+, 20%
58	59	F	Breast	Invasive carcinoma of no special type	T2N0M0	2	IIA	Malignant	+	-	3+	+, 25%
59	48	F	Breast	Invasive carcinoma of no special type	T3N0M0	2	IIB	Malignant	+++	++	0	+, 20%
60	46	F	Breast	Invasive carcinoma of no special type	T2N0M0	2	IIA	Malignant	-	-	3+	+, 60%
61	39	F	Breast	Invasive carcinoma of no special type	T2N0M0	*	IIA	Malignant	*	*	*	*
62	54	F	Breast	Invasive carcinoma of no special type	T2N3M0	2	IIIC	Malignant	+	-	3+	+, 5%
63	49	F	Breast	Invasive carcinoma of no special type	T4N0M0	2	IIIB	Malignant	+++	++	0	+, 3%
64	45	F	Breast	Invasive carcinoma of no special type	T3N1M0	2	IIIA	Malignant	++	-	3+	+, 5%
65	35	F	Breast	Invasive carcinoma of no special type	T2N0M0	2	IIA	Malignant	+++	+++	0	+, 3%
66	67	F	Breast	Invasive carcinoma of no special type	T3N0M0	2	IIB	Malignant	+++	+	0	+, 3%
67	42	F	Breast	Invasive carcinoma of no special type	T3N0M0	2	IIB	Malignant	-	-	3+	+, 5%
68	44	F	Breast	Invasive carcinoma of no special type	T3N0M0	2	IIB	Malignant	+	-	3+	+, 10%
69	42	F	Breast	Invasive carcinoma of no special type	T3N0M0	2	IIB	Malignant	+	-	3+	+, 5%
70	44	F	Breast	Invasive carcinoma of no special type	T2N0M0	2	IIA	Malignant	+++	+	0	+, 5%
72	43	F	Breast	Invasive carcinoma of no special type	T2N0M0	2	IIA	Malignant	+++	+++	0	+, 3%
73	57	F	Breast	Invasive carcinoma of no special type	T2N0M0	2	IIA	Malignant	+++	+++	3+	+, 5%
74	48	F	Breast	Invasive carcinoma of no special type	T4N2M0	2	IIIB	Malignant	++	+++	0	+, 10%
75	46	F	Breast	Invasive carcinoma of no special type	T4N0M0	2	IIIB	Malignant	+++	+++	3+	+, 10%

76	39	F	Breast	Invasive carcinoma of no special type	T2N0M0	2	IIA	Malignant	++	+	0	+, 3%
77	54	F	Breast	Invasive carcinoma of no special type	T2N3M0	2	IIIC	Malignant	+	-	3+	+, 10%
78	49	F	Breast	Invasive carcinoma of no special type	T4N0M0	2	IIIB	Malignant	+++	++	0	+, 5%
79	45	F	Breast	Invasive carcinoma of no special type	T3N1M0	2	IIIA	Malignant	++	-	3+	+, 20%
80	35	F	Breast	Invasive carcinoma of no special type	T2N0M0	2	IIA	Malignant	+++	+++	0	+, 3%
81	67	F	Breast	Invasive carcinoma of no special type	T3N0M0	2	IIB	Malignant	+++	+	0	+, 3%
82	42	F	Breast	Invasive carcinoma of no special type	T3N0M0	2	IIB	Malignant	-	-	3+	+, 20%
83	44	F	Breast	Invasive carcinoma of no special type	T3N0M0	2	IIB	Malignant	+	-	3+	+, 3%
84	42	F	Breast	Invasive carcinoma of no special type	T3N0M0	2	IIB	Malignant	+	-	3+	+, 3%
85	44	F	Breast	Invasive carcinoma of no special type	T2N0M0	2	IIA	Malignant	+++	+	0	+, 10%
86	54	F	Breast	Invasive carcinoma of no special type	T3N0M0	2	IIB	Malignant	-	-	3+	+, 20%
87	43	F	Breast	Invasive carcinoma of no special type	T2N0M0	2	IIA	Malignant	+++	+++	0	+, 10%
88	57	F	Breast	Invasive carcinoma of no special type	T2N0M0	2	IIA	Malignant	+++	+++	3+	+, 10%
89	48	F	Breast	Invasive carcinoma of no special type	T4N2M0	2	IIIB	Malignant	++	+++	0	+, 10%
90	46	F	Breast	Invasive carcinoma of no special type	T4N0M0	2	IIIB	Malignant	+++	+++	3+	+, 10%
92	65	F	Breast	Invasive carcinoma of no special type	T1N2M0	2	IIIA	Malignant	-	-	0	+, 5%
93	48	F	Breast	Invasive carcinoma of no special type	T3N1M0	2	IIIA	Malignant	+++	-	0	+, 3%
94	37	F	Breast	Invasive carcinoma of no special type	T2N1M0	2	IIB	Malignant	-	-	0	+, 40%
95	43	F	Breast	Invasive carcinoma of no special type	T2N0M0	2	IIA	Malignant	+++	++	0	+, 20%
96	45	F	Breast	Invasive carcinoma of no special type	T2N0M0	3	IIA	Malignant	-	-	0	+, 30%
97	32	F	Breast	Invasive carcinoma of no special type	T1N1M0	3	IIA	Malignant	+++	+	0	+, 15%
98	46	F	Breast	Invasive carcinoma of no special type	T2N1M0	3	IIB	Malignant	-	-	3+	+, 15%
99	50	F	Breast	Invasive carcinoma of no special type	T2N0M0	3	IIA	Malignant	+++	-	0	+, 60%
100	37	F	Breast	Invasive carcinoma of no special type	T3N0M0	3	IIB	Malignant	++	-	0	+, 30%
101	66	F	Breast	Invasive carcinoma of no special type	T2N0M0	3	IIA	Malignant	+++	-	3+	+, 15%
102	75	F	Breast	Invasive carcinoma of no special type	T2N1M0	3	IIB	Malignant	++	+	0	+, 20%
103	40	F	Breast	Invasive carcinoma of no special type	T2N0M0	3	IIA	Malignant	-	-	0	+, 15%
104	49	F	Breast	Invasive carcinoma of no special type	T2N2M0	3	IIB	Malignant	-	-	3+	-
105	40	F	Breast	Invasive carcinoma of no special type	T3N2M0	3	IIIA	Malignant	-	-	0	+, 15%
107	65	F	Breast	Invasive carcinoma of no special type	T1N2M0	2	IIIA	Malignant	-	-	0	+, 5%
108	48	F	Breast	Invasive carcinoma of no special type	T3N1M0	2	IIIA	Malignant	+++	-	0	+, 3%
109	37	F	Breast	Invasive carcinoma of no special type	T2N1M0	2	IIB	Malignant	-	-	0	+, 30%
110	43	F	Breast	Invasive carcinoma of no special type	T2N0M0	2	IIA	Malignant	+++	++	0	+, 10%
111	45	F	Breast	Invasive carcinoma of no special type	T2N0M0	3	IIA	Malignant	-	-	0	+, 30%
112	32	F	Breast	Invasive carcinoma of no special type	T1N1M0	3	IIA	Malignant	+++	+	0	+, 15%
113	46	F	Breast	Invasive carcinoma of no special type	T2N1M0	3	IIB	Malignant	-	-	3+	+, 15%
114	50	F	Breast	Invasive carcinoma of no special type	T2N0M0	3	IIA	Malignant	+++	-	0	+, 60%
115	37	F	Breast	Invasive carcinoma of no special type	T3N0M0	3	IIB	Malignant	++	-	0	+, 40%
116	66	F	Breast	Invasive carcinoma of no special type	T2N0M0	3	IIA	Malignant	+++	-	3+	+, 20%
117	75	F	Breast	Invasive carcinoma of no special type	T2N1M0	*	IIB	Malignant	++	+	0	+, 15%
118	40	F	Breast	Invasive carcinoma of no special type	T2N0M0	3	IIA	Malignant	-	-	0	+, 50%
120	40	F	Breast	Invasive carcinoma of no special type	T3N2M0	3	IIIA	Malignant	-	-	0	+, 10%
121	53	F	Breast	Invasive carcinoma of no special type	T4N1M0	3	IIIB	Malignant	+++	++	0	+, 30%
122	45	F	Breast	Invasive carcinoma of no special type	T3N0M0	3	IIB	Malignant	+++	+++	0	+, 10%
123	52	F	Breast	Invasive carcinoma of no special type	T2N0M0	3	IIA	Malignant	-	-	3+	+, 20%
124	51	F	Breast	Invasive carcinoma of no special type	T2N0M0	3	IIA	Malignant	-	-	0	+, 60%
125	68	F	Breast	Invasive carcinoma of no special type	T2N0M0	3	IIA	Malignant	-	-	0	+, 20%
126	46	F	Breast	Invasive carcinoma of no special type	T2N0M0	3	IIA	Malignant	+++	+++	0	+, 15%
127	35	F	Breast	Invasive carcinoma of no special type	T4N1M0	3	IIIB	Malignant	-	-	3+	+, 15%
128	33	F	Breast	Invasive carcinoma of no special type	T2N0M0	3	IIA	Malignant	+++	+++	0	+, 10%
129	38	F	Breast	Invasive carcinoma of no special type	T2N0M0	3	IIA	Malignant	+	++	0	+, 15%
130	60	F	Breast	Invasive carcinoma of no special type	T4N0M0	3	IIIB	Malignant	-	-	3+	+, 3%
131	58	F	Breast	Invasive carcinoma of no special type	T3N2M0	3	IIIA	Malignant	+++	+	0	+, 10%
133	34	F	Breast	Invasive carcinoma of no special type	T2N0M0	3	IIA	Malignant	+++	+++	0	+, 60%
134	49	F	Breast	Invasive carcinoma of no special type	T4N2M0	3	IIIB	Malignant	-	-	3+	+, 10%
136	53	F	Breast	Invasive carcinoma of no special type	T4N1M0	3	IIIB	Malignant	+++	++	0	+, 20%
137	45	F	Breast	Invasive carcinoma of no special type	T3N0M0	3	IIB	Malignant	+++	+++	0	+, 10%
138	52	F	Breast	Invasive carcinoma of no special type	T2N0M0	3	IIA	Malignant	-	-	3+	+, 30%
139	51	F	Breast	Invasive carcinoma of no special type	T2N0M0	3	IIA	Malignant	-	-	0	+, 50%
140	68	F	Breast	Invasive carcinoma of no special type	T2N0M0	3	IIA	Malignant	-	-	0	+, 10%
141	46	F	Breast	Invasive carcinoma of no special type	T2N0M0	3	IIA	Malignant	+++	+++	0	+, 15%
142	35	F	Breast	Invasive carcinoma of no special type	T4N1M0	*	IIIB	Malignant	-	-	3+	+, 2%
143	33	F	Breast	Invasive carcinoma of no special type	T2N0M0	3	IIA	Malignant	+++	+++	0	+, 15%
144	38	F	Breast	Invasive carcinoma of no special type	T2N0M0	3	IIA	Malignant	+	++	0	+, 15%
145	60	F	Breast	Invasive carcinoma of no special type	T4N0M0	3	IIIB	Malignant	-	-	3+	+, 3%
146	58	F	Breast	Invasive carcinoma of no special type	T3N2M0	3	IIIA	Malignant	+++	++	0	+, 10%
147	38	F	Breast	Invasive carcinoma of no special type	T3N1M0	3	IIIA	Malignant	-	-	0	+, 5%
148	34	F	Breast	Invasive carcinoma of no special type	T2N0M0	3	IIA	Malignant	+++	+++	0	+, 60%
149	49	F	Breast	Invasive carcinoma of no special type	T4N2M0	3	IIIB	Malignant	-	-	3+	+, 5%
150	40	F	Breast	Invasive carcinoma of no special type	T2N0M0	3	IIA	Malignant	+	-	0	+, 50%

Supplementary Table 2.4: Patient sample clinical data (Sheet 3: Single-section slides)

CLINICAL ANNOTATIONS			
ID	**Sex**	**Diagnosis**	
07-14590 B2	F	Breast	Ductal carcinoma in situ
08-12846 B13	F	Breast	Invasive ductal carcinoma
07-44058 B6	F	Breast	Ductal carcinoma in situ
08-16350 B1	F	Breast	Mixed DCIS/IDC
08-39725 D30	F	Breast	Ductal carcinoma in situ
06-7188 A15	F	Breast	Mixed DCIS/IDC
08-16226 B3	F	Breast	Invasive ductal carcinoma
07-36811 A10	F	Breast	Mixed DCIS/IDC
06-4646 D3	F	Breast	Mixed DCIS/IDC
10-28260 A35	F	Breast	Mixed DCIS/IDC
07-43931 B14	F	Breast	Ductal carcinoma in situ
08-34690 B15	F	Breast	Mixed DCIS/IDC
07-19044 A5	F	Breast	Ductal carcinoma in situ
07-22117 A8	F	Breast	Mixed DCIS/IDC
07-10040 A-3-5	F	Breast	Mixed DCIS/IDC
08-13178 A18	F	Breast	Invasive ductal carcinoma
10-24112 A21	F	Breast	Invasive ductal carcinoma
08-35820 A2	F	Breast	Ductal carcinoma in situ
06-7182 A11	F	Breast	Ductal carcinoma in situ
06-22124 A5	F	Breast	Ductal carcinoma in situ
06-3663 D12	F	Breast	Mixed DCIS/IDC
06-2353 A11	F	Breast	Mixed DCIS/IDC
08-3224 A4	F	Breast	Mixed DCIS/IDC
10-44180 A10	F	Breast	Mixed DCIS/IDC
08-16087 A4	F	Breast	Invasive ductal carcinoma

Bridging text

The two studies presented in this thesis investigate the contribution of the MNK1/2-eIF4E signaling axis in promoting mechanisms of breast cancer progression. While both studies focus on the same signaling node, they differ in which elements of the TME they investigate. This approach is necessary for continued efforts to assess the relevance of MNK1/2 inhibitors in a clinical setting, as these inhibitors act systemically to inhibit MNK1 and MNK2 and are not selective against tumor cells alone. In Chapter 2, we examined the role that eIF4E phosphorylation plays in regulating stromal cell-derived ECM in the mammary gland. We demonstrated that targeting phospho-eIF4E reduced collagen-I deposition and altered collagen fiber spatial orientation, contributing towards a less-metastatic TME. Importantly, this work has helped to advance our understanding of the critical role that translational control plays in non-tumoral components of the TME. However, there remain many unanswered questions regarding the function of MNK1/2-eIF4E signaling within tumor cells themselves. Thus, in Chapter 3, we shift focus to study the pro-metastatic functions of tumor-intrinsic MNK1 kinase. Specifically, we generate a genetic model of MNK1 ablation in breast cancer cells to explore the role this kinase plays in regulating stem cell features and subsequent metastatic potential. These studies help to address an unmet clinical need, as they aim to understand whether MNK1/2 inhibitors could represent a promising clinical strategy for patients diagnosed with metastatic breast cancer. Improving therapeutic options for this group of patients remains the overarching goal of this body of work as a whole.

Chapter 3 – Targeting tumor-intrinsic MNK1 kinase restricts metabolic flexibility to diminish breast cancer liver metastasis

This chapter is presented in the form of a manuscript in preparation for publication as an original research article:

Preston SEJ, Dahabieh MS, Richard VR, Gonçalves C, Gagnon N, Dakin E, Zahedi RP, Borchers CH, Jones RG, Miller Jr. WH, del Rincón SV. Targeting tumor-intrinsic MNK1 kinase restricts metabolic flexibility to diminish breast cancer liver metastasis. *In preparation* (2023).

3.1 Abstract

Dysregulation of the MNK1/2-eIF4E axis promotes breast cancer progression, partly by influencing cancer stem cells (CSCs). These self-renewing cell populations contribute to metastasis, recurrence, and chemotherapeutic resistance, making them a clinically relevant target. The role of the MNK1/2-eIF4E pathway in regulating CSCs, however, is yet to be explored. Herein, we generated MNK1 knock-out breast cancer cell lines, resulting in diminished CSC properties *in vitro* and slowed tumor growth *in vivo*. Using a multi-omics approach, we functionally demonstrated that loss of MNK1 restricts tumor cell metabolic flexibility by reducing glycolysis and increasing dependence on oxidative phosphorylation. This translated to suppressed metastasis of MNK1 KO cells to the liver, but not the lung. Analysis of TCGA BRCA patient data validated the positive correlation between MNK1 and glycolytic enzyme protein expression. This study defines metabolic regulation as a previously unknown consequence of targeting MNK1/2, that may be therapeutically exploited.

3.2 Introduction

Breast cancer (BC) is the most commonly diagnosed cancer among women, and the second leading cause of cancer-related death[1]. For patients with non-metastatic disease, 5-year survival rates range between 86% and 99%[2]. However, approximately one-third of BC patients will present with distant-site metastases, after which the 5-year survival rate is reduced to approximately 27%[2]. Prognosis is particularly poor for patients diagnosed with liver metastasis (BCLM), a common secondary site for BC; even with systemic hormone- and/or chemotherapy median survival is only 20 months[3]. Stage IV BC is considered incurable with currently available therapies, thus the ability to reduce BC metastasis remains an unmet clinical need.

Perturbations in mRNA translation are well-known to promote cellular transformation and malignant progression[4], as exemplified by the MNK1/2-eIF4E axis[5]. Eukaryotic initiation factor 4E (eIF4E) binds to the 5' cap of mRNAs to mediate cap-dependent translation. eIF4E is phosphorylated on serine 209 by Mitogen-activated Protein Kinase Interacting Kinases 1/2 (MNK1/2)[6,7]. Although the precise function of this phosphorylation event remains contentious in the field, it is clear that MNK-mediated phosphorylation of eIF4E enhances cellular transformation[8]. Moreover, eIF4E phosphorylation has been well-established as promoting disease progression, in part due to the increased translation of a subset of pro-invasive and pro-survival mRNAs[9–11]. Our team has published studies demonstrating that phospho-eIF4E-deficient mice are protected against developing lung metastases in both spontaneous and orthotopic models of murine BC[10–12]. In addition, we have explored the multi-faceted role of the

MNK1/2-eIF4E axis across non-tumoral components of the tumor microenvironment (TME), including the immune cell landscape[11–14] and stromal cell-derived extracellular matrix[15]. Clinically, the expression of phospho-eIF4E has been associated with poor patient prognosis in multiple cancer types[9,16], encouraging the pharmacological development of MNK1/2 inhibitors that are currently in clinical trials (NCT04261218, NCT03690141, NCT04622007).

We have previously reported that tumor-intrinsic MNK1 signaling promotes primary BC tumor progression from ductal carcinoma *in situ* to invasive ductal carcinoma[17]. This study was the first to recognize a link between MNK1 and breast cancer stem cells (BCSCs), showing that modulating MNK1 expression altered BCSC properties *in vitro* and *in vivo*. Increasing evidence suggests that BCSCs, a small pool of undifferentiated and self-renewing tumor cells, are the powerhouse behind tumor progression, therapeutic resistance, and metastasis[18–22]. There are several biomarkers, signaling activities and biological features that define and characterize CSC pools[23]. In particular, CSCs maintain a remarkable ability to reprogramme their metabolic state to adapt to environmental changes[24–26], which is thought to be critical for their ability to proliferate. Reports from this emerging field implicate glycolysis as a crucial metabolic pathway for CSC populations, including BCSCs, to sustain stemness and self-renewal, and highlight oxidative phosphorylation (OxPhos) and glutamine metabolism as functionally important in some cases[26,27]. While MNK1 has been implicated in regulating stemness[17,28,29], the precise functional role of this kinase in BCSCs, and how this impacts metastatic potential to different organ sites, remains unknown. Metabolic flexibility is especially interesting in the

context of metastasis, as recent literature describes tissue-specific metabolic dependencies of metastatic cells. For instance, glycolytic-dominant metabolism can be advantageous for BC metastasis to the liver[30], whereas lung metastases rely largely on OxPhos[31] and uptake of environmental pyruvate[32], and brain metastases require fatty acid synthesis to fuel their growth[33].

In this study, we sought to expand our understanding of how MNK1 contributes to BCSC properties. Our results suggest that MNK1 impacts BCSC function, rather than frequency, ultimately impacting tumor growth rates *in vivo*. We performed protein and gene expression analyses, metabolite tracing and bioenergetic profiling to uncover that MNK1 regulates tumor cell glycolysis. Furthermore, we determined that genetic and pharmacologic inhibition of MNK1 restricts tumor cell metabolic flexibility and increases energetic dependence on OxPhos, resulting in suppressed metastasis to the liver but not the lung. Finally, by interrogating mass spectrometry-derived protein data from the Cancer Genome Atlas (TCGA) Breast Cancer (BRCA) PanCancer Atlas, we demonstrate that MNK1 expression positively correlates with the expression of glycolysis-related enzymes. Together, our findings report the metabolic consequences of disrupting MNK1 in breast cancer cells and highlight the potential utility of MNK1/2 inhibitors as therapeutic agents in targeting tumor metabolism to reduce metastasis.

3.3 Results

3.3.1 MNK1 ablation in 4T1 cells alters stemness phenotypes in vitro and in vivo

To better understand the contribution of tumor-intrinsic MNK1 to breast cancer stemness and metastasis, we chose to knock-out MNK1 (MNK1 KO) from the 4T1 murine breast cancer cell line. Using CRISPR-Cas9, we generated and pursued two MNK1 KO cell lines (herein referred to as sg-*MKNK1*-1 and sg-*MKNK1*-2) alongside a sgRNA-null control (herein referred to as Cas9CTL). Western blotting confirmed the absence of MNK1 in both KO cell lines, alongside an expected decrease in the phosphorylation of eIF4E (*Fig. 3.1A*). 4T1 cell viability was not altered by the loss of MNK1 (*Fig. 3.1B*), nor was the proliferative rate under standard monolayer culture conditions (*Fig. 3.1C*). We have previously shown that phosphorylation of eIF4E, the primary substrate of MNK1 kinase, promotes the epithelial-to-mesenchymal transition (EMT)[10]. In line with these findings, we found that MNK1 KO 4T1 cells appear more epithelial-like than their Cas9CTL counterparts, as illustrated by the altered expression of several EMT-associated proteins (*Fig. 3.1D*). Given our interest in CSCs, and the known link between EMT and development of CSC-like features[34], we next chose to culture Cas9CTL and MNK1 KO cells on low-adherence plastic to assess tumorsphere formation, wherein individual cells maintain the ability to self-renew while avoiding anoikis. While all cell lines tested were able to form spheres, their morphology differed drastically between groups, as MNK1 KO tumorspheres appeared smaller, rounder, and less disordered than Cas9CTL tumorspheres (*Fig. 3.1E*). Subsequent quantification confirmed a significant reduction in the average size of a tumorsphere in both sg-*MKNK1*-1 and sg-*MKNK1*-2 cell lines

compared to Cas9CTL (*Fig. 3.1F*), without changing the number of tumorspheres formed (*Fig. 3.1G*). In addition, we profiled the impact of MNK1 KO on the activity of aldehyde dehydrogenases (ALDH), an enzyme group whose activity are enhanced in CSCs[35]. As expected, MNK1 KO significantly reduced the ALDH activity of 4T1 cells when measured by flow cytometry (*Fig. 3.1H*). We next assessed whether MNK1 KO cells differ from their control counterparts in tumor outgrowth *in vivo*. Thus, we injected Cas9CTL and MNK1 KO 4T1 cells into the mammary fat pads of BALB/c mice. Immunohistochemistry confirms that sg-*MKNK1*-1 and sg-*MKNK1*-2 tumors remain devoid of MNK1 expression (*Fig. 3.1I*). Tumors derived from MNK1 KO cell lines grew significantly slower than those from Cas9CTL cells (*Fig. 3.1J*). Finally, we monitored tumor formation from serially diluted concentrations of Cas9CTL and MNK1 KO cells; a gold-standard for assessing stemness *in vivo*. MNK1 KO cells exhibited similar tumor-initiation capacity compared to Cas9CTL, even at the lowest cell concentration (*Fig. 3.1K*). Coupled with our *in vitro* observations, the data from this orthotopic model suggest that MNK1 ablation may not dictate the frequency of CSCs within a population, but rather the functional capabilities of the CSC pool.

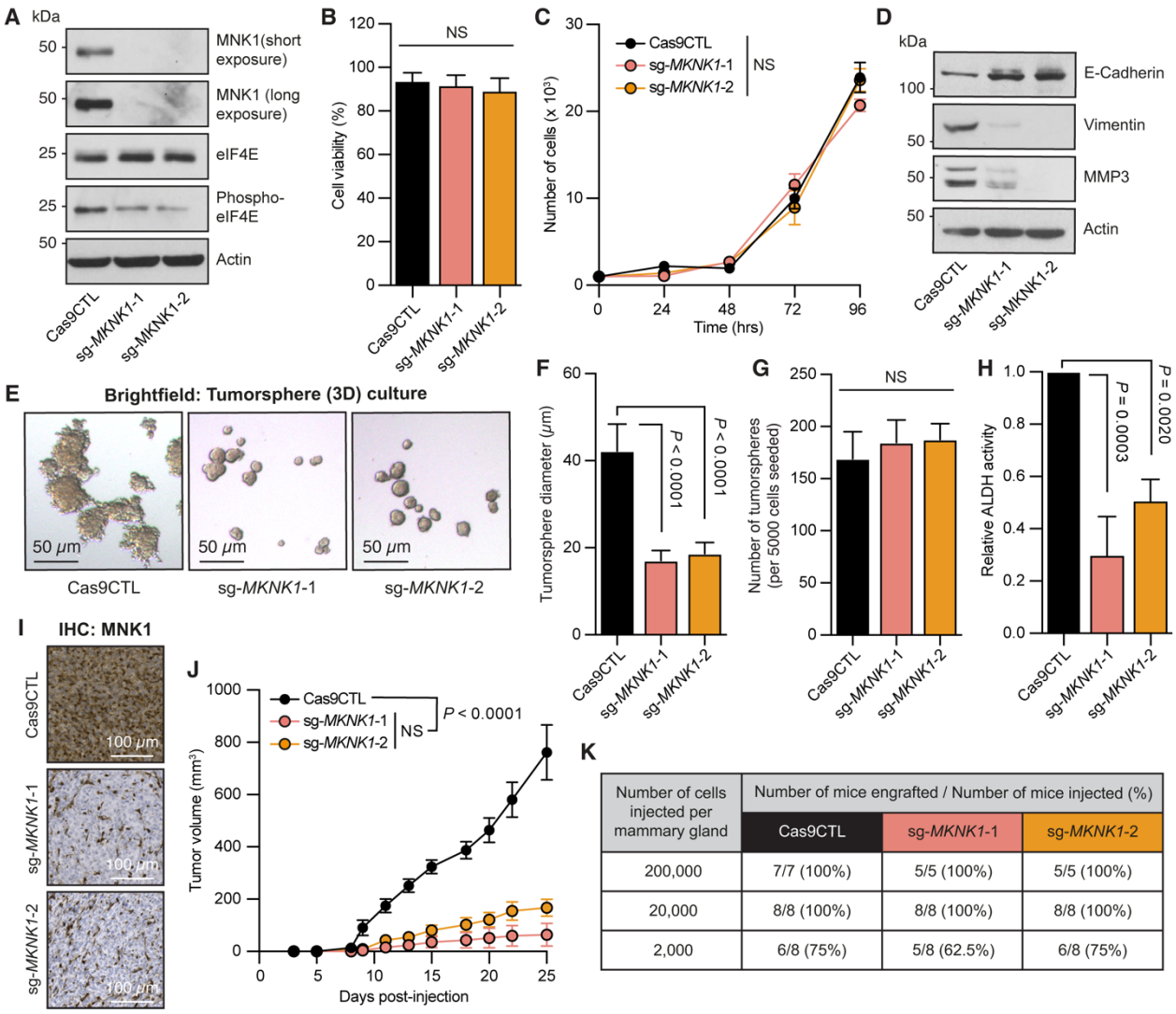

K

Number of cells injected per mammary gland	Number of mice engrafted / Number of mice injected (%)		
	Cas9CTL	sg-*MKNK1*-1	sg-*MKNK1*-2
200,000	7/7 (100%)	5/5 (100%)	5/5 (100%)
20,000	8/8 (100%)	8/8 (100%)	8/8 (100%)
2,000	6/8 (75%)	5/8 (62.5%)	6/8 (75%)

Figure 3.1. (**A**) Western blot analysis of the indicated proteins in Cas9CTL, sg-*MKNK1*-1 and sg-*MKNK1*-2 4T1 cells. (**B**) Percentage of live cells of indicated cell lines. Error bars represent SD, one-way ANOVA with Tukey's multiple comparison test, *n* = 4 per group. (**C**) Proliferation of indicated cell lines in complete media over 96 hours following serum starvation. Error bars represent SD, two-way ANOVA with Tukey's multiple comparison test, *n* = 3. (**D**) Western blot analysis of the indicated proteins in Cas9CTL, sg-*MKNK1*-1 and sg-*MKNK1*-2 4T1 cells. (**E**) Representative brightfield images of the indicated cell lines grown under low-adherence tumorsphere culture. (**F and G**) Average tumorsphere size (**F**) and tumorsphere number (**G**) grown from 5000 of the indicated cells under low-adherence cultures. Quantification performed on tumorspheres 7 days post-seeding. Error bars represent SD, one-way ANOVA with Tukey's multiple comparison test, *n* = 3 (25 spheres analyzed per cell line per repeat). (**H**) Quantification of ALDH activity in the indicated cell lines. Data represent percentage ALDH+ cells, error bars represent SD, one-way ANOVA with Tukey's multiple comparison test, *n* = 3. (**I**) Representative images of IHC staining against MNK1 (DAB) in indicated tumors. (**J**) Growth rates of tumors formed from the indicated cell lines following mammary fat pad injection. Error bars represent SEM, two-way ANOVA with Tukey's multiple comparison test, *n* = 7 (Cas9CTL) 5 (sg-*MKNK1*-1

and sg-*MKNK1*-2). (**K**) Number and percentage of mice engrafted following mammary fat pad injection of serially diluted Cas9CTL, sg-*MKNK1*-1 and sg-*MKNK1*-2 cell lines.

3.3.2 Multi-omics analysis highlights alterations in glycolysis and oxidative phosphorylation pathways in MNK1 KO 4T1 cells

BCSCs are regulated by several major signaling pathways and possess multiple biological features that help maintain their activity. We used a multi-omics approach to understand the mechanism by which MNK1 ablation regulates 4T1 stem-like behaviour. Matched RNA-sequencing (RNA-seq) and mass spectrometry-based discovery proteomics were performed on Cas9CTL, sg-*MKNK1*-1 and sg-*MKNK1*-2 cell lines in quadruplicate (*Fig. 3.2A, 3.2B*). As expected, loss of MNK1 resulted in the differential expression of numerous targets at both the RNA (*Fig. 3.2C*) and protein level (*Fig. 3.2D*), a large proportion of which were common to both MNK1 KO clones. Functional enrichment analyses were performed to identify biological processes that were commonly differentially expressed between Cas9CTL and MNK1 KO cells. In line with our data that MNK1 ablation dampens stem-cell properties, gene set enrichment analysis (GSEA) of our RNA-seq suggested that Wnt and Hedgehog signaling pathways, known to be critical in maintaining BCSC features, were downregulated in both MNK1 KO cell lines compared to Cas9CTL (*Fig. 3.2E*). Moreover, our proteomics data support EMT being repressed in MNK1 KO cells, as indicated by IPA enrichment analysis (*Fig. 3.2F*). Curiously, both RNA-seq and mass spectrometry data independently supported that glycolysis/gluconeogenesis pathways were strongly repressed in MNK1 KO cells, while OxPhos was increased at the RNA level (*Fig. 3.2E-G*). Western blotting was used to verify the reduced expression of several glycolysis-related enzymes in sg-*MKNK1*-1 and sg-

MKNK1-2 cells relative to Cas9CTL (*Fig. 3.2H*), as informed by our proteomics data. These findings provide strong evidence to suggest that 4T1 cells lacking MNK1 have rewired their metabolism to depend more on OxPhos and less on glycolysis. This supports the notion that MNK1 KO cells have dampened stemness properties (*Fig. 3.1*), as a glycolytic-dominant metabolism has been shown to play a functional role in regulating BCSC populations[36–38]. Previous work by Dupuy et al. has further identified a gene signature that underpins high glycolytic activity in 4T1 cells to provide a selective advantage in their ability to metastasize to the liver. We probed the expression of this signature in our Cas9CTL and MNK1 KO cell lines and found it was significantly reduced in sg-*MKNK1*-1 and sg-*MKNK1*-2 cells at the protein (*Fig. 3.2I*) and RNA level (*Fig. 3.2J*). Additionally, we analysed publicly available microarray data from Dupuy et al. (GEO: GSE62598) and found that *in vivo*-selected liver-tropic 4T1 cells have an increased expression of *MKNK1*, but not *MKNK2*, compared to parental cells (*Fig. 3.2K*). Together these findings suggest a correlation between MNK1 expression in tumor cells and their maintenance of metabolic pro-liver metastasis features

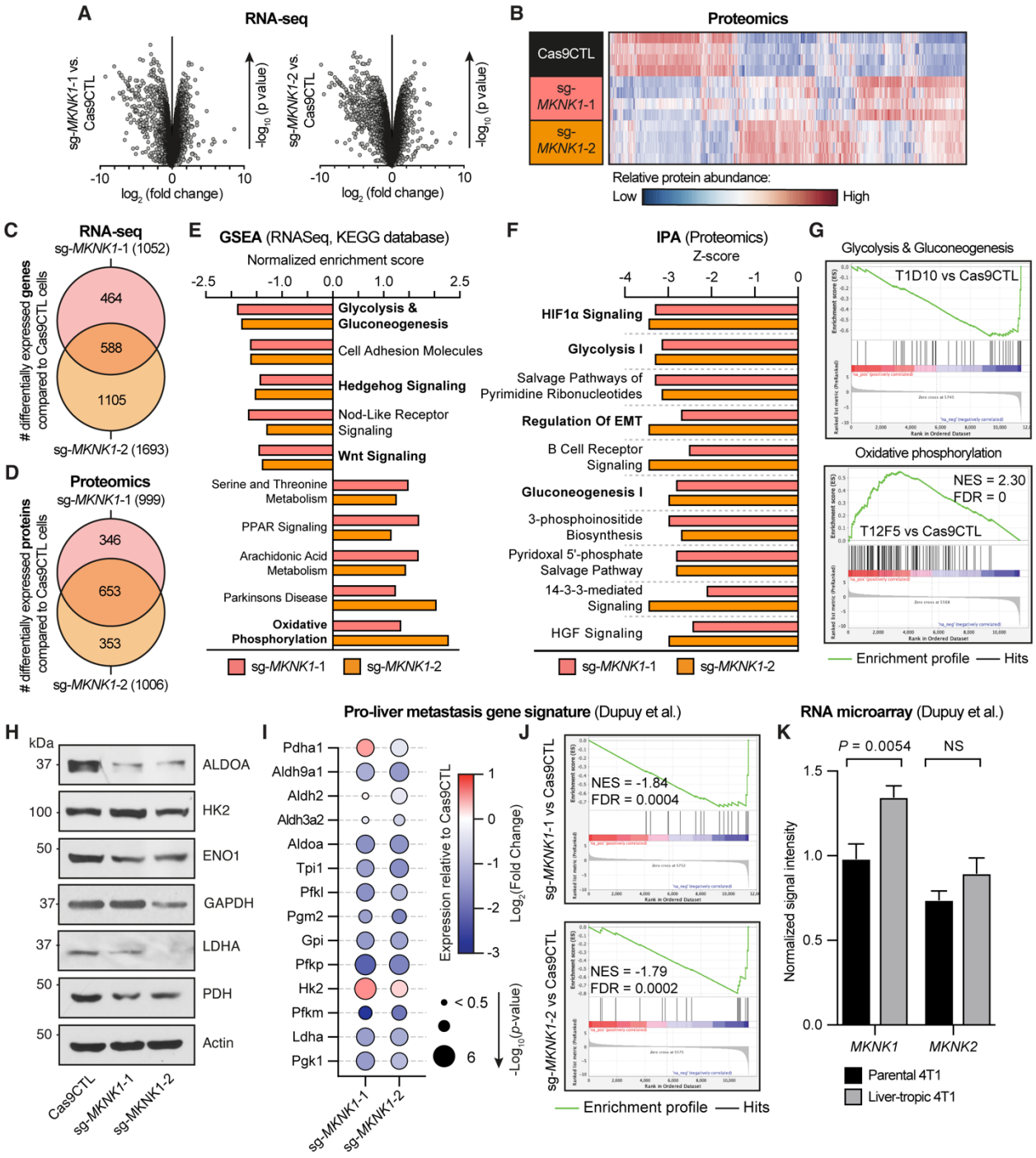

Figure 3.2. (**A**) Volcano plots comparing differential gene expression between the indicated cell lines as indicated by RNA-seq. All data are averages of four independent replicates. (**B**) Heatmap expressing relative abundance values for all proteins identified by mass spectrometry in the indicated cell lines. All data are averages of four independent replicates. (**C and D**) Venn diagrams visualize the number of differentially expressed genes (**C**) and proteins (**D**) when comparing the indicated cell lines. (**E**) Gene Set Enrichment Analysis (GSEA) of RNA-seq data through the KEGG database. Signatures shown represent the top 5 up- and downregulated pathways relative

to Cas9CTL cells, according to normalized enrichment scores. Only signatures with significant differential regulation (adjusted p value < 0.1) in both sg-*MKNK1* cell lines are shown Bar colour denotes cell line. (**F**) Ingenuity Pathway Analysis (IPA) of proteomics data in the indicated cell lines relative to Cas9CTL cells. Pathways shown represent the top 10 differentially expressed, irrespective of direction of regulation, according to enrichment z-score values. (**G**) Representative GSEA plots comparing the expression of the listed gene signatures between Cas9CTL and sg-*MKNK1* cell lines. Normalized Enrichment Scores (NES) and False Discovery Rates (FDR) are indicated. (**H**) Western blot analysis of the indicated proteins in Cas9CTL, sg-*MKNK1*-1 and sg-*MKNK1*-2 4T1 cells. (**I and J**) Expression of a pro-liver metastasis metabolic gene signature across RNA-seq and proteomics datasets. Proteomics data are shown as a bubble plot (**I**); bubble colour corresponds with relative expression of the listed protein in sg-*MKNK1* cells relative to Cas9CTL, bubble size corresponds to *p* value. RNA-seq data are shown as GSEA plots (**J**); NES and FDR values are listed. (**K**) Expression of *MKNK1* and *MKNK2* in parental 4T1 cells and a population of 4T1 cells that have undergone in vivo selection to enrich for liver-tropic features. Values acquired from publicly-available RNA microarray data. Error bars represent SD, multiple unpaired t-tests with Welch correction and Holm-Sidak multiple comparison test, $n = 3$.

3.3.3 Experimental metastasis models demonstrate that MNK1 ablation significantly dampens metastatic tumor outgrowth in the liver, but not the lung.

From our multi-omics profiling (*Fig. 3.2*) we postulated that MNK1 KO 4T1 cells may have a reduced ability to metastasize to the liver. To address this, we used intrasplenic injections of tumor cells to model experimental liver metastasis (*Fig. 3.3A*), as this allows us to robustly replicate the later stages of the metastatic cascade independent of differences in primary tumor growth. We found that mice injected with MNK1 KO cells had significantly fewer visible metastases on the livers at 21 days post-injection, compared to their Cas9CTL counterparts (*Fig. 3.3B*), leading to a marked increase in mouse survival (*Fig. 3.3C*). We also performed intrasplenic injection of a pool of five independent sg-*MKNK1* 4T1 cell lines, to confirm that the observed effect was not an artefact of clonal selection and found an equal level of reduction in liver tumor burden (*Supp. Fig. 3.1A*). To ensure that metastases visible on the surface of the liver were representative of total tumor burden, we performed quantification of H&E-stained step-

sections of tumor-bearing livers (*Fig. 3.3D*). As expected, we confirmed that livers harboring MNK1 KO 4T1 cells had a significantly lower number of total metastases (*Fig. 3.3E*) as well as reduced overall percentage tumor burden (*Fig. 3.3F*). Next, we were curious to understand whether this strong protection against the development of liver metastases was due to the inability of MNK1 KO cells to extravasate out of the vasculature, or a failure to colonize and outgrow thereafter. To answer this question, we developed an *in vivo* seeding competition assay whereby an equal ratio of Cas9CTL and MNK1 KO cells, each tagged with a different colour of CellTracker dye, were intrasplenically injected into the same mouse. Two days post-injection we perfused the liver to flush the vasculature and remove any tumor cells that had failed to extravasate, before assessing relative cell abundance by flow cytometry (*Fig. 3.3G*). Using this protocol, we demonstrated that neither sg-*MKNK1*-1 or sg-*MKNK1*-2 cells had a defect in their extravasation ability compared to Cas9CTL (*Fig. 3.3H*), therefore leading us to conclude that MNK1 has an important role following tumor cell colonization in the liver microenvironment. To determine if MNK1 KO cells had a general inability to metastasize, we performed tail vein injections of Cas9CTL and MNK1 KO 4T1 cells (*Fig. 3.3I*). Interestingly, MNK1 KO resulted in only a mild reduction in the ability of 4T1 cells to form metastases in the lung, even though tumor growth in the liver was severely diminished (*Fig. 3.3J,* representative images: *Supp. Fig. 3.1B*). This suggests that the anti-metastatic effects of tumor-intrinsic MNK1 ablation are influenced by tissue-specific microenvironments.

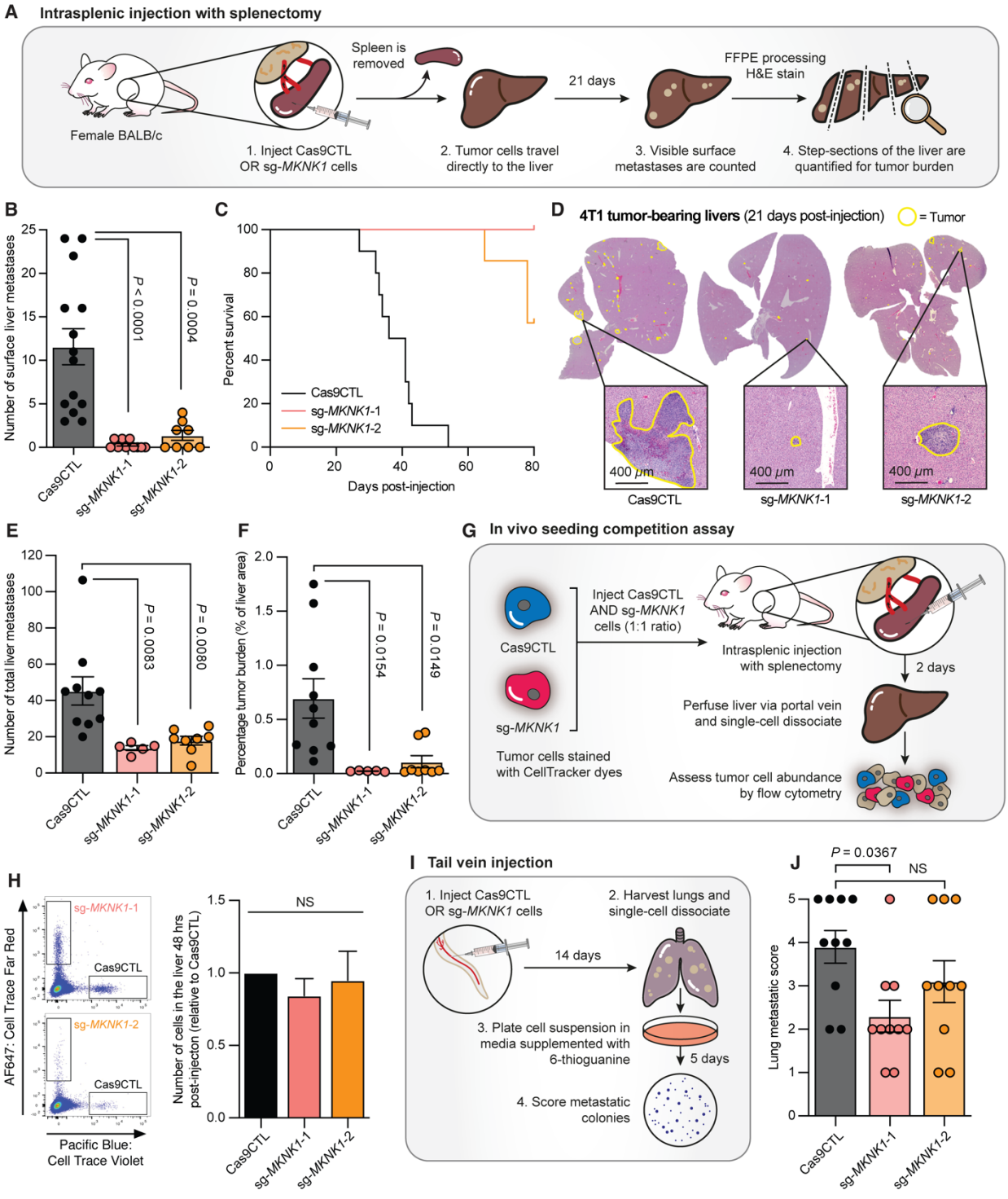

Figure 3.3. (**A**) Schematic of the intrasplenic injection experimental design, including duration and end-point liver processing. (**B**) Number of metastases visible on the liver surface 21 days post- intrasplenic injection of the indicated cell lines. Error bars represent SEM, $n = 14$ (Cas9CTL) 10 (sg-*MKNK1*-1) 8 (sg-*MKNK1*-2). (**C**) Kaplan-Meier curves showing mouse survival following intrasplenic injection of the indicated cell lines, $n = 10$ (Cas9CTL), 8 (sg-*MKNK1*-1) 7 (sg-*MKNK1*-

2). (**D**) Representative images of H&E-stained tumor-bearing livers at 21 days post-injection. Cell lines are indicated, and yellow borders denote the tumor edge. (**E and F**) Quantification of metastatic tumor burden in H&E-stained liver sections in the indicated conditions, showing the average total number of metastases (**E**) and percentage tumor area (**F**) per liver. Error bars represent SEM, *n* = 10 (Cas9CTL) 5 (sg-*MKNK1*-1) 8 (sg-*MKNK1*-2). (**G**) Schematic detailing the experimental design of an in vivo seeding competition assay, using CellTracker dyes to assess the relative ability of two cell lines to extravasate. (**H**) Representative flow cytometry plots and relative quantification of the number of sg-*MKNK1* cells in the liver 48 hours post-injection, compared to Cas9CTL cells in the same liver. Error bars represent SEM, *n* = 7 (Cas9CTL:sg-*MKNK1*-1) 5 (Cas9CTL:sg-*MKNK1*-2). (**I**) Schematic of tail vein injection experimental design, including duration and end-point lung processing. (**J**) Tumor burden in the liver 14 days following tail vein injection of the indicated cell lines. Data are an average of scores from 4 independent examiners per sample. Error bars represent SEM, *n* = 10 per group. **For B, E, F, H and J**: one-way ANOVA with Tukey's multiple comparison test.

3.3.4 Stable isotope tracing confirms that MNK1 KO cells have reduced glycolytic activity and altered glutamine metabolism.

There is a growing appreciation that the metabolic state and flexibility of a tumor cell can dictate tissue-specific tropism as well as the success of metastatic dissemination. It therefore seemed likely that the metastasis-protective effects of MNK1 KO observed *in vivo* (*Fig. 3.3B-F*) might be due to changes in their cellular metabolism. Given the results of our multi-omics functional enrichment analyses (*Fig. 3.2E, 3.2F*), and the fact that the liver is a gluconeogenic tissue, we chose to assess functional differences in the use of glucose between MNK1 KO and Cas9CTL cells. We performed stable isotope tracer analysis (SITA) using U-[^{13}C]-glucose, pulsing cells with the labelled metabolite for 4 hours before mass spectrometry analysis (*Fig. 3.4A*). The presented data represent labelled metabolite pool sizes only, as we observed only minor differences in the fractional enrichment of ^{13}C across metabolites between groups. However, the full mass isotopomer distribution (MID) profiles for all metabolites shown are in the supplementary data (*Supp. Fig. 3.2*), in accordance with standard expression in the field. As expected, we found that

the pool sizes of U-[^{13}C]-glucose-derived pyruvate (*Fig. 3.4B*) and lactate (*Fig. 3.4C*) were lower in MNK1 KO cells compared to Cas9CTL. Interestingly, analysis of the conditioned-media revealed no difference in the secretion of labelled lactate into the media, despite reduced intracellular pools (*Fig. 3.4D*). In contrast to the glycolytic pathway, we observed largely similar TCA cycle activity across all cell lines. Both MNK1 KO and Cas9CTL cells replenish their pools of TCA intermediates principally through pyruvate dehydrogenase (citrate and malate m+2) rather than through pyruvate carboxylase and malic enzymes (citrate and malate m+3) (*Supp. Fig. 3.2D, 3.2E*). In addition, there were no differences in the pool sizes of TCA cycle intermediates citrate, malate, and aspartate (m+2) between groups (*Fig 3.4E-G*). Overall, these data suggest that MNK1 ablation reduces the glycolytic activity of 4T1 cells.

Upregulated glutamine metabolism is another key metabolic feature of transformed cells[39] and is thought to be another important substrate for CSC populations[40]. We therefore chose to perform subsequent SITA experiments using U-[^{13}C]-glutamine (*Fig. 3.4H*). We observed no consistent differences in general glutamine uptake (*Fig. 3.4I*), conversion to glutamate (*Fig. 3.4J*), or reductive carboxylation as indicated by the fractional enrichment of citrate m+5 in MNK1 KO cells compared to Cas9CTL (*Supp. Fig. 3.2I*). Although glutamine is a key anaplerotic substrate for the TCA cycle, the size of the labelled citrate (m+4) pool in MNK1 KO cells was reduced compared to Cas9CTL (*Fig. 3.4K*). Equal pool sizes of labelled malate (m+4) indicate that glutamine carbons are able to flow into the TCA cycle in all cell lines (*Fig. 3.4L*) but are diverted towards aspartate conversion, which has been identified as a limiting metabolite for tumor cell proliferation[41],

in MNK1 KO cells than in Cas9CTL (*Fig. 3.4M*). In addition, MNK1 KO cells preferentially use more U-[^{13}C]-glutamine-derived carbons than Cas9CTL for *de novo* glutathione (GSH) synthesis (*Fig. 3.4N*). This might suggest increased levels of oxidative stress in MNK1 KO cells, as reduced GSH is a vital scavenger of reactive oxygen species (ROS).

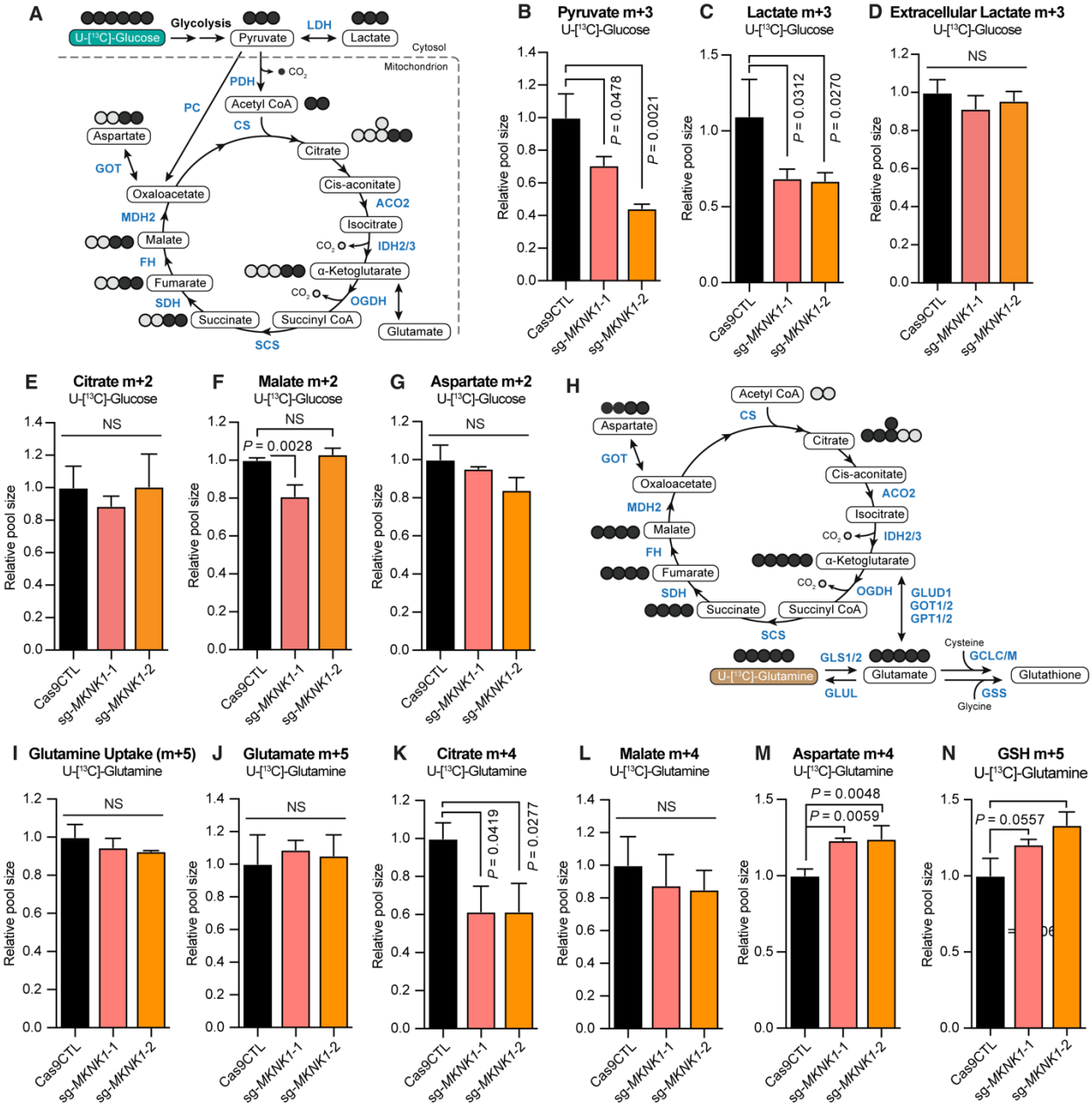

Fig. 3.4 (legend on following page)

Figure 3.4. (**A**) Stable isotope tracing diagram for U-[^{13}C]-glucose through glycolysis and into the TCA cycle via pyruvate dehydrogenase and pyruvate carboxylase. (**B-D**) U-[^{13}C]-glucose tracing

into glycolysis (pyruvate, lactate, and extracellular lactate m+3, 4-hour tracer) in the indicated cell lines expressed as relative size of the labelled pool. (**E-G**) U-[^{13}C]-glucose tracing into the TCA cycle via pyruvate dehydrogenase (citrate, malate, and aspartate m+2, 4-hour tracer) in the indicated cell lines expressed as relative size of the labelled pool. (**H**) Stable isotope tracing diagram for U-[^{13}C]-glutamine into the TCA cycle and glutathione synthesis. (**I-N**) U[^{13}C]-glutamine tracing to glutamate (glutamine uptake and glutamate m+5, 4-hour tracer) and into the TCA cycle (citrate, malate, and aspartate m+4, 4-hour tracer) or through to glutathione synthesis (GSH m+5, 4-hour tracer) in the indicated cell lines expressed as relative size of the labelled pool. **Panels B-G and I-N**: Experiments were performed in technical triplicates and repeated three times. Graphs shown correspond to one representative experiment; error bars represent SD of technical triplicates. Statistics shown were calculated for technical repeats, one-way ANOVA with Tukey's multiple comparison test.

3.3.5 Bioenergetic assessment of MNK1 KO cells reveals a dependence on oxidative phosphorylation.

There are two main mechanisms through which cells produce ATP – glycolysis and OxPhos coupled with the TCA cycle (*Fig. 3.5A*)[42]. Having confirmed reduced glycolytic activity in MNK1 KO cells (*Fig. 3.4B, 3.4C*), we hypothesized that these cells may have functionally adapted to more heavily rely on OxPhos to meet their energetic demands. We first assessed broad mitochondrial features and found that MNK1 KO cells have increased mitochondrial mass compared to Cas9CTL (*Fig. 3.5B*), as well as greater production of mitochondrial ROS (*Fig. 3.5C*). This is an expected consequence of increased mitochondrial dependence and aligns with the upregulation of GSH synthesis in MNK1 KO cells observed from our SITA experiments (*Fig. 3.4N*). In agreement with this, our proteomics data suggest MNK1 KO cells have upregulated expression of several isoforms of NADH:ubiquinone oxidoreductase (Complex I) (*Supp. Fig. 3.3A*). We next performed bioenergetic profiling of Cas9CTL and MNK1 KO cells using the Seahorse XF-bioanalyzer platform. We observed no change in the extracellular acidification rate (ECAR) of MNK1 KO and Cas9CTL cells (*Fig. 3.5D*), which was unsurprising given our

SITA results demonstrating no difference in lactate secretion into the media (*Fig. 3.4D*). Additionally, there were no differences in oxygen consumption rates (OCR) across cell lines (*Fig. 3.5E*), despite reduced glycolytic activity in MNK1 KO cells. From these findings, we interpret that both Cas9CTL and MNK1 KO 4T1 cells primarily use OxPhos to meet their energetic needs when grown under monolayer (two-dimensional) culture conditions. This may explain why MNK1 KO 4T1 cells show no proliferation defects *in vitro* (*Fig. 3.1C*), where nutrient availability is high and metabolic stress is low, but a strong repression in tumor outgrowth in the mammary fat pad and liver (*Fig. 3.1J, Fig. 3.3B-F*), where metabolic demands are more complex. Specifically, several reports across cancer types have demonstrated that metastatic tumor cells in the liver TME favour a glycolytic-dominant metabolism[30,43–45]. Thus, we next chose to assess the impact of inhibiting OxPhos on tumor cell cultures, thereby mimicking the metabolic stresses of the liver TME. MNK1 KO cells were sensitive to treatment with the ATP synthase inhibitor oligomycin, which significantly reduced cell growth, while Cas9CTL cells remained resistant to this effect (*Fig. 3.5F*). These data support the conclusion that MNK1 KO 4T1 cells have reduced metabolic flexibility and are particularly disadvantaged in an environment that favours glycolysis over OxPhos.

As MNK1/2 inhibitors are currently in clinical trials, we next chose to investigate how well our findings translate into a therapeutic context. Our team has previously shown that the inhibitors SEL201 and EFT508 effectively block MNK1/2 activity, robustly inhibiting eIF4E phosphorylation[12,13,46,47]. Western blotting confirmed that these MNKi repress MNK1/2 activity in this model, as indicated by complete repression of eIF4E

phosphorylation, without reducing MNK1 expression (*Fig. 3.5G*). We found that combination treatment of MNKi with oligomycin phenocopied our genetic MNK1 KO model, resulting in a significant reduction in tumor cell growth compared to either MNKi or oligomycin treatment alone (*Fig. 3.5H*). We repeated these assays in three human BC cell lines; T47D, MCF7 and MDA-MB-231. While baseline sensitivity to oligomycin treatment was cell line-dependent, the combination of MNKi with oligomycin resulted in the strongest repression in cell growth (*Supp. Fig. 3.3B-D*). Encouraged by these results, we investigated the efficacy of using a MNKi to target liver metastasis *in vivo*. Mice were pre-dosed with EFT508 immediately prior to intrasplenic injection of Cas9CTL 4T1 cells, followed by drug dosing until endpoint (*Supp. Fig. 3.3E*). However, EFT508 treatment alone was insufficient to reduce tumor burden in the liver, as quantified by the number of surface metastases at 21 days post-injection (*Supp. Fig. 3.3F*). We next attempted to model dual targeting of MNK1/2 and OxPhos *in vivo* by combining treatments of EFT508 and IACS-010759, a potent inhibitor of mitochondrial Complex I[48]. Unexpectedly, two-thirds of the mice dosed with IACS-010759 died, assumably due to acute drug toxicity, and the experiment was suspended (data not shown). In summary, our findings highlight changes in tumor cell metabolism as a previously unknown consequence of using MNK1/2 inhibitors, but underscore the need for additional *in vivo* studies to better understand their application in combination with other therapies.

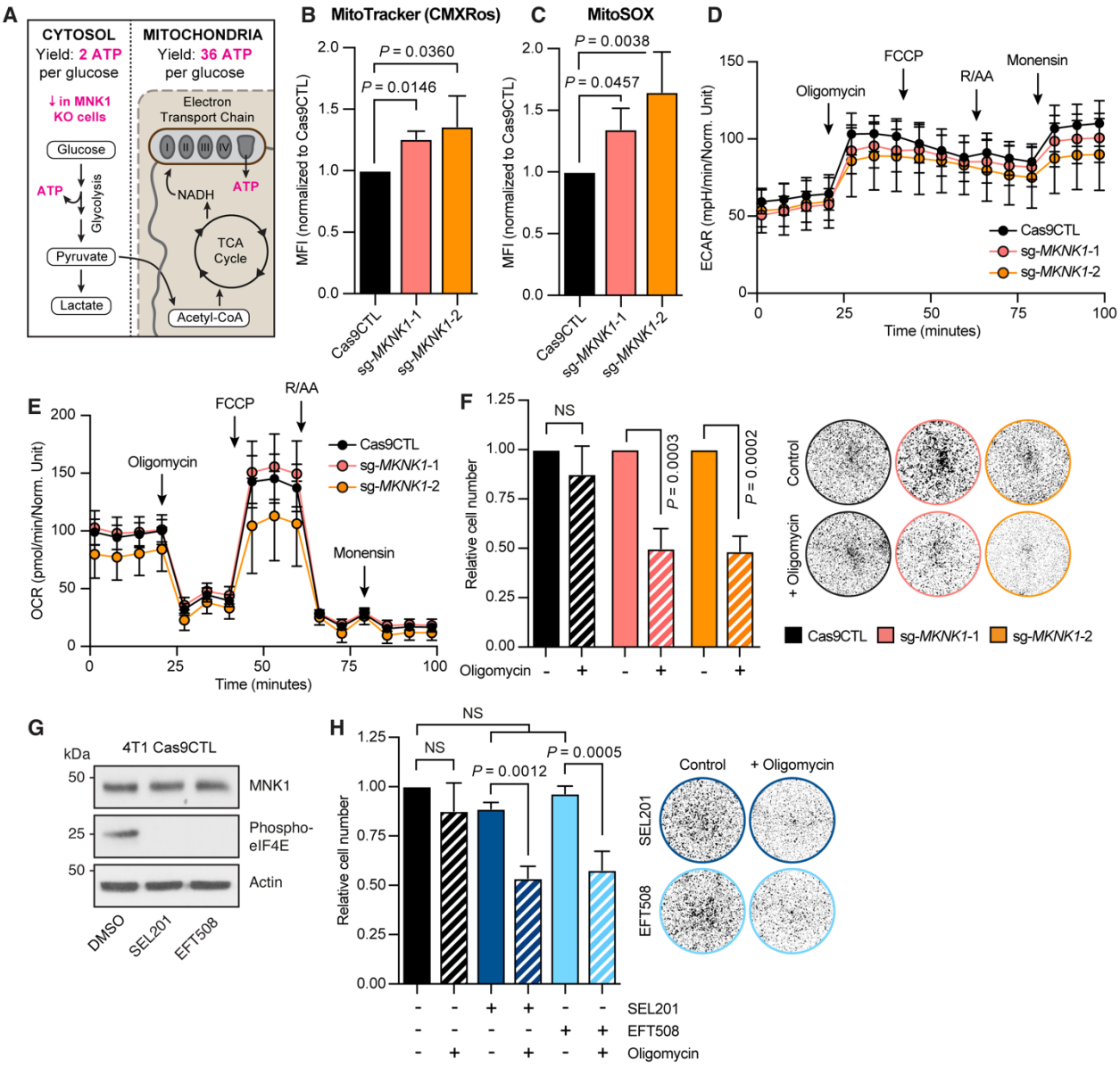

Figure 3.5. (**A**) Schematic of the two main mechanisms of cellular ATP production: glycolysis and oxidative phosphorylation coupled with the TCA cycle. (**B and C**) Average mitochondrial mass (**B**) and mitochondrial ROS levels (**C**) of the indicated cell lines as assessed by flow cytometry. Error bars represent SD, one-way ANOVA with Tukey's multiple comparison test, $n = 4$ per group. (**D and E**) Analysis of oxygen consumption rate (OCR) (**D**) and extracellular acidification rate (ECAR) (**E**) in indicated cell lines. All values are normalized to cell number per well. Experiments were performed across 30 wells per cell line and repeated twice. Data shown display one representative repeat, error bars represent SD of technical repeats. (**F**) Effect of oligomycin treatment on in vitro cell growth in the indicated conditions. Oligomycin was removed after 8 hours, and cell numbers quantified 48 hours post-treatment. Data are shown relative to a solvent control within each group. Representative images are included. Error bars represent SD, two-way ANOVA with Tukey's multiple comparison test, $n = 3$ per group. (**G**) Western blot analysis of the indicated proteins in Cas9CTL, sg-*MKNK1*-1 and sg-*MKNK1*-2 4T1 cells. (**H**) Effect of combining oligomycin, SEL201 and EFT508 on in vitro cell growth of Cas9CTL 4T1 cells. Cells receiving

MNKi treatment were dosed throughout the experiment, oligomycin was removed after 8 hours. All cell numbers were quantified at 48 hours post-oligomycin treatment and are shown relative to the no treatment group. Data for oligomycin treatment without MNKi are the same as shown in panel F. Representative images are included. Error bars represent SD, two-way ANOVA with Tukey's multiple comparison test, $n = 3$ per group

3.3.6 MNK1 protein expression correlates with glycolysis in TCGA breast cancer patient data.

Our data thus far support that tumor-intrinsic MNK1 signaling regulates glycolysis to promote liver metastasis in pre-clinical mouse models. To further study the link between MNK1 and glycolysis in human disease, we explored protein data from the PanCancer Atlas Breast Invasive Carcinoma data set deposited on TCGA. First, we stratified 102 patients by their expression of MNK1, detected by mass spectrometry, and assessed the relative expression status of other proteins involved in glycolysis, as defined by the KEGG database pathway. We observed a visible correlation between breast cancer samples with high MNK1 expression and high expression of several components of the glycolysis pathway, including LDHA, PFKP and ENO1 (*Fig. 3.6A*). Analysis of multiple hits identified by our initial proteomics screening confirmed significant positive correlations of MNK1 expression and glycolytic enzymes, with Pearson correlation coefficients ranging from 0.48 to 0.65 (*Fig. 3.6B*). Of note, largely similar correlations were found between MNK2 expression and the same enzymes (*Supp. Fig. 3.4A*). In addition, we performed single-sample GSEA projections (ssGSEA) using this protein data to calculate an enrichment score per patient independent of phenotype labelling. This score represents the relative activity level of a given biological process, rather than the expression of a subset of genes, which can then be correlated against other metrics.

Using this method, we validated that MNK1 expression is strongly correlated (coefficient = 0.40) with an ssGSEA enrichment score for glycolysis (*Fig. 3.6C*) but not OxPhos (coefficient = 0.098) (*Fig. 3.6D*). This suggests that MNK1 may regulate glycolytic activity in patients without affecting OxPhos, in line with our own pre-clinical observations reported herein. Interestingly, we observe an equally strong correlation between glycolysis enrichment scores and the expression of PDK1 (*Supp. Fig. 3.4B*), an enzyme that has been reported to facilitate the adaptation to a glycolytic dominant metabolism in liver-tropic cells[30]. Finally, although not statistically significant, overall survival of breast cancer patients can be separated based on MNK1 expression alone, with the high MNK1-expressing group having a numerically worse prognosis compared to the low MNK1 group (*Fig. 3.6E*). Taken together, these results suggest the potential clinical relevance of blocking MNK1 activity, through appropriate use of a MNK inhibitor, to modulate tumor metabolic features and target tissue-specific metabolic dependencies.

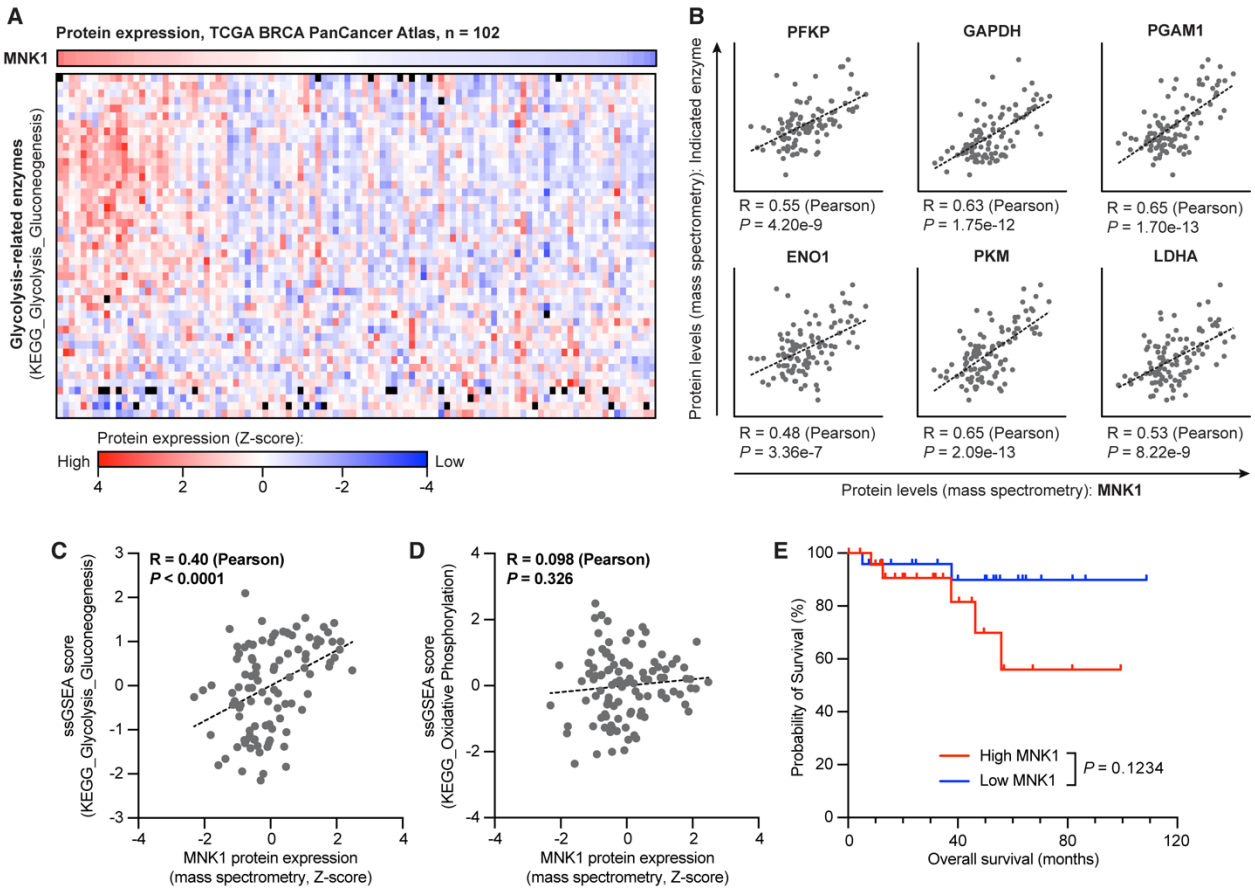

Figure 3.6. (**A**) Heatmap visualizing the relative protein expression of MNK1 and glycolysis-related enzymes, as listed in the KEGG_Glycolysis_Gluconeogenesis MSigDB gene set. Data are stratified according to MNK1 expression. Each column represents one patient, each row represents one protein/enzyme. Rows were clustered according to average linkage hierarchical clustering (**B**) Correlation of MNK1 protein expression with the protein expression of listed enzymes. Pearson rank-order, dashed lines show linear regression. *P* and r values are indicated. (**C and D**) Correlation of MNK1 protein expression with ssGSEA enrichment scores for the glycolysis/gluconeogenesis (**C**) and oxidative phosphorylation (**D**) pathways. Pearson rank-order, dashed lines show linear regression. *P* and r values are indicated. **For A-D**: *n* = 102. (**E**) Kaplan-Meier curve showing overall survival of patient with high versus low MNK1 protein expression. Log-rank (Mantel-Cox) test, *n* = 25 per group.

3.4 Discussion

CSCs are critical components of successful tumor initiation, progression, and metastasis[18–22], but our therapeutic tools for targeting these populations in secondary sites remain limited. Defining the molecular mechanisms that underpin CSC populations

is therefore critical to inspire new strategies to prevent metastasis in patients. Here, through our investigation of stemness features regulated by MNK1, we showed that targeting of MNK1 limits the metabolic flexibility of BC tumor cells by reducing glycolysis, which we validated using metabolomics and bioenergetic profiling. Importantly, we showed that this led to strongly repressed primary tumor growth *in vivo* and almost entirely abolished metastasis to the liver, but not the lung. We also observed that MNK1 expression is positively correlated with expression of the glycolytic pathway in human patient samples.

This study sheds new light on the signaling pathways that contribute to the complex changes in cellular metabolism that facilitate metastasis. The Warburg effect observes that, unlike normal cells, tumor cells ferment glucose into lactate through aerobic glycolysis, even in the presence of sufficient oxygen concentrations and functional mitochondria to support oxidative phosphorylation. Although a definitive explanation of this phenomenon remains elusive, it has been suggested that this switch to a less-efficient metabolism affords tumor cells the ability to generate biomass needed for proliferation, in addition to ATP[42]. Indeed, it is thought that BCSC populations are largely driven by high rates of glycolysis[24], at least in the primary site. One study even demonstrates that a metabolic switch from OxPhos to aerobic glycolysis is essential for the function of BCSCs and enhances tumorigenicity *in vitro* and *in vivo* by reducing the levels of reaction oxygen species to maintain β-catenin signaling, which is critical for maintenance of pluripotency[37]. This aligns with previous data that stem cells specifically rely on glycolysis as they have limited oxidative capacity due to a poorly developed

mitochondrial network[49]. The data presented here support this conclusion as MNK1 KO cells, with reduced glycolytic activity, have significantly reduced growth rates of tumorspheres *in vitro* (*Fig. 3.1E-G*) and primary tumors *in vivo* (*Fig. 3.1J*). Our knowledge of the metabolic processes that dictate metastatic success and tropism, however, are less advanced. The "Seed and Soil" theory, alongside more recent work by Schild et al.[50], proposes that specific cancer cells evolve to have distinct metabolic signatures that pre-determine their propensity to colonize a distant tissue. Furthermore, it has been suggested that only cells with metabolic flexibility, a hallmark of CSCs, have the intrinsic ability to survive in secondary sites[51]. Some studies have provided evidence for organ-specific metastatic abilities of CSC subpopulations in multiple cancers[45,52,523]. Although this study does not assess the metabolic function of CSCs specifically, we predict that the restricted metabolic flexibility caused by targeting MNK1 would be disadvantageous to CSC and non-CSC pools alike. Moreover, we show that this disadvantage is not equal across metastatic sites; inhibiting MNK1 activity more strongly reduces the ability for a given tumor cell to survive in the liver than in the lung (*Fig. 3.3B-F, 3.3J*), independent of its ability to extravasate from the vasculature (*Fig. 3.3H*).

Importantly, our analysis of protein expression data from BC patients (*Fig. 3.6*) suggests that targeting MNK1 to impact tumor cell metabolism may translate from murine to human studies. We show that genetic MNK1 KO models of BC are protected against metastatic outgrowth in the liver (*Fig. 3.3B-F*), but use of EFT508 alone was unable to phenocopy this result (*Supp. Fig. 3.3E, 3.3F*). We hypothesize that there may be unknown consequences of broadly blocking MNK activity across the TME using a MNK1/2 inhibitor,

as opposed to the more specific tumor-intrinsic targeting of our genetic model. In particular, we do not know how blocking MNK pharmacologically will impact the cooperative metabolic networks that exist between cell types of the TME[54]. Further research is required to better understand these interactions. However, we have shown *in vitro* that blocking MNK1 increases tumor cell sensitivity to the OxPhos inhibitor oligomycin, and that treatment with both metabolic inhibitors significantly reduces tumor cell growth in multiple breast cancer cell lines (*Fig. 3.5F, 3.5H and Supp. Fig. 3.3B-D*). It may therefore be necessary to combine a MNKi with an OxPhos inhibitor to adequately restrict metabolic flexibility of tumor cells *in vivo*, even in the liver microenvironment. We propose this novel drug combination as a potential strategy to target metastases across tissues with distinct metabolic requirements by simultaneously impacting the two primary mechanisms of ATP production. This is a crucial target in metastasizing tumor cells as sufficient ATP generation is emerging as a critical threshold for successful cell seeding[55]. MNKi are well-tolerated in patients and currently under clinical investigation across cancer types and treatment modalities (NCT04261218, NCT03690141, NCT04622007). Several drugs targeting aspects of mitochondrial metabolism are either already FDA-approved or in clinical trials, including metformin[56,57] and atovaquone[58]. However, clinical benefit of these inhibitors is yet to be achieved in the context of oncology. We performed preliminary studies *in vivo* using combined treatment of EFT508 and the Complex I inhibitor IACS-010759, which had been advanced into Phase I clinical trials at the time (NCT02882321 and NCT03291938). These trials were recently discontinued due to emerging dose-limiting toxicities, including neuropathy in approximately 50% of patients and physiological

changes indicative of neuropathy in mice[59]. This matches our observations that IACS-010759 led to signs of toxicity in our mouse models. Future studies are therefore needed to assess how to effectively combine MNKi with OxPhos inhibition, and to determine what stage of the metastatic cascade these drugs could be applied for clinical benefit.

One question that remains unanswered in our study is: by what mechanism does blocking MNK1 downregulate glycolysis? Although eIF4E is the only validated substrate for MNK1/2 kinases, we do not formally assess whether the phenotypes we observe are a consequence of altered translational control by phospho-eIF4E. It is conceivable that there may be eIF4E-independent effects of modulating MNK expression and/or activity that the field is unaware of. Moreover, a translationally-mediated mechanism may exist either directly or indirectly. Phospho-eIF4E may regulate the translation of glycolytic enzymes themselves, or of an upstream mediator such as HIF1α, as was emphasized by our proteomics data (*Fig. 3.2F*). Interestingly, the EMT-associated protein Snail, known to be under translational control of phospho-eIF4E[10], has been shown to silence the promoter of *FBP1*, resulting in an induction of glycolysis and CSC-like properties in basal-like BC[37]. Future studies should be carried out to understand which of these mechanisms, if any, are at play in our models. Regardless, this work contributes new findings to an ever-expanding body of literature that highlights translational machinery as a central node for regulating energetic balance and cellular metabolism[60–64].

Ultimately, this study upholds the viability or pursing metabolic pathways as targets to reduce metastasis. We have gained an increased understanding of the contribution that MNK1 kinase plays in controlling BCSC populations, while further identifying reduced

glycolysis as a previously unknown functional consequence of targeting MNK1/2. Better understanding of the metabolic dependencies of metastatic BC cells in tissue-specific microenvironments may prove useful in identifying vulnerabilities that can be exploited, through use of a MNKi, to improve therapeutic efficacy.

3.5 Experimental Procedures

Cell culture and treatments

4T1 cells were kindly donated by Dr. Peter Siegel (McGill University) and cultured in DMEM High Glucose (Wisent Bio Products) supplemented with 10% FBS, 1.5 g/L sodium bicarbonate,10 mM HEPES, and antibiotics. MCF7, T47D and MDA-MB-231 cell lines were purchased from ATCC and cultured in DMEM High Glucose (Wisent Bio Products) supplemented with 10% FBS and antibiotics. Cells were sub-cultured upon reaching approximately 90% confluence by trypsinization and subsequent dilution. Cell lines were maintained at low passage number prior to use, and viability was determined via trypan blue exclusion. For all cell treatments, drugs were supplemented into complete growth media at the indicated concentrations. SEL201 was provided by Selvita and used at 2.5 μM. EFT508 (Tomivosertib) was purchased from Selleckchem (#S8275) and used at 1 μM. Oligomycin was purchased from MP Biomedicals (#151786) and used at 1 μM. For tumorsphere culture: cell lines were trypsinized, dissociated into single cells, and seeded in ultra-low adherence 6 well plates (Corning, #3471) at 5000 cells per well. Brightfield images were captured at 5 days post-seeding. Tumorsphere number and size were quantified using ImageJ.

Generation of MNK1 knock-out cell lines

CRISPR-mediated MNK1 KO cell lines were generated as previously described[17]. In summary, parental 4T1 cells were transfected with Cas9-GFP/sgRNA plasmids. 48 hours post-transfection, GFP^+ cells (transient fluorescence) were single-cell sorted by FACS and expanded in culture. The resulting clones were screened for absent expression of MNK1 by Western blot, and selected clones were further validated by Sanger sequencing of genomic DNA. Two clones were selected for follow-up investigation *in vitro* and *in vivo*, termed sg-*MKNK1*-1 and sg-*MKNK1*-2. A sgRNA-null control cell line was generated using the same transfection protocol with the Cas9-GFP plasmid only, termed Cas9CTL. Where indicated, a pool of 5 sg-*MKNK1* clones were combined together in equal proportions (20% of the total cell population per clone). Plasmids and sgRNA constructs were purchased from GenScript, using the pSpCas9 BB-2A-GFP (PX458) vector. Two CRISPR guide RNA sequences were designed to target murine *MKNK1*: TCGAAGTCGAGTGTTCCGTG and GACGTCCCGCACCACTCTAC.

Mouse model and orthotopic mammary fat pad injection

Wild-type female BALB/c mice were purchased from Charles River Laboratories (Saint-Constant, Canada) and subsequently bred in-house. All tumor cell injections were performed on mice approximately 8 weeks of age. Animal experiments were conducted according to the regulations established by the Canadian Council of Animal Care, using protocols approved by the McGill University Animal Care and Use Committee. For

orthotopic injections: 2 x 10^5 4T1 cells (Cas9CTL, sg-*MKNK1*-1 and sg-*MKNK1*-2) were suspended in PBS and injected into the inguinal mammary fat pad of mice. Tumor initiation was measured as the number of days post-injection at which a palpable mass had formed. Tumor length (L) and width (W) were routinely measured over time, with tumor volume calculated using the formula $V=3.1416/6*L*W^2$. At 25 days post-injection, mice were euthanized and primary tumors were excised, formalin-fixed, and paraffin embedded (FFPE). For the limiting dilution experiment: serially diluted concentrations (2 x 10^5, 2 x 10^4, 2 x 10^3) of Cas9CTL, sg-*MKNK1*-1 or sg-*MKNK1*-2 4T1 cells were suspended in PBS and injected into the inguinal mammary fat pad of mice. Tumors were allowed to form for 8 weeks post-injection. Mice were considered as engrafted upon the formation of a palpable mass.

Experimental metastasis mouse models: intrasplenic and tail vein injections

Intrasplenic injections (with splenectomy) were used to model experimental liver metastasis. Mice were anaesthetized, hair on the left flank removed, and a small incision made in the skin and peritoneum below the ribcage. 1 x 10^5 4T1 cells (Cas9CTL, sg-*MKNK1*-1 or sg-*MKNK1*-2) were suspended in PBS and injected directly into the spleen using a 26-gauge needle. Cells travel via the splenic vein and hepatic portal vein directly to the liver. Following injection, vasculature connecting the spleen and the pancreas was ligated using nonabsorbable braided silk suture (FST, #18020-60). Vessels were subsequently cut and the spleen removed – this is necessary to prevent the formation of a primary splenic tumor. The peritoneum was then sutured shut and the skin closed using

wound clips. Mouse body weight was monitored every 3 to 4 days, before being euthanized at 21 days post-injection. At endpoint, the number of metastases visible on the liver surface were quantified before FFPE processing. Mice with extrahepatic metastases were excluded from the study. For survival cohorts: mice were euthanized upon signs of moribundity or a 20% drop in bodyweight, whichever presented first. For treatment cohorts: mice were randomly grouped prior to treatment. EFT508 was dissolved in a solution of 10% 1-methyl-2-pyrrolidinone and 90% propylene glycol, with 1 equivalent of HCl, for administration by oral gavage at a dose of 10 mg/kg bodyweight per mouse, 5 times per week. The first dose was administered approximately 1 hour prior to intrasplenic injection. Tail vein injections were used to model experimental lung metastasis; 1 x 10^5 4T1 cells (Cas9CTL, sg-*MKNK1*-1 or sg-*MKNK1*-2) were injected into the tail vein of each mouse. At 14 days post-injection, mice were euthanized, lungs were excised and dissociated into single cells using the gentleMACS Octo Dissociator (Miltenyi Biotech, #130-096-427). Cell suspensions were cultured in the presence of 30 μM 6-thioguanine (Sigma-Aldrich, #A4660); these conditions are toxic to cells other than the naturally resistant 4T1. After 5 days, remaining 4T1 colonies were fixed with 4% PFA for 15 min at room temperature, stained with 0.5% crystal violet for 30 min at room temperature, and metastatic burden scored by four independent individuals.

In vivo seeding competition assay

4T1 cells (Cas9CTL, sg-*MKNK1*-1 or sg-*MKNK1*-2) were labelled using CellTrace Violet (Invitrogen, #34571) or Far Red (Invitrogen, #C34564) dyes according to

manufacturer instructions prior to intrasplenic injection. Each mouse received a total of 1 x 10^6 cells comprised of one MNK1 KO clone and Cas9CTL cell lines at a 1:1 ratio, with each cell line labelled using a different colour of CellTrace dye. At 48 hrs post-injection, mice were euthanized and the liver perfused via the hepatic portal vein with 15 mL of cold PBS. Following this, livers were excised and single-cell dissociated using the gentleMACS Octo Dissociator (Miltenyi Biotech, #130-096-427). Cell suspensions were then analyzed on an LSR Fortessa (BD) for the presence of fluorescent tumor cells.

RNA sequencing and analysis

RNA was isolated form Cas9CTL, sg-*MKNK1*-1 and sg-*MKNK1*-2 pellets in quadruplicate using the Absolutely RNA Miniprep Kit (Agilent, #400800). RNA concentration and quality was assessed using a BioAnalyzer (Agilent). Library preparation was performed using the KAPA mRNA HyperPrep kit (Roche). Samples were sequenced on a Nextseq HighOutput 2x75bp flow cell with a yield of approximately 20M single-end reads per sample. FASTQ data was normalized using the Nextflow nf-core pipeline (DOI: 10.5281/zenodo.1400710) and expressed as log-transformed counts per million reads mapped ($\log_{10}$CPM). The DEseq2 package was used to identify differentially expressed genes by calculating the fold change in $\log_{10}$CPM values between MNK1 KO (sg-*MKNK1*-1 or sg-*MKNK1*-2) and Cas9CTL cells using default settings. Results were then filtered based on fold change (greater than 2 in either direction) and adjusted p-value (less than 0.05). *P*-values were calculated using the Wald test with FDR/Benjamini-Hochberg multiple comparison test. Functional enrichment analyses were performed on

pre-ranked fold change data using gene set enrichment analysis software (version 4.1.0) and the KEGG molecular signature database.

Preparation of cell lines for proteome analysis

Quadruplicates of 4T1 Cas9CTL and MNK1 KO (sg-*MKNK1*-2 and sg-*MKNK1*-2) cell lines were lysed by the addition of 100 μL of lysis buffer containing 5% SDS in 100 mM TRIS pH 8.5 and heating the samples (95 °C) for 10 minutes. Samples were consequently subjected to probe based ultrasonication (Thermo Sonic Dismembrator), and clarified by centrifugation at 21,000 x g for 5 minutes. 5% of the resulting extract was reserved for the determination of protein concentration using bicinchonic acid assay (BCA) (Thermo/Pierce). The remainder of the cell lysates were reduced in 20 mM tris(2-carboxyethyl)phosphine for 30 minutes at 60 °C, and alkylated in 25 mM iodoacetamide for 30 minutes in the dark at room temperature. 50 μg of protein was proteolytically digested with trypsin (Promega, sequencing grade) overnight at 37°C using S-TRAP micro cartridges (Protifi). Peptides were eluted from S-TRAP micro cartridges sequentially with 50 mM ammonium bicarbonate, 0.2% formic acid, and 50% acetonitrile respectively. Peptide-containing eluates were frozen at -80 °C and lyophilized to dryness using a vacuum centrifuge (Labconco). Peptide samples were reconstituted in 0.1% formic acid, to a final concentration of 150 ng/μL.

LC-MS/MS data acquisition and analysis

An equivalent of 1 μg of protein was analyzed by nanoflow LC-MS/MS using an Easy-nLC 1200 system coupled to a Q Exactive Plus (both Thermo Fisher Scientific). Samples were first loaded onto a pre-column (Acclaim PepMap 100 C18, 3 μm, 75 μm ID x 2 cm length, Thermo Fisher Scientific) for online desalting, and then separated using a 100 minute gradient with an Acclaim PepMap 100 C18 analytical column (2 μm particle, 75 μm ID x 250 mm, Thermo Fisher Scientific) using water with 0.1% formic acid (mobile phase A) and 84% acetonitrile with 0.1% formic acid (mobile phase B) at 300 nL/min from 3-40 %B. MS acquisition was conducted in data dependent acquisition mode (DDA), based on the top 15 most intense precursor ions (+2 to +4 charge state). Full MS scans were acquired at 70K resolution from 350 – 1500 m/z (AGC 1E6, 50ms max injection time), and MS2 spectra were collected at 17.5K resolution (AGC 2E4, 64ms max injection time) using a normalized collision energy (NCE) of 28. Dynamic exclusion was set to 40 sec. Acquired MS/MS data were analyzed using Proteome Discoverer (PD) version 2.5 (Thermo Fisher Scientific). Database searching was conducted using the Sequest HT node, using a reference mouse proteome FASTA file containing only reviewed canonical sequences downloaded from Uniprot (downloaded February 28th, 2019). Label free quantitation was conducted using the Minora feature detection node. Proteins were quantified based on unique peptides, scaled based on total peptide abundance, and missing values were imputed using the low abundance resampling method. Protein expression ratios were calculated based on protein abundance, and p-values were calculated using ANOVA (individual proteins) within PD 2.5. Only proteins quantified with

at least 1 protein unique peptide in 3 out of 4 biological replicates from at least one sample group were retained. Statistical significance of differentially expressed proteins was based on a 2-sigma fold-change cut-off (effectively 2-fold change), as well as having an FDR adjusted p-value less than 0.05. Statistically differentially expressed proteins were used an input for canonical pathway enrichment analysis using Ingenuity Pathway Analysis software (Qiagen).

Metabolomics

For each biological replicate, 4T1 Cas9CTL and MNK1 KO (sg-*MKNK1*-1 and sg-*MKNK1*-2) cells were seeded at 62,500 cells per well in technical triplicate in a 6-well tissue culture treated plate (Corning) and cultured in 4T1 complete media (defined above). The following day, cells were examined, media was aspirated, replaced with fresh media, and incubated for another 20h. Next, media for ^{13}C-[U] glucose (Cambridge Isotopes) tracing was prepared using a base media of 1X DMEM (Wisent, #319-062) subsequently supplemented with sodium pyruvate, glutamine, HEPES and sodium bicarbonate to concentrations equivalent to 4T1 complete media. Next a 5X (125 mM) solution of ^{13}C-[U] glucose was prepared by dissolving [U]-^{13}C-glucose in the supplemented 1X DMEM media. 4T1 complete media was then aspirated from all wells and replaced with 2 mL of supplemented 1X DMEM media, while 0.5 mL of 5X [U]-13C glucose was added overtop, giving a final concentration of 25 mM, and incubated (or traced) at 5% CO2, 37°C for 4 hours. Two wells of unlabeled controls were seeded for each cell line, which contained 2 mL of supplemented 1X DMEM media, and 0.5 mL of

5X 12C glucose at a final concentration of 25 mM and incubated as above for 4h. In addition, to normalize downstream metabolomic intensity values to cell number, 3 wells per cell line were seeded in 4T1 complete media and counted at the experimental endpoint. To prepare the cells for metabolomic profiling, after 4h incubation, plates were immediately placed overtop ice and media aspirated. Next, wells were washed twice with 1 mL of 0.9% saline. Following saline aspiration, plates were placed over dry ice for 5 minutes, wrapped in aluminum foil and immediately placed in -80 °C. Cells were lysed and processed using the stable isotope labeling and metabolomics method published in Kaymak et al. (2022)[65].

Seahorse bioenergetic profiling

Prior to bioenergetic profiling using the seahorse Mitostress test kit (Agilent Technologies), 4T1 Cas9CTL and MNK1 KO (sg-*MKNK1*-1 and sg-*MKNK1*-2) cells were seeded at 5000 cells per well in a 96-well Seahorse XFe96 FluxPak plate (Agilent Technologies) and incubated with 80 μL of DMEM (see conditions above) for 24h in 5% CO_2, 37°C incubator until approximately 70% confluence was reached. In addition, 24h prior to bioenergetic profiling, the Seahorse flux assay kit was calibrated with 200 μL of Milli-Q water (Millipore) and left in a non-CO_2, 37°C incubator for 24h. The following day, seeded cells were examined for appropriate confluence, 80 μL DMEM culture media was gently removed using a multi-channel pipette, and replaced with 140 μL of SFX assay medium: SFX DMEM base media (Agilent technologies), supplemented with 1 mM Sodium Pyruvate, 2 mM glutamine, 10 mM glucose (final concentrations), pH 7.4 (at

37°C). In addition, water was removed from the flux assay kit and replaced with Seahorse XF calibrant solution (Agilent technologies) and incubated at 37°C (non-CO_2) for 2-3h hours prior to conducting bioenergetic profiling. During the 2-3h incubation, Mitostress test kit drugs: oligomycin, Carbonyl cyanide-4 (trifluoromethoxy) phenylhydrazone (FCCP), Rotenone/Antimycin A (R/AA) and Monensin were dissolved in SFX assay medium to working concentrations of 16, 9, 5 and 220 μM, respectively. Next, 20 μL of each drug was pipetted into injection ports A,B,C, and D, respectively. Final drug concentrations of oligomycin, FCCP, R/AA and Monensin were 2, 1, 0.5 and 20.1 μM, respectively. Following the 2-3h incubation of the extracellular flux assay kit, probes were calibrated in the Seahorse bioanalyzer. After, the flux assay kit was replaced, with the 96 well plate containing Cas9CTL and MNK KO cells, while the drugs within ports remained in the machine. Oligomycin, FCCP, Rotenone/Antimycin A and Monensin were automatically injected overtop cells at 20, 40, 60 and 80 minutes, respectively. Oxygen consumption rate (OCR) and extracellular acidification rate (ECAR) were both measured. OCR and ECAR values were normalized to cell number based on crystal violet staining and absorption at 595 nm following solubilization.

Histology and immunohistochemistry (IHC)

Following FFPE-processing, all samples were sectioned at 4 *μ*m thickness according to staining requirements. Tumor-bearing livers were step-sectioned (2 steps, 200 *μ*m between steps) for subsequent staining with hematoxylin and eosin (H&E) as previously described[17]. IHC stainings were performed on primary tumor and tumor-

bearing liver tissues. Slides were deparaffinized, rehydrated and subjected to heat-induced antigen retrieval. Endogenous peroxidase activity was quenched for 15 min in 10% hydrogen peroxide, and tissues were blocked in 10% donkey serum (Jackson ImmunoResearch, #017-000-121). Tissues were then stained with an antibody specific to MNK1 (tumors; 1:50 dilution). Stainings were visualized using ImmPACT DAB (Vector Laboratories, #SK-4105) and counter-stained with Harris-modified hematoxylin (EMD Millipore, #638A-85). All stained slides were imaged using a Zeiss AxioScan.Z1 slide scanner and analyzed using QuPath version 0.2.3. See Supplementary Table 3.1 for antibody details.

Immunoblotting

Immunoblotting was performed as previously detailed[15]. Briefly, protein lysates were isolated from cell pellets using RIPA buffer (150 mmol/L Tris-HCl pH 7, 150 mmol/L NaCl, 1% NP-40, 1% sodium deoxycholate, 0.1% sodium dodecyl sulfate). Protein concentrations were measured by Bradford reagent assay (Bio-Rad), separated on a 10% SDS-PAGE gel, and transferred to nitrocellulose membranes. Membranes were blocked in 5% non-fat milk and incubated in primary antibody dilutions overnight at 4 °C. The following day, membranes were incubated with secondary antibody at room temperature for 1 hr. Membranes were then revealed using ECL Prime Western Blotting Detection Reagent (Amersham) and Ultra-High Contrast Western Blotting film. Antibody information is listed in Supplementary Table 3.1.

Cell proliferation growth curves

4T1 cells (Cas9CTL, sg-*MKNK1*-1 and sg-*MKNK1*-2) were serum-starved for 16 hours prior to seeding in 96 well plates at a density of 1000 cells per well. At 24 hr intervals, up to 96 hr post-seeding, cells were fixed in 4% paraformaldehyde (PFA) for 15 min at room temperatures and stored in 0.4% PFA. Fixed cells were stained with 0.5% crystal violet at endpoint for 30 min at room temperature. The following day, crystal violet was dissolved in 10% acetic acid and absorbance was measured at 590 nm using a plate reader. Cell proliferation over time was calculated relative to a standard curve of known cell number.

Mitochondrial assessment by flow cytometry

4T1 cells (Cas9CTL, sg-*MKNK1*-1 or sg-*MKNK2*-1) were trypsinized, centrifuged at 300 x g for 5 min, and washed in PBS. 1 x 10^5 cells were stained with 1 μM MitoSOX mitochondrial superoxide indicator (Invitrogen, #M36008) or 200 nM MitoTracker CMXRos (Invitrogen, #M7512) according to manufacturer directions. After staining, cells were rinsed once in PBS and fluorescence was assessed on an LSR Fortessa (BD).

Aldefluor assay

ALDH activity was measured according to ALDEFLUOR Kit instructions (StemCell Technologies, #01700). Briefly, 1 x 10^6 cells were suspended in the provided buffer and incubated with 1.5 μM BODIPY-aminoacetaldehyde for 30 min at 37 °C. Using this protocol, ALDH activity is proportional to cellular fluorescence, as measured using an

LSR Fortessa (BD). Background fluorescence was accounted for by treating cells with 15 μM diethylaminobenzaldehyde, a selective inhibitor of ALDH (negative control). Data were analyzed using FlowJo version 10.7.1.

Analysis of publicly-available TCGA patient data

The TCGA Breast Invasive Carcinoma PanCancer Atlas database was accessed through cBioPortal. Analysis was limited to only patients for whom MNK1 protein expression Z-score and overall survival data was available (n = 102). Protein expression data was isolated for all hits within the KEGG_Glycolysis_Gluconeogenesis molecular signature and for MNK1. ssGSEA was subsequently performed according to methodology described in Barbie et al. (2009)[66], using KEGG_Glycolysis_Gluconeogenesis and KEGG_Oxidative_Phosphorylation gene sets. Pearson rank-order calculations were performed to correlate MNK1 protein expression with individual proteins of interest and ssGSEA enrichment scores. Analysis of overall survival data was performed on the highest and lowest quartile of patients when ranked by MNK1 protein expression.

Statistics

Prism 9 software (GraphPad) was used to perform statistical testing. Details of the statistical testing performed for all relevant figure panels can be found in figure legends. P-values for the differences of means between groups were calculated using unpaired t-tests, one-way ANOVA, two-way ANOVA and Pearson rank-order correlations, with

multiple comparison tests as appropriate. P-values less than 0.05 were considered statistically significant.

3.6 Data availability

Data supporting the findings of this study are available within the manuscript and its supplementary material. Full omics datasets and functional enrichment analyses are available from the authors upon reasonable request.

3.7 Acknowledgements

The authors wish to thank Jennifer Huber, the IRIC Next Generation Sequencing Core Facility (Université de Montréal), the IRIC Histology Core Facility (Université de Montréal), Dr. Naciba Benlimame and Lilian Canetti for their technical support. We extend our gratitude to Kathy Ann Forner and Véronique Michaud for their expertise and assistance in developing animal models.

3.8 References

1. Bray, F. *et al.* Global cancer statistics 2018: GLOBOCAN estimates of incidence and mortality worldwide for 36 cancers in 185 countries. *CA. Cancer J. Clin.* **68**, 394–424 (2018).
2. American Cancer Society. *Cancer Facts & Figures 2020*. (2020).
3. Zhao, H.-Y., Gong, Y., Ye, F.-G., Ling, H. & Hu, X. Incidence and prognostic factors of patients with synchronous liver metastases upon initial diagnosis of breast cancer: a population-based study. *Cancer Manag. Res.* **10**, 5937–5950 (2018).
4. Chu, J., Cargnello, M., Topisirovic, I. & Pelletier, J. Translation Initiation Factors: Reprogramming Protein Synthesis in Cancer. *Trends Cell Biol.* **26**, 918–933 (2016).
5. Lazaris-Karatzas, A., Montine, K. S. & Sonenberg, N. Malignant transformation by a eukaryotic initiation factor subunit that binds to mRNA 5' cap. *Nature* **345**, 544–547

(1990).
6. Waskiewicz, A. J., Flynn, A., Proud, C. G. & Cooper, J. A. Mitogen-activated protein kinases activate the serine/threonine kinases Mnk1 and Mnk2. *EMBO J.* **16**, 1909–1920 (1997).
7. Waskiewicz, A. J. *et al.* Phosphorylation of the cap-binding protein eukaryotic translation initiation factor 4E by protein kinase Mnk1 in vivo. *Mol. Cell. Biol.* **19**, 1871–1880 (1999).
8. Topisirovic, I., Ruiz-Gutierrez, M. & Borden, K. L. B. Phosphorylation of the eukaryotic translation initiation factor eIF4E contributes to its transformation and mRNA transport activities. *Cancer Res.* **64**, 8639–8642 (2004).
9. Furic, L. *et al.* eIF4E phosphorylation promotes tumorigenesis and is associated with prostate cancer progression. *Proc. Natl. Acad. Sci. U. S. A.* **107**, 14134–14139 (2010).
10. Robichaud, N. *et al.* Phosphorylation of eIF4E promotes EMT and metastasis via translational control of SNAIL and MMP-3. *Oncogene* **34**, 2032–2042 (2015).
11. Robichaud, N. *et al.* Translational control in the tumor microenvironment promotes lung metastasis: Phosphorylation of eIF4E in neutrophils. *Proc. Natl. Acad. Sci. U. S. A.* **115**, E2202–E2209 (2018).
12. Guo, Q. *et al.* The MNK1/2-eIF4E Axis Supports Immune Suppression and Metastasis in Postpartum Breast Cancer. *Cancer Res.* **81**, 3876–3889 (2021).
13. Huang, F. *et al.* Inhibiting the MNK1/2-eIF4E axis impairs melanoma phenotype switching and potentiates antitumor immune responses. *J. Clin. Invest.* **131**, (2021).
14. Bartish, M. *et al.* MNK2 governs the macrophage antiinflammatory phenotype. *Proc. Natl. Acad. Sci. U. S. A.* **117**, 27556–27565 (2020).
15. Preston, S. E. J. *et al.* Phosphorylation of eIF4E in the stroma drives the production and spatial organisation of collagen type I in the mammary gland. *Matrix Biol.* **111**, 264–288 (2022).
16. Carter, J. H. *et al.* Phosphorylation of eIF4E serine 209 is associated with tumour progression and reduced survival in malignant melanoma. *Br. J. Cancer* **114**, 444–453 (2016).
17. Guo, Q. *et al.* MNK1/NODAL Signaling Promotes Invasive Progression of Breast Ductal Carcinoma In Situ. *Cancer Res.* **79**, 1646–1657 (2019).
18. Ricardo, S. *et al.* Breast cancer stem cell markers CD44, CD24 and ALDH1: expression distribution within intrinsic molecular subtype. *J. Clin. Pathol.* **64**, 937–946 (2011).
19. Rabinovich, I. *et al.* Cancer stem cell markers ALDH1 and CD44+/CD24- phenotype and their prognosis impact in invasive ductal carcinoma. *Eur. J. Histochem.* **62**, (2018).
20. Albini, A. *et al.* Cancer stem cells and the tumor microenvironment: interplay in tumor heterogeneity. *Connect. Tissue Res.* **56**, 414–425 (2015).
21. Clevers, H. The cancer stem cell: premises, promises and challenges. *Nat. Med.* **17**, 313–319 (2011).
22. Lin, C.-Y., Barry-Holson, K. Q. & Allison, K. H. Breast cancer stem cells: are we ready to go from bench to bedside? *Histopathology* **68**, 119–137 (2016).
23. Zhang, X., Powell, K. & Li, L. Breast Cancer Stem Cells: Biomarkers, Identification and Isolation Methods, Regulating Mechanisms, Cellular Origin, and Beyond. *Cancers (Basel).* **12**, (2020).
24. Sancho, P., Barneda, D. & Heeschen, C. Hallmarks of cancer stem cell metabolism. *Br. J. Cancer* **114**, 1305–1312 (2016).
25. Bartlome, S. & Berry, C. C. Recent insights into the effects of metabolism on breast cancer cell dormancy. *Br. J. Cancer* **127**, 1385–1393 (2022).
26. Chen, K. *et al.* The metabolic flexibility of quiescent CSC: implications for chemotherapy resistance. *Cell Death Dis.* **12**, 835 (2021).

27. Yadav, U. P. *et al.* Metabolic Adaptations in Cancer Stem Cells . *Frontiers in Oncology* vol. 10 (2020).
28. Lim, S. *et al.* Targeting of the MNK-eIF4E axis in blast crisis chronic myeloid leukemia inhibits leukemia stem cell function. *Proc. Natl. Acad. Sci. U. S. A.* **110**, E2298-307 (2013).
29. Bell, J. B. *et al.* MNK Inhibition Disrupts Mesenchymal Glioma Stem Cells and Prolongs Survival in a Mouse Model of Glioblastoma. *Mol. Cancer Res.* **14**, 984–993 (2016).
30. Dupuy, F. *et al.* PDK1-Dependent Metabolic Reprogramming Dictates Metastatic Potential in Breast Cancer. *Cell Metab.* **22**, 577–589 (2015).
31. Davis, R. T. *et al.* Transcriptional diversity and bioenergetic shift in human breast cancer metastasis revealed by single-cell RNA sequencing. *Nat. Cell Biol.* **22**, 310–320 (2020).
32. Elia, I. *et al.* Breast cancer cells rely on environmental pyruvate to shape the metastatic niche. *Nature* **568**, 117–121 (2019).
33. Ferraro, G. B. *et al.* Fatty acid synthesis is required for breast cancer brain metastasis. *Nat. Cancer* **2**, 414–428 (2021).
34. Mani, S. A. *et al.* The epithelial-mesenchymal transition generates cells with properties of stem cells. *Cell* **133**, 704–715 (2008).
35. Ginestier, C. *et al.* ALDH1 is a marker of normal and malignant human mammary stem cells and a predictor of poor clinical outcome. *Cell Stem Cell* **1**, 555–567 (2007).
36. Folmes, C. D. L. *et al.* Somatic Oxidative Bioenergetics Transitions into Pluripotency-Dependent Glycolysis to Facilitate Nuclear Reprogramming. *Cell Metab.* **14**, 264–271 (2011).
37. Dong, C. *et al.* Loss of FBP1 by Snail-Mediated Repression Provides Metabolic Advantages in Basal-like Breast Cancer. *Cancer Cell* **23**, 316–331 (2013).
38. Yuen, C. A., Asuthkar, S., Guda, M. R., Tsung, A. J. & Velpula, K. K. Cancer stem cell molecular reprogramming of the Warburg effect in glioblastomas: a new target gleaned from an old concept. *CNS Oncol.* **5**, 101–108 (2016).
39. DeBerardinis, R. J. *et al.* Beyond aerobic glycolysis: transformed cells can engage in glutamine metabolism that exceeds the requirement for protein and nucleotide synthesis. *Proc. Natl. Acad. Sci. U. S. A.* **104**, 19345–19350 (2007).
40. Liao, J. *et al.* Regulation of stem-like cancer cells by glutamine through β-catenin pathway mediated by redox signaling. *Mol. Cancer* **16**, 51 (2017).
41. Garcia-Bermudez, J. *et al.* Aspartate is a limiting metabolite for cancer cell proliferation under hypoxia and in tumours. *Nat. Cell Biol.* **20**, 775–781 (2018).
42. Vander Heiden, M. G., Cantley, L. C. & Thompson, C. B. Understanding the Warburg effect: the metabolic requirements of cell proliferation. *Science* **324**, 1029–1033 (2009).
43. Li, J. *et al.* CircRPN2 Inhibits Aerobic Glycolysis and Metastasis in Hepatocellular Carcinoma. *Cancer Res.* **82**, 1055–1069 (2022).
44. Zhao, S. *et al.* LncRNA MIR17HG promotes colorectal cancer liver metastasis by mediating a glycolysis-associated positive feedback circuit. *Oncogene* **40**, 4709–4724 (2021).
45. Nimmakayala, R. K. *et al.* Metabolic programming of distinct cancer stem cells promotes metastasis of pancreatic ductal adenocarcinoma. *Oncogene* **40**, 215–231 (2021).
46. Zhan, Y. *et al.* MNK1/2 inhibition limits oncogenicity and metastasis of KIT-mutant melanoma. *J. Clin. Invest.* **127**, 4179–4192 (2017).
47. Yang, W. *et al.* MNK1 signaling induces an ANGPTL4-mediated gene signature to drive melanoma progression. *Oncogene* **39**, 3650–3665 (2020).
48. Tsuji, A., Akao, T., Masuya, T., Murai, M. & Miyoshi, H. IACS-010759, a potent inhibitor of glycolysis-deficient hypoxic tumor cells, inhibits mitochondrial respiratory complex I

through a unique mechanism. *J. Biol. Chem.* **295**, 7481–7491 (2020).
49. Facucho-Oliveira, J. M., & St John, J. C. The relationship between pluripotency and mitochondrial DNA proliferation during early embryo development and embryonic stem cell differentiation. *Stem Cell Rev. Rep.* **5**, 140-58 (2009).
50. Schild, T., Low, V., Blenis, J. & Gomes, A. P. Unique Metabolic Adaptations Dictate Distal Organ-Specific Metastatic Colonization. *Cancer Cell* **33**, 347–354 (2018).
51. Lehuédé, C., Dupuy, F., Rabinovitch, R., Jones, R. G. & Siegel, P. M. Metabolic Plasticity as a Determinant of Tumor Growth and Metastasis. *Cancer Res.* **76**, 5201–5208 (2016).
52. Hu, J., Li, G., Zhang, P., Zhuang, X. & Hu, G. A CD44v(+) subpopulation of breast cancer stem-like cells with enhanced lung metastasis capacity. *Cell Death Dis.* **8**, e2679 (2017).
53. Gao, W. *et al.* Isolation and phenotypic characterization of colorectal cancer stem cells with organ-specific metastatic potential. *Gastroenterology* **145**, 636–46.e5 (2013).
54. Danhier, P. *et al.* Cancer metabolism in space and time: Beyond the Warburg effect. *Biochim. Biophys. acta. Bioenerg.* **1858**, 556–572 (2017).
55. Bergers, G. & Fendt, S.-M. The metabolism of cancer cells during metastasis. *Nat. Rev. Cancer* **21**, 162–180 (2021).
56. Goodwin, P. J. *et al.* Effect of Metformin vs Placebo on Invasive Disease–Free Survival in Patients With Breast Cancer: The MA.32 Randomized Clinical Trial. *JAMA* **327**, 1963–1973 (2022).
57. Col, N. F., Ochs, L., Springmann, V., Aragaki, A. K. & Chlebowski, R. T. Metformin and breast cancer risk: a meta-analysis and critical literature review. *Breast Cancer Res. Treat.* **135**, 639–646 (2012).
58. Lv, Z., Yan, X., Lu, L., Su, C. & He, Y. Atovaquone enhances doxorubicin's efficacy via inhibiting mitochondrial respiration and STAT3 in aggressive thyroid cancer. *J. Bioenerg. Biomembr.* **50**, 263–270 (2018).
59. Yap, T. A. *et al.* Complex I inhibitor of oxidative phosphorylation in advanced solid tumors and acute myeloid leukemia: phase I trials. *Nat. Med.* **29**, 115–126 (2023).
60. Leibovitch, M. & Topisirovic, I. Dysregulation of mRNA translation and energy metabolism in cancer. *Adv. Biol. Regul.* **67**, 30–39 (2018).
61. Mossmann, D., Park, S. & Hall, M. N. mTOR signalling and cellular metabolism are mutual determinants in cancer. *Nat. Rev. Cancer* **18**, 744–757 (2018).
62. Fooks, K. *et al.* EIF4A inhibition targets bioenergetic homeostasis in AML MOLM-14 cells in vitro and in vivo and synergizes with cytarabine and venetoclax. *J. Exp. Clin. Cancer Res.* **41**, 340 (2022).
63. Morita, M. *et al.* mTORC1 controls mitochondrial activity and biogenesis through 4E-BP-dependent translational regulation. *Cell Metab.* **18**, 698–711 (2013).
64. Sheinboim, D. *et al.* An Exercise-Induced Metabolic Shield in Distant Organs Blocks Cancer Progression and Metastatic Dissemination. *Cancer Res.* **82**, 4164–4178 (2022).
65. Kaymak, I. *et al.* Carbon source availability drives nutrient utilization in CD8(+) T cells. *Cell Metab.* **34**, 1298-1311.e6 (2022).
66. Barbie, D. A. *et al.* Systematic RNA interference reveals that oncogenic KRAS-driven cancers require TBK1. *Nature* **462**, 108–112 (2009).

3.9 Supplementary material

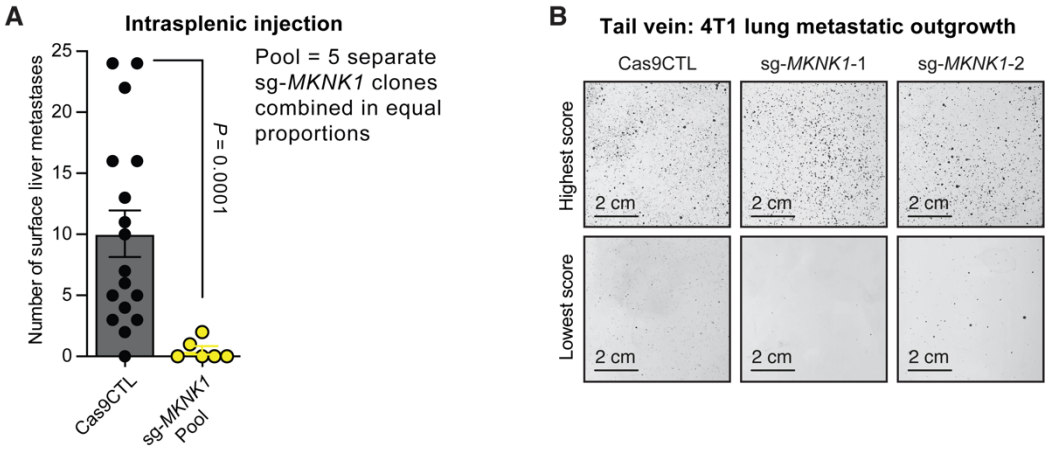

Supplementary Figure 3.1. (**A**) Number of metastases visible on the liver surface 21 days post-intrasplenic injection of Cas9CTL cells or a pool of 5 independent sg-*MKNK1* cell lines. Data in the Cas9CTL group are the same as shown in Fig. 3B. Error bars represent SEM, unpaired t-test with Welch's correction, n = 14 (Cas9CTL) 6 (sg-*MKNK1* pool). (**B**) Representative images of tumor burden in the lungs of mice 14 days post-tail vein injection of the indicated cell lines. Images display ex vivo culture of single-cell dissociated tumor-bearing lungs, following selection of tumor cells after 5 days of 6-thioguanine treatment. The highest and lowest scoring samples are shown from a total of 10 per group.

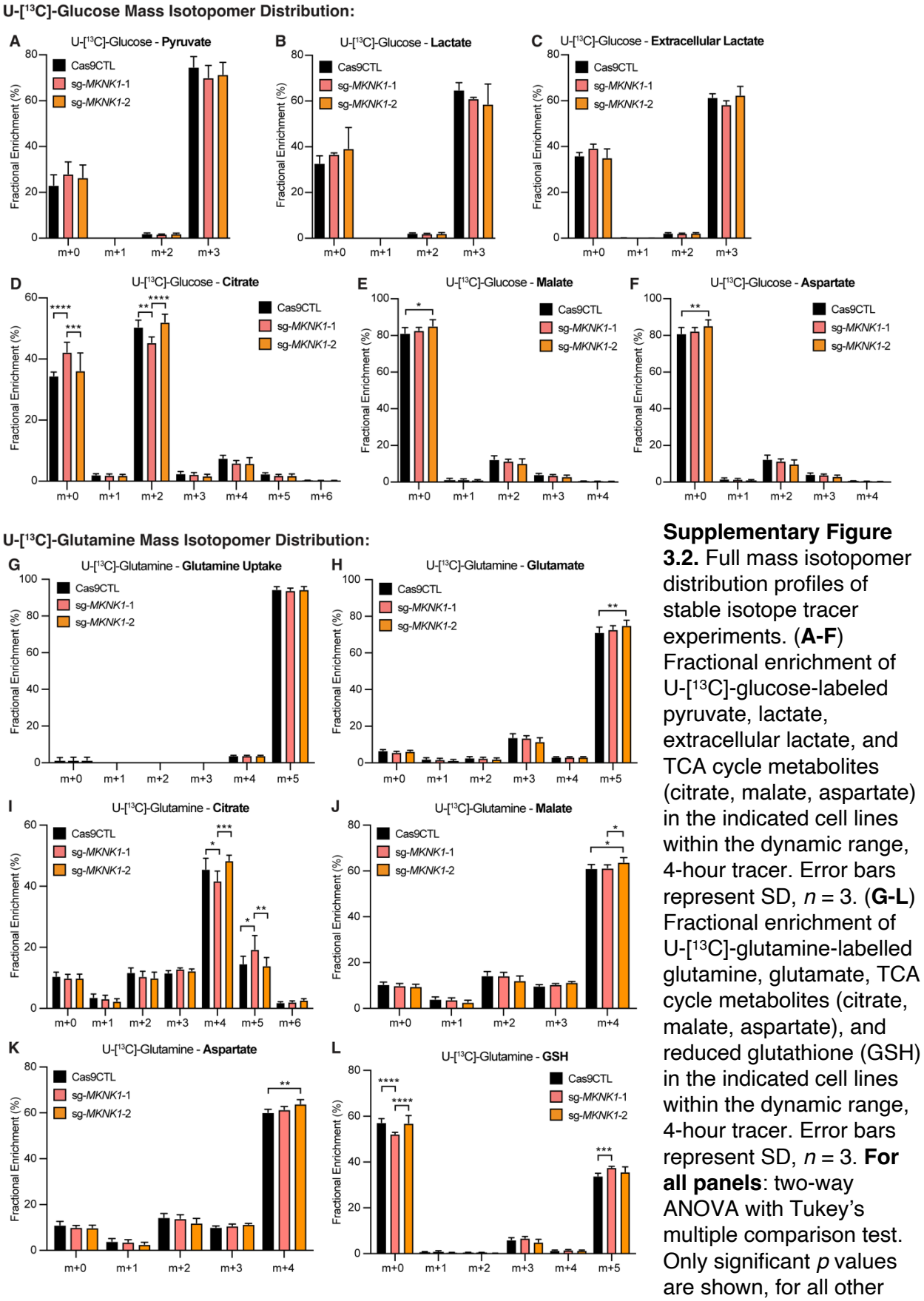

Supplementary Figure 3.2. Full mass isotopomer distribution profiles of stable isotope tracer experiments. (**A-F**) Fractional enrichment of U-[^{13}C]-glucose-labeled pyruvate, lactate, extracellular lactate, and TCA cycle metabolites (citrate, malate, aspartate) in the indicated cell lines within the dynamic range, 4-hour tracer. Error bars represent SD, $n = 3$. (**G-L**) Fractional enrichment of U-[^{13}C]-glutamine-labelled glutamine, glutamate, TCA cycle metabolites (citrate, malate, aspartate), and reduced glutathione (GSH) in the indicated cell lines within the dynamic range, 4-hour tracer. Error bars represent SD, $n = 3$. **For all panels**: two-way ANOVA with Tukey's multiple comparison test. Only significant p values are shown, for all other comparisons $p > 0.05$.

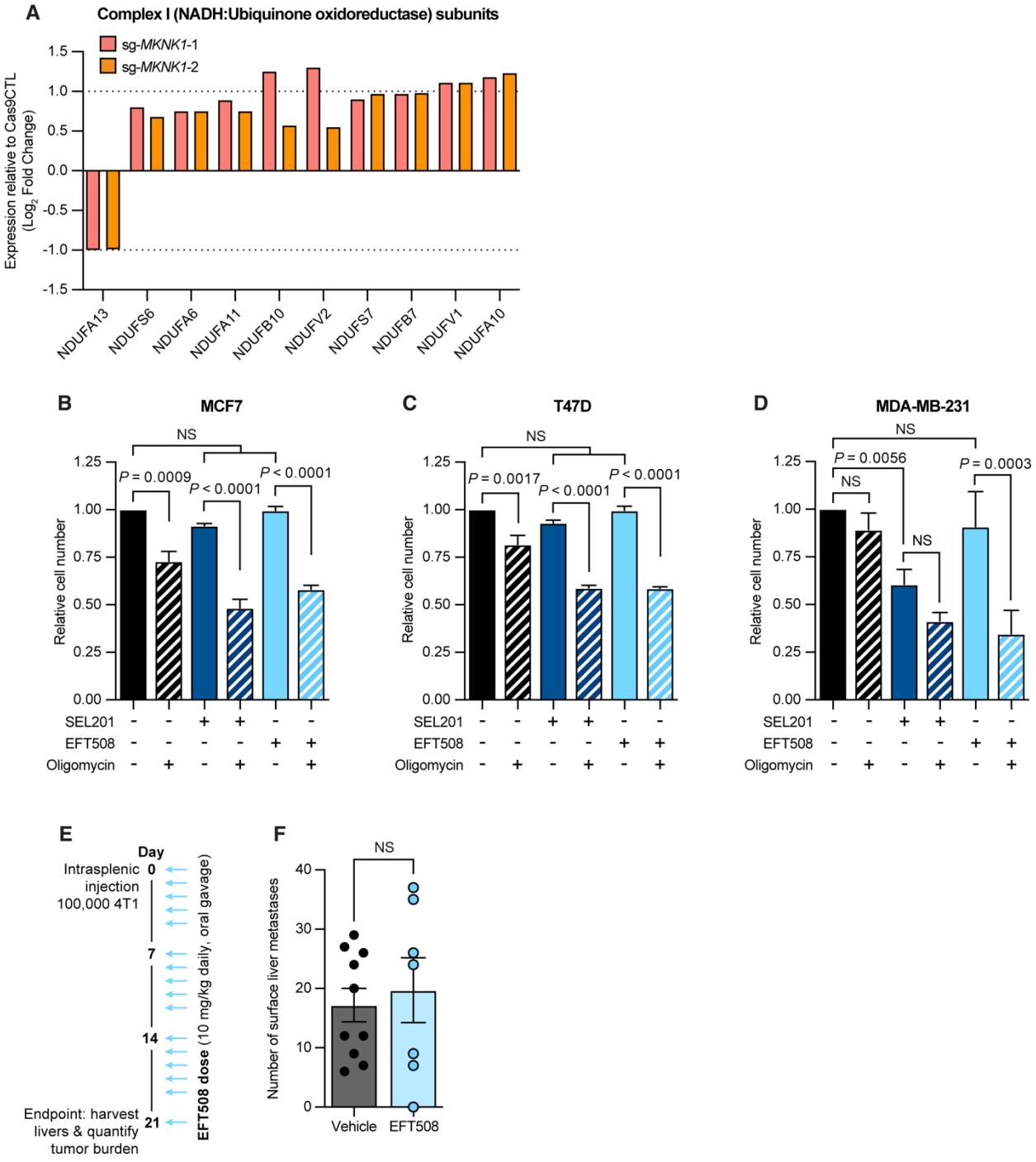

Supplementary Figure 3.3. (**A**) Relative expression of the listed subunits of NADH:ubiquinone oxidoreductase in sg-*MKNK1*-1 or sg-*MKNK1*-2 cell lines, shown as relative to the expression in Cas9CTL cells. Bar colour denotes cell line. Values are shown as a single fold change, calculated from proteomics data run in quadruplicates. (**B-D**) Effect of combining oligomycin, SEL201 and EFT508 on in vitro cell growth of MCF7 (**B**), T47D (**C**), and MDA-MB-231 (**D**) cells. Cells receiving MNKi treatment were dosed throughout the experiment, oligomycin was removed after 8 hours. All cell numbers were quantified at 48 hours post-oligomycin treatment and are shown relative to the no treatment group. Error bars represent SD, two-way ANOVA with Tukey's multiple

comparison test, *n* = 2 (MCF7 and T47D) 3 (MDA-MB-231). (**E**) Schematic detailing the dosing regimen for EFT508 treatment in vivo following intrasplenic injection. EFT508 was dosed at a concentration of 10 mg/kg/day via oral gavage, using a 5 on/2 off schedule, for a total of 16 doses over 21 days. (**F**) Quantification of surface metastases on mouse livers 21 days post-intrasplenic injection of Cas9CTL 4T1 cells, treated with EFT508 or vehicle control. Error bars represent SEM, unpaired t-test with Welch's correction, *n* = 10 (vehicle) 7 (EFT508).

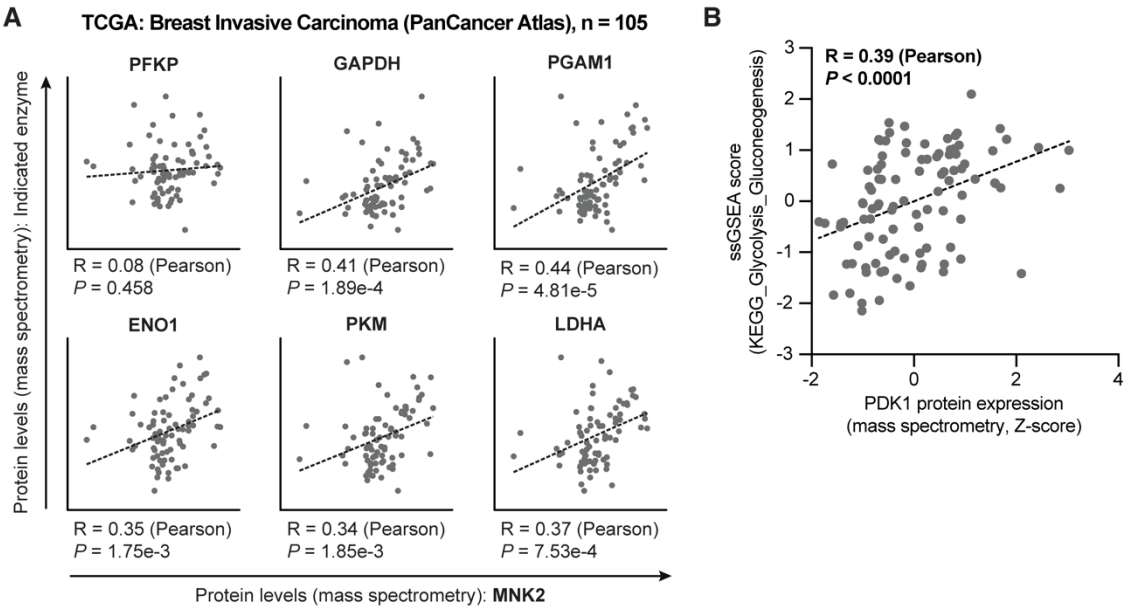

Supplementary Figure 3.4. (**A**) Correlation of MNK2 protein expression with the protein expression of listed enzymes. Pearson rank-order, dashed lines show linear regression. *P* and r values are indicated. (**B**) Correlation of PDK1 protein expression with ssGSEA enrichment scores for the glycolysis/gluconeogenesis pathway. Pearson rank-order, dashed lines show linear regression. *P* and r values are indicated. **All panels**: *n* = 102.

Supplementary Table 1: Antibody information - all antibodies used for western blotting (WB), immunohistochemistry (IHC)

Target	Reactivity	Application	Supplier	Catalog	Clone
MNK1	Human, Mouse	WB, IHC	Cell Signaling	2195	C4C1
eIF4E	Human, Mouse, Rat, Dog, Chicken, Frog	WB	BD	610270	87
Phospho-eIF4E (S209)	Human, Mouse, Rat, Monkey	WB	Cell Signaling	9741	
Actin	Multi-species (incl. Human, Mouse, Rat)	WB	Sigma-Aldrich	A5441	AC-15
E-Cadherin	Human, Mouse, Rat, Dog	WB	BD	610181	36
Vimentin	Multi-species (incl. Human, Mouse, Rat)	WB	BD	550513	RV202
MMP3	Human, Mouse, Rat	WB	Abcam	ab52915	EP1186Y
ALDOA	Human, Mouse, Monkey	WB	Cell Signaling	8060	D73H4
HK2	Human, Mouse, Rat, Monkey	WB	Cell Signaling	2867	C64G5
ENO1	Human, Mouse, Rat, Monkey	WB	Cell Signaling	3810	
GAPDH	Human, Mouse, Rat, Monkey	WB	Cell Signaling	5174	D16H11
LDHA	Human, Mouse, Rat, Monkey	WB	Cell Signaling	2012	
PDH	Human, Mouse, Rat, Monkey	WB	Cell Signaling	3205	C54G12

Chapter 4 – Discussion and future directions

4.1 Comprehensive scholarly discussion of all findings

The therapeutic options currently available for patients diagnosed with metastatic breast cancer are limited in their choice and efficacy. These patients face low survival rates and will likely succumb to disease, as metastasis remains the leading cause of breast cancer-related death[63,68]. The findings presented in Chapters 2 and 3 focus on genetic and pharmacological targeting of the MNK1/2-eIF4E pathway, aiming to further understand the potential clinical utility of MNK1/2 inhibitors for cancer management. We approached these studies by investigating this signaling axis in non-tumor components of the TME, as well as in the tumor cells themselves, and have gained new perspectives on the biological role of MNK1/2-eIF4E in promoting mechanisms of breast cancer progression and metastasis. In Chapter 2, we characterized how eIF4E phosphorylation regulates the post-transcriptional production of collagen type I in the mammary gland and dictates collagen fiber alignment at the tumor-stroma boundary to promote local invasion. This provides insight on how MNK1/2 inhibitors could be used to target pro-invasive features of the ECM in breast cancer. In Chapter 3, we explored how loss of tumor-intrinsic MNK1 kinase reduced glycolytic activity and metabolic flexibility, thereby leading to increased energetic dependence on OxPhos. We showed that one consequence of this switch away from glycolytic metabolism was diminished metastasis of MNK1-null tumor cells to the liver, but not the lung. These studies have identified previously unknown or under-explored impacts of MNK1/2-eIF4E signaling in the breast TME. Beyond this, they contribute to an ever-growing body of literature examining the pro-oncogenic

functions of critical regulators of translational control. Detailed summaries of the data presented are included within the main body of this thesis. The remainder of this chapter serves to highlight additional points of discussion, study limitations, and future experimental directions.

4.1.1 Exploring the potential clinical use of MNK1/2 inhibitors

It is important to emphasize that the over-arching goal of the work presented in this thesis was to assess whether the appropriate use of MNK1/2 inhibitors may be of clinical benefit in metastatic breast cancer patients. Fulfilling this goal required two approaches. First, we used the inhibitors SEL201 and EFT508 *in vivo* to assess whether blocking of MNK1/2 can recapitulate the effects of genetically inhibiting eIF4E phosphorylation or MNK1 expression. Second, we performed preliminary translational work to investigate if the phenotypes discovered using murine breast cancer models were supported using patient data, both tumor biopsies and analyses of publicly available datasets. From these data, we proposed that use of MNK1/2 inhibitors in combination with other therapies could potentially be leveraged to impact aspects of tumor biology that have so far proven difficult to target, namely ECM remodelling and cellular metabolism.

The ECM is now recognized to be an important player in the acquisition of therapeutic resistance to anti-cancer agents[156–160], but ECM-targeting therapies have so far been largely unsuccessful (see section 1.2.3). In Chapter 2, we demonstrated how SEL201 was sufficient to negate the anti-PD-1-mediated induction of intratumoral collagen deposition (*Fig. 2.7F-G*); a recently identified mechanism of resistance to

immunotherapy that has been suggested to act through multiple cell types, including CAFs and tumor cells[161]. Additionally, alignment of collagen fibers at tumor margins, the orientation of which we have shown is regulated by phospho-eIF4E (*Fig. 2.3 and Fig. 2.5C*), has been shown to inhibit anti-tumor immune cell infiltration[250]. Dual-targeting using MNK1/2 inhibitors with ICIs therefore represents a promising therapeutic combination. Indeed, these data strengthen our previously published conclusions that MNK1/2 inhibitors augment the efficacy of immunotherapies[238,241], including data demonstrating that SEL201 increases the abundance of $CD8^+$ T cells in breast cancer lung metastases in the context of anti-PD-1 treatment[241]. This aligns with other evidence illustrating that high mammographic density correlates with increased collagen deposition and immune cell influx[251,252].

Targeting metabolic-pathways and -dependencies of tumor cells has gained significant attention in recent years, with several strategies currently under clinical investigation in breast cancer patients (reviewed in Wang *et al.*, 2021[253]). Unfortunately, similar to therapies aimed at the ECM, targeting cellular metabolism is yet to demonstrate clinical efficacy in cancer patients despite promising preclinical results. For example, combination of the glycolytic inhibitor 2-deoxy-D-glucose with docetaxel was found to be tolerable in patients, but achieved no significant anti-cancer response[254]. Moreover, the repurposing of metformin as an anti-cancer agent has also been widely studied, owing to its extensive use in treating metabolic disorders and favorable risk-benefit profile[255]. Results from clinical trials have so far yielded conflicting results, with some demonstrating

that metformin could improve patient prognosis[255,256], while others show no improvements in survival or the efficacy of combined drugs[257,258].

It is likely that this apparent gap in the success of preclinical and clinical studies stems from an incomplete knowledge of the metabolic pathways driving breast cancer. We continue to improve our understanding of fundamental oncometabolism principles, as emphasized in a recent publication from Bartman *et al.* (2022), which sought to measure the absolute rates of ATP production from glycolysis versus the TCA cycle. Their results question the common assumption that tumors are metabolically hyperactive compared to surrounding normal tissue. Instead, they report that primary tumors produce ATP at a slower rate than surrounding normal tissue, which is accommodated by the downregulation of tissue-specific energetically-expensive processes, such as protein synthesis in pancreatic cancer[259]. In Chapter 3, we demonstrate that treatment with EFT508 monotherapy is insufficient to protect against metastatic tumor outgrowth in the liver, despite promising *in vitro* data (*Fig. 3.5*). We hypothesize reasons for this, including the need for therapeutic combinations to successfully limit tumor cell metabolic flexibility. As such, we propose that MNK1/2 inhibitors may require combination with drugs targeting mitochondrial metabolism, such as metformin, as a way of simultaneously inhibiting two common mechanisms of ATP production. We further suggest that there may be differences in tumor-intrinsic versus whole-TME targeting of MNK1/2. For example, $CD8^+$ T cells are known to rapidly engage metabolic machinery within minutes of activation, inducing a rapid upregulation of aerobic glycolysis to fuel their subsequent proliferation[260,261]. If a MNKi is capable of impacting tumor cell metabolism, it may also

affect the metabolic needs of $CD8^+$ T cells, or other immune cell types, in ways that reduce their effector function. Additionally, as highlighted above, there likely are variables influencing site-specific metabolic dependencies that remain unknown and are therefore not controlled for in our models.

While it is tempting to hypothesize the utility of MNK1/2 inhibitors in treating patients with metastatic breast cancer, we present our findings with caution. The data presented in Chapters 2 and 3 are encouraging, but future preclinical and clinical studies are needed to improve our understanding of the downstream impacts of targeting MNK1/2. Treatment combinations and dosing timelines will be particularly important to determine, to uncover which steps of the metastatic cascade may benefit from MNK1/2 inhibition. Furthermore, in light of data determining the metabolic dependencies of site-specific breast cancer metastases[191–194], detailed triage of patients may prove useful in deciding those who would benefit most from a MNK1/2 inhibitor.

4.1.2 Research limitations and future directions

4.1.2.1 Aspects of MNK1/2-eIF4E biology that remain contentious in the field

Although it is clear that the phosphorylation of eIF4E on S209 greatly enhances eIF4E-mediated cellular transformation[226], studies aiming to understand the precise molecular function of this phosphorylation event have been conflicting and controversial. Some have concluded that S209 phosphorylation promotes eIF4E binding to the mRNA 5' cap, formation of the eIF4F complex and therefore the initiation of translation[262–267]. Other studies have demonstrated that eIF4E phosphorylation is not required for eIF4F

complex assembly or translation initiation[268–270]. Similarly, it has been theorized that phosphorylation of S209 allows for the formation of a salt-bridge with lysine 159 that would stabilize cap binding in a hydrophobic pocket of eIF4E[271], in agreement with data suggesting that phosphorylated eIF4E has increased affinity and decreased dissociation rates for the 5' cap[272,273]. However, subsequent crystallography modelling concluded that this salt-bridge would destabilize the cap binding from eIF4E[274], which corroborates alternate data that phospho-eIF4E has a marked reduction in mRNA cap affinity[275]. Clearly these data are contradictory and remain incompletely understood. In Chapter 2, we present polysome profiling of wild-type and phospho-eIF4E-deficient mammary gland fibroblasts, consistent with the idea that eIF4E phosphorylation bolsters the translation of *COL1A1* mRNA (*Supp. Fig. 2.3*). The discrepancies described above do not invalidate these findings, but rather limit our understanding of the molecular mechanism of action through which they occur.

In addition to the functional consequences of eIF4E phosphorylation, there are gaps in our knowledge of its upstream kinases, MNK1 and MNK2. In Chapter 3, we chose to investigate the impact of ablating tumor-intrinsic MNK1 specifically, due in part to the current understanding that MNK1 activity is induced by extracellular stimuli such as cytokines, growth factors, and nutrient availability, whereas MNK2 activity is constitutive being largely unresponsive to upstream activation of p38 and ERK1/2 MAPKs[235,236]. However, a lack of reliable antibodies targeting MNK2 has made studying MNK2-specific functions difficult, and there may be unknown roles for this isoform in the models we used. We assume that the low levels of eIF4E phosphorylation we observe in MNK1 KO 4T1

cells (*Fig. 3.1A*) are a result of MNK2-mediated phosphorylation, but we have been unable to assess this directly. Generation of MNK2 KO and MNK1/2 double KO tumor cell lines would help provide tools to study isoform-specific contributions of the MNK kinases during breast cancer metastasis.

Similarly, we do not know whether the phenotypes observed upon loss of tumor-intrinsic MNK1 (Chapter 3) are a result of down-regulated eIF4E phosphorylation or from an alternative eIF4E-independent mechanism. eIF4E is the only *in vivo* validated substrate for MNK1/2[225], but several other proteins have been suggested as targets of MNK-based phosphorylation. These include cytosolic phospholipase A2 (cPLA2)[276], polypyrimidine tract-binding protein-associated splicing factor (PSF)[277], heterogeneous nuclear riboprotein A1 (hnRNPA1)[278], and Sprouty2 (SPRY2)[279,280], all of which have been suggested to be functionally relevant in tumor biology[277,281–288]. It is possible that the metastasis-protective effect of ablating MNK1 in 4T1 cells occurs via one of these proteins or another unidentified substrate, or perhaps through a MNK1-regulated mechanism that is independent of its kinase activity. A model of tumor cell-intrinsic phospho-eIF4E-deficiency (eIF4E$^{S209A/S209A}$) would be useful in addressing this, which we hypothesize would phenocopy the results of MNK1 KO tumors cells if the mechanism of action is dependent on reduced eIF4E phosphorylation.

4.1.2.2 Choice of model when investigating fibroblast-derived ECM

In Chapter 2, we examined phospho-eIF4E-deficiency in tissue resident fibroblasts specifically, demonstrating that fibroblasts isolated from S209A mammary glands have

reduced collagen-I production relative to their wild-type counterparts (*Fig. 2.3*). Our understanding of CAF biology has advanced greatly in recent years, highlighting over-simplifications in our study design that warrant mention. Although we chose to isolate primary mammary gland-resident fibroblasts, rather than use mouse embryonic fibroblasts or a fibroblast cell line such as NIH/3T3, we did not model CAFs directly. Isolated mammary gland fibroblasts were not exposed to a TME *in vivo* or *ex vivo*, thereby removing the effects of cell-cell interactions or TME-derived external stimuli that likely impact the transition from a normal tissue-resident fibroblast (NF) to a CAF. A study of matched NFs and CAFs from several murine breast cancer models demonstrated morphological differences between the two cell types, and could denote CAFs specifically based on their expression of the surface markers CD49b, CD87 and CD95[289]. NFs were characterized by CD39 expression but were found to upregulate CAF-associated markers upon *in vitro* propagation, including CD87, Sca-1 and Ly-6C which correlated with increased proliferative activity[289]. It is worth noting that we would not expect CAFs to behave differently from NFs in terms of their regulation of collagen production by phospho-eIF4E. We confirmed that tumors grown in the mammary glands of phospho-eIF4E-deficient mice were surrounded by less collagen than tumors in their wild-type counterparts (*Fig. 2.5H*), and that blocking eIF4E phosphorylation reduced immunotherapy-induced intratumoral collagen deposition (*Fig. 2.7*). As CAFs are the primary source of collagen production in the TME[112,113], it is therefore likely that these observations are a result of reduced collagen production in phospho-eIF4E-deficient CAFs.

The advancement of single-cell technologies in recent years has further provided insight into the heterogeneity of CAF populations. This young field continues to evolve at rapid speed, but it is now well-established that there are distinct populations of CAFs in in breast cancers that differ in their surface marker expression profile and biological function[290–296]. Early studies defined three broad CAF subtypes: myofibroblastic CAFs, inflammatory CAFs, and antigen-presenting CAFs[297]. Since then, additional CAF classifications have emerged, and we are beginning to understand the role of specific subtypes in immune exclusion[295], immunotherapy resistance[294], and metastasis[292]. The relative contributions of pro- versus anti-tumor CAF subpopulations to breast cancer progression requires extensive further investigation. These studies will be particularly relevant for treatments aimed at CAFs in the TME, such as FAP-targeting antibodies, as discussed in Chapter 1 (see section 1.2.3). It is reasonable to question whether the current clinical failures of such approaches are a result of this newly-identified fibroblast heterogeneity. It may be that specific pro-tumor CAF subsets need to be targeted to improve patient outcomes, rather than approaches that act more broadly.

To expand upon the findings of Chapter 2, additional studies should be performed to assess whether phospho-eIF4E-mediated control of fibroblast-derived collagen is maintained in CAF populations as well as NFs. An improved understanding of the spatial landscape of CAF subpopulations, and the impact of inhibiting eIF4E phosphorylation on this distribution, is vital. Utilizing technologies such as PhenoCycler, a highly multiplexed imaging platform at single-cell resolution, will allow for assessment of CAF heterogeneity and localization relative to relevant structures in the TME, such as locally invasive tumor

edges or the vasculature. Analyzing ECM-producing CAFs at the tumor-stroma boundary in this way may help to illuminate the involvement of phospho-eIF4E in controlling collagen fiber orientation and subsequent tumor cell invasion.

4.1.2.3 Assessment of ATP production in MNK1 knock-out tumor cells

As previously discussed, we propose in Chapter 3 that combination targeting of MNK1/2 and OxPhos may be an unexplored therapeutic option for breast cancer metastasis. We observed that MNK1 KO cells have impaired rates of glycolysis (*Fig. 3.4*) and subsequently that dual inhibition of MNK1/2 and OxPhos, via oligomycin treatment, significantly reduced tumor cell growth *in vitro* (*Fig. 3.5*). We assume that this is an effect of dampened ATP production in inhibited cells, based on the knowledge that glycolysis and the TCA cycle (linked with OxPhos) are the two dominant mechanisms of cellular energy production. However, we do not assess ATP levels directly. Future studies should therefore be performed to question this assumption in our models. The recently developed SCENITH methodology provides an elegant way of measuring global metabolic profiles via flow cytometry[298]. This technique would allow for assessment of ATP levels in cultured Cas9CTL and MNK1 KO cell lines, *ex vivo* processed tumor samples, or even patient-derived cell types. Moreover, the capacity of SCENITH to analyze metabolism at the single cell level could theoretically allow for the correlation of MNK1 protein expression with glycolytic activity or ATP level in heterogenous cell populations.

4.1.2.4 Additional models of liver-tropic metastatic cancers

A limitation of the study presented in Chapter 3 is the restricted tumor cell model used. The 4T1 tumor model is one of the most commonly used syngeneic mouse models of breast cancer and has been extensively studied. However, beyond breast cancer, the liver is a common site of metastasis for several other cancer types. These include colorectal cancer (CRC), for which incidence rates are unexpectedly increasing in younger adults[299], and pancreatic ductal adenocarcinoma (PDAC), an aggressive cancer that is the third-leading contributor to cancer mortality in the United States[300]. For patients diagnosed with metastatic CRC or PDAC, 5-year survival rates are 12.5%[301] and 0.5%[302] respectively. It would therefore be worthwhile to assess whether tumor-intrinsic MNK1 plays a role in promoting metastasis in murine models of these strongly liver-tropic cancers. Evidence in the literature suggests that the regulation of glycolysis is functionally relevant in CRC and PDAC progression, and in activity of their CSC populations, further supporting targeting of MNK1 in this context. CRC is a multi-factorial disease with several genetic drivers, but multiple studies have reported that modulation of glucose metabolism is critical for self-renewal and proliferation of intestinal stem cells (reviewed in La Vecchia *et al.,* 2020[303]), which are known to be the cell-of-origin for CRC tumorigenesis[303–305]. Indeed, the oncogenic long noncoding RNA MIR17HG has been shown to promote CRC liver metastasis *in vivo* by upregulating glycolysis through increased hexokinase-1 expression[306]. Similarly, seminal work by Ying *et al*. (2012) demonstrated that PDAC initiation and progression is driven by KRAS-mediated activation of anabolic glucose metabolism[307]. Targeting KRAS signaling was subsequently shown to promote tumor

regression, but ultimately relapsed due to the emergence of a CSC-like cell population with an OxPhos-dominant metabolism[308]. Recent work has clarified that two subsets of CSCs exist in PDAC with unique metabolic signatures for organotropic metastasis; cells that form lung metastases maintain an oxidative metabolism whereas cells in the liver utilize aerobic glycolysis and fatty acid oxidation[309]. In combination with the results presented in Chapter 3, these findings provide a strong rationale for exploring the role of MNK1 in CRC and PDAC metastasis. By generating MNK1 KO CRC or PDAC cell lines, we could assess the impact of MNK1 ablation on tumor cell glycolytic activity and site-specific metastasis. It may be that the impact of MNK1 on tumor cell metabolism is relevant in disease models other than breast cancer.

4.2 Final conclusion and summary

The work presented in this thesis explores previously unknown roles of the MNK1/2-eIF4E axis in promoting mechanisms of breast cancer metastasis. These include regulation of the mammary gland ECM that depends on the phosphorylation status of eIF4E, and the impact of tumor-intrinsic MNK1 kinase on BCSC features and tumor cell metabolic flexibility. The objectives of these studies were as follows:

1. To determine whether the MNK1/2-eIF4E axis plays a role in regulating the composition of the mammary gland ECM.
2. To investigate if ECM derived from a phospho-eIF4E-deficient context contributes to a less metastatic TME compared to wild-type.

3. To improve our understanding of the functional role that tumor-intrinsic MNK1 kinase plays in regulating BCSC populations and/or features.
4. To identify previously unknown consequences of pharmacologically inhibiting MNK1/2 and test the efficacy of these inhibitors in reducing breast cancer metastasis *in vivo*.
5. To explore the potential clinical relevance of targeting the MNK1/2-eIF4E axis through the translation of our findings into breast cancer patient samples.

To meet these objectives, we accomplished the following:

1. Using proteomics and *ex vivo* assessment of primary fibroblasts, we characterized differences in the composition of ECM derived wild-type and eIF4E$^{S209A/S209A}$ mammary glands. Specifically, we showed that phospho-eIF4E-deficient fibroblasts produce less collagen type I than their wild-type counterparts, due in part to translational regulation of *COL1A1* mRNA.
2. Confocal and second-harmonic generation microscopy were performed to demonstrate that collagen fibers in phospho-eIF4E-deficient S209A mammary glands exhibit altered topology compared to wild-type glands. Specifically, collagen fibers at the tumor-stroma boundary in S209A mice run predominantly in parallel with the tumor edge, a phenotype associated with reduced local invasion and tumor spread, while collagen fibers radiate outwards in wild-type mice. In addition, we demonstrated that phospho-eIF4E-deficiency protects against ECM-induced tumor cell invasion, partially driven by collagen signaling through the collagen receptor DDR2.

3. We generated CRISPR-mediated knock-out tumor cell lines to assess the impact of MNK1 kinase on BCSC features. In combination with multi-omics analysis and bioenergetic assessment, we found that tumor-intrinsic MNK1 ablation restricted tumor cell metabolic flexibility by reducing glycolytic activity and increasing dependence on OxPhos, resulting in reduced liver metastasis *in vivo*.
4. In Chapter 2, we demonstrated that treatment with SEL201 blocks anti-PD-1-induced intratumoral collagen deposition in the mammary gland. In Chapter 3, although treatment with EFT508 alone was insufficient to protect against liver metastatic outgrowth, results from our *in vitro* studies led us to propose that combination of MNK1/2 and OxPhos inhibitors may be therapeutically relevant.
5. In Chapter 2, our immunostainings of breast cancer patient samples identified a positive correlation between phospho-eIF4E and collagen-I protein levels, and improved our understanding of the heterogeneity of eIF4E phosphorylation within the stromal compartment of the breast TME. In Chapter 3, we performed analysis of publicly-available TCGA data and identified strong positive correlations between the protein expression of MNK1 and multiple glycolytic enzymes in patient tumors samples.

Chapter 5 – References (Chapters 1 and 4)

1. Ferlay, J. *et al.* Cancer statistics for the year 2020: An overview. *Int. J. cancer* (2021) doi:10.1002/ijc.33588.
2. Bray, F. *et al.* Global cancer statistics 2018: GLOBOCAN estimates of incidence and mortality worldwide for 36 cancers in 185 countries. *CA. Cancer J. Clin.* **68**, 394–424 (2018).
3. Bray, F. *et al.* Cancer Incidence in Five Continents: Inclusion criteria, highlights from Volume X and the global status of cancer registration. *Int. J. cancer* **137**, 2060–2071 (2015).
4. Sharma, R. Breast cancer incidence, mortality and mortality-to-incidence ratio (MIR) are associated with human development, 1990-2016: evidence from Global Burden of Disease Study 2016. *Breast Cancer* **26**, 428–445 (2019).
5. Torre, L. A., Siegel, R. L., Ward, E. M. & Jemal, A. Global Cancer Incidence and Mortality Rates and Trends--An Update. *Cancer Epidemiol. Biomarkers Prev.* **25**, 16–27 (2016).
6. Ginsburg, O. *et al.* The global burden of women's cancers: a grand challenge in global health. *Lancet (London, England)* **389**, 847–860 (2017).
7. Sankaranarayanan, R. *et al.* Cancer survival in Africa, Asia, and Central America: a population-based study. *Lancet. Oncol.* **11**, 165–173 (2010).
8. Allemani, C. *et al.* Global surveillance of cancer survival 1995-2009: analysis of individual data for 25,676,887 patients from 279 population-based registries in 67 countries (CONCORD-2). *Lancet (London, England)* **385**, 977–1010 (2015).
9. Key, T. J. *et al.* Sex hormones and risk of breast cancer in premenopausal women: a collaborative reanalysis of individual participant data from seven prospective studies. *Lancet. Oncol.* **14**, 1009–1019 (2013).
10. Folkerd, E. & Dowsett, M. Sex hormones and breast cancer risk and prognosis. *Breast* **22 Suppl 2**, S38-43 (2013).
11. Zhang, X., Tworoger, S. S., Eliassen, A. H. & Hankinson, S. E. Postmenopausal plasma sex hormone levels and breast cancer risk over 20 years of follow-up. *Breast Cancer Res. Treat.* **137**, 883–892 (2013).
12. Key, T., Appleby, P., Barnes, I. & Reeves, G. Endogenous sex hormones and breast cancer in postmenopausal women: reanalysis of nine prospective studies. *J. Natl. Cancer Inst.* **94**, 606–616 (2002).
13. Giordano, S. H. Breast Cancer in Men. *N. Engl. J. Med.* **378**, 2311–2320 (2018).
14. McGuire, A., Brown, J. A. L., Malone, C., McLaughlin, R. & Kerin, M. J. Effects of age on the detection and management of breast cancer. *Cancers (Basel).* **7**, 908–929 (2015).
15. Benz, C. C. Impact of aging on the biology of breast cancer. *Crit. Rev. Oncol. Hematol.* **66**, 65–74 (2008).
16. Collaborative Group on Hormonal Factors in Breast. Familial breast cancer: collaborative reanalysis of individual data from 52 epidemiological studies including 58,209 women with breast cancer and 101,986 women without the disease. *Lancet (London, England)* **358**, 1389–1399 (2001).
17. Wu, H.-C. *et al.* Breast cancer family history and allele-specific DNA methylation in the legacy girls study. *Epigenetics* **13**, 240–250 (2018).
18. Shiovitz, S. & Korde, L. A. Genetics of breast cancer: a topic in evolution. *Ann. Oncol. Off. J. Eur. Soc. Med. Oncol.* **26**, 1291–1299 (2015).
19. Shahbandi, A., Nguyen, H. D. & Jackson, J. G. TP53 Mutations and Outcomes in Breast Cancer: Reading beyond the Headlines. *Trends in cancer* **6**, 98–110 (2020).

20. Corso, G., Intra, M., Trentin, C., Veronesi, P. & Galimberti, V. CDH1 germline mutations and hereditary lobular breast cancer. *Fam. Cancer* **15**, 215–219 (2016).
21. Kechagioglou, P. *et al.* Tumor suppressor PTEN in breast cancer: heterozygosity, mutations and protein expression. *Anticancer Res.* **34**, 1387–1400 (2014).
22. Chen, J. & Lindblom, A. Germline mutation screening of the STK11/LKB1 gene in familial breast cancer with LOH on 19p. *Clin. Genet.* **57**, 394–397 (2000).
23. Crawford, B. *et al.* Multi-gene panel testing for hereditary cancer predisposition in unsolved high-risk breast and ovarian cancer patients. *Breast Cancer Res. Treat.* **163**, 383–390 (2017).
24. Renwick, A. *et al.* ATM mutations that cause ataxia-telangiectasia are breast cancer susceptibility alleles. *Nat. Genet.* **38**, 873–875 (2006).
25. Rahman, N. *et al.* PALB2, which encodes a BRCA2-interacting protein, is a breast cancer susceptibility gene. *Nat. Genet.* **39**, 165–167 (2007).
26. Seal, S. *et al.* Truncating mutations in the Fanconi anemia J gene BRIP1 are low-penetrance breast cancer susceptibility alleles. *Nat. Genet.* **38**, 1239–1241 (2006).
27. Meijers-Heijboer, H. *et al.* Low-penetrance susceptibility to breast cancer due to CHEK2(*)1100delC in noncarriers of BRCA1 or BRCA2 mutations. *Nat. Genet.* **31**, 55–59 (2002).
28. Hill, D. A., Prossnitz, E. R., Royce, M. & Nibbe, A. Temporal trends in breast cancer survival by race and ethnicity: A population-based cohort study. *PLoS One* **14**, e0224064 (2019).
29. Yedjou, C. G. *et al.* Health and Racial Disparity in Breast Cancer. *Adv. Exp. Med. Biol.* **1152**, 31–49 (2019).
30. American Cancer Society. *Breast Cancer Facts & Figures, 2015–2016*. (2016).
31. Pathy, N. B. *et al.* Breast cancer in a multi-ethnic Asian setting: results from the Singapore-Malaysia hospital-based breast cancer registry. *Breast* **20 Suppl 2**, S75-80 (2011).
32. Agarwal, G., Pradeep, P. V, Aggarwal, V., Yip, C.-H. & Cheung, P. S. Y. Spectrum of breast cancer in Asian women. *World J. Surg.* **31**, 1031–1040 (2007).
33. Li, C. I., Malone, K. E. & Daling, J. R. Differences in breast cancer hormone receptor status and histology by race and ethnicity among women 50 years of age and older. *Cancer Epidemiol. Biomarkers Prev.* **11**, 601–607 (2002).
34. Bernstein, L. Epidemiology of endocrine-related risk factors for breast cancer. *J. Mammary Gland Biol. Neoplasia* **7**, 3–15 (2002).
35. Albrektsen, G., Heuch, I., Hansen, S. & Kvåle, G. Breast cancer risk by age at birth, time since birth and time intervals between births: exploring interaction effects. *Br. J. Cancer* **92**, 167–175 (2005).
36. Titus-Ernstoff, L. *et al.* Menstrual factors in relation to breast cancer risk. *Cancer Epidemiol. Biomarkers Prev.* **7**, 783–789 (1998).
37. Kim, E. Y. *et al.* Mammographic breast density, its changes, and breast cancer risk in premenopausal and postmenopausal women. *Cancer* **126**, 4687–4696 (2020).
38. Chen, X., Wang, Q., Zhang, Y., Xie, Q. & Tan, X. Physical Activity and Risk of Breast Cancer: A Meta-Analysis of 38 Cohort Studies in 45 Study Reports. *Value Heal.* **22**, 104–128 (2019).
39. Kyu, H. H. *et al.* Physical activity and risk of breast cancer, colon cancer, diabetes, ischemic heart disease, and ischemic stroke events: systematic review and dose-response meta-analysis for the Global Burden of Disease Study 2013. *BMJ* **354**, i3857 (2016).
40. Kolb, R. & Zhang, W. Obesity and Breast Cancer: A Case of Inflamed Adipose Tissue.

Cancers (Basel). **12**, (2020).
41. Wang, X. *et al.* Body Mass Index at Diagnosis as a Prognostic Factor for Early-Stage Invasive Breast Cancer after Surgical Resection. *Oncol. Res. Treat.* **42**, 195–201 (2019).
42. James, F. R. *et al.* Obesity in breast cancer--what is the risk factor? *Eur. J. Cancer* **51**, 705–720 (2015).
43. Rachdaoui, N. & Sarkar, D. K. Effects of alcohol on the endocrine system. *Endocrinol. Metab. Clin. North Am.* **42**, 593–615 (2013).
44. Erol, A., Ho, A. M.-C., Winham, S. J. & Karpyak, V. M. Sex hormones in alcohol consumption: a systematic review of evidence. *Addict. Biol.* **24**, 157–169 (2019).
45. Fiolet, T. *et al.* Consumption of ultra-processed foods and cancer risk: results from NutriNet-Santé prospective cohort. *BMJ* **360**, k322 (2018).
46. Terry, P. D. & Rohan, T. E. Cigarette smoking and the risk of breast cancer in women: a review of the literature. *Cancer Epidemiol. Biomarkers Prev.* **11**, 953–971 (2002).
47. World Health Organization. *WHO Classification of Tumours of the Breast*. vol. 4 (IARC, 2012).
48. Cavalli, F., Kaye, S. B., Hansen, H. H., Armitage, J. O. & Piccart-Gebhart, M. *Textbook of medical oncology*. (CRC Press, 2009).
49. Amin, M. B. *et al.* The Eighth Edition AJCC Cancer Staging Manual: Continuing to build a bridge from a population-based to a more 'personalized' approach to cancer staging. *CA Cancer J Clin* vol. 67 93–99 (2017).
50. Perou, C. M. *et al.* Molecular portraits of human breast tumours. *Nature* **406**, 747–752 (2000).
51. Sørlie, T. *et al.* Gene expression patterns of breast carcinomas distinguish tumor subclasses with clinical implications. *Proc. Natl. Acad. Sci. U. S. A.* **98**, 10869–10874 (2001).
52. Harbeck, N. *et al.* Breast cancer. *Nat. Rev. Dis. Prim.* **5**, 66 (2019).
53. Howlader, N. *et al.* US incidence of breast cancer subtypes defined by joint hormone receptor and HER2 status. *J. Natl. Cancer Inst.* **106**, (2014).
54. Weigelt, B., Baehner, F. L. & Reis-Filho, J. S. The contribution of gene expression profiling to breast cancer classification, prognostication and prediction: a retrospective of the last decade. *J. Pathol.* **220**, 263–280 (2010).
55. Eroles, P., Bosch, A., Pérez-Fidalgo, J. A. & Lluch, A. Molecular biology in breast cancer: intrinsic subtypes and signaling pathways. *Cancer Treat. Rev.* **38**, 698–707 (2012).
56. Ades, F. *et al.* Luminal B breast cancer: molecular characterization, clinical management, and future perspectives. *J. Clin. Oncol.* **32**, 2794–2803 (2014).
57. Prat, A. *et al.* Molecular features and survival outcomes of the intrinsic subtypes within HER2-positive breast cancer. *J. Natl. Cancer Inst.* **106**, (2014).
58. Kanu, N. *et al.* DNA replication stress mediates APOBEC3 family mutagenesis in breast cancer. *Genome Biol.* **17**, 185 (2016).
59. Lehmann, B. D. *et al.* Identification of human triple-negative breast cancer subtypes and preclinical models for selection of targeted therapies. *J. Clin. Invest.* **121**, 2750–2767 (2011).
60. Wang, D.-Y., Jiang, Z., Ben-David, Y., Woodgett, J. R. & Zacksenhaus, E. Molecular stratification within triple-negative breast cancer subtypes. *Sci. Rep.* **9**, 19107 (2019).
61. Lehmann, B. D. & Pietenpol, J. A. Clinical implications of molecular heterogeneity in triple negative breast cancer. *Breast* **24 Suppl 2**, S36-40 (2015).
62. Newman, L. A., Reis-Filho, J. S., Morrow, M., Carey, L. A. & King, T. A. The 2014 Society of Surgical Oncology Susan G. Komen for the Cure Symposium: triple-negative breast cancer. *Ann. Surg. Oncol.* **22**, 874–882 (2015).

63. American Cancer Society. *Cancer Facts & Figures 2020*. (2020).
64. Mariotto, A. B., Etzioni, R., Hurlbert, M., Penberthy, L. & Mayer, M. Estimation of the Number of Women Living with Metastatic Breast Cancer in the United States. *Cancer Epidemiol. Biomarkers Prev.* **26**, 809–815 (2017).
65. Gobbini, E. *et al.* Time trends of overall survival among metastatic breast cancer patients in the real-life ESME cohort. *Eur. J. Cancer* **96**, 17–24 (2018).
66. Fidler, I. J. The pathogenesis of cancer metastasis: the 'seed and soil' hypothesis revisited. *Nat. Rev. Cancer* **3**, 453–458 (2003).
67. Lambert, A. W., Pattabiraman, D. R. & Weinberg, R. A. Emerging Biological Principles of Metastasis. *Cell* **168**, 670–691 (2017).
68. Cardoso, F. *et al.* 4th ESO-ESMO International Consensus Guidelines for Advanced Breast Cancer (ABC 4). *Ann. Oncol.* **29**, 1634–1657 (2018).
69. Buonomo, O. C. *et al.* New insights into the metastatic behavior after breast cancer surgery, according to well-established clinicopathological variables and molecular subtypes. *PLoS One* **12**, e0184680 (2017).
70. Adam, R. *et al.* Is liver resection justified for patients with hepatic metastases from breast cancer? *Ann. Surg.* **244**, 897–898 (2006).
71. Zhao, H.-Y., Gong, Y., Ye, F.-G., Ling, H. & Hu, X. Incidence and prognostic factors of patients with synchronous liver metastases upon initial diagnosis of breast cancer: a population-based study. *Cancer Manag. Res.* **10**, 5937–5950 (2018).
72. Haloua, M. H. *et al.* A systematic review of oncoplastic breast-conserving surgery: current weaknesses and future prospects. *Ann. Surg.* **257**, 609–620 (2013).
73. Joshi, S. C., Khan, F. A., Pant, I. & Shukla, A. Role of radiotherapy in early breast cancer: an overview. *Int. J. Health Sci. (Qassim).* **1**, 259–264 (2007).
74. Rastogi, P. *et al.* Preoperative chemotherapy: updates of National Surgical Adjuvant Breast and Bowel Project Protocols B-18 and B-27. *J. Clin. Oncol.* **26**, 778–785 (2008).
75. Rouzier, R. *et al.* Breast cancer molecular subtypes respond differently to preoperative chemotherapy. *Clin. Cancer Res.* **11**, 5678–5685 (2005).
76. Tremont, A., Lu, J. & Cole, J. T. Endocrine Therapy for Early Breast Cancer: Updated Review. *Ochsner J.* **17**, 405–411 (2017).
77. Drăgănescu, M. & Carmocan, C. Hormone Therapy in Breast Cancer. *Chirurgia (Bucur).* **112**, 413–417 (2017).
78. Peto, R. *et al.* Comparisons between different polychemotherapy regimens for early breast cancer: meta-analyses of long-term outcome among 100,000 women in 123 randomised trials. *Lancet (London, England)* **379**, 432–444 (2012).
79. Davies, C. *et al.* Relevance of breast cancer hormone receptors and other factors to the efficacy of adjuvant tamoxifen: patient-level meta-analysis of randomised trials. *Lancet (London, England)* **378**, 771–784 (2011).
80. Maximiano, S., Magalhães, P., Guerreiro, M. P. & Morgado, M. Trastuzumab in the Treatment of Breast Cancer. *BioDrugs* **30**, 75–86 (2016).
81. Ishii, K., Morii, N. & Yamashiro, H. Pertuzumab in the treatment of HER2-positive breast cancer: an evidence-based review of its safety, efficacy, and place in therapy. *Core Evid.* **14**, 51–70 (2019).
82. Moreira, C. & Kaklamani, V. Lapatinib and breast cancer: current indications and outlook for the future. *Expert Rev. Anticancer Ther.* **10**, 1171–1182 (2010).
83. Park, J. W. *et al.* Adaptive Randomization of Neratinib in Early Breast Cancer. *N. Engl. J. Med.* **375**, 11–22 (2016).
84. Riccardi, F. *et al.* Exemestane and Everolimus combination treatment of hormone receptor positive, HER2 negative metastatic breast cancer: A retrospective study of 9

cancer centers in the Campania Region (Southern Italy) focused on activity, efficacy and safety. *Mol. Clin. Oncol.* **9**, 255–263 (2018).
85. Steger, G. G., Gnant, M. & Bartsch, R. Palbociclib for the treatment of postmenopausal breast cancer - an update. *Expert Opin. Pharmacother.* **17**, 255–263 (2016).
86. Shah, A. *et al.* FDA Approval: Ribociclib for the Treatment of Postmenopausal Women with Hormone Receptor-Positive, HER2-Negative Advanced or Metastatic Breast Cancer. *Clin. Cancer Res.* **24**, 2999–3004 (2018).
87. André, F. *et al.* Alpelisib for PIK3CA-Mutated, Hormone Receptor-Positive Advanced Breast Cancer. *N. Engl. J. Med.* **380**, 1929–1940 (2019).
88. Kim, S.-B. *et al.* Ipatasertib plus paclitaxel versus placebo plus paclitaxel as first-line therapy for metastatic triple-negative breast cancer (LOTUS): a multicentre, randomised, double-blind, placebo-controlled, phase 2 trial. *Lancet. Oncol.* **18**, 1360–1372 (2017).
89. Zhang, Q. *et al.* Exploratory clinical study of chidamide, an oral subtype-selective histone deacetylase inhibitor, in combination with exemestane in hormone receptor-positive advanced breast cancer. *Chin. J. Cancer Res.* **30**, 605–612 (2018).
90. Pegram, M. D. & Reese, D. M. Combined biological therapy of breast cancer using monoclonal antibodies directed against HER2/neu protein and vascular endothelial growth factor. *Semin. Oncol.* **29**, 29–37 (2002).
91. Robson, M. *et al.* Olaparib for Metastatic Breast Cancer in Patients with a Germline BRCA Mutation. *N. Engl. J. Med.* **377**, 523–533 (2017).
92. Litton, J. K. *et al.* Talazoparib in Patients with Advanced Breast Cancer and a Germline BRCA Mutation. *N. Engl. J. Med.* **379**, 753–763 (2018).
93. Sharma, P. & Allison, J. P. Immune checkpoint targeting in cancer therapy: toward combination strategies with curative potential. *Cell* **161**, 205–214 (2015).
94. Planes-Laine, G. *et al.* PD-1/PD-L1 Targeting in Breast Cancer: The First Clinical Evidences Are Emerging. A Literature Review. *Cancers (Basel).* **11**, (2019).
95. De La Cruz, L. M. & Czerniecki, B. J. Immunotherapy for Breast Cancer is Finally at the Doorstep: Immunotherapy in Breast Cancer. *Ann. Surg. Oncol.* **25**, 2852–2857 (2018).
96. Plitas, G. *et al.* Regulatory T Cells Exhibit Distinct Features in Human Breast Cancer. *Immunity* **45**, 1122–1134 (2016).
97. Miller, L. D. *et al.* Immunogenic Subtypes of Breast Cancer Delineated by Gene Classifiers of Immune Responsiveness. *Cancer Immunol. Res.* **4**, 600–610 (2016).
98. Liu, Z., Li, M., Jiang, Z. & Wang, X. A Comprehensive Immunologic Portrait of Triple-Negative Breast Cancer. *Transl. Oncol.* **11**, 311–329 (2018).
99. Stanton, S. E., Adams, S. & Disis, M. L. Variation in the Incidence and Magnitude of Tumor-Infiltrating Lymphocytes in Breast Cancer Subtypes: A Systematic Review. *JAMA Oncol.* **2**, 1354–1360 (2016).
100. Thomas, A. *et al.* Tumor mutational burden is a determinant of immune-mediated survival in breast cancer. *Oncoimmunology* **7**, e1490854 (2018).
101. Emens, L. A. *et al.* LBA16 IMpassion130: Final OS analysis from the pivotal phase III study of atezolizumab + nab-paclitaxel vs placebo + nab-paclitaxel in previously untreated locally advanced or metastatic triple-negative breast cancer. *Annals of Oncology* vol. 31 S1148 (2020).
102. Miles, D. *et al.* Primary results from IMpassion131, a double-blind, placebo-controlled, randomised phase III trial of first-line paclitaxel with or without atezolizumab for unresectable locally advanced/metastatic triple-negative breast cancer. *Ann. Oncol.* **32**, 994–1004 (2021).
103. Cortes, J. *et al.* Pembrolizumab plus chemotherapy versus placebo plus chemotherapy for previously untreated locally recurrent inoperable or metastatic triple-negative breast

cancer (KEYNOTE-355): a randomised, placebo-controlled, double-blind, phase 3 clinical trial. *Lancet (London, England)* **396**, 1817–1828 (2020).
104. Schmid, P. *et al.* VP7-2021: KEYNOTE-522: Phase III study of neoadjuvant pembrolizumab + chemotherapy vs. placebo + chemotherapy, followed by adjuvant pembrolizumab vs. placebo for early-stage TNBC. *Ann. Oncol.* **32**, 1198–1200 (2021).
105. Hanahan, D. & Coussens, L. M. Accessories to the crime: functions of cells recruited to the tumor microenvironment. *Cancer Cell* **21**, 309–322 (2012).
106. Quail, D. F. & Joyce, J. A. Microenvironmental regulation of tumor progression and metastasis. *Nat. Med.* **19**, 1423–1437 (2013).
107. Smyth, M. J., Dunn, G. P. & Schreiber, R. D. Cancer immunosurveillance and immunoediting: the roles of immunity in suppressing tumor development and shaping tumor immunogenicity. *Adv. Immunol.* **90**, 1–50 (2006).
108. Boudreau, A., van't Veer, L. J. & Bissell, M. J. An 'elite hacker': breast tumors exploit the normal microenvironment program to instruct their progression and biological diversity. *Cell Adh. Migr.* **6**, 236–248 (2012).
109. De Palma, M., Biziato, D. & Petrova, T. V. Microenvironmental regulation of tumour angiogenesis. *Nat. Rev. Cancer* **17**, 457–474 (2017).
110. Bonnans, C., Chou, J. & Werb, Z. Remodelling the extracellular matrix in development and disease. *Nat. Rev. Mol. Cell Biol.* **15**, 786–801 (2014).
111. Winkler, J., Abisoye-Ogunniyan, A., Metcalf, K. J. & Werb, Z. Concepts of extracellular matrix remodelling in tumour progression and metastasis. *Nat. Commun.* **11**, 5120 (2020).
112. Hinz, B. *et al.* Recent developments in myofibroblast biology: paradigms for connective tissue remodeling. *Am. J. Pathol.* **180**, 1340–1355 (2012).
113. Houthuijzen, J. M. & Jonkers, J. Cancer-associated fibroblasts as key regulators of the breast cancer tumor microenvironment. *Cancer Metastasis Rev.* **37**, 577–597 (2018).
114. Jayadev, R. & Sherwood, D. R. Basement membranes. *Curr. Biol.* **27**, R207–R211 (2017).
115. Pickup, M. W., Mouw, J. K. & Weaver, V. M. The extracellular matrix modulates the hallmarks of cancer. *EMBO Rep.* **15**, 1243–1253 (2014).
116. Naba, A. *et al.* The matrisome: in silico definition and in vivo characterization by proteomics of normal and tumor extracellular matrices. *Mol. Cell. Proteomics* **11**, M111.014647-M111.014647 (2012).
117. Krasny, L. *et al.* Comparative proteomic assessment of matrisome enrichment methodologies. *Biochem. J.* **473**, 3979–3995 (2016).
118. Naba, A. *et al.* The extracellular matrix: Tools and insights for the "omics" era. *Matrix Biol.* **49**, 10–24 (2016).
119. Zhao, Y. *et al.* Extracellular Matrix: Emerging Roles and Potential Therapeutic Targets for Breast Cancer. *Front. Oncol.* **11**, 650453 (2021).
120. Vasvani, S., Kulkarni, P. & Rawtani, D. Hyaluronic acid: A review on its biology, aspects of drug delivery, route of administrations and a special emphasis on its approved marketed products and recent clinical studies. *Int. J. Biol. Macromol.* **151**, 1012–1029 (2020).
121. Yurchenco, P. D. Basement membranes: cell scaffoldings and signaling platforms. *Cold Spring Harb. Perspect. Biol.* **3**, (2011).
122. Singh, P., Carraher, C. & Schwarzbauer, J. E. Assembly of fibronectin extracellular matrix. *Annu. Rev. Cell Dev. Biol.* **26**, 397–419 (2010).
123. Mouw, J. K., Ou, G. & Weaver, V. M. Extracellular matrix assembly: a multiscale deconstruction. *Nat. Rev. Mol. Cell Biol.* **15**, 771–785 (2014).

124. Ricard-Blum, S. The collagen family. *Cold Spring Harb. Perspect. Biol.* **3**, a004978 (2011).
125. Iacobuzio-Donahue, C. A., Argani, P., Hempen, P. M., Jones, J. & Kern, S. E. The desmoplastic response to infiltrating breast carcinoma: gene expression at the site of primary invasion and implications for comparisons between tumor types. *Cancer Res.* **62**, 5351–5357 (2002).
126. Kauppila, S., Stenbäck, F., Risteli, J., Jukkola, A. & Risteli, L. Aberrant type I and type III collagen gene expression in human breast cancer in vivo. *J. Pathol.* **186**, 262–268 (1998).
127. Provenzano, P. P. *et al.* Collagen density promotes mammary tumor initiation and progression. *BMC Med.* **6**, 11 (2008).
128. Gao, H. *et al.* Multi-organ Site Metastatic Reactivation Mediated by Non-canonical Discoidin Domain Receptor 1 Signaling. *Cell* **166**, 47–62 (2016).
129. Zhang, K. *et al.* The collagen receptor discoidin domain receptor 2 stabilizes SNAIL1 to facilitate breast cancer metastasis. *Nat. Cell Biol.* **15**, 677–687 (2013).
130. Levental, K. R. *et al.* Matrix Crosslinking Forces Tumor Progression by Enhancing Integrin Signaling. *Cell* **139**, 891–906 (2009).
131. Yuzhalin, A. E., Lim, S. Y., Kutikhin, A. G. & Gordon-Weeks, A. N. Dynamic matrisome: ECM remodeling factors licensing cancer progression and metastasis. *Biochim. Biophys. acta. Rev. cancer* **1870**, 207–228 (2018).
132. Guo, Y. P. *et al.* Growth factors and stromal matrix proteins associated with mammographic densities. *Cancer Epidemiol. Biomarkers Prev.* **10**, 243–248 (2001).
133. McCormack, V. A. & dos Santos Silva, I. Breast density and parenchymal patterns as markers of breast cancer risk: a meta-analysis. *Cancer Epidemiol. Biomarkers Prev.* **15**, 1159–1169 (2006).
134. Kerlikowske, K. *et al.* Automated and Clinical Breast Imaging Reporting and Data System Density Measures Predict Risk for Screen-Detected and Interval Cancers: A Case-Control Study. *Ann. Intern. Med.* **168**, 757–765 (2018).
135. Nguyen-Ngoc, K.-V. *et al.* ECM microenvironment regulates collective migration and local dissemination in normal and malignant mammary epithelium. *Proc. Natl. Acad. Sci. U. S. A.* **109**, E2595-604 (2012).
136. Velez, D. O. *et al.* 3D collagen architecture induces a conserved migratory and transcriptional response linked to vasculogenic mimicry. *Nat. Commun.* **8**, 1651 (2017).
137. Maller, O. *et al.* Collagen architecture in pregnancy-induced protection from breast cancer. *J. Cell Sci.* **126**, 4108–4110 (2013).
138. Provenzano, P. P., Inman, D. R., Eliceiri, K. W., Trier, S. M. & Keely, P. J. Contact guidance mediated three-dimensional cell migration is regulated by Rho/ROCK-dependent matrix reorganization. *Biophys. J.* **95**, 5374–5384 (2008).
139. Conklin, M. W. *et al.* Aligned collagen is a prognostic signature for survival in human breast carcinoma. *Am. J. Pathol.* **178**, 1221–1232 (2011).
140. Lämmermann, T. *et al.* Rapid leukocyte migration by integrin-independent flowing and squeezing. *Nature* **453**, 51–55 (2008).
141. Salmon, H. *et al.* Matrix architecture defines the preferential localization and migration of T cells into the stroma of human lung tumors. *J. Clin. Invest.* **122**, 899–910 (2012).
142. Paszek, M. J. *et al.* The cancer glycocalyx mechanically primes integrin-mediated growth and survival. *Nature* **511**, 319–325 (2014).
143. Kessenbrock, K., Plaks, V. & Werb, Z. Matrix metalloproteinases: regulators of the tumor microenvironment. *Cell* **141**, 52–67 (2010).
144. Castro-Castro, A. *et al.* Cellular and Molecular Mechanisms of MT1-MMP-Dependent

Cancer Cell Invasion. *Annu. Rev. Cell Dev. Biol.* **32**, 555–576 (2016).
145. Lodillinsky, C. *et al.* p63/MT1-MMP axis is required for in situ to invasive transition in basal-like breast cancer. *Oncogene* **35**, 344–357 (2016).
146. Sabeh, F. *et al.* Tumor cell traffic through the extracellular matrix is controlled by the membrane-anchored collagenase MT1-MMP. *J. Cell Biol.* **167**, 769–781 (2004).
147. Feinberg, T. Y. *et al.* Divergent Matrix-Remodeling Strategies Distinguish Developmental from Neoplastic Mammary Epithelial Cell Invasion Programs. *Dev. Cell* **47**, 145-160.e6 (2018).
148. Ardi, V. C., Kupriyanova, T. A., Deryugina, E. I. & Quigley, J. P. Human neutrophils uniquely release TIMP-free MMP-9 to provide a potent catalytic stimulator of angiogenesis. *Proc. Natl. Acad. Sci. U. S. A.* **104**, 20262–20267 (2007).
149. Madsen, D. H. *et al.* Tumor-Associated Macrophages Derived from Circulating Inflammatory Monocytes Degrade Collagen through Cellular Uptake. *Cell Rep.* **21**, 3662–3671 (2017).
150. Zajac, E. *et al.* Angiogenic capacity of M1- and M2-polarized macrophages is determined by the levels of TIMP-1 complexed with their secreted proMMP-9. *Blood* **122**, 4054–4067 (2013).
151. Deryugina, E. I. *et al.* Tissue-infiltrating neutrophils constitute the major in vivo source of angiogenesis-inducing MMP-9 in the tumor microenvironment. *Neoplasia* **16**, 771–788 (2014).
152. Stuelten, C. H. *et al.* Breast cancer cells induce stromal fibroblasts to express MMP-9 via secretion of TNF-alpha and TGF-beta. *J. Cell Sci.* **118**, 2143–2153 (2005).
153. Gaggioli, C. *et al.* Fibroblast-led collective invasion of carcinoma cells with differing roles for RhoGTPases in leading and following cells. *Nat. Cell Biol.* **9**, 1392–1400 (2007).
154. Goetz, J. G. *et al.* Biomechanical remodeling of the microenvironment by stromal caveolin-1 favors tumor invasion and metastasis. *Cell* **146**, 148–163 (2011).
155. Glentis, A. *et al.* Cancer-associated fibroblasts induce metalloprotease-independent cancer cell invasion of the basement membrane. *Nat. Commun.* **8**, 924 (2017).
156. Leask, A. A centralized communication network: Recent insights into the role of the cancer associated fibroblast in the development of drug resistance in tumors. *Semin. Cell Dev. Biol.* **101**, 111–114 (2020).
157. Kesh, K. *et al.* Therapy Resistance, Cancer Stem Cells and ECM in Cancer: The Matrix Reloaded. *Cancers (Basel).* **12**, (2020).
158. Saatci, O. *et al.* Targeting lysyl oxidase (LOX) overcomes chemotherapy resistance in triple negative breast cancer. *Nat. Commun.* **11**, 2416 (2020).
159. Helleman, J. *et al.* Association of an extracellular matrix gene cluster with breast cancer prognosis and endocrine therapy response. *Clin. Cancer Res.* **14**, 5555–5564 (2008).
160. Cordes, N., Blaese, M. A., Plasswilm, L., Rodemann, H. P. & Van Beuningen, D. Fibronectin and laminin increase resistance to ionizing radiation and the cytotoxic drug Ukrain in human tumour and normal cells in vitro. *Int. J. Radiat. Biol.* **79**, 709–720 (2003).
161. Peng, D. H. *et al.* Collagen promotes anti-PD-1/PD-L1 resistance in cancer through LAIR1-dependent CD8(+) T cell exhaustion. *Nat. Commun.* **11**, 4520 (2020).
162. Roma-Rodrigues, C., Mendes, R., Baptista, P. V & Fernandes, A. R. Targeting Tumor Microenvironment for Cancer Therapy. *Int. J. Mol. Sci.* **20**, (2019).
163. Neuzillet, C. *et al.* Targeting the TGFβ pathway for cancer therapy. *Pharmacol. Ther.* **147**, 22–31 (2015).
164. Winer, A., Adams, S. & Mignatti, P. Matrix Metalloproteinase Inhibitors in Cancer Therapy: Turning Past Failures Into Future Successes. *Mol. Cancer Ther.* **17**, 1147–1155 (2018).

165. Chan, N. *et al.* Influencing the Tumor Microenvironment: A Phase II Study of Copper Depletion Using Tetrathiomolybdate in Patients with Breast Cancer at High Risk for Recurrence and in Preclinical Models of Lung Metastases. *Clin. Cancer Res.* **23**, 666–676 (2017).
166. Chandel, N. S. Mitochondria as signaling organelles. *BMC Biol.* **12**, 34 (2014).
167. DeBerardinis, R. J., Lum, J. J., Hatzivassiliou, G. & Thompson, C. B. The biology of cancer: metabolic reprogramming fuels cell growth and proliferation. *Cell Metab.* **7**, 11–20 (2008).
168. Vander Heiden, M. G., Cantley, L. C. & Thompson, C. B. Understanding the Warburg effect: the metabolic requirements of cell proliferation. *Science* **324**, 1029–1033 (2009).
169. Warburg, O., Posener, K. & Negelein, E. The metabolism of cancer cells. *Biochem Z* **152**, 319–344 (1924).
170. Warburg, O. On respiratory impairment in cancer cells. *Science* **124**, 269–270 (1956).
171. DeBerardinis, R. J. & Thompson, C. B. Cellular metabolism and disease: what do metabolic outliers teach us? *Cell* **148**, 1132–1144 (2012).
172. Sciacovelli, M. *et al.* Fumarate is an epigenetic modifier that elicits epithelial-to-mesenchymal transition. *Nature* **537**, 544–547 (2016).
173. Wallace, D. C. Mitochondria and cancer. *Nat. Rev. Cancer* **12**, 685–698 (2012).
174. DeBerardinis, R. J. & Chandel, N. S. Fundamentals of cancer metabolism. *Sci. Adv.* **2**, e1600200 (2016).
175. Weinberg, F. *et al.* Mitochondrial metabolism and ROS generation are essential for Kras-mediated tumorigenicity. *Proc. Natl. Acad. Sci. U. S. A.* **107**, 8788–8793 (2010).
176. Whitaker-Menezes, D. *et al.* Hyperactivation of oxidative mitochondrial metabolism in epithelial cancer cells in situ: visualizing the therapeutic effects of metformin in tumor tissue. *Cell Cycle* **10**, 4047–4064 (2011).
177. Danhier, P. *et al.* Cancer metabolism in space and time: Beyond the Warburg effect. *Biochim. Biophys. acta. Bioenerg.* **1858**, 556–572 (2017).
178. Sonveaux, P. *et al.* Targeting lactate-fueled respiration selectively kills hypoxic tumor cells in mice. *J. Clin. Invest.* **118**, 3930–3942 (2008).
179. Bonuccelli, G. *et al.* Ketones and lactate 'fuel' tumor growth and metastasis: Evidence that epithelial cancer cells use oxidative mitochondrial metabolism. *Cell Cycle* **9**, 3506–3514 (2010).
180. Zheng, J. Energy metabolism of cancer: Glycolysis versus oxidative phosphorylation (Review). *Oncol. Lett.* **4**, 1151–1157 (2012).
181. DeBerardinis, R. J. *et al.* Beyond aerobic glycolysis: transformed cells can engage in glutamine metabolism that exceeds the requirement for protein and nucleotide synthesis. *Proc. Natl. Acad. Sci. U. S. A.* **104**, 19345–19350 (2007).
182. DeBerardinis, R. J. & Cheng, T. Q's next: the diverse functions of glutamine in metabolism, cell biology and cancer. *Oncogene* **29**, 313–324 (2010).
183. Pavlides, S. *et al.* The reverse Warburg effect: aerobic glycolysis in cancer associated fibroblasts and the tumor stroma. *Cell Cycle* **8**, 3984–4001 (2009).
184. Ko, Y.-H. *et al.* Glutamine fuels a vicious cycle of autophagy in the tumor stroma and oxidative mitochondrial metabolism in epithelial cancer cells: implications for preventing chemotherapy resistance. *Cancer Biol. Ther.* **12**, 1085–1097 (2011).
185. Lehuédé, C., Dupuy, F., Rabinovitch, R., Jones, R. G. & Siegel, P. M. Metabolic Plasticity as a Determinant of Tumor Growth and Metastasis. *Cancer Res.* **76**, 5201–5208 (2016).
186. Payen, V. L., Porporato, P. E., Baselet, B. & Sonveaux, P. Metabolic changes associated with tumor metastasis, part 1: tumor pH, glycolysis and the pentose phosphate pathway. *Cell. Mol. Life Sci.* **73**, 1333–1348 (2016).

187. Porporato, P. E., Payen, V. L., Baselet, B. & Sonveaux, P. Metabolic changes associated with tumor metastasis, part 2: Mitochondria, lipid and amino acid metabolism. *Cell. Mol. Life Sci.* **73**, 1349–1363 (2016).
188. Elia, I., Doglioni, G. & Fendt, S.-M. Metabolic Hallmarks of Metastasis Formation. *Trends Cell Biol.* **28**, 673–684 (2018).
189. Bergers, G. & Fendt, S.-M. The metabolism of cancer cells during metastasis. *Nat. Rev. Cancer* **21**, 162–180 (2021).
190. Schild, T., Low, V., Blenis, J. & Gomes, A. P. Unique Metabolic Adaptations Dictate Distal Organ-Specific Metastatic Colonization. *Cancer Cell* **33**, 347–354 (2018).
191. Andrzejewski, S. *et al.* PGC-1α Promotes Breast Cancer Metastasis and Confers Bioenergetic Flexibility against Metabolic Drugs. *Cell Metab.* **26**, 778-787.e5 (2017).
192. Elia, I. *et al.* Breast cancer cells rely on environmental pyruvate to shape the metastatic niche. *Nature* **568**, 117–121 (2019).
193. Davis, R. T. *et al.* Transcriptional diversity and bioenergetic shift in human breast cancer metastasis revealed by single-cell RNA sequencing. *Nat. Cell Biol.* **22**, 310–320 (2020).
194. Dupuy, F. *et al.* PDK1-Dependent Metabolic Reprogramming Dictates Metastatic Potential in Breast Cancer. *Cell Metab.* **22**, 577–589 (2015).
195. Ferraro, G. B. *et al.* Fatty acid synthesis is required for breast cancer brain metastasis. *Nat. Cancer* **2**, 414–428 (2021).
196. Tanabe, A. & Sahara, H. The Metabolic Heterogeneity and Flexibility of Cancer Stem Cells. *Cancers (Basel).* **12**, (2020).
197. Batlle, E. & Clevers, H. Cancer stem cells revisited. *Nat. Med.* **23**, 1124–1134 (2017).
198. Clevers, H. The cancer stem cell: premises, promises and challenges. *Nat. Med.* **17**, 313–319 (2011).
199. Albini, A. *et al.* Cancer stem cells and the tumor microenvironment: interplay in tumor heterogeneity. *Connect. Tissue Res.* **56**, 414–425 (2015).
200. Lytle, N. K., Barber, A. G. & Reya, T. Stem cell fate in cancer growth, progression and therapy resistance. *Nat. Rev. Cancer* **18**, 669–680 (2018).
201. Rabinovich, I. *et al.* Cancer stem cell markers ALDH1 and CD44+/CD24- phenotype and their prognosis impact in invasive ductal carcinoma. *Eur. J. Histochem.* **62**, (2018).
202. Ponti, D. *et al.* Isolation and in vitro propagation of tumorigenic breast cancer cells with stem/progenitor cell properties. *Cancer Res.* **65**, 5506–5511 (2005).
203. Fillmore, C. M. & Kuperwasser, C. Human breast cancer cell lines contain stem-like cells that self-renew, give rise to phenotypically diverse progeny and survive chemotherapy. *Breast Cancer Res.* **10**, R25 (2008).
204. Charafe-Jauffret, E. *et al.* Breast cancer cell lines contain functional cancer stem cells with metastatic capacity and a distinct molecular signature. *Cancer Res.* **69**, 1302–1313 (2009).
205. Zhang, X., Powell, K. & Li, L. Breast Cancer Stem Cells: Biomarkers, Identification and Isolation Methods, Regulating Mechanisms, Cellular Origin, and Beyond. *Cancers (Basel).* **12**, (2020).
206. Al-Hajj, M., Wicha, M. S., Benito-Hernandez, A., Morrison, S. J. & Clarke, M. F. Prospective identification of tumorigenic breast cancer cells. *Proc. Natl. Acad. Sci. U. S. A.* **100**, 3983–3988 (2003).
207. Ginestier, C. *et al.* ALDH1 is a marker of normal and malignant human mammary stem cells and a predictor of poor clinical outcome. *Cell Stem Cell* **1**, 555–567 (2007).
208. Yang, L. *et al.* Targeting cancer stem cell pathways for cancer therapy. *Signal Transduct. Target. Ther.* **5**, 8 (2020).
209. Peng, F. *et al.* Glycolysis gatekeeper PDK1 reprograms breast cancer stem cells under

hypoxia. *Oncogene* **37**, 1062–1074 (2018).
210. Ciavardelli, D. *et al.* Breast cancer stem cells rely on fermentative glycolysis and are sensitive to 2-deoxyglucose treatment. *Cell Death Dis.* **5**, e1336 (2014).
211. Dong, C. *et al.* Loss of FBP1 by Snail-Mediated Repression Provides Metabolic Advantages in Basal-like Breast Cancer. *Cancer Cell* **23**, 316–331 (2013).
212. Nakano, A. *et al.* Glycolysis inhibition inactivates ABC transporters to restore drug sensitivity in malignant cells. *PLoS One* **6**, e27222 (2011).
213. Lee, K.-M. *et al.* MYC and MCL1 Cooperatively Promote Chemotherapy-Resistant Breast Cancer Stem Cells via Regulation of Mitochondrial Oxidative Phosphorylation. *Cell Metab.* **26**, 633-647.e7 (2017).
214. Han, S. *et al.* CPT1A/2-Mediated FAO Enhancement—A Metabolic Target in Radioresistant Breast Cancer. *Frontiers in Oncology* vol. 9 (2019).
215. Wang, T. *et al.* JAK/STAT3-Regulated Fatty Acid β-Oxidation Is Critical for Breast Cancer Stem Cell Self-Renewal and Chemoresistance. *Cell Metab.* **27**, 136-150.e5 (2018).
216. Fabian, M. R., Sonenberg, N. & Filipowicz, W. Regulation of mRNA translation and stability by microRNAs. *Annu. Rev. Biochem.* **79**, 351–379 (2010).
217. Sonenberg, N. & Hinnebusch, A. G. Regulation of translation initiation in eukaryotes: mechanisms and biological targets. *Cell* **136**, 731–745 (2009).
218. Jackson, R. J., Hellen, C. U. T. & Pestova, T. V. The mechanism of eukaryotic translation initiation and principles of its regulation. *Nat. Rev. Mol. Cell Biol.* **11**, 113–127 (2010).
219. Gingras, A. C., Raught, B. & Sonenberg, N. eIF4 initiation factors: effectors of mRNA recruitment to ribosomes and regulators of translation. *Annu. Rev. Biochem.* **68**, 913–963 (1999).
220. Sonenberg, N., Morgan, M. A., Merrick, W. C. & Shatkin, A. J. A polypeptide in eukaryotic initiation factors that crosslinks specifically to the 5'-terminal cap in mRNA. *Proc. Natl. Acad. Sci. U. S. A.* **75**, 4843–4847 (1978).
221. Sonenberg, N., Rupprecht, K. M., Hecht, S. M. & Shatkin, A. J. Eukaryotic mRNA cap binding protein: purification by affinity chromatography on sepharose-coupled m7GDP. *Proc. Natl. Acad. Sci. U. S. A.* **76**, 4345–4349 (1979).
222. Haghighat, A. & Sonenberg, N. eIF4G Dramatically Enhances the Binding of eIF4E to the mRNA 5′-Cap Structure. *J. Biol. Chem.* **272**, 21677–21680 (1997).
223. Castelli, L. M. *et al.* The 4E-BP Caf20p Mediates Both eIF4E-Dependent and Independent Repression of Translation. *PLoS Genet.* **11**, e1005233 (2015).
224. Flynn, A. & Proud, C. G. Serine 209, not serine 53, is the major site of phosphorylation in initiation factor eIF-4E in serum-treated Chinese hamster ovary cells. *J. Biol. Chem.* **270**, 21684–21688 (1995).
225. Waskiewicz, A. J. *et al.* Phosphorylation of the cap-binding protein eukaryotic translation initiation factor 4E by protein kinase Mnk1 in vivo. *Mol. Cell. Biol.* **19**, 1871–1880 (1999).
226. Topisirovic, I., Ruiz-Gutierrez, M. & Borden, K. L. B. Phosphorylation of the eukaryotic translation initiation factor eIF4E contributes to its transformation and mRNA transport activities. *Cancer Res.* **64**, 8639–8642 (2004).
227. Furic, L. *et al.* eIF4E phosphorylation promotes tumorigenesis and is associated with prostate cancer progression. *Proc. Natl. Acad. Sci. U. S. A.* **107**, 14134–14139 (2010).
228. Robichaud, N. *et al.* Translational control in the tumor microenvironment promotes lung metastasis: Phosphorylation of eIF4E in neutrophils. *Proc. Natl. Acad. Sci. U. S. A.* **115**, E2202–E2209 (2018).
229. Robichaud, N. *et al.* Phosphorylation of eIF4E promotes EMT and metastasis via translational control of SNAIL and MMP-3. *Oncogene* **34**, 2032–2042 (2015).
230. Truitt, M. L. *et al.* Differential Requirements for eIF4E Dose in Normal Development and

Cancer. *Cell* **162**, 59–71 (2015).
231. Fukunaga, R. & Hunter, T. MNK1, a new MAP kinase-activated protein kinase, isolated by a novel expression screening method for identifying protein kinase substrates. *EMBO J.* **16**, 1921–1933 (1997).
232. Waskiewicz, A. J., Flynn, A., Proud, C. G. & Cooper, J. A. Mitogen-activated protein kinases activate the serine/threonine kinases Mnk1 and Mnk2. *EMBO J.* **16**, 1909–1920 (1997).
233. O'Loghlen, A. *et al.* Identification and molecular characterization of Mnk1b, a splice variant of human MAP kinase-interacting kinase Mnk1. *Exp. Cell Res.* **299**, 343–355 (2004).
234. Slentz-Kesler, K. *et al.* Identification of the human Mnk2 gene (MKNK2) through protein interaction with estrogen receptor beta. *Genomics* **69**, 63–71 (2000).
235. Scheper, G. C., Morrice, N. A., Kleijn, M. & Proud, C. G. The mitogen-activated protein kinase signal-integrating kinase Mnk2 is a eukaryotic initiation factor 4E kinase with high levels of basal activity in mammalian cells. *Mol. Cell. Biol.* **21**, 743–754 (2001).
236. Parra, J. L., Buxadé, M. & Proud, C. G. Features of the catalytic domains and C termini of the MAPK signal-integrating kinases Mnk1 and Mnk2 determine their differing activities and regulatory properties. *J. Biol. Chem.* **280**, 37623–37633 (2005).
237. Zhan, Y. *et al.* MNK1/2 inhibition limits oncogenicity and metastasis of KIT-mutant melanoma. *J. Clin. Invest.* **127**, 4179–4192 (2017).
238. Huang, F. *et al.* Inhibiting the MNK1/2-eIF4E axis impairs melanoma phenotype switching and potentiates antitumor immune responses. *J. Clin. Invest.* **131**, (2021).
239. Sorrells, D. L. *et al.* Detection of eIF4E gene amplification in breast cancer by competitive PCR. *Ann. Surg. Oncol.* **5**, 232–237 (1998).
240. Carter, J. H. *et al.* Phosphorylation of eIF4E serine 209 is associated with tumour progression and reduced survival in malignant melanoma. *Br. J. Cancer* **114**, 444–453 (2016).
241. Guo, Q. *et al.* The MNK1/2-eIF4E Axis Supports Immune Suppression and Metastasis in Postpartum Breast Cancer. *Cancer Res.* **81**, 3876–3889 (2021).
242. Guo, Q. *et al.* MNK1/NODAL Signaling Promotes Invasive Progression of Breast Ductal Carcinoma In Situ. *Cancer Res.* **79**, 1646–1657 (2019).
243. Bartish, M. *et al.* MNK2 governs the macrophage antiinflammatory phenotype. *Proc. Natl. Acad. Sci. U. S. A.* **117**, 27556–27565 (2020).
244. Gerson-Gurwitz, A. *et al.* Zotatifin, an eIF4A-Selective Inhibitor, Blocks Tumor Growth in Receptor Tyrosine Kinase Driven Tumors. *Frontiers in Oncology* vol. 11 (2021).
245. Wu, M., Zhang, C., Li, X.-J., Liu, Q. & Wanggou, S. Anti-Cancer Effect of Cap-Translation Inhibitor 4EGI-1 in Human Glioma U87 Cells: Involvement of Mitochondrial Dysfunction and ER Stress. *Cell. Physiol. Biochem.* **40**, 1013–1028 (2016).
246. Descamps, G. *et al.* The cap-translation inhibitor 4EGI-1 induces apoptosis in multiple myeloma through Noxa induction. *Br. J. Cancer* **106**, 1660–1667 (2012).
247. Chen, L. *et al.* Tumor suppression by small molecule inhibitors of translation initiation. *Oncotarget* **3**, 869–881 (2012).
248. Yi, T., Kabha, E., Papadopoulos, E. & Wagner, G. 4EGI-1 targets breast cancer stem cells by selective inhibition of translation that persists in CSC maintenance, proliferation and metastasis. *Oncotarget* **5**, 6028–6037 (2014).
249. Li, Z. *et al.* Inhibiting the MNK-eIF4E-β-catenin axis increases the responsiveness of aggressive breast cancer cells to chemotherapy. *Oncotarget* **8**, 2906–2915 (2017).
250. Sun, X. *et al.* Tumour DDR1 promotes collagen fibre alignment to instigate immune exclusion. *Nature* (2021) doi:10.1038/s41586-021-04057-2.

251. Huo, C. W. *et al.* High mammographic density is associated with an increase in stromal collagen and immune cells within the mammary epithelium. *Breast Cancer Res.* **17**, 79 (2015).
252. Huo, C. W. *et al.* High mammographic density in women is associated with protumor inflammation. *Breast Cancer Res.* **20**, 92 (2018).
253. Wang, L., Zhang, S. & Wang, X. The Metabolic Mechanisms of Breast Cancer Metastasis. *Frontiers in Oncology* vol. 10 (2021).
254. Raez, L. E. *et al.* A phase I dose-escalation trial of 2-deoxy-D-glucose alone or combined with docetaxel in patients with advanced solid tumors. *Cancer Chemother. Pharmacol.* **71**, 523–530 (2013).
255. Ben Sahra, I., Le Marchand-Brustel, Y., Tanti, J.-F. & Bost, F. Metformin in cancer therapy: a new perspective for an old antidiabetic drug? *Mol. Cancer Ther.* **9**, 1092–1099 (2010).
256. Sonnenblick, A. *et al.* Impact of Diabetes, Insulin, and Metformin Use on the Outcome of Patients With Human Epidermal Growth Factor Receptor 2-Positive Primary Breast Cancer: Analysis From the ALTTO Phase III Randomized Trial. *J. Clin. Oncol.* **35**, 1421–1429 (2017).
257. Zhao, Y. *et al.* A randomized phase II study of aromatase inhibitors plus metformin in pre-treated postmenopausal patients with hormone receptor positive metastatic breast cancer. *Oncotarget* **8**, 84224–84236 (2017).
258. Lega, I. C., Fung, K., Austin, P. C. & Lipscombe, L. L. Metformin and breast cancer stage at diagnosis: a population-based study. *Curr. Oncol.* **24**, e85–e91 (2017).
259. Bartman, C. R. *et al.* Slow TCA flux and ATP production in primary solid tumours but not metastases. *Nature* **614**, 349–357 (2023).
260. Gubser, P. M. *et al.* Rapid effector function of memory CD8+ T cells requires an immediate-early glycolytic switch. *Nat. Immunol.* **14**, 1064–1072 (2013).
261. Menk, A. V *et al.* Early TCR Signaling Induces Rapid Aerobic Glycolysis Enabling Distinct Acute T Cell Effector Functions. *Cell Rep.* **22**, 1509–1521 (2018).
262. Huang, J. T. & Schneider, R. J. Adenovirus inhibition of cellular protein synthesis involves inactivation of cap-binding protein. *Cell* **65**, 271–280 (1991).
263. Morley, S. J., Rau, M., Kay, J. E. & Pain, V. M. Increased phosphorylation of eukaryotic initiation factor 4 alpha during activation of T lymphocytes correlates with increased eIF-4F complex formation. *Biochem. Soc. Trans.* **21**, 397S (1993).
264. Boal, T. R. *et al.* Regulation of eukaryotic translation initiation factor expression during T-cell activation. *Biochim. Biophys. Acta* **1176**, 257–264 (1993).
265. Beretta, L. *et al.* Differential regulation of translation and eIF4E phosphorylation during human thymocyte maturation. *J. Immunol.* **160**, 3269–3273 (1998).
266. Takei, N., Kawamura, M., Hara, K., Yonezawa, K. & Nawa, H. Brain-derived neurotrophic factor enhances neuronal translation by activating multiple initiation processes: comparison with the effects of insulin. *J. Biol. Chem.* **276**, 42818–42825 (2001).
267. Dyer, J. R. *et al.* An activity-dependent switch to cap-independent translation triggered by eIF4E dephosphorylation. *Nat. Neurosci.* **6**, 219–220 (2003).
268. McKendrick, L., Morley, S. J., Pain, V. M., Jagus, R. & Joshi, B. Phosphorylation of eukaryotic initiation factor 4E (eIF4E) at Ser209 is not required for protein synthesis in vitro and in vivo. *Eur. J. Biochem.* **268**, 5375–5385 (2001).
269. Morley, S. J. & Naegele, S. Phosphorylation of eukaryotic initiation factor (eIF) 4E is not required for de novo protein synthesis following recovery from hypertonic stress in human kidney cells. *J. Biol. Chem.* **277**, 32855–32859 (2002).
270. Knauf, U., Tschopp, C. & Gram, H. Negative regulation of protein translation by mitogen-

activated protein kinase-interacting kinases 1 and 2. *Mol. Cell. Biol.* **21**, 5500–5511 (2001).
271. Marcotrigiano, J., Gingras, A.-C., Sonenberg, N. & Burley, S. K. Cocrystal Structure of the Messenger RNA 5' Cap-Binding Protein (eIF4E) Bound to 7-methyl-GDP. *Cell* **89**, 951–961 (1997).
272. Shibata, S., Morino, S., Tomoo, K., In, Y. & Ishida, T. Effect of mRNA cap structure on eIF-4E phosphorylation and cap binding analyses using Ser209-mutated eIF-4Es. *Biochem. Biophys. Res. Commun.* **247**, 213–216 (1998).
273. Minich, W. B., Balasta, M. L., Goss, D. J. & Rhoads, R. E. Chromatographic resolution of in vivo phosphorylated and nonphosphorylated eukaryotic translation initiation factor eIF-4E: increased cap affinity of the phosphorylated form. *Proc. Natl. Acad. Sci. U. S. A.* **91**, 7668–7672 (1994).
274. Lama, D. & Verma, C. S. Deciphering the mechanistic effects of eIF4E phosphorylation on mRNA-cap recognition. *Protein Sci.* **29**, 1373–1386 (2020).
275. Scheper, G. C. *et al.* Phosphorylation of eukaryotic initiation factor 4E markedly reduces its affinity for capped mRNA. *J. Biol. Chem.* **277**, 3303–3309 (2002).
276. Hefner, Y. *et al.* Serine 727 phosphorylation and activation of cytosolic phospholipase A2 by MNK1-related protein kinases. *J. Biol. Chem.* **275**, 37542–37551 (2000).
277. Buxadé, M., Morrice, N., Krebs, D. L. & Proud, C. G. The PSF.p54nrb complex is a novel Mnk substrate that binds the mRNA for tumor necrosis factor alpha. *J. Biol. Chem.* **283**, 57–65 (2008).
278. Buxadé, M. *et al.* The Mnks are novel components in the control of TNF alpha biosynthesis and phosphorylate and regulate hnRNP A1. *Immunity* **23**, 177–189 (2005).
279. Edwin, F., Anderson, K. & Patel, T. B. HECT domain-containing E3 ubiquitin ligase Nedd4 interacts with and ubiquitinates Sprouty2. *J. Biol. Chem.* **285**, 255–264 (2010).
280. DaSilva, J., Xu, L., Kim, H. J., Miller, W. T. & Bar-Sagi, D. Regulation of sprouty stability by Mnk1-dependent phosphorylation. *Mol. Cell. Biol.* **26**, 1898–1907 (2006).
281. Linkous, A. & Yazlovitskaya, E. Cytosolic phospholipase A2 as a mediator of disease pathogenesis. *Cell. Microbiol.* **12**, 1369–1377 (2010).
282. Mitobe, Y. *et al.* PSF Promotes ER-Positive Breast Cancer Progression via Posttranscriptional Regulation of ESR1 and SCFD2. *Cancer Res.* **80**, 2230–2242 (2020).
283. Tsukahara, T., Haniu, H. & Matsuda, Y. PTB-associated splicing factor (PSF) is a PPARγ-binding protein and growth regulator of colon cancer cells. *PLoS One* **8**, e58749 (2013).
284. Tsukahara, T., Matsuda, Y. & Haniu, H. PSF knockdown enhances apoptosis via downregulation of LC3B in human colon cancer cells. *Biomed Res. Int.* **2013**, 204973 (2013).
285. Roy, R., Huang, Y., Seckl, M. J. & Pardo, O. E. Emerging roles of hnRNPA1 in modulating malignant transformation. *Wiley Interdiscip. Rev. RNA* **8**, (2017).
286. Chen, Y. *et al.* High expression of hnRNPA1 promotes cell invasion by inducing EMT in gastric cancer. *Oncol. Rep.* **39**, 1693–1701 (2018).
287. Park, J.-W. *et al.* Sprouty2 enhances the tumorigenic potential of glioblastoma cells. *Neuro. Oncol.* **20**, 1044–1054 (2018).
288. Saini, M., Verma, A. & Mathew, S. J. SPRY2 is a novel MET interactor that regulates metastatic potential and differentiation in rhabdomyosarcoma. *Cell Death Dis.* **9**, 237 (2018).
289. Agorku, D. J. *et al.* CD49b, CD87, and CD95 Are Markers for Activated Cancer-Associated Fibroblasts Whereas CD39 Marks Quiescent Normal Fibroblasts in Murine Tumor Models. *Frontiers in Oncology* vol. 9 (2019).

290. Costa, A. *et al.* Fibroblast Heterogeneity and Immunosuppressive Environment in Human Breast Cancer. *Cancer Cell* **33**, 463-479.e10 (2018).
291. Bartoschek, M. *et al.* Spatially and functionally distinct subclasses of breast cancer-associated fibroblasts revealed by single cell RNA sequencing. *Nat. Commun.* **9**, 5150 (2018).
292. Pelon, F. *et al.* Cancer-associated fibroblast heterogeneity in axillary lymph nodes drives metastases in breast cancer through complementary mechanisms. *Nat. Commun.* **11**, 404 (2020).
293. Venning, F. A. *et al.* Deciphering the temporal heterogeneity of cancer-associated fibroblast subpopulations in breast cancer. *J. Exp. Clin. Cancer Res.* **40**, 175 (2021).
294. Kieffer, Y. *et al.* Single-Cell Analysis Reveals Fibroblast Clusters Linked to Immunotherapy Resistance in Cancer. *Cancer Discov.* **10**, 1330–1351 (2020).
295. Cremasco, V. *et al.* FAP Delineates Heterogeneous and Functionally Divergent Stromal Cells in Immune-Excluded Breast Tumors. *Cancer Immunol. Res.* **6**, 1472–1485 (2018).
296. Sebastian, A. *et al.* Single-Cell Transcriptomic Analysis of Tumor-Derived Fibroblasts and Normal Tissue-Resident Fibroblasts Reveals Fibroblast Heterogeneity in Breast Cancer. *Cancers* vol. 12 (2020).
297. Elyada, E. *et al.* Cross-Species Single-Cell Analysis of Pancreatic Ductal Adenocarcinoma Reveals Antigen-Presenting Cancer-Associated Fibroblasts. *Cancer Discov.* **9**, 1102–1123 (2019).
298. Argüello, R. J. *et al.* SCENITH: A Flow Cytometry-Based Method to Functionally Profile Energy Metabolism with Single-Cell Resolution. *Cell Metab.* **32**, 1063-1075.e7 (2020).
299. Siegel, R. L. *et al.* Colorectal cancer statistics, 2017. *CA. Cancer J. Clin.* **67**, 177–193 (2017).
300. Siegel, R. L., Miller, K. D. & Jemal, A. Cancer statistics, 2020. *CA. Cancer J. Clin.* **70**, 7–30 (2020).
301. Cronin, K. A. *et al.* Annual Report to the Nation on the Status of Cancer, part I: National cancer statistics. *Cancer* **124**, 2785–2800 (2018).
302. Bengtsson, A., Andersson, R. & Ansari, D. The actual 5-year survivors of pancreatic ductal adenocarcinoma based on real-world data. *Sci. Rep.* **10**, 16425 (2020).
303. La Vecchia, S. & Sebastián, C. Metabolic pathways regulating colorectal cancer initiation and progression. *Semin. Cell Dev. Biol.* **98**, 63–70 (2020).
304. Barker, N. *et al.* Crypt stem cells as the cells-of-origin of intestinal cancer. *Nature* **457**, 608–611 (2009).
305. Merlos-Suárez, A. *et al.* The Intestinal Stem Cell Signature Identifies Colorectal Cancer Stem Cells and Predicts Disease Relapse. *Cell Stem Cell* **8**, 511–524 (2011).
306. Zhao, S. *et al.* LncRNA MIR17HG promotes colorectal cancer liver metastasis by mediating a glycolysis-associated positive feedback circuit. *Oncogene* **40**, 4709–4724 (2021).
307. Ying, H. *et al.* Oncogenic Kras maintains pancreatic tumors through regulation of anabolic glucose metabolism. *Cell* **149**, 656–670 (2012).
308. Viale, A. *et al.* Oncogene ablation-resistant pancreatic cancer cells depend on mitochondrial function. *Nature* **514**, 628–632 (2014).
309. Nimmakayala, R. K. *et al.* Metabolic programming of distinct cancer stem cells promotes metastasis of pancreatic ductal adenocarcinoma. *Oncogene* **40**, 215–231 (2021).